Inclusive Jet and Dijet Production
in Polarized Proton-Proton Collisions
at $\sqrt{s}$ =200 GeV at RHIC

by

Tai Sakuma

Submitted to the Department of Physics
in partial fulfillment of the requirements for the degree of

Doctor of Science

at the

MASSACHUSETTS INSTITUTE OF TECHNOLOGY

February 2010

Author . . . .
Department of Physics
December 30, 2009

Certified by . . . .
Bernd Surrow
Associate Professor of Physics
Thesis Supervisor

Accepted by . . . .
Krishna Rajagopal
Professor of Physics; Associate Head for Education, Physics

Inclusive Jet and Dijet Production

in Polarized Proton-Proton Collisions

at $\sqrt{s}$ =200 GeV at RHIC

by

Tai Sakuma

Abstract

The inclusive jet cross section, the dijet cross section, and the dijet longitudinal double spin asymmetry $\mathcal{A}_{\mathrm{LL}}$ in polarized proton-proton collisions at $\sqrt{s} = 200$ GeV are measured with a data sample of 5.4 pb^{-1} collected with the STAR detector during RHIC Run-6. The inclusive jet cross section is measured as a function of jet transverse momentum p_{T} in the range of $13 < p_{\mathrm{T}} < 66$ GeV in the mid-rapidity region $|\eta| \leq 0.8$. The results are in agreement with NLO pQCD predictions. The dijet cross section and the dijet $\mathcal{A}_{\mathrm{LL}}$ are measured as a function of dijet mass M_{jj} in the range of $24 < M_{\mathrm{jj}} < 118$ GeV. The dijet cross section is in agreement with NLO pQCD predictions. The dijet $\mathcal{A}_{\mathrm{LL}}$ is compared with NLO pQCD predictions based on various parametrizations of polarized gluon distributions of the proton. The results are inconsistent with large gluon polarization and expected to lead to a constrain on the polarized gluon distribution.

Thesis Supervisor: Bernd Surrow
Title: Associate Professor of Physics

Acknowledgments

I would like to thank Bernd Surrow for letting me work on important topics in the field. I would like to thank Robert Redwine for his guidance.

I would like to thank Renee Fatemi and Stephen Trentalange for their feedback on the analysis and the thesis.

I would like to thank Sheela Marston for her friendship and the sweater.

I would like to thank Mariya Barch for being supportive.

I would like to thank Naohito Saito for his encouragement in pursuing my academic career.

Contents

Chapter 1

Introduction

Spin in Static Constituent Quark Model of the Proton

In a model of the proton, the proton is composed of three stationary massive quarks, each of which weighs approximately one third of the proton mass. This model, called the *static constituent quark model*, is the simplest model of the proton. It can correctly reproduce many properties of the proton from the quantum numbers of the three quarks. For example; the charge of the proton is the sum of the charge of the three quarks; the isospin of the proton is a spin sum of the isospin of the three quarks; the magnetic moment of the proton is approximately equal to the expectation value of the sum of the magnetic momentum operators of the three quarks for the totally antisymmetric three quark state.

The static constituent quark model, however, incorrectly attributes the proton spin to the spin of the three quarks. In this model, the quarks are in the *s*-wave state and possess no orbital angular momentum; the spin of the proton is equal to a spin sum of the spin of the three quarks, i.e., the fraction of the proton spin carried by the quark spin (Σ) is one: $\Sigma = 1$. This model prediction has been disproved by experimental results.

Polarized Deep Inelastic Scattering and "*Spin Crisis*"

Deep inelastic scattering (DIS) is widely used to probe the structure of the proton. It is a scattering of leptons from hadrons in the kinematic region in which the scattering

3

can be considered as a process in which the leptons strike almost free *partons*, namely, almost free quarks. DIS is the process that led to the discovery of quarks inside of the proton in 1969[1]. The advantage of using leptons as a probe is due to the fact that leptons have no internal structure and do not clutter up the environment with their fragments as composite particles would do. The spin structure of the proton can be probed with *polarized deep inelastic scattering* (pDIS), in which the spin states of both initial leptons and initial hadrons are polarized.

In 1988, by using pDIS, the European Muon Collaboration (EMC) reported that the fraction of the proton spin carried by the quark spin is small; $\Sigma = 0.14 \pm 0.9 \pm 0.21$ [2], contradicting the static constituent quark model. This contradiction is referred to as "*spin crisis*." More recent result from the COMPASS experiment showed a larger value; $\Sigma = 0.33 \pm 0.03 \pm 0.05$ [3], but it holds that the quark spin carries a small fraction of the proton spin.

Spin in Relativistic Constituent Quark Model of the Proton

The prediction of the static constituent quark model, $\Sigma = 1$, is altered when the motion of the quarks is taken into account. Quarks inside the proton are not as massive or stationary as hypothesized in the static constituent quark model. On the contrary, their mass is tiny, less than 1% of the proton mass, and their motion is highly relativistic; a large fraction of the proton mass is due to the kinetic energy of the quarks. Relativistic motion of a quark obeys the Dirac equation, solutions to which in a spherical potential of a proton model indicate the orbital motion of the quark. In *relativistic constituent quark models*, about 35% of the proton spin is carried by the orbital motion of the quarks, and the quark spin contributes about 65% of the proton spin, i.e., $\Sigma \simeq 0.65$, which however still contradicts the measured value.

Quantum Chromodynamics and Gluon Spin

In relativistic constituent quark models, the motion of quarks is considered, whereas the dynamics of quarks is ignored. The *strong interaction*, the dynamic force that binds quarks into protons, is described by a quantum gauge field theory, *quantum*

chromodynamics (QCD). In QCD, the strong interaction is mediated by *gluons*, vector bosons of the theory, and the charge of the strong interaction is called *color*, which takes one of three values. QCD has a distinctive feature called *asymptotic freedom*. It is the property in which the coupling of the strong interaction is weak at a large momentum scale and strong at a small momentum scale.

QCD allows the gluon spin to share the proton spin with the quark spin. The quark spin contribution is proportional to the expectation value of quark axial-vector current operators for the proton state. In general, an axial-vector current is not conserved in the presence of vector fields, in this case gluons, unless the gauge invariance is abandoned. This feature, called *axial anomaly*, permits that the gluon spin contribution to the proton spin, ΔG, to have a non-zero value [4].

Polarized Deep Inelastic Scattering and ΔG

Because leptons do not directly couple with gluons, polarized deep inelastic scattering is not as sensitive to ΔG as it is to Σ. Even so, dynamics of the gluons slightly influence deep inelastic scattering in the form of the Q^2-*evolution*. Several analyses have been carried out to extract ΔG from the Q^2-evolution. However, since the Q^2-evolution is slow and the present pDIS data cover a limited range of Q^2, ΔG is little constrained from the existing pDIS data [5, 6, 7, 8, 9].

Although gluons are not involved in *leading-order* processes in DIS, they are in some *higher-order* processes. Such processes can be detected by observing hadrons in final states simultaneously with scattered leptons, *semi-inclusive deep inelastic scattering* (SIDIS). ΔG has been somewhat restricted by polarized SIDIS [10, 11, 12, 13].

ΔG and Polarized Proton-proton Collisions at RHIC

In *proton-proton collisions*, on the other hand, gluons participate in leading-order processes. The *Relativistic Heavy Ion Collider* (RHIC) in the *Brookhaven National Laboratory* is the world first polarized proton-proton collider, which has been in operation since 2000. The spin program at RHIC, *RHIC-Spin*, aims to probe the spin structure

of the proton, in particular gluons, and determine ΔG by using *polarized proton-proton collisions*.

Parton-level Kinematics and Dijets

Probing the proton structure with proton-proton collisions is more complicated than with deep inelastic scattering in the sense that it is more difficult to determine the kinematics of parton-level interactions. In two-particle-to-two-particle interactions in which the momenta of the two initial particles are on the fixed axis, the momenta of the four particles are determined if the momenta of one initial particle and one final particle or the momenta of the two final particles are known.

In DIS, kinematics of parton-level interactions can be always determined since the momenta of initial and final leptons are known; the initial momenta of the leptons are fixed by beam energy, and the final momenta of the leptons can be measured.

In proton-proton collisions, however, the initial momenta of partons are not fixed by beam energy. Therefore, the momenta of both final particles are needed in order to determine the kinematics of parton-level interactions. When final states of the parton-level interactions are quarks or gluons, they are subject to *confinement*; these final state particles fragment into many hadrons and can be observed as *jets* of particles. A possible way to determine the kinematics of parton-level interaction is to measure two jets in final states, *dijets*, and estimate the momenta of the partons from properties of the dijets, which is the main topic of this thesis.

Jets and the STAR Detector

The *STAR detector* is installed at one of the two locations at which RHIC can collide *longitudinally* polarized protons. The STAR detector is well suited for a measurement of jets. It has full-azimuth calorimeter which measures the energy and the momentum directions of neutral particles, and tracking devices which measure the momenta of charged particles. Jets can be reconstructed from data collected with the calorimeter and the tracking devices.

Double Longitudinal Spin Asymmetry $\mathcal{A}_{\mathrm{LL}}$

The *double longitudinal spin asymmetry* $\mathcal{A}_{\mathrm{LL}}$ is an asymmetry of the cross sections in polarized proton-proton collisions with the parallel and anti-parallel initial polarization states. $\mathcal{A}_{\mathrm{LL}}$, which is sensitive to ΔG, is primary quantity to measure to investigate the spin structure of the proton. This thesis presents the first measurement of the dijet $\mathcal{A}_{\mathrm{LL}}$ after it shows the cross sections of the inclusive jet and dijet productions.

Part I

Spin Physics
and
the STAR Experiment

Chapter 2

Gluon Polarization in the Proton

The proton spin can be carried by the spin and the orbital motion of the quarks and the gluons:

$$\frac{1}{2} = \frac{1}{2}\Sigma + \Delta G + L_q + L_g,$$

where Σ, ΔG, L_q, and L_g are the contributions from the quark spin, the gluon spin, the orbital motion of the quarks, and the orbital motion of the gluons, respectively. The quark spin contribution Σ has been measured by polarized deep inelastic scattering; a recent result is $\Sigma = 0.33 \pm 0.03 \pm 0.05$ [3]. The quark spin contributes only a fraction of the proton spin.

The primary object of the RHIC-Spin program is to measure the gluon spin contribution ΔG. The gluon's contribution ΔG is the first moment of the *polarized gluon distribution function* $\Delta g(x)$:

$$\Delta G = \int_0^1 \Delta g(x)\mathrm{d}x.$$

The polarized gluon distribution is the difference between the parton distributions for gluons with the spin parallel and anti-parallel to the spin of the proton:

$$\Delta g(x, Q^2) = g^+(x, Q^2) - g^-(x, Q^2). \tag{2.1}$$

ΔG can be experimentally measured by constraining $\Delta g(x)$.

In longitudinally polarized proton-proton collisions, the *longitudinal double spin asymmetry* $\mathcal{A}_{\mathrm{LL}}$ is defined as the ratio of the difference and the sum of the cross sections for parallel and anti-parallel initial spin states as follows:

$$\mathcal{A}_{\mathrm{LL}} = \frac{\Delta\sigma}{\sigma} = \frac{(\sigma^{++} + \sigma^{--}) - (\sigma^{+-} + \sigma^{-+})}{(\sigma^{++} + \sigma^{--}) + (\sigma^{+-} + \sigma^{-+})},$$

where the superscripts $\pm$ of the cross sections $\sigma^{\pm\pm}$ indicate the spin states of the two colliding protons. $\mathcal{A}_{\mathrm{LL}}$ is the primary quantity to measure as this quantity is sensitive to the polarized gluon distribution of the proton. In the framework of the *QCD factorization*, $\mathcal{A}_{\mathrm{LL}}$ can be interpreted as:

$$\mathcal{A}_{\mathrm{LL}} = \frac{\displaystyle\sum_{i,j} \int \mathrm{d}x_1 \int \mathrm{d}x_2 \Delta f_i(x_1, Q^2) \Delta f_j(x_2, Q^2) \hat{a}_{\mathrm{LL}} \hat{\sigma}(\cos\theta^*)}{\displaystyle\sum_{i,j} \int \mathrm{d}x_1 \int \mathrm{d}x_2 f_i(x_1, Q^2) f_j(x_2, Q^2) \hat{\sigma}(\cos\theta^*)}. \tag{2.2}$$

Parton-level cross section $\hat{\sigma}(\cos\theta^*)$ and spin asymmetry $\hat{a}_{\mathrm{LL}}(\cos\theta^*)$ can be calculated with *perturbative QCD*. Unpolarized parton distributions $f_i(x_2, Q^2)$ are well measured by unpolarized experiments. When $\mathcal{A}_{\mathrm{LL}}$ is measured, polarized parton distributions $\Delta f_i(x_1, Q^2)$ are related to known quantities in the formula.

It is important to verify if $\mathcal{A}_{\mathrm{LL}}$ can be interpreted in the framework of the QCD factorization. This can be done by the cross section:

$$\sigma = \sum_{i,j} \int \mathrm{d}x_1 \int \mathrm{d}x_2 f_i(x_1, Q^2) f_j(x_2, Q^2) \hat{\sigma}(\cos\theta^*). \tag{2.3}$$

RHS of the formula is the convolution of known and calculable quantities. Therefore, this formula can be tested by comparing with measured cross sections.

$\mathcal{A}_{\mathrm{LL}}$ was first measured in a target experiment at FNAL [14]. At RHIC, since the first longitudinally polarized proton-proton collision in 2002, $\mathcal{A}_{\mathrm{LL}}$ has been rigorously measured in the PHENIX and STAR experiments for various final states at a wide range of rapidity at $\sqrt{s} = 62$ and $200\,\mathrm{GeV}$ [15, 16, 17, 18, 19]. In the early stage of

the experiment, in which the luminosity and polarization were limited, $\mathcal{A}_{LL}$ was measured primarily for final states which were copiously produced in the collisions, e.g., inclusive jets, inclusive pions. While PHENIX has its advantage in measuring neutral pions with its highly segmented ($\Delta\eta \times \Delta\varphi = 0.01 \times 0.01$) electromagnetic calorimeter, STAR has strength in measuring jets because of its full-azimuth electromagnetic calorimeter and tracking device.

The inclusive jet $\mathcal{A}_{LL}$ measured with the STAR detector is one of the results from RHIC that put a constraint on ΔG. Figure 2-1 shows $\mathcal{A}_{LL}$ for inclusive jet production in polarized proton-proton collisions at $\sqrt{s} = 200$ GeV at the mid-rapidity $-0.7 < \eta < 0.9$. The data were collected with the STAR detector during RHIC Run-6. The impact of the value of ΔG was quantitatively evaluated within the framework of the
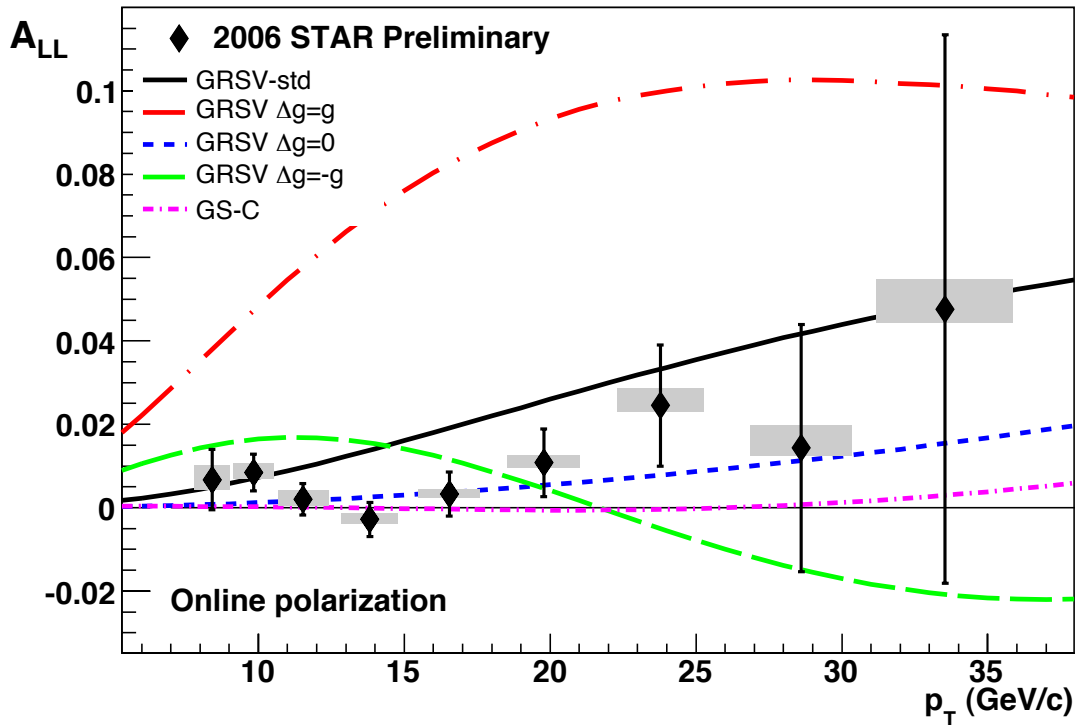
Figure 2-1: Longitudinal double spin asymmetry $\mathcal{A}_{LL}$ for inclusive jet production in polarization proton-proton collisions at $\sqrt{s} = 200$ GeV measured with the STAR detector. The data were collected during RHIC Run-6. The vertical bars show the statistical. The gray boxes show the systematic uncertainties. The curves show NLO calculations based on the GRSV and GS-C polarized parton distributions.

GRSV parametrization. The probed range of x was $0.02 < x < 0.3$. The results exclude $\Delta G < -0.7$ and $\Delta G > 0.2$ and with C.L. 90%.

In the analysis of the inclusive jet $\mathcal{A}_{\mathrm{LL}}$ mentioned above, a range of possible ΔG is estimated by comparing the data with theoretical predictions calculated based on existing models of the polarized parton distributions. The converse of this, determining polarized parton distributions based on which a theoretical calculation reproduces measured asymmetries, can more directly address the spin structure of proton.

The principle of a *global analysis* of polarized parton distributions is the following. At some initial scale μ_0, flexible forms of parametrized functions are assumed to describe the polarized parton distributions. The Q^2-evolution of the assumed polarized parton distributions can be calculated by perturbative QCD to the scale of each data point. Then, experimentally measurable quantities such as $\mathcal{A}_{\mathrm{LL}}$ can be calculated by perturbative QCD with the polarized parton distributions at the energy scale of the data points. Some statistic such as χ^2, which quantifies a goodness of fit, is assigned to each data point by comparing measured values and the calculated values. Polarized parton distributions can be determined by finding the parameters of the functions which can reproduce a set of measurable quantities that fit experimental data.

Figure 2-2 shows models of the polarized parton distributions from three working groups: GRSV, GS, and DSSV. In the figure, fifteen models of the polarized gluon distribution from GRSV [6] are shown. GRSV STD was obtained so as to fit polarized DIS data. The polarized gluon distribution is obtained from the Q^2 evolutions of the polarized quark distributions. However, since the Q^2 evolutions are only logarithmic and slow, the uncertainty on GRSV STD is very large. GRSV provides three extreme models of the polarized gluon distributions, GRSV MAX, GRSV MIN, GRSV ZERO, which have the inputs: $\Delta g = g, -g, 0$, respectively at the scale of 0.4 GeV. These three extreme models also well describe pDIS data. Series of GRSV have the same functional form as GRSV STD but have different first moments.

GS-C [5] determined from the structure function $g_1(x, Q^2)$ measured by polarized DIS. They provide three polarized gluon distributions which equally well reproduce the pDIS data. One of the three models GS-C has distinctive shape with large gluon polarization in low-x.

DSSV [20] incorporates $\mathcal{A}_{LL}$ for neutral pions from PHENIX and $\mathcal{A}_{LL}$ for inclusive jets from STAR. It is found that $\Delta g(x, Q^2)$ is small in the range of x probed by PHENIX and STAR.
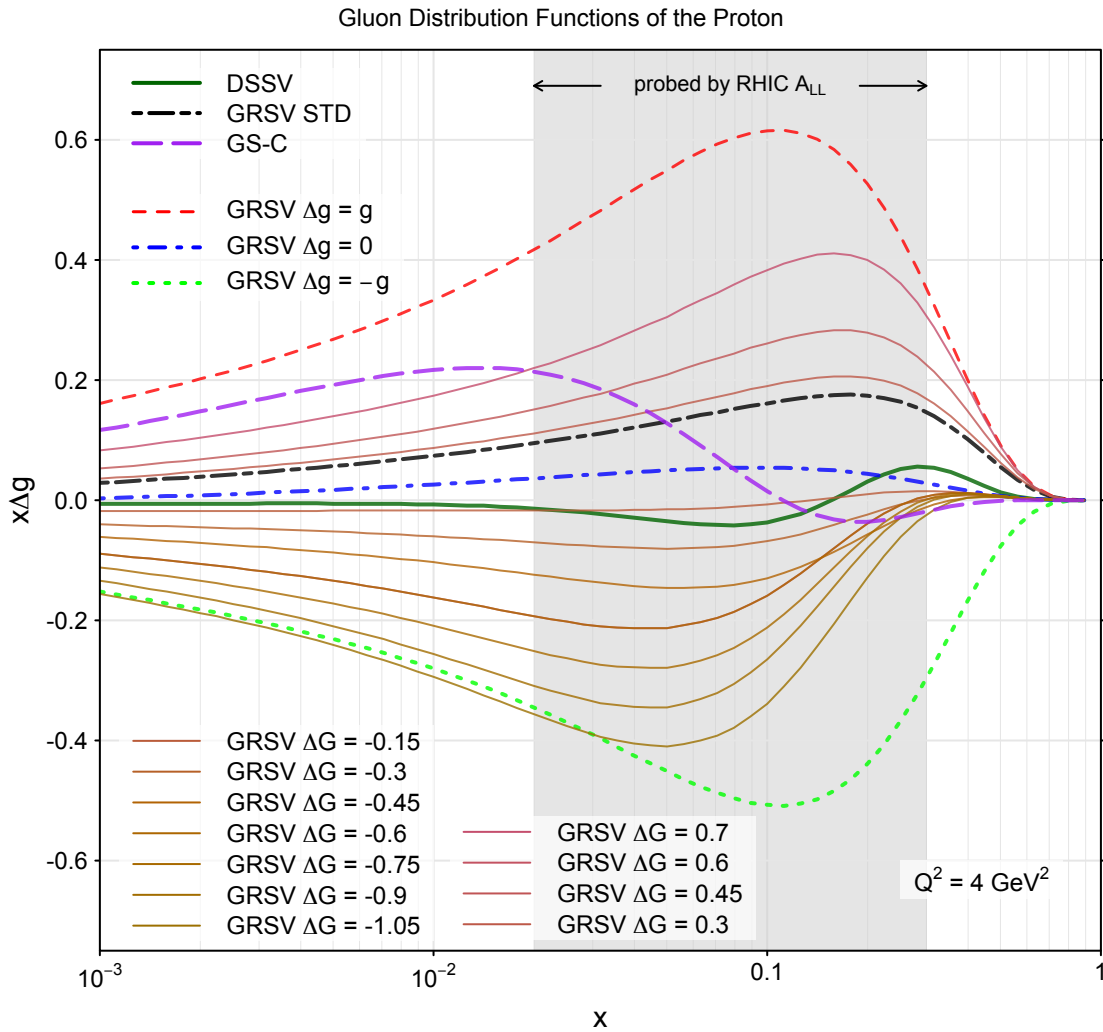
Figure 2-2: Models of polarized gluon distributions of the proton [20, 6, 5].

Chapter 3

RHIC

The *Relativistic Heavy Ion Collider* (RHIC) [21], located in the *Brookhaven National Laboratory* (BNL), Upton, NY, is a *polarized proton-proton collider* with the center of mass energy up to 500 GeV. Its design luminosity is $2 \times 10^{32} \text{cm}^{-2}\text{s}^{-1}$ at 500 GeV and the design polarization is 70%. Its primary goal as a polarized proton collider is to probe the spin structure of the protons, and in particular, to understand how gluons and (anti-)quarks in protons form the proton spin. RHIC has another operational mode: *heavy ion* mode. Its main purpose in this mode is to create and observe a *quark-gluon plasma* (QGP), a high temperature, high density QCD phase in which quarks and gluons are deconfined from hadrons.

This chapter describes RHIC as a polarized proton-proton collider, including a brief history, the layout of the accelerator complex, the proton beam path, devices need to maintain and measure the polarization, and the beam bunch structure.

A Brief History of RHIC

RHIC was built in an existing empty tunnel originally dug to host the cancelled project ISABEL. RHIC was first proposed in 1984 and the construction began in 1991.

$\sqrt{s}$	$50 \sim 500$ GeV
Luminosity	$2 \times 10^{32}\text{cm}^{-2}\text{s}^{-1}$ for $\sqrt{s} = 500$ GeV
Polarization	70%

Table 3.1: RHIC polarized proton mode design parameters
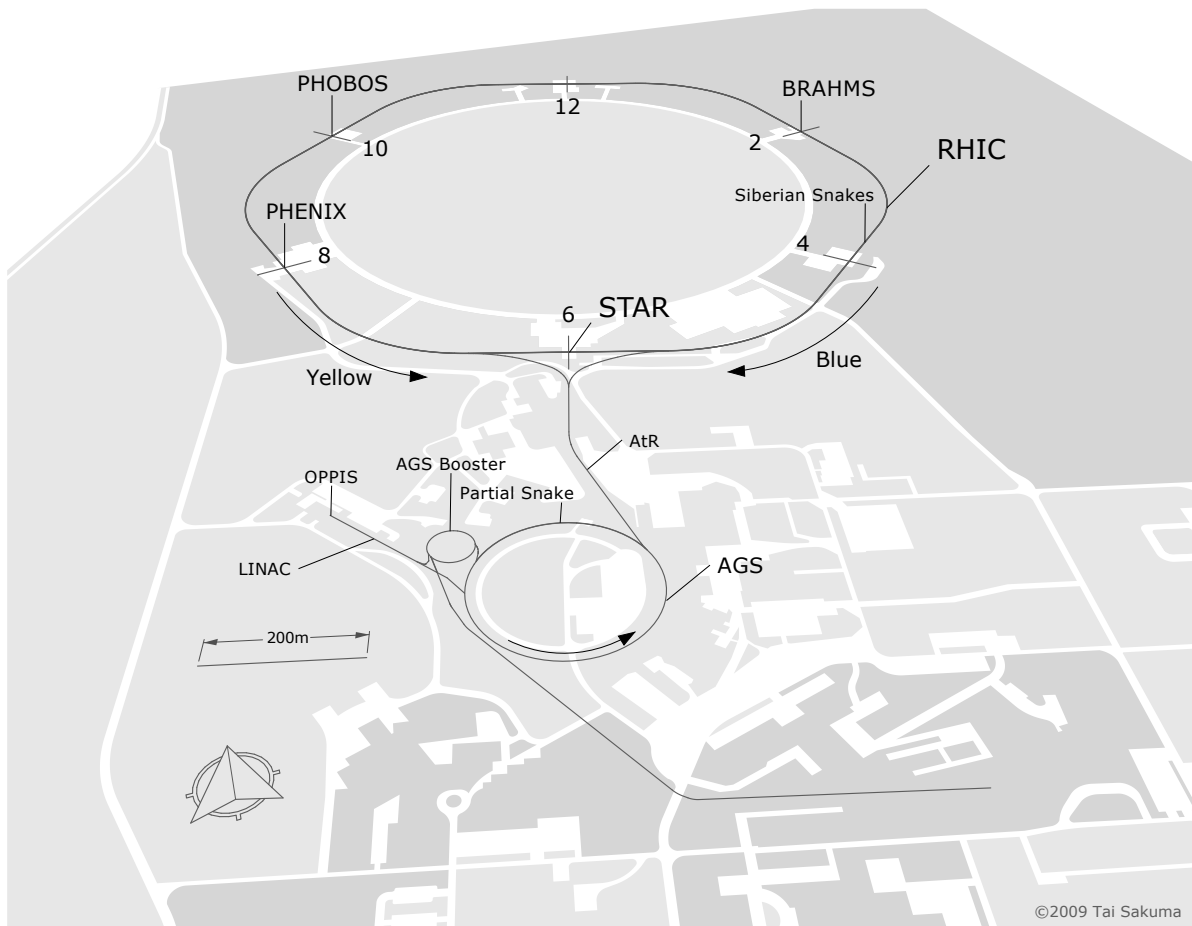
Figure 3-1: Layout of the RHIC accelerator complex.

The first collision was gold-gold in 2000 (Run-1). The first polarized proton collision was in 2001 (Run-2). The subsequent polarized proton runs are summarized in Table 3.2. The 200 GeV proton-proton collision data from Run-6 are used in this thesis. Run-6 is briefly summarized in section 5.1.

Run	$\sqrt{s}$ [GeV]	$\int \mathcal{L}\mathbf{d}t[\mathbf{pb^{-1}}]^a$	Polarization[b]
Run-2	200	0.47	14%
Run-3	200	2.5	34%
Run-4	200	3.2	46%
Run-5	200	12.7	46%
Run-6	200	44.9	58%
	62	0.325	50%
Run-8	200	19.2	44%
Run-9	500	52.6	56%
	200	53.5	34%

[a] Delivered luminosity at STAR
[b] Average polarization

Table 3.2: RHIC polarized proton-proton runs

The Layout of the RHIC Accelerator Complex

RHIC consists of two 3,833 m circumference rings, *"Yellow"* and *"Blue"* with six *interaction points* (IPs). The beam circulates counterclockwise in the Yellow ring and clockwise in the Blue ring. The layout of the accelerator complex is represented in Figure 3-1. The IPs are located at the 12, 2, 4, 6, 8, 10 o'clock positions of the RHIC rings. The STAR detector is installed at the 6 o'clock position. Two other experiments, Phenix and BRAHMS, are conducted at the 8 o'clock and the 2 o'clock positions, respectively. The PHOBOS experiment was located at the 10 o'clock position.

The Polarized Proton Source

The polarized proton beam starts from the *optically pumped polarized ion source* (OPPIS) [22]. OPPIS produces 500 μA of polarized H$^-$ ions in a 300 μs pulse. In OPPIS, when protons are passed through an *optically pumped alkali-metal vapor*, the protons

capture polarized electrons and become hydrogen atoms with polarized electrons. Then, in a weak magnetic field, the protons of the hydrogen atoms become polarized by the *hyperfine interaction* with the polarized electrons. The hydrogen atoms are again passed through an alkali-metal vapor and capture electrons and become H^- ions.

The Polarized Proton Beam Path

The polarized proton beam takes the following path. Produced by OPPIS, the polarized H^- ions are accelerated by a RFQ (*Radio Frequency Quadrupole*) magnet and 200 MHz *LINAC* to 200 MeV. Then, the electrons are stripped and the polarized protons are injected in the *AGS Booster*, where the polarized proton beam is accelerated up to 2.465 GeV. The beam continues to be accelerated up to 24.3 GeV in the AGS (*Alternating Gradient Synchrotron*) and then transferred into the RHIC rings. RHIC accelerates the polarized protons up to their final energy and collides them at the IPs.

Siberian Snakes and the Partial Snake

The protons are highly polarized (85-90%) when they are produced by OPPIS. The polarization needs to be maintained along the beam path during the acceleration to the collisions. To maintain the polarization, two *Siberian Snakes* [23] in each RHIC ring and one *partial snake* [24] in the AGS ring are installed. These snakes rotate the spin orientation of the polarized protons so that the depolarising resonance conditions can never be met.

Polarimeter

The proton beam polarization is measured by two types of polarimeter: a *pC CNI polarimeter* and a *polarized H jet polarimeter* [25]. The *pC* CNI polarimeter can measure the polarization in short periods of time because of the large cross section and large asymmetry of the *pC* elastic scattering in the *Coulomb-Nuclear Interference* (CNI) region. With the *pC* CNI polarimeter, the polarization is measured several times within a fill, which typically lasts for many hours. Each measurement takes less than 2 minutes to reach a statistical accuracy of about ±2%. The polarized *H* jet polarimeter, on

the other hand, offers more precise measurement. It is used to measure the absolute value of the polarization and calibrate the *pC* CNI polarimeter.

Spin Rotators

The protons are transversely polarized when they are produced and accelerated and when they circulate the RHIC rings. RHIC has *spin rotators* at both sides of the IPs for both rings at the 6 o'clock and 8 o'clock positions. These spin rotators allow STAR and PHENIX to collect data in longitudinally polarized proton collisions as well as transversely polarized proton collisions.

Beam Bunches

During Run-6, 120 *RF buckets* were used to hold *beam bunches*. The bunches are numbered from 0 to 119. Typically, the last nine buckets were unfilled for beam abortion. Those buckets are called *abort gaps*. Other unfilled buckets are *kicked bunches*, which were filled normally, but kicked transversely after injection in order to enhance the betatron oscillations used to diagnose beam characteristics. In Run-6, the first Yellow bunch crossed with the first Blue bunch at 4 o'clock position. Thus, at STAR, the Yellow bunch 0 crossed with the Blue bunch 80. The *BBC coincidence rates*, which is described in section 4.4, per bunch crossing for a particular run are plotted in Figure 3-2. The *bunch crossings* at STAR is also numbered, with the order defined by the Yellow beam. For example, the bunch crossing between the Yellow bunch 0 and the Blue bunch 80 is called bunch crossing 0.

Spin Patterns

While the polarization of proton bunches alternate in the Blue ring ($+-+-+-+-\cdots$), the polarization of proton bunch pairs alternate in the Yellow ring ($++--++--\cdots$). As a consequence, data in all four combinations of the polarization of collisions $((++),(+-),(-+),(--),\cdots)$ can be collected in a single run, which reduces systematic errors that would occur if different polarization data were collected in different runs.
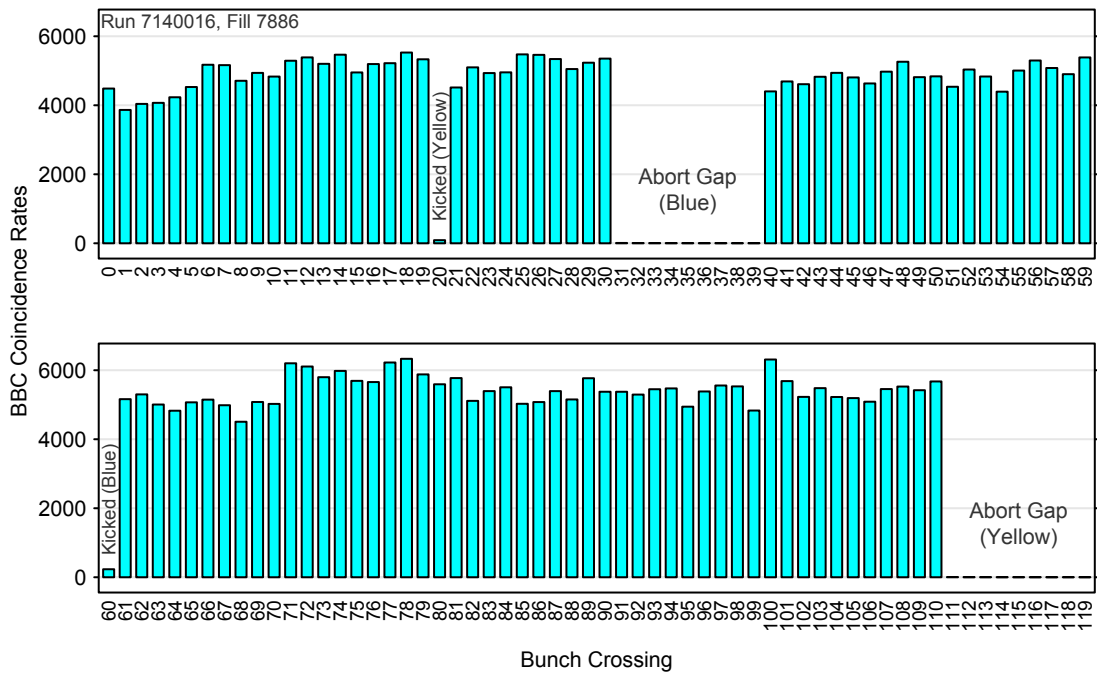
Figure 3-2: BBC coincidence rates per bunch crossing.

Chapter 4

The STAR Detector

STAR, *the Solenoidal Tracker At RHIC*, was built to measure wide varieties of nuclear interactions occurring at high energy heavy ion collisions and polarized proton collisions. Figure 4-1 shows the cross sectional view of the STAR detector.

The STAR *interaction point* (IP) is located at the 6 o'clock position of the RHIC ring. At this IP, the Yellow beam comes from the west and the Blue beam comes from the east (Figure 3-1). The *STAR coordinate system* has its origin at the center of the IP. The z-axis is along the beam line pointing to the west side. The y-axis points up and the x-axis points outward from the RHIC ring (south).

This chapter describes the detector subsystems relevant to the measurements presented in this thesis: the *Time Projection Chamber* (TPC), the *Barrel Electromagnetic Calorimeter* (BEMC), the *Solenoidal magnets*, and the *Beam-Beam Counters* (BBC).

η=-1   η=0   η=1

BEMC

TPC

η=2

BBC →   ← BBC

7.3 m

+y

+z

IP

Blue →   ← Yellow

East   West

7.3 m

©2009 Tai Sakuma
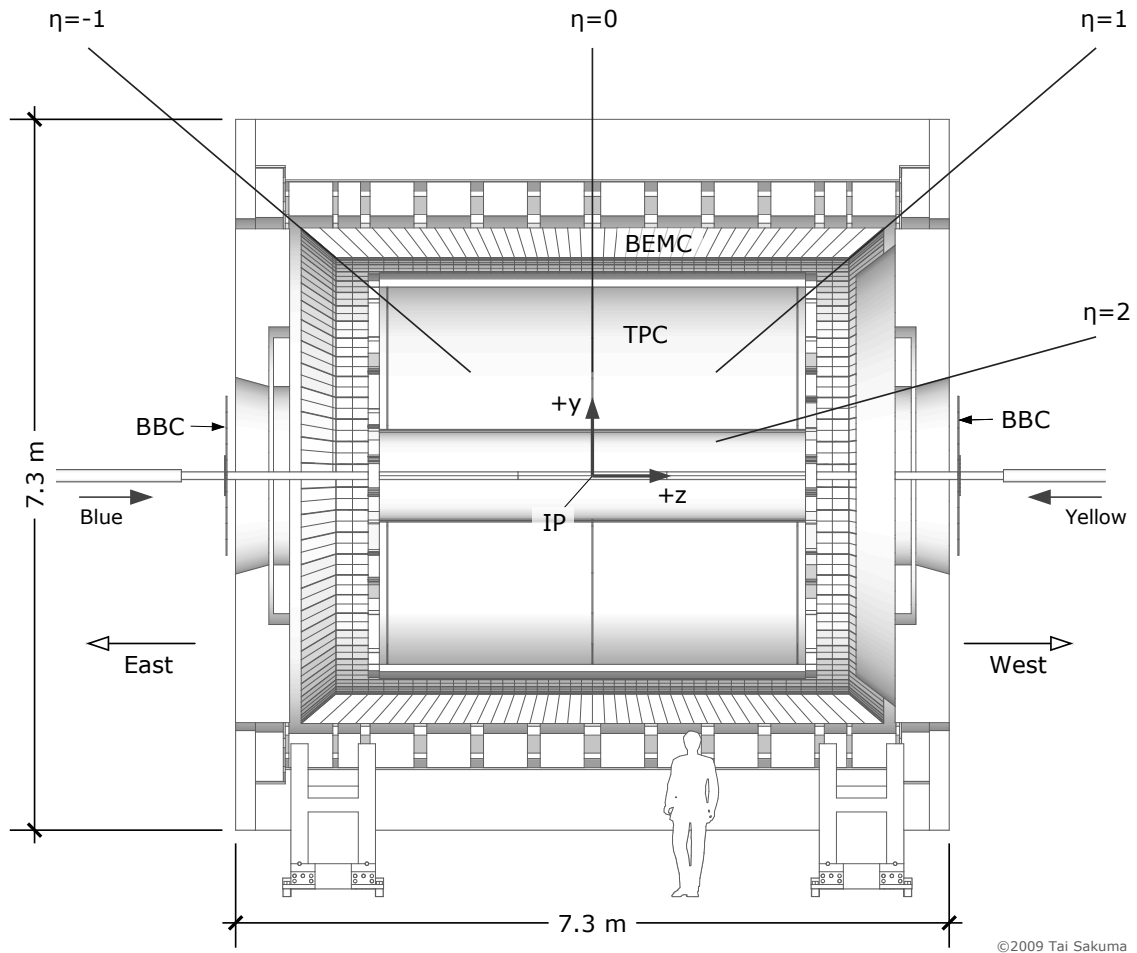
Figure 4-1: The STAR detector

4.1 Time Projection Chamber (TPC)

The *Time Projection Chamber* (TPC) [26] is the primary tracking system of the STAR detector. It has a cylindrical shape operated within a solenoidal magnetic field. Its acceptance is $|\eta| < 1.8$ with full azimuth. Recording tracks of the charged particles, it provides the momentum measurements over a range from 100 MeV to 30 GeV and particle identification for the particles with a momentum range from 100 MeV to 1 GeV. In this thesis, the particle momenta measured with TPC are used while the particle identifications are not.

The TPC is a type of gaseous ionization detector that provides a three dimensional image of the charged particle's tracks. When the charged particles pass through TPC, they ionize the gas atoms filled there and remove the electrons from the atoms. These electrons drift in the uniform electric field, along the z-axis, towards *multiwire proportional chambers* (MWPC) at the end caps. The projections of the tracks on the x-y plane are measured by the positions in the MWPC that the drifting electrons hit, and the z-directions of the tracks are measured by the drift time.

The chamber is divided into half by the *central membrane* (CM). The central membrane is the cathode at -28 kV. The grounds are located 2.1 m away from the membrane at both ends. The central membrane, ground planes, *inner field cage* (IFC), and *outer field cages* (OFC) form a conducting structure that defines a uniform electric field of 134 V/m. The electric field is parallel to the magnetic fields, which prevents the drifting electrons from diffusing.

η=0

η=-1

OFC

η=1

η=-1.8

Membrane

η=1.8

IP

Ground

IFC

1.5 m

2.1 m
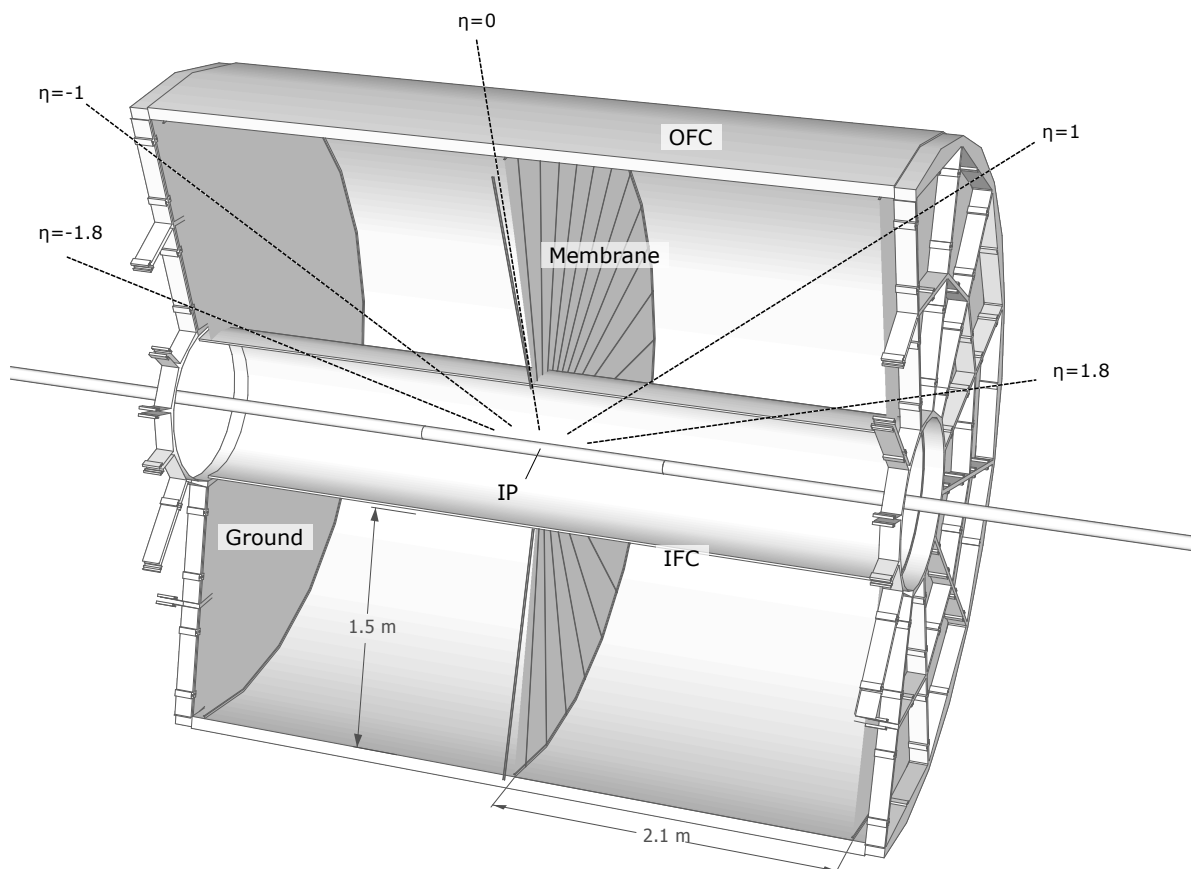
©2009 Tai Sakuma

Figure 4-2: The time projection chamber

4.2   Barrel Electromagnetic Calorimeter (BEMC)

The *Barrel Electromagnetic Calorimeter* (BEMC) is the primary calorimeter at mid-rapidity [27]. It is a cylindrical annulus which surrounds the TPC. The inner radius and outer radius are 223.5 mm and 262.999 mm, respectively. The BEMC covers $|\eta| < 1$ with full azimuth and has a depth of about twenty radiation lengths ($20X_0$) at $\eta = 0$. The BEMC measures the position and energy of the incident particles. It is a fast detector and is used to trigger high-p_T events.

The BEMC is built from 120 *modules*: 60 modules on the west side and 60 modules on the east side. Each module covers 0.1 in φ and 1 in η. The BEMC is a sampling calorimeter with the innermost layer consisting of a plastic scintillator. Subsequent layers alternate between lead and plastic scintillators for 20 layers each. The first two plastic scintillator layers are 6 mm thick. The rest of 19 plastic scintillator layers and all the lead layers are 5 mm thick. *Shower maximum detectors* (SMD) are installed between the 5th lead layer and the 6th scintillator layer.

Each module contains forty calorimeter *towers*: two in the φ direction and 20 in the η direction. The BEMC has 4,800 (=120 × 40) towers in total. Each tower covers $\Delta\eta \times \Delta\varphi = 0.05 \times 0.05$. The towers are projective towards the IP.

η=-1

η=0

η=1

262.999cm

223.500cm
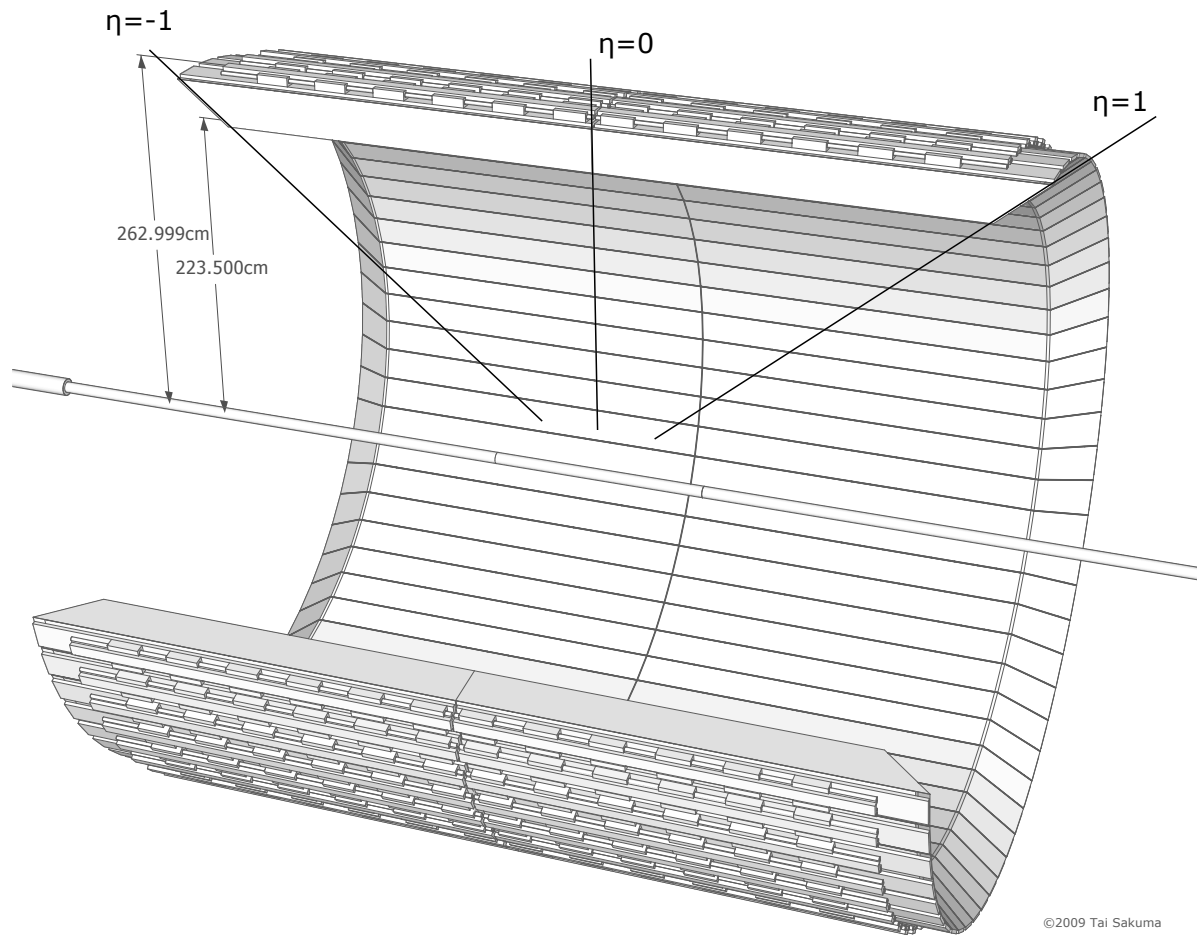
©2009 Tai Sakuma

Figure 4-3: The Barrel Electromagnetic Calorimeter (BEMC)

Sc 21
Sc 20
Sc 19
Sc 18
Sc 17
Sc 16
Sc 15
Sc 14
Sc 13
Sc 12
Sc 11
Sc 10
Sc 9
Sc 8
Sc 7
Sc 6

Pb 20
Pb 19
Pb 18
Pb 17
Pb 16
Pb 15
Pb 14
Pb 13
Pb 12
Pb 11
Pb 10
Pb 9
Pb 8
Pb 7
Pb 6

SMD

Sc 5
Sc 4
Sc 3
Sc 2
Sc 1

Pb 5
Pb 4
Pb 3
Pb 2
Pb 1

6.985cm

25.992cm

30.299cm

22.816cm
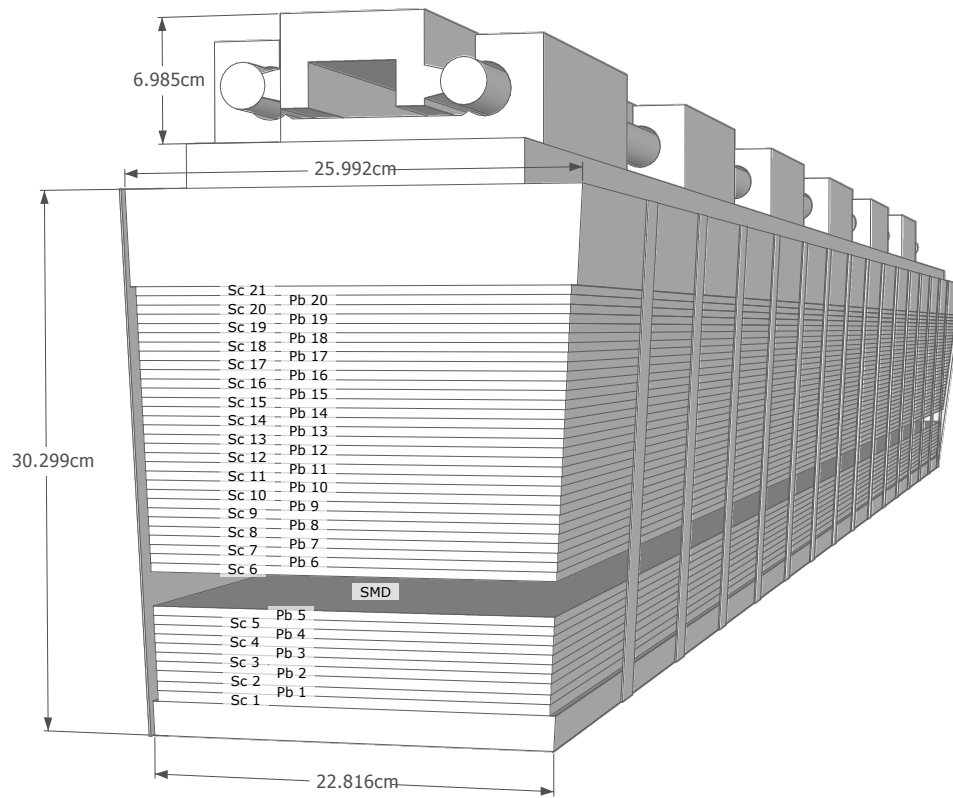
©2009 Tai Sakuma

Figure 4-4: a BEMC Module

η=0   η=0.1   η=0.2   η=0.3   η=0.4   η=0.5   η=0.6   η=0.7   η=0.8   η=0.9   η=1

Δφ=0.05   Δη=0.05
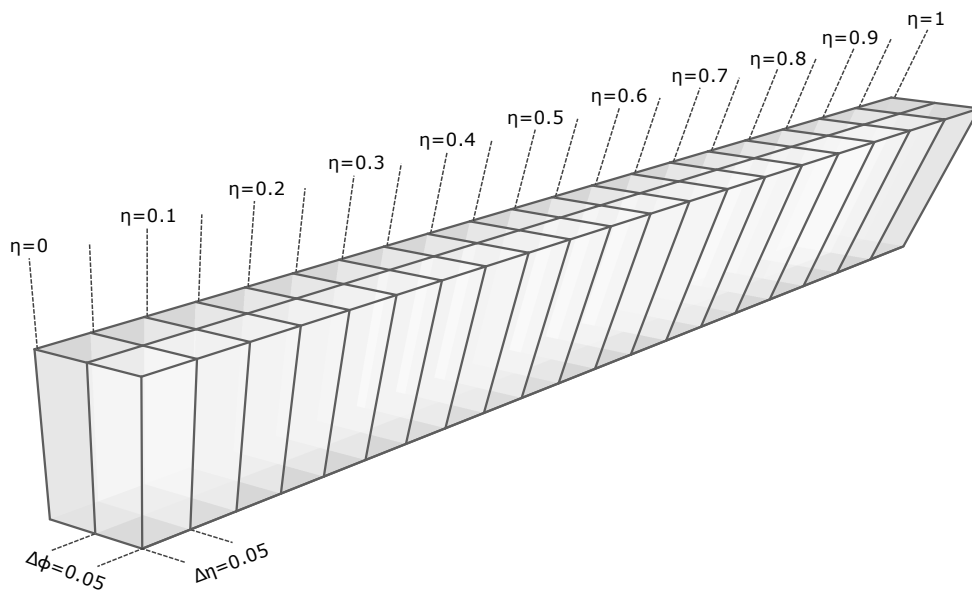
©2009 Tai Sakuma

Figure 4-5: The geometry of the calorimeter towers in a BEMC module

4.3   Solenoidal Magnet

The magnet subsystem provides the TPC with a near uniform magnetic field [28]. Its operation range is $0.25 < |B_z| < 0.5$ T. This thesis uses data collected in a 0.5 T operation. The magnet subsystem consists of current-carrying aluminum coils and a steel structure.

There are three types of coils: *main coils*, *space trim coils*, and *pole-tip trim coils*. The main coils and the space trim coils have inter radius 2.65 m and outer radius 3 m. Main coils are thicker (0.45 m) than the space trim coils (0.23 m). Both the space trim and pole-tip trim coils were tuned to improve the uniformity of the magnetic field to a few percent.

The steel structure supports the coil and provides a return path for the magnetic flux. This steel structure is in the form of thirty *backlegs* that surround the main coil and space trim coils. At the both ends of the backlegs are *inner rings* and *outer rings*. The inner diameters of the *pole-tips* have a conical shape at $|\eta| = 2$. The entire detector and magnet assembly is supported on two *cradles*, located at the east and west ends.

45cm

23cm

Space Trim Coil   Main Coil   Outer Ring

Inner Ring

Backleg

3m   2.65m

η=2

Pole tip trim coil

Pole tip

Cradle

©2009 Tai Sakuma
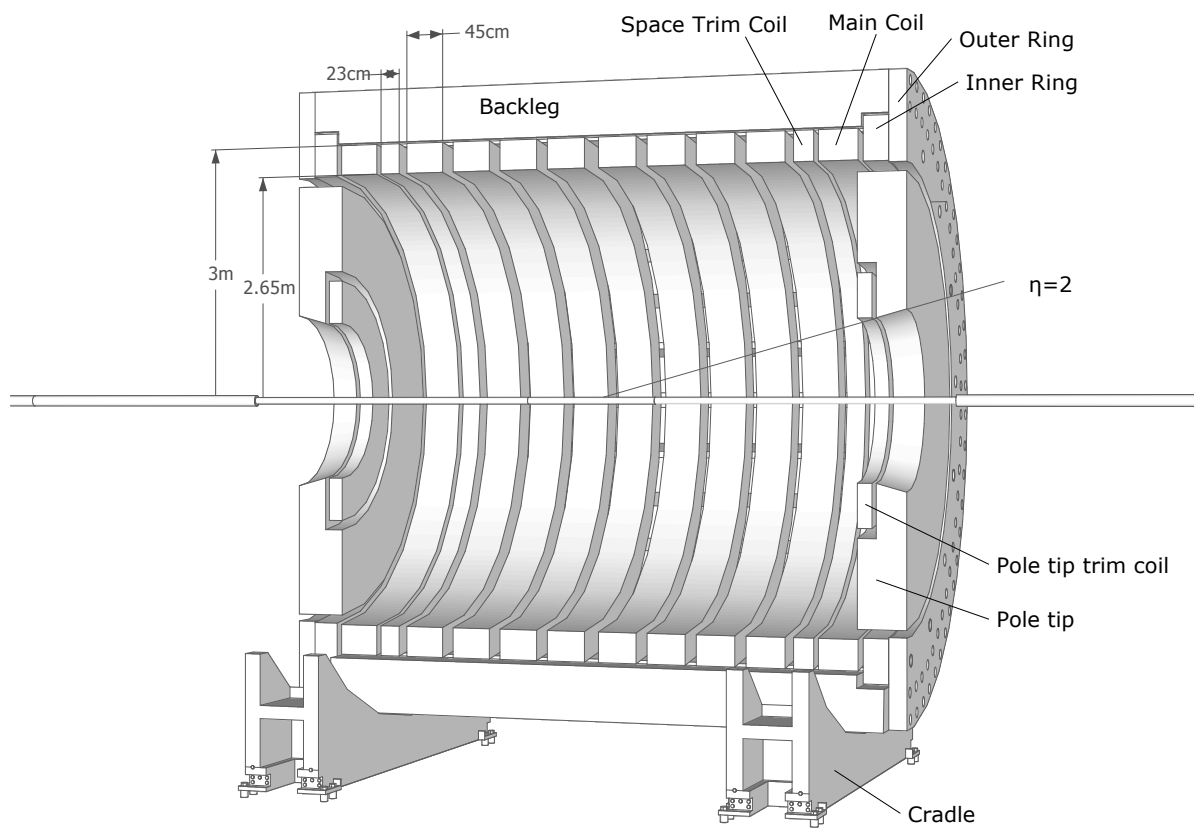
Figure 4-**6:** The solenoidal magnet subsystem.

4.4 Beam-Beam Counters (BBC)

The *Beam-Beam Counters* (BBC) [29] are scintillator annuli of large and small hexagonal tiles, installed 3.7 m east and west along the beam line from the IP. Their acceptance is approximately $3.3 < |\eta| < 5.0$.
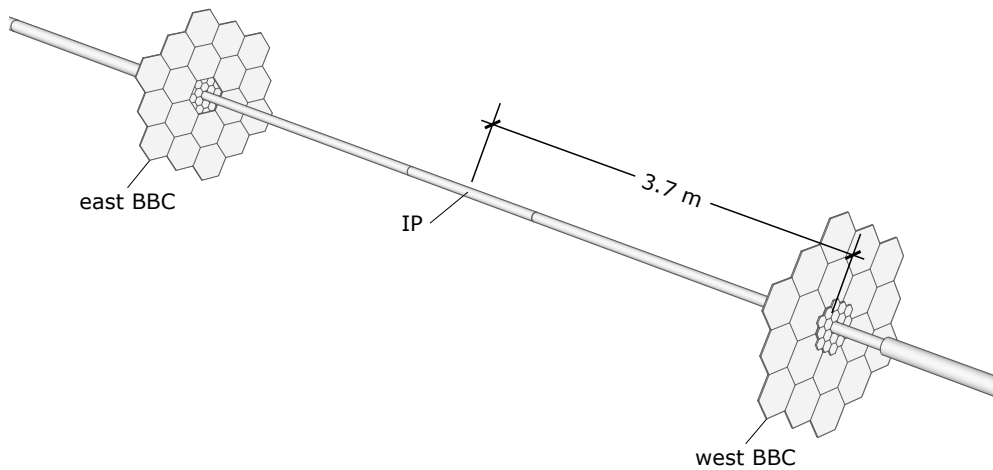
Figure 4-7: The Beam-Beam Counters (BBC)

The BBCs are used to trigger *minimum bias* (MINB) events. The MINB condition is a coincidence between the east BBC and the west BBC. The cross section of the MINB events is [30]

$$\sigma_{\mathrm{MB}} = 26.1 \pm 2.0 \text{ mb.} \tag{4.1}$$

The MC simulation estimates that 87% ± 8% of non-singly diffractive collisions cause the MINB trigger [29].

The coincidence has some allowed time difference. This difference is measured as 4-bit values called *timebin*. There are fifteen timebins, which roughly corresponds to the vertex position of the events. The vertex distributions for each timebin are shown in Figure 5-10.

Part II

Inclusive Jets

Chapter 5

Event Selection

The data presented in this thesis were collected during RHIC Run-6, which is briefly summarized in Section 5.1. Data from 293 STAR runs in 37 RHIC fills were selected for this thesis (Section 5.2). Section 5.3 to Section 5.5 show integrated luminosity, relative luminosity, and polarization for those runs. Events were selected based on triggers, timebins, and vertices for the cross section measurements. Section 5.6 describes triggers. Section 5.7 discusses timebins and vertices.

5.1   Summary of RHIC Run-6

RHIC Run-6 [31] started in February 2006 and ended in June 2006. Run-6 was entirely dedicated to polarized proton collisions. In Run-6, RHIC ran at four different beam energies: two for data collection and two for machine development. STAR and PHENIX collected data in the collisions at $\sqrt{s} = 200$ GeV and 62.4 GeV for physics analyses. BRAHMS collected data in 62.4 GeV collisions. In addition to physics runs, RHIC carried out machine development runs at very low energy (23 GeV), which is lower than the design value, and high energy (500 GeV). STAR and PHENIX participated in the 500 GeV development runs as well.

In Run-6, RHIC was in the 200 GeV mode for twelve weeks. After a short period of development runs with Run-5 trigger configurations, STAR started collecting data with longitudinally polarized collisions. The orientation of the polarization changed twice: once to transverse and once back to longitudinal. Thereafter the collision

35
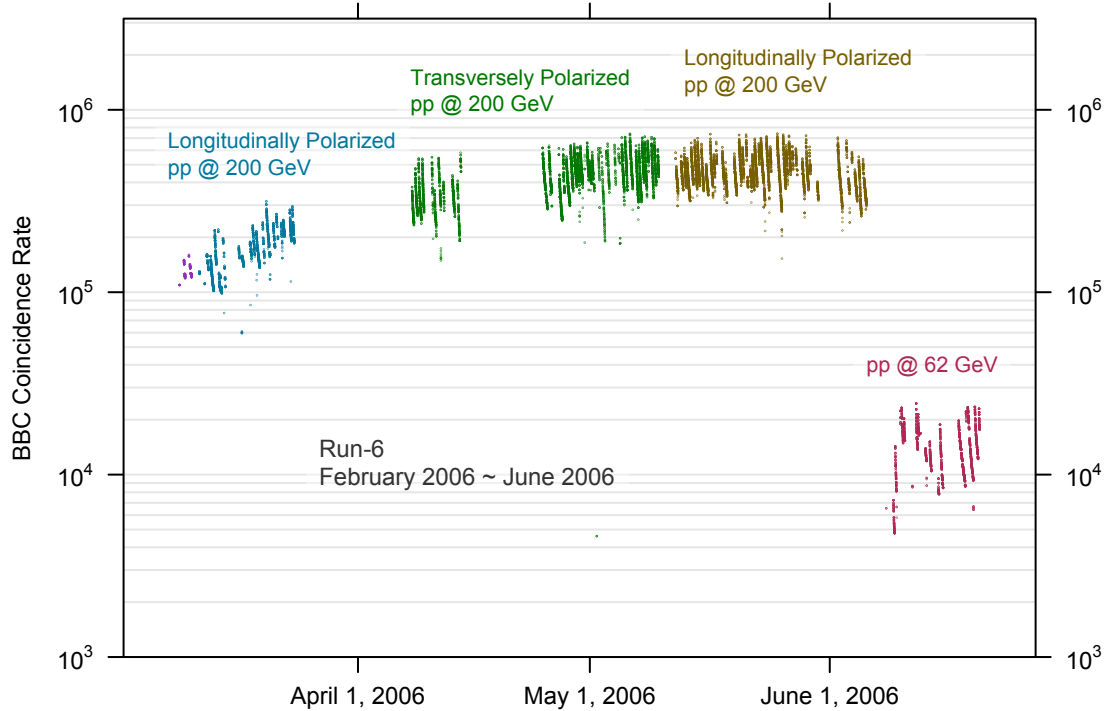
Figure 5-1: The BBC coincidence rates during Run-6. Each dot represents a STAR
run.

energy changed to 62 GeV. Figure 5-1 shows the BBC coincidence rates, which are
proportional to luminosity, during Run-6.

The data sample used in this thesis were collected during the second longitudinal
period, in particular during the 37 *RHIC fills* listed in Figure 5-2. A typical fill lasted
approximately eight hours, and was normally terminated by aborting the beams to
beam dumps. A few fills ended with unplanned events such as magnet quenches or
requests from the experiments. The STAR data collection was divided into several
runs, the *STAR runs*, each of which was typically about 30 to 40 minutes long when it
was successful. As an example, Figure 5-3 shows the start and end time of the STAR
runs in one particular successful fill.
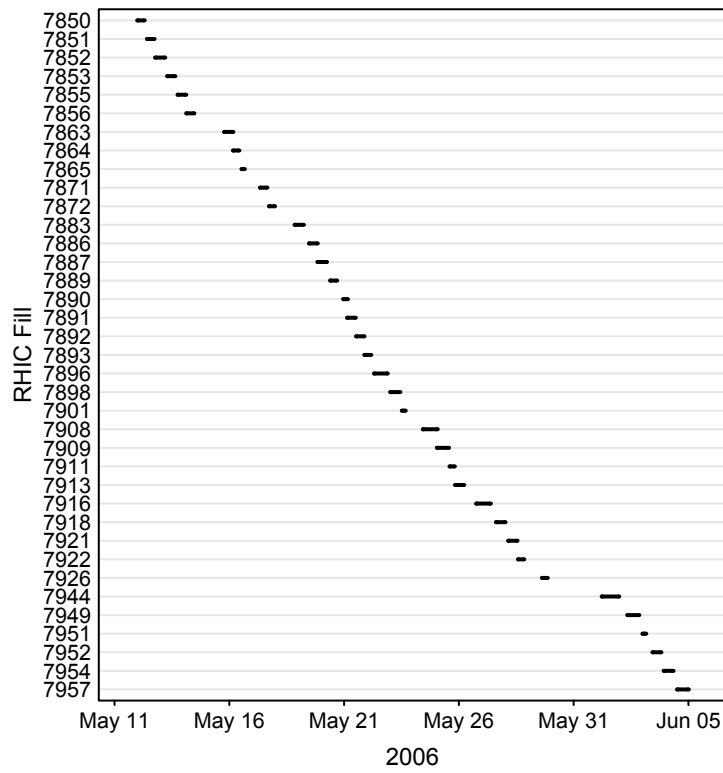
Figure 5-2: The RHIC fills in the second longitudinal period of Run-6.
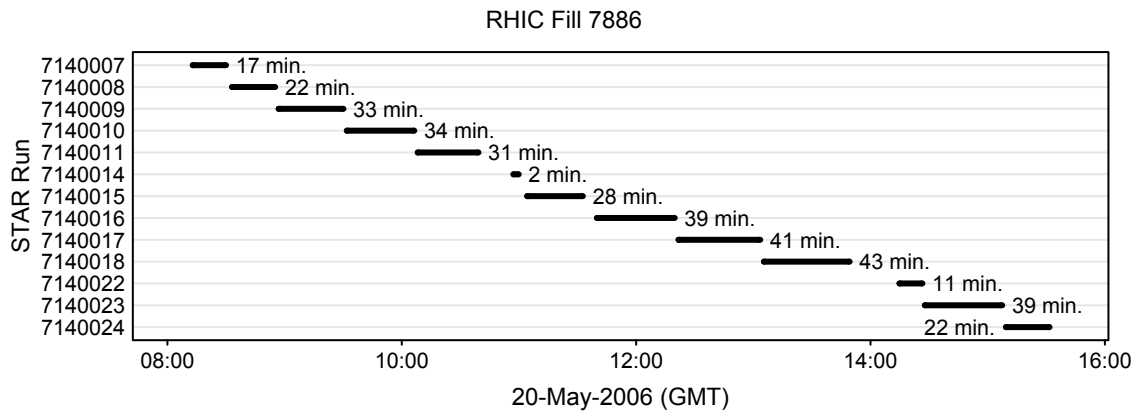
Figure 5-3: The start and end time of the STAR runs during the RHIC fill 7886.

5.2   Selection of 293 STAR Runs

During the second longitudinal period, 1,713 runs were marked successful online, among which 1,109 runs were data collections for physics analyses. The other runs addressed development and maintenance purposes such as machine tests, pedestal measurements, and calibrations. Among the 1,109 runs, 553 runs were in the *ppProductionLong* trigger setup, which was the primary trigger setup for the data collection in the second longitudinal period. After discarding very short runs (less than one minute), there were a total of 449 runs left in the *ppProductionLong* trigger setup.

Global Setup Name	Development	1st Long.	Trans.	2nd Long.
ppProductionJPsi	0	0	0	38
ppProductionLongNoEmc	0	0	0	49
ppProductionLong	0	0	0	449
ppProductionTransNoEMC	0	0	54	0
ppProductionTransFPDonly	0	0	25	0
ppProductionTrans	0	0	591	0
barrelBackground	0	27	44	36
ppProduction	0	423	0	0
pp2006MinBias	0	139	105	108
OldPPProduction	31	0	0	0
minbiasSetup	266	0	0	0

Table 5.1: The numbers of the runs in the global run trigger setups for physics data collection and the run periods. There were many other setups for development and maintenance.

Data from 293 runs were selected for this thesis. The data from those runs passed quality assurance (QA) and contain all necessary information for the cross section and the A_{LL} measurements. The cross section measurements and the A_{LL} measurements have different requirements for data contents and quality; the runs that meet both criteria are used in the analyses. The following QA tests were conducted.

Jets After jet reconstruction (described in Chapter 6), the distributions of run average of various jet properties such as multiplicity, jet p_T were examined and outliers were rejected.

BBC coincidence BBC coincidences were counted with twelve VME histogramming modules (*the STAR scaler boards*) in time series. Various distributions of the BBC coincidence rates were examined and outlier were rejected. The BBC coincidence counts were used to determine timebins of events, luminosity and relative luminosity of runs. The runs with reliable BBC coincidence rates were used in the analyses.

Spin pattern The runs in the RHIC fills for which the spin patterns were uniquely and unambiguously determined were selected.

Polarization The runs in the RHIC fills for which the polarization was measured were selected.

5.3 Luminosity for 293 STAR Runs

The integrated luminosity for the 293 runs selected in the previous section was calculated from the number of the MINB events and the MINB cross section. The MINB condition and the MINB cross section are given in Section 4.4. The number of the recorded MINB events for the 293 runs is

$$N_{\mathrm{MB}}^{\mathrm{recorded}} = 248997. \tag{5.1}$$

The average prescale factor for those runs is

$$\langle \mathrm{PS_{MB}} \rangle = 565407.3. \tag{5.2}$$

The product $N_{\text{MB}}^{\text{recorded}} \cdot \langle \text{PS}_{\text{MB}} \rangle$ gives the total number of the MINB events:

$$N_{\text{MB}}^{\text{triggered}} = N_{\text{MB}}^{\text{recorded}} \cdot \langle \text{PS}_{\text{MB}} \rangle.$$

From the values in (4.1), (5.1), and (5.2), the integrated luminosity for the 293 runs is

$$\int \mathcal{L} \mathrm{d}t = \frac{N_{\text{MB}}^{\text{recorded}} \cdot \langle \text{PS}_{\text{MB}} \rangle}{\sigma_{\text{MB}}} = 5.39 \pm 0.41 \text{ pb}^{-1}.$$

This value was used in the cross section measurements.

5.4   Relative Luminosity for 293 STAR Runs

Relative luminosities are ratios of luminosities for different spin states of the proton beams. Six of them are defined as follows:

$$R_1 = \frac{\mathcal{L}^{++} + \mathcal{L}^{+-}}{\mathcal{L}^{--} + \mathcal{L}^{-+}} \qquad\qquad R_4 = \frac{\mathcal{L}^{++}}{\mathcal{L}^{--}}$$

$$R_2 = \frac{\mathcal{L}^{++} + \mathcal{L}^{-+}}{\mathcal{L}^{--} + \mathcal{L}^{+-}} \qquad\qquad R_5 = \frac{\mathcal{L}^{+-}}{\mathcal{L}^{--}}$$

$$R_3 = \frac{\mathcal{L}^{++} + \mathcal{L}^{--}}{\mathcal{L}^{+-} + \mathcal{L}^{-+}} \qquad\qquad R_6 = \frac{\mathcal{L}^{-+}}{\mathcal{L}^{--}},$$

where $\pm$ indicates the spin states of the proton beam; the Yellow beam first and the Blue beam last. The relative luminosities were measured by the BBCs for each run. Figure 5-4 shows the relative luminosities for the 293 runs. The relative luminosities were used in spin asymmetry measurements.
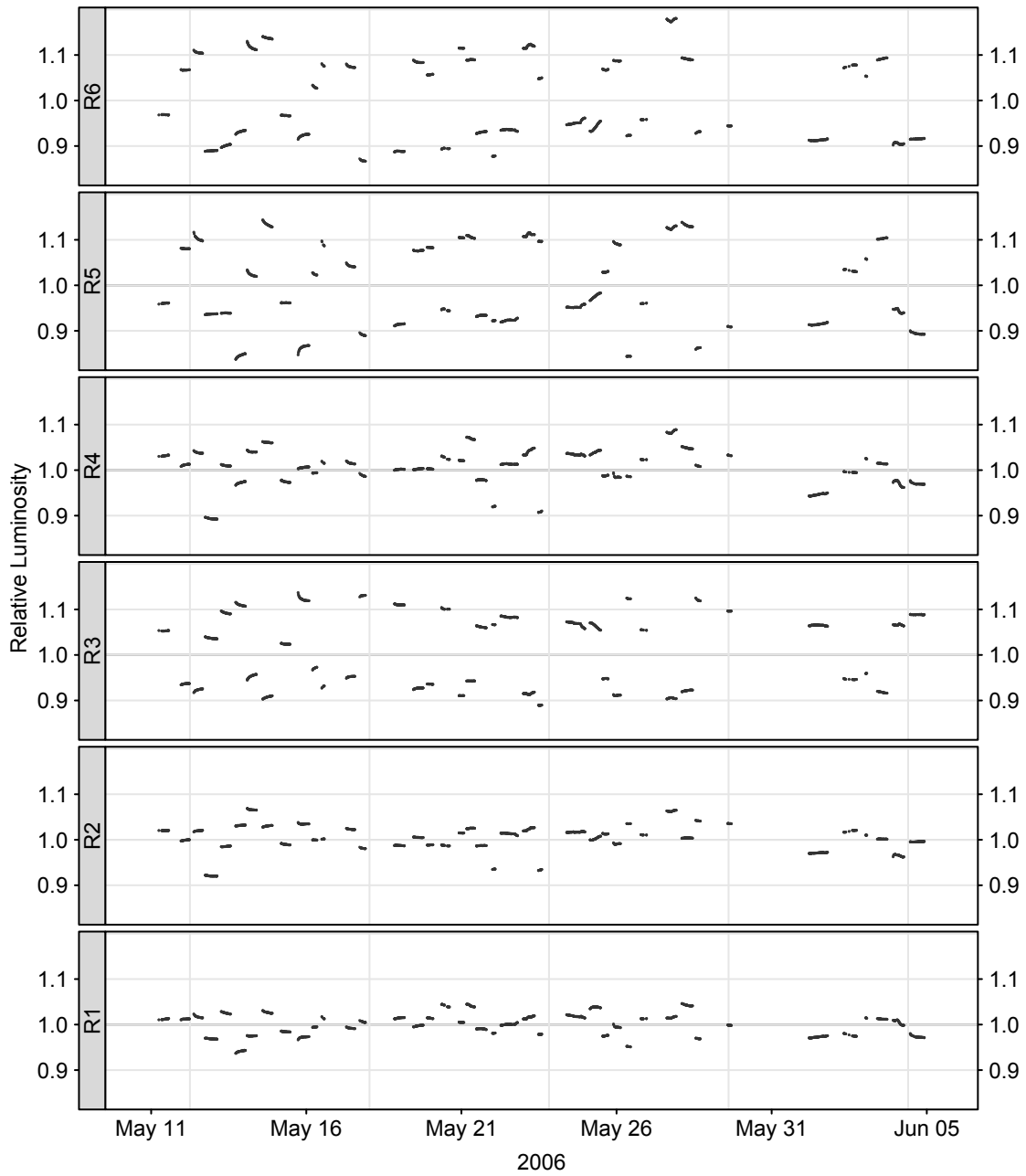
Figure 5-4: Relative luminosity during the 2nd longitudinal period. Each dot represents one STAR run.

5.5   Polarization for 37 RHIC Fill

As discussed in Chapter 3, the polarization was measured by the *pC* CNI polarimeter and the polarized *H* jet polarimeter. The polarization was determined for each RHIC fill. Figure 5-5 shows the polarization during the second longitudinal period of RHIC Run-6. The average polarization for the Yellow beam and the Blue beam were $\overline{P_Y} = 59\%$ and $\overline{P_B} = 56\%$, respectively.
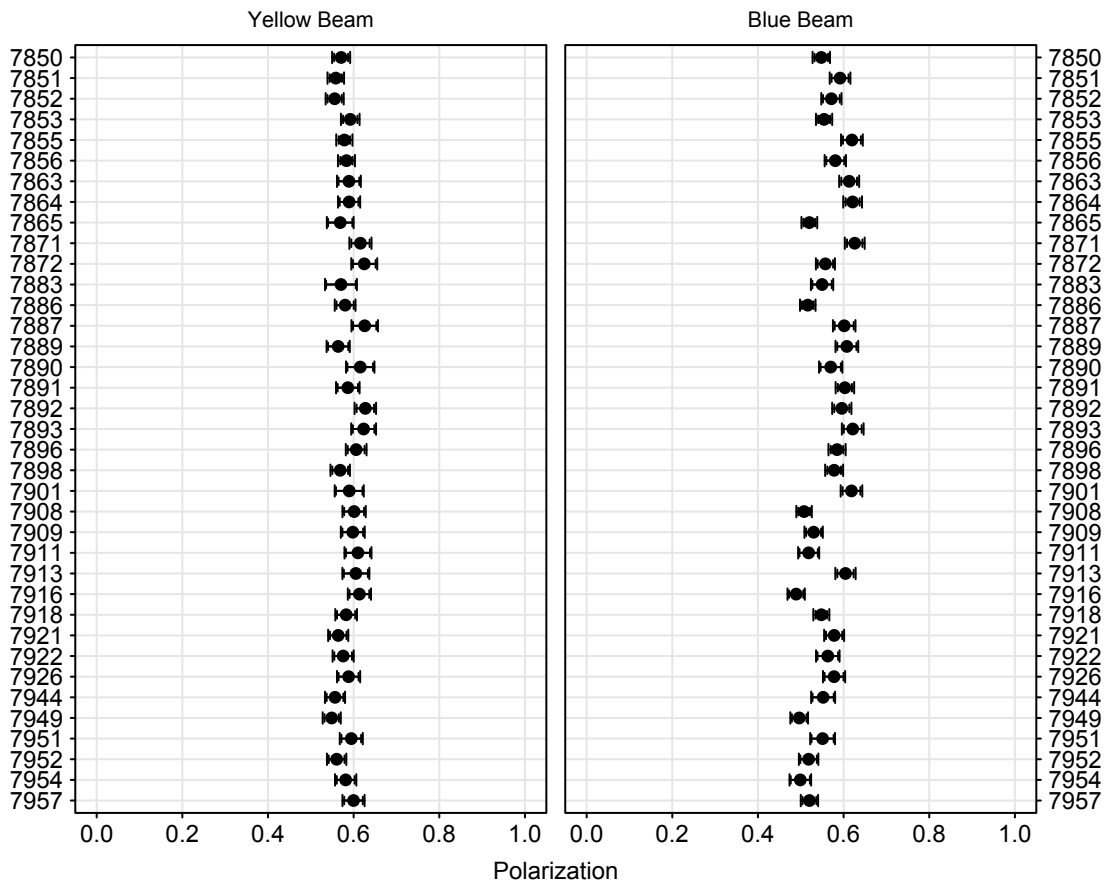
Figure 5-5: Polarization, statistical error, quadratic sum of statistical error and systematic error

5.6 Jet Triggers and E_T Thresholds

The BHT2 Trigger and the BJP1 Trigger

Events were recorded online if they satisfy the requirements of at least one of the active triggers during the run. Approximately thirty triggers were active in the *pp-ProductionLong* setup.
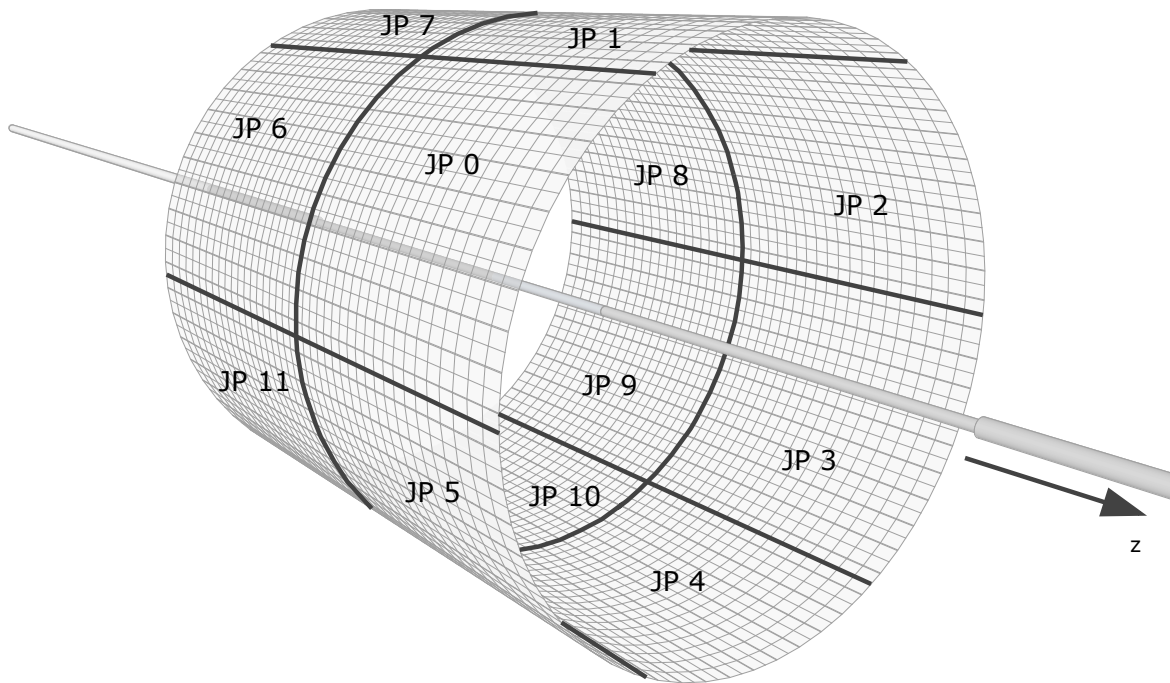
©2009 Tai Sakuma

Figure 5-6: The locations of the twelve jet patches of the BJP1 trigger. The size of a jet patch is 1.0×1.0 in the $\eta - \varphi$ coordinate system. Each jet patch contains 400 BEMC towers.

Two triggers were primarily used in this thesis: the BHT2 (*Barrel High Tower* 2) trigger and the BJP1 (*Barrel Jet Patch* 1) trigger. Both triggers require the MINB condition, defined in Section 4.4. In addition, the BHT2 trigger requires a minimum transverse energy E_T deposit in a BEMC tower, and the BJP1 trigger requires a mini-

mum energy deposit in a *patch* of calorimeter towers ($\Delta\eta \times \Delta\varphi = 1 \times 1$). The locations of the jet patches are depicted in Figure 5-6. The table 5.3 summarizes these triggers.

	ID	$\Delta\eta \times \Delta\varphi$	Threshold	
			DSM ADC	E_T
BHT2	137213	0.05×0.05	24	~ 5.4 GeV
BJP1	137222	1×1	60	~ 8.3 GeV

MINB Condition: The BBC west and east coincidence

Table 5.3: Triggers

Offline Trigger Thresholds

The trigger thresholds required offline analysis were set to be higher transverse energies E_T than required by hardware. At the time of the data collection, the trigger thresholds were predetermined in terms of the DSM[1] ADC[2] values. Because the calorimeter gains are not uniform over the BEMC towers, the trigger efficiencies in terms of E_T have *turn-on curves*. In Run-5, the trigger turn-on curves for a barrel high tower trigger and a barrel jet patch trigger were measured with the same types of the triggers with the lower thresholds.

In Run-5, the MC simulation estimated that the turn-on was somewhat faster than the data (Figure 5-7). The trigger turn-on curves in the Run-6 data could not be measured because of the lack of the same types of the triggers with lower thresholds. They were estimated by the MC simulation (Figure 5-8). If the situation is similar between Run-5 and Run-6, the trigger turn-ons in the Run-6 data should be somewhat slower than the turn-ons in the MC simulation.

To make the trigger thresholds uniform in terms of E_T, offline trigger thresholds were applied on E_T at the values somewhat greater than the upper edges of the trigger turn-on curves of the MC simulation. The offline thresholds are 7.0 GeV for the the

---

[1]Data Storage and Manipulation
[2]Analog to Digital Converter

BHT2 trigger and 10.8 GeV for the BJP1 trigger:

$$7.0 \text{ GeV} < \quad (\text{Trigger Tower } E_T)$$

$$10.8 \text{ GeV} < (\text{Trigger Jet Patch } E_T).$$
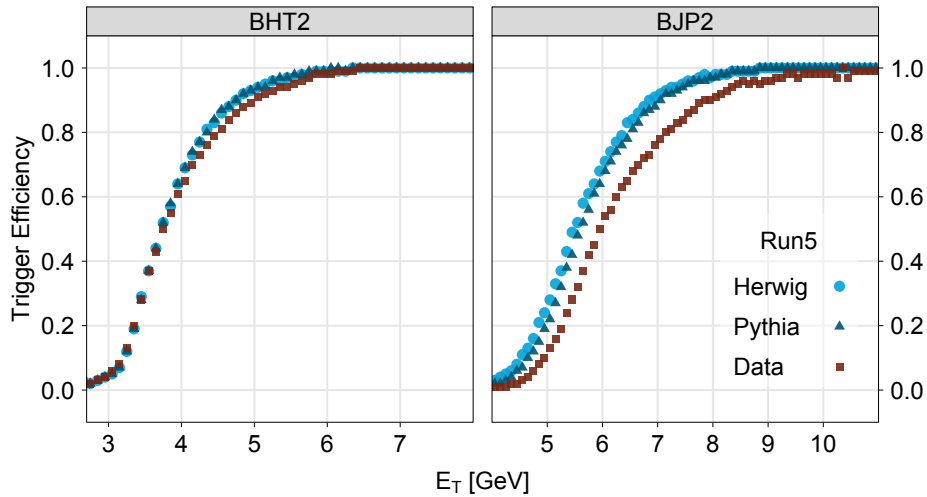
Figure 5-7: The measured trigger efficiencies in Run-5 with the MC simulated efficiencies. The turn-ons in the data are slower than those in the MC simulation.
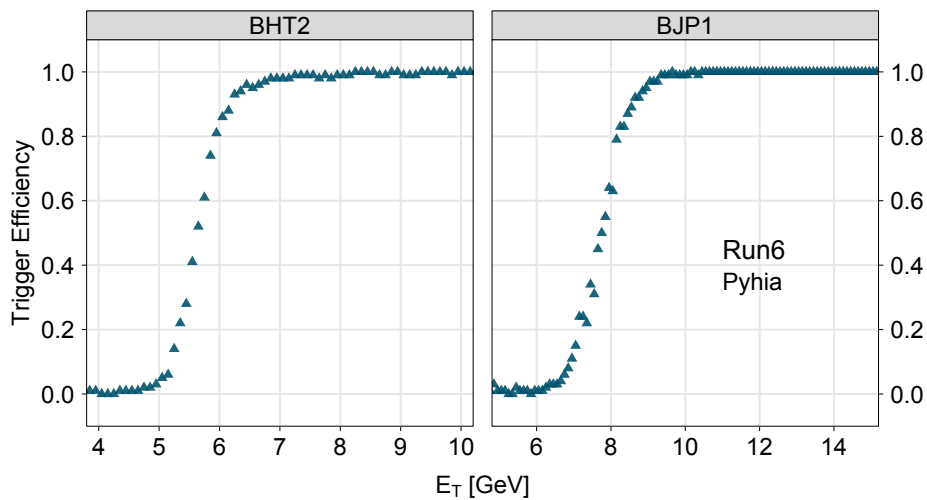
Figure 5-8: The trigger efficiencies in Run-6 evaluated by the MC simulation.

Trigger E_T Distributions

Figure 5-9 compares the trigger E_T distributions in the data and in the MC simulation. The data and the MC simulation have very different distributions. While the MC distribution is approximately a rapid exponential fall-off, the data appears to have two components: a rapid fall-off, which is consistent with the MC simulation, and a slow fall-off. The cause of the slow fall-off is unknown. Possibilities include background, and non-QCD events, hot towers, non-linearity of the detector response.
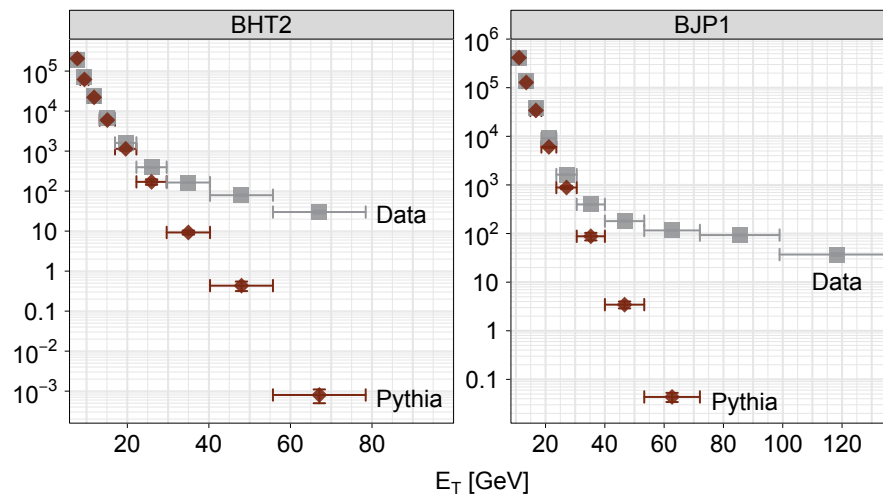
Figure 5-9: Comparisons of the distributions of the E_T deposits between the data and the MC events. The MC distributions are normalized to have the same number of the total events as data.

5.7   Vertex and Timebin

In Run-6, the FWHM (*full-width half maximum*) proton bunch length was about 8 ns, which corresponds to 2.4 m. The distance between the membrane and the ground plane of the TPC is 2.1 m (Figure 4-2). Clearly, a non-negligible fraction of collisions would occur appreciably away from the IP. On the other hand, the detector is optimized to measure events occurring at the IP. For example, the BEMC towers are projective towards the IP (Figure 4-5), and the membrane of the TPC is installed at $z = 0$ (Figure 4-2).
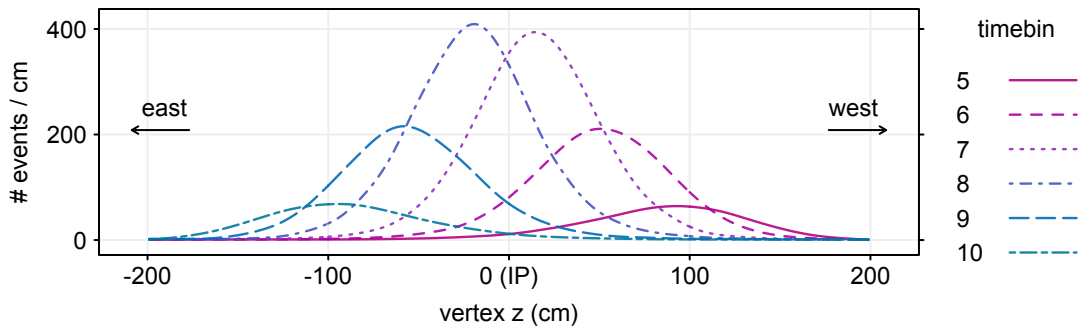
Figure 5-10: The vertex distributions of MINB events in each timebin.

Normal practice is to select events close to the IP by applying a vertex-*z* cut. However, this cut requires that events have reconstructed vertices. In this thesis, instead, *timebin*, described in Section 4.4, is used to select events because all BHT2 events and BJP1 events have measured timebins by definition since the BBC coincidence is a trigger condition.

Figure 5-10 shows the vertex distributions of the MINB events by timebins. The IP is between the centers of the timbebin 7 and the timebin 8. The centers of the vertex distributions are shifted toward the east side for the timebins 9 and 10 and

Timebin	MINB	BHT2	BJP1
1	3	9	18
2	50	85	180
3	271	594	1379
4	1446	3581	7367
5	7082	15894	28159
6	20227	38971	61403
7	33873	62467	89424
8	34584	60593	86302
9	20198	36398	53948
10	7756	15372	24756
11	1718	3831	7025
12	332	790	1495
13	38	62	141
14	6	8	12

Table 5.4: The numbers of the events with reconstructed vertices for each timebin for each trigger. The MINB events are prescaled.
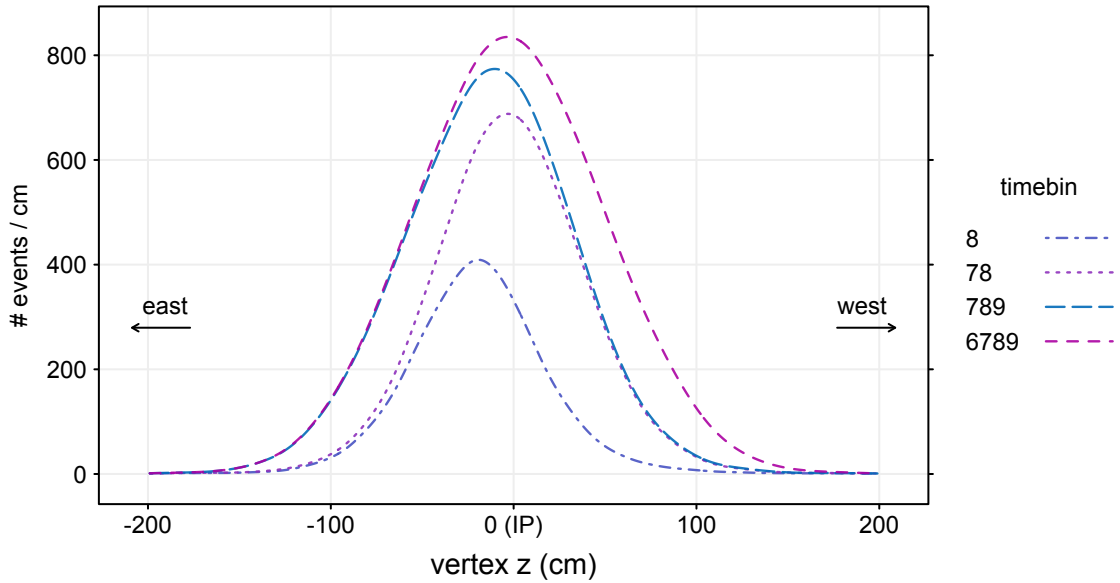
Figure 5-11: The vertex distributions of MINB events in each timebin set.

the west side for the timebins 6 and 5. The numbers of the events with reconstructed vertices in each timebin is given in Table 5.4.

In this thesis, events in the timebins 6, 7, 8, and 9 are used in four different combinations of timebins: 8, 78, 789, and 6789. Figure 5-11 shows the vertex distributions of the MINB events in each combination of the timebins.

The fraction of the MINB events that are accepted by the timebin selections is the correction factor $\mathcal{C}_{tb}$:

$$\mathcal{C}_{tb} = \frac{N_{MINB}^{tb}}{N_{MINB}}, \tag{5.3}$$

Timebin	$\mathcal{C}_{tb} \pm \delta\mathcal{C}_{tb}(\text{stat.})$
8	0.2620 ± 0.00088
78	0.5263 ± 0.00100
789	0.6796 ± 0.00094
6789	0.8406 ± 0.00073

Table 5.5: The Correction Factors $\mathcal{C}_{tb}$

The table 5.5 gives the values of the correction factors $\mathcal{C}_{\text{tb}}$. The determination of $\mathcal{C}_{\text{tb}}$ is much simpler than the determination of the corrections that would have to be made if vertex cuts had been used. $\mathcal{C}_{\text{tb}}$ was used in cross section measurements.

Chapter 6

Jet Definition

6.1   Jets at Three Levels

Jets are sprays of particles which are moving approximately in the same direction from the collision point. Jets can be defined at three different levels: the *parton level*, the *hadron level*, and the *detector level*. The parton-level jets are outgoing partons of the hard interactions (Figure 6-2). For example, in leading-order (LO) perturbative quantum chromodynamics (pQCD) of $2 \rightarrow 2$ interactions, two outgoing partons are each parton-level jets. In next-to-leading-order (NLO) pQCD calculations, there are at most three outgoing partons. Two of the outgoing partons moving in a similar direction may form a parton-level jet, while momentum balance normally ensures that the third parton is a separate parton-level jet (Figure 6-1). The hadron-level jets are composed of products of hadronization and particle decay of the outgoing partons (Figure 6-3). They are predominantly hadrons, but may contain leptons and photons as well. The detector-level jets are detector responses to the hadron-level

Levels	Components
The Parton Level	Outgoing partons produced in hard scattering
The Hadron Level	Products of hadronization and particle decay
The Detector Level	Energy deposits in BEMC towers and tracks left in the TPC

Table 6.1: The Three Levels of Jets
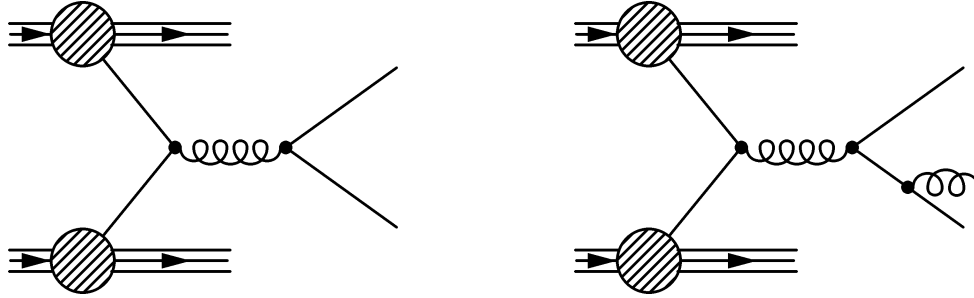
Figure 6-1: In LO pQCD calculations (*left*), two outgoing partons are each parton-level jets. NLO pQCD calculations have at most three outgoing partons (*right*). Two outgoing partons moving in a similar direction form a parton-level jet. An isolated outgoing parton is a parton-level jet by itself.

jets. In the case of this thesis, they are made of energy deposits in BEMC towers and charged tracks reconstructed in the TPC (Figure 6-4).

An aim of the jet measurement is to evaluate the parton-level kinematics. However, the parton-level information degrades in the transitions of each jet level to the next. Hadron-level jet momenta are not identical to the corresponding parton-level jet momenta. Jets, which are color charged at the parton level, exchange their color charge with other jets or remnant partons and become color-neutral at the hadron level. While exchanging color charge, the jets gain or lose momentum carried by the exchanged color charge. From the hadron level to the detector level, the kinematical information suffers from the limitations of the experiment, such as trigger efficiency and detector resolutions.

Sensible comparison between theory and experiment requires unequivocal definition of jets at each level and evaluation of the systematic effects of each transition. In an experiment, jets are reconstructed at the detector level, whereas perturbative QCD calculations predict jet productions at the parton level. One way to evaluate the systematic effects of the transitions is to use MC events because jets can be reconstructed at all three levels in MC simulation.

Figure 6-2: A high-p_T back-to-back dijet event at the parton level.

Figure 6-3: A high-p_T back-to-back dijet event at the hadron level.
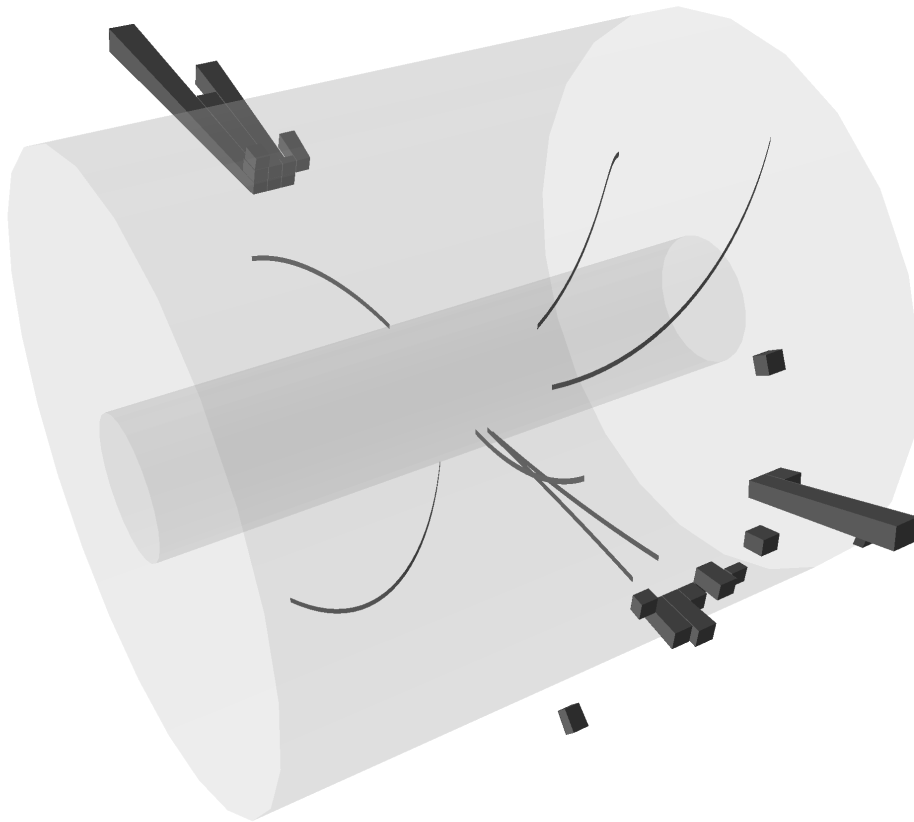
©2009 Tai Sakuma

Figure 6-4: A high-p_T back-to-back dijet event at the detector level. The solid trajectories indicate TPC track measurements while the lego blocks indicate energy deposited in the BEMC towers.

This chapter describes the parts of the jet definition common to all three levels and those specific to the detector-level jets. The jet definition specific to the hadron-level jets and the parton-level jets in the MC simulation is described in Chapter 7.

6.2 Jet Reconstruction

The jet reconstruction takes three steps. First, four-momenta are constructed from components of jets. The components are different at different jet levels as mentioned in the previous section. Second, jets are defined as particular sets of four-momenta selected by a jet-finding algorithm. Finally, four-momenta of jets are determined from the kinematical properties of the four-momenta selected as jets. Only the first step is different for different jet levels. The second and third steps deal with only four-momenta and employ a common jet definition and jet-finding algorithm, as a result, are independent of the jet level.

Step	Name	
1	Four-momentum construction	Different for each jet level
2	Jet finding	Common to all jet levels
3	Four-momentum recombination	Common to all jet levels

Table 6.2: The three steps of jet reconstruction

6.2.1 Four-Momentum Construction (Detector Level)

This subsection describes the four-momentum construction for the detector-level jets. The four-momentum construction at the parton level and the hadron level are described in Chapter 7. A four-momentum for detector-level jets is constructed from each TPC track and BEMC tower. Table 6.3 summarizes the parameters of the construction.

Tracks are required to have at least twelve hits on the MWPC (*multi-wire proportional chamber*) located at the ends of the TPC. The number of hits of each track is required to be greater than fifty-one percent of the possible hits to eliminate *split tracks*.

The 3,871 towers that passed QA are used in this thesis. In each event, the towers used are the ones with ADC values greater than twice the root mean square of the pedestal noise distributions from the pedestal mean.

In order to avoid measuring the same charged particles twice both in the TPC and in the BEMC, if tracks point to a BEMC tower, the energy that a MIP would leave in the tower is subtracted from the tower energy (or the tower energy is set to zero if the MIP energy is greater than the tower energy).

After the MIP energy subtraction, cuts are applied to the distance of closest approach (DCA) and its radial component (DCA_{xy}) to reject a background of pile-up tracks.

Both charged tracks and neutral energies have three components of their four-momenta reconstructed. Three-momenta (p_x, p_y, p_z) of tracks are reconstructed in the TPC. The amount of energy (E) deposited in towers and the directions (η, φ) of

Track Selection		
# hits > 12		
# hits / # possible hits > 0.51		
Tower Selection		
3,871 towers that passed QA out of the 4,800 towers		
ADC > Pedestal+2×RMS		
Tower Energy Correction for Tracks		
MIP energy subtraction		
Pile-up Track Removal		
$\lvert \text{DCA} \rvert \leq 3.0$ cm		
	≤ 2.0 cm	if $p_\text{T}^\text{track} < 0.5$ GeV
DCA_{xy}	$\leq 3.0 - 2.0 \times p_\text{T}^\text{track}$ cm	if $0.5 \leq p_\text{T}^\text{track} < 1.0$ GeV
	≤ 1.0 cm	if $1.0 \leq p_\text{T}^\text{track}$
Four-Momentum Construction		
Photon mass (0.0 GeV) for towers		
Charged pion mass (0.13975 GeV) for tracks		
$p_\text{T} \geq 0.2$ GeV		

Table 6.3: Parameters of the four-momentum construction for detector-level jets

the towers from the vertex positions are the three components of the reconstructed tower energies. In order to construct four-momenta out of three variables, tracks are assumed to have the mass of a charged pion (139.75 MeV), and towers are assumed to be massless.

After four-momenta are constructed from the BEMC towers and the tracks in the TPC, those with p_T greater than 200 MeV are sent to a jet-finding algorithm.

6.2.2 The Mid-Point Cone Algorithm

The *mid-point cone jet-finding algorithm*[32] is used to find jets. The mid-point cone algorithm works in the η - φ coordinate plane. It defines jets as collections of four-momenta which lie within a specific radius of a circle (R). The specific radius is called the *cone radius* and is 0.7 in this thesis. The radius 0.7 is the radius up to which the approximation which is used to define jets in the NLO pQCD calculation is valid [33]. The mid-point cone algorithm has two steps: find proto-jets first, then split and merge proto-jets to jets.

Proto-jets

The first step of the mid-point cone algorithm is to find all *proto-jets* in a given event. Proto-jets are defined as the collections of the four-momenta inside the cones whose axes coincide with the E_T-weighted centroid of the four-momenta. A proto-jet may share four-momenta with other proto-jets. The mid-point cone algorithm is a seed-based algorithm: it finds proto-jets around seeds. There are two types of seeds in the algorithm: four-momenta and *mid-points*. The algorithm sorts the list of the four-momenta by E_T in descending order. Then, the algorithm uses the first four-momenta in the sorted list as a seed and finds a proto-jet around the seed. Subsequently, in the order of the sorted list, the algorithm uses four-momenta which are not yet a part of proto-jets as seeds and finds proto-jets around them. After reaching the end of the four-momenta list, the algorithm creates the list of mid-points of all pairs of the proto-jets. It then uses the mid-points as seeds and finds further proto-jets around mid-points.

Split-and-Merge

The second step is the *split-and-merge*. Proto-jets are allowed to share four-momenta with other proto-jets, but jets are not. The algorithm decides whether to split or merge two proto-jets that have common four-momenta based on the fractions of the energy shared by the two proto-jets. If the fraction is smaller than a specific value, which is 0.5 in this thesis, the proto-jets are split into two jets, and the shared four-momenta are assigned to the closest jets. If the fraction is greater than the specific value, the proto-jets are merged into a single jet.

Cone Radius	=	0.7
Split/Merge Fraction	=	0.5

Table 6.4: Parameters of the Mid-Point Cone Algorithm

6.2.3 *E-scheme* (Four-Vector Recombination Scheme)

The last step of the jet reconstruction is to recombine the four-momenta and define four-momenta of the jets. The recombination scheme used is referred to as *E-scheme* or the *four-vector recombination scheme* in the ref.[32], in which four-momenta of the jets are the four-vector sum of the collections of the four-momenta that define the jets.

$$p^{\text{jet}} = (E^{\text{jet}}, p_x^{\text{jet}}, p_y^{\text{jet}}, p_z^{\text{jet}}) = \left(\sum_{i \in \text{jet}} E^i, \sum_{i \in \text{jet}} p_x^i, \sum_{i \in \text{jet}} p_y^i, \sum_{i \in \text{jet}} p_z^i \right)$$

This scheme might appear to give an obvious definition of the jet four-momenta. However, there are other schemes used in the literature [32].

6.3 Correction for Pile-Up (Detector Level)

In an environment where luminosity is high and/or a bunch crossing interval is short, multiple events may occur in a single bunch crossing or an event may leave a signal in another event triggered by neighboring bunch crossings. Such events are called *pile-up* events. To account for the effect of the pile-up events, 50 MeV is subtracted

from the jet p_T.

$$p_T^{\text{corrected}} = p_T - 50 \text{ MeV}$$

This correction is applied only in the data. It is not applied in the MC events, since pile-up events are not simulated.

6.4 Detector η and BEMC Acceptance (Detector Level)

This selection is applied to avoid using jets reconstructed at the edge of the BEMC acceptance. The *detector η* of a jet is the position of the BEMC that the four-momenta of the jet crosses (Figure 6-5). The detector η and the jet η coincide for jets in the events for which the vertex positions are at the IP, namely, $z = 0$ in the formula. The acceptance of the BEMC is $-1.0 <$ detector $\eta < 1.0$. The following cut is applied:

$$-0.7 < (\text{detector } \eta) < 0.7.$$

6.5 Neutral Energy Ratio and Background (Detector Level)

This selection is applied to reject *beam-gas background*. As described in Section 6.2, detector-level jets are composed of tracks in the TPC and energy deposits in the BEMC. *Neutral energy ratio R_T* is the fraction of jet transverse energy E_T reconstructed from energy deposits in the BEMC:

$$R_T = \frac{E_T^{\text{neutral}}}{E_T^{\text{jet}}}.$$

Figure 6-6 and Figure 6-7 show the relation between jet E_T reconstructed from energy deposits in the BEMC (neutral E_T) and that from tracks in the TPC (track E_T) in eight different jet p_T ranges. The R_T distribution has a peak approximately at 1/3 for high-p_T jets, the reason for which is discussed in Section 8.2. The line $R_T = 1/3$ is drawn in the figures. As jet p_T decreases, the neutral energy ratio R_T increases in order for jets to contain more neutral energy than the trigger thresholds. In other words, the low-p_T jets have higher R_T due to trigger biases.
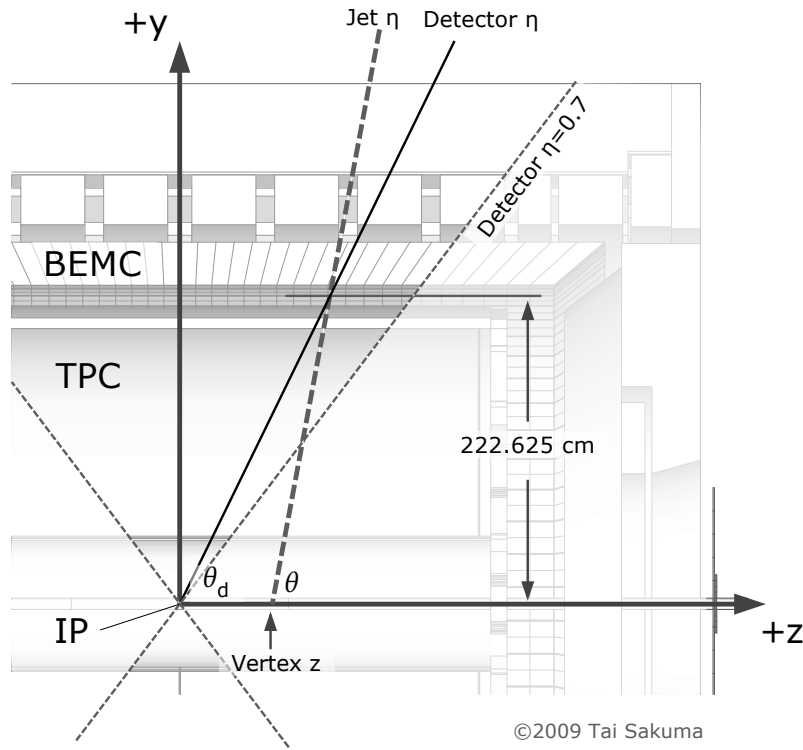
Figure 6-5: Jet η and detector η

Beam-gas background is likely to have high R_T. In the figures, the background events are clearly isolated from the signal events in high p_T ranges. The following cuts applied to reject the background events:

$$R_\mathrm{T} < 1.0 \quad (5 < p_\mathrm{T} \leq 17.31 \text{ GeV})$$

$$R_\mathrm{T} < 0.99 \, (17.31 < p_\mathrm{T} \leq 21.3 \text{ GeV})$$

$$R_\mathrm{T} < 0.97 \, (21.3 < p_\mathrm{T} \leq 26.19 \text{ GeV})$$

$$R_\mathrm{T} < 0.90 \, (26.19 \text{ GeV} < p_\mathrm{T}).$$

The cuts are indicated by the shaded ares in the figures.
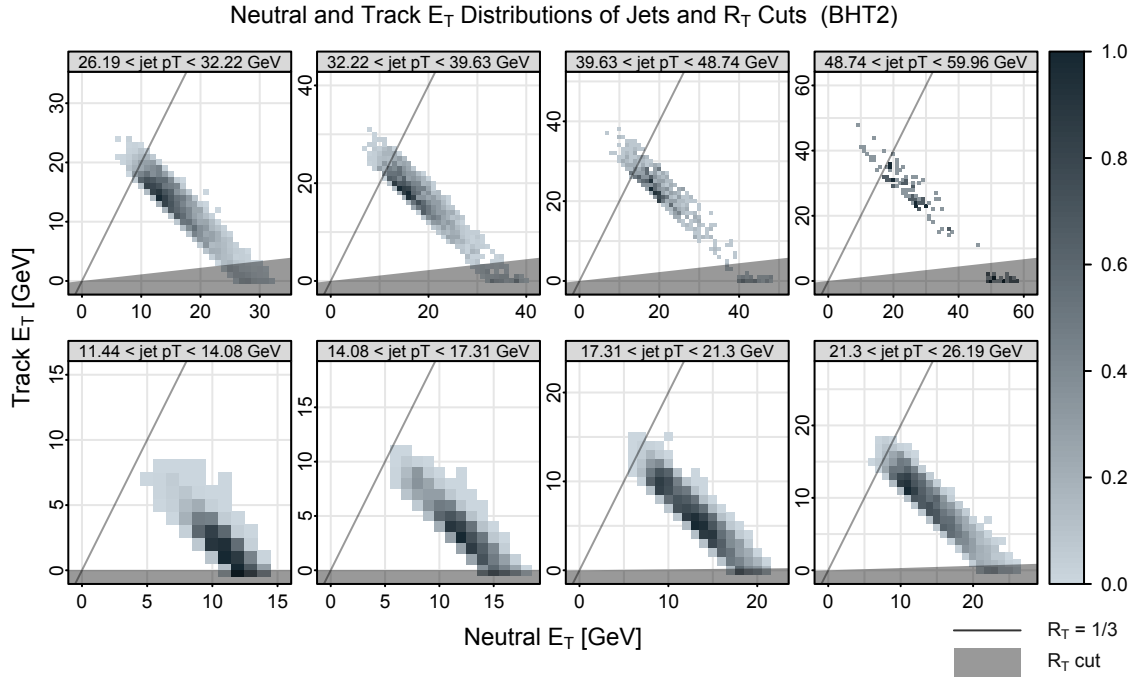
Figure 6-6: Level plots of neutral and track E_T distributions in jets in eight different jet p_T ranges for the BHT2 events. The distributions are separately normalized in each panel. The shaded areas indicate the R_T cuts. The solid lines are $R_T = 1/3$.

6.6 Trigger Jets (Detector Level)

Trigger jets are the jets that caused the trigger. Only trigger jets are used in the inclusive jet measurement. In the dijet measurements, at least one jet of the dijets is required to be a trigger jet. Jets that caused the triggers are identified by the following conditions.

BHT2 Jets contain at least one tower with energy deposit greater than the trigger threshold (7.0 GeV).

BJP1 Jets deposit more energy than the trigger threshold (10.8 GeV) in the triggered jet patch.
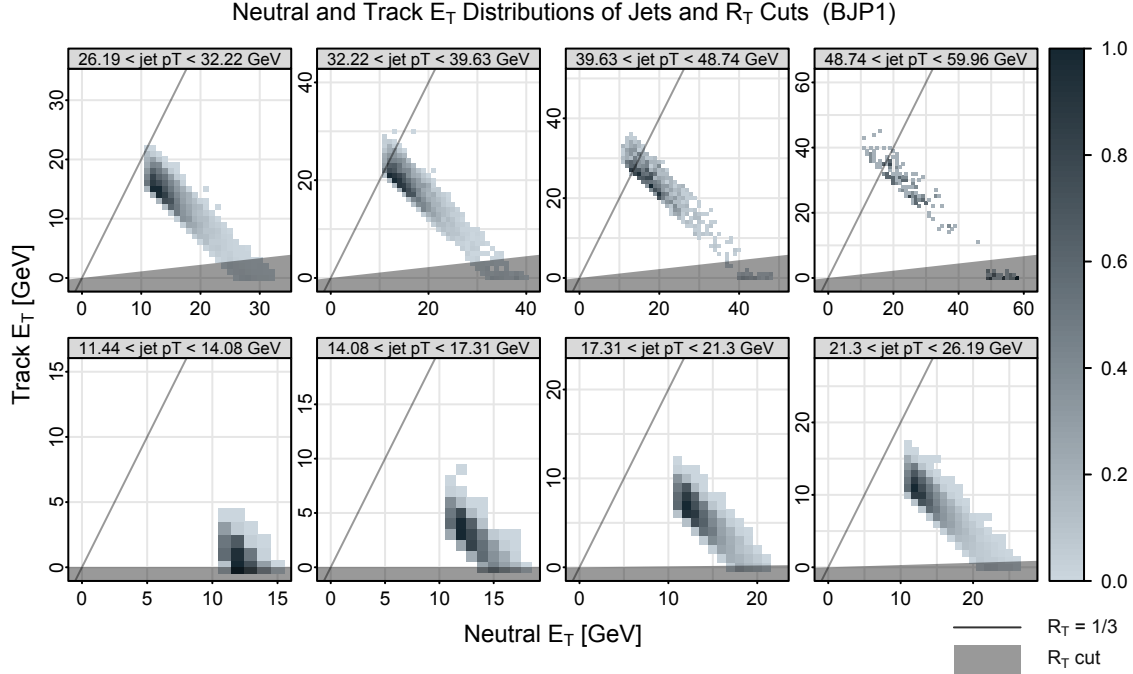
Figure 6-7: The same as the Figure 6-6 but for the BJP1 events.

6.7 Phase Space and Jet Pseudo-Rapidity η

Data and theory predictions need to be compared in the same phase space. A phase space of inclusive jets can be specified by three variables. The three variables in the inclusive jet cross section measurement are jet transverse momentum p_T, jet pseudo-rapidity η, and azimuthal angle φ. Jet production has no azimuth dependence in longitudinally polarized collisions. The range of p_T is specified in Section 9.2. This section discusses the η range.

The detector η cut discussed in Section 6.4 roughly defines the jet η range of the measurement. The following formula gives the relation among detector η, jet η, and the z-vertex position (see Figure 6-5):

$$(\text{detector } \eta) = -\log \tan \left\{ \frac{1}{2} \text{atan} \left(\frac{222.625 \text{ cm}}{222.625 \text{ cm} \cdot \cot(2\text{atan}(\exp(-(\text{jet } \eta)))) + (\text{vertex } z[\text{cm}])} \right) \right\}.$$

This relation is illustrated in Figure 6-8. The range of jet η specified by the detector η cut ($|(\text{detector } \eta)| \leq 0.7$) depends on the vertex position. The vertex distributions for each timebin selection are shown in Figure 5-11.
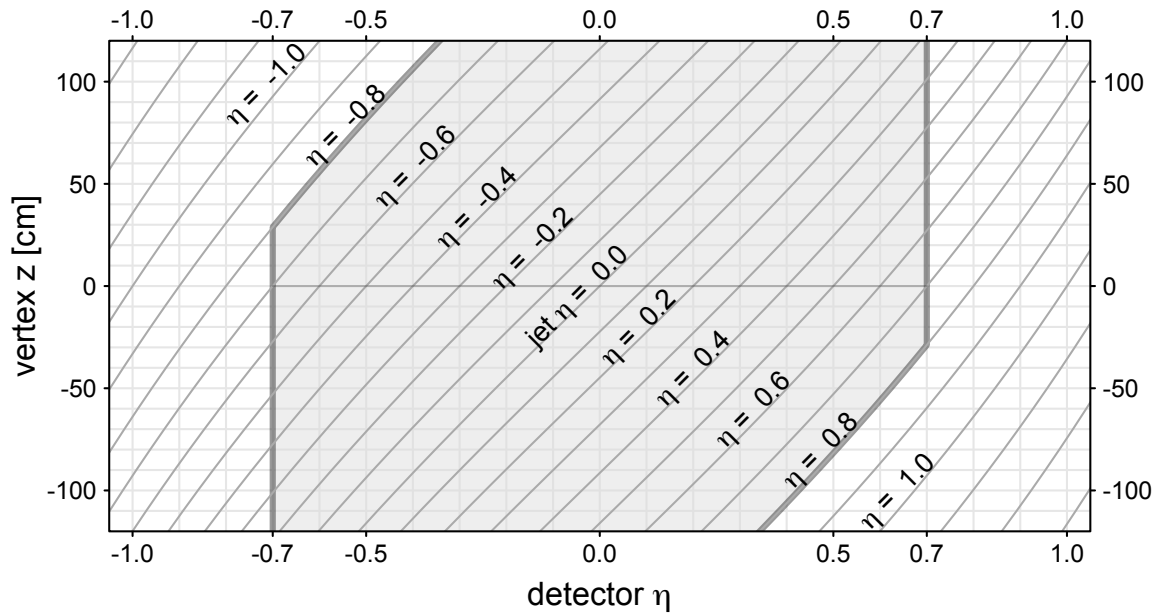
Figure 6-8: The relation among jet η, detector η, and the z-vertex position.

In order to specify a definite jet η range, the following jet η cut is applied.

$$-0.8 < (\text{jet } \eta) < 0.8.$$

Given timebin selections and the detector η cut, a sufficient number of jet samples can be collected in this η range. In the MC simulation, this cut is applied at all three jet levels.

6.8   Jet Yields

Table 6.5 gives the reconstructed jet yields in each timebin set for each trigger.

	BJP1				BHT2			
p_T **[GeV]**	**Timebin 8**	**78**	**789**	**6789**	**8**	**78**	**789**	**6789**
9.30-10.32	0	0	0	0	3927	8135	10281	12527
10.32-11.44	244	511	615	755	4570	9320	11749	14385
11.44-12.69	2500	5032	6175	7503	4779	9635	12074	14783
12.69-14.08	4692	9537	11863	14329	4410	9103	11544	14253
14.08-15.61	5930	11867	14931	18280	4202	8381	10646	13112
15.61-17.31	6246	12521	15855	19347	3690	7380	9448	11593
17.31-19.20	6100	12283	15481	19017	3216	6556	8210	10106
19.20-21.30	5464	10927	13913	17115	2575	5230	6682	8204
21.30-23.62	4567	9277	11790	14419	1959	4025	5129	6338
23.62-26.19	3733	7304	9330	11390	1428	2898	3756	4623
26.19-29.05	2594	5162	6563	8023	1021	2005	2540	3141
29.05-32.22	1679	3355	4345	5319	664	1330	1721	2115
32.22-35.73	937	1919	2496	3113	392	794	1013	1249
35.73-39.63	475	1009	1292	1618	208	473	590	726
39.63-43.95	252	493	639	760	126	250	325	393
43.95-48.74	106	206	257	331	65	128	158	197
48.74-54.06	35	67	96	124	23	42	62	79
54.06-59.96	10	24	33	42	8	17	25	33
59.96-66.49	4	8	11	16	1	5	6	10

Table 6.5: The jet yields in each timebin set for each trigger.

Chapter 7

Monte Carlo Simulation

The Monte Carlo (MC) simulated events are generated to:

- determine off-line trigger threshold,

- unfold the hadron-level jet cross section,

- estimate the effect of hadronization and underlying events,

- evaluate the trigger bias on the dijet $\mathcal{A}_{\mathrm{LL}}$,

- and calculate the mass shift in the dijet $\mathcal{A}_{\mathrm{LL}}$.

This chapter describes the MC event production and the jet reconstruction in the MC simulation.

7.1 MC Event Production

The events are generated by the Pythia 6.410 event generator [34] with the CTEQ5L parton distributions [35]. The detector responses to the events are simulated with a GEANT3 [36] based STAR detector simulation program.

The MC Event Data Sets

The cross section of high-$\hat{p}_{\mathrm{T}}$ events in proton collisions has a rapidly decreasing $\hat{p}_{\mathrm{T}}$ dependence. The cross section in the $\hat{p}_{\mathrm{T}}$ range for which MC events need to be generated extends nine orders of magnitude. To generate MC events in a range of $\hat{p}_{\mathrm{T}}$ over

such a wide span of cross section, the MC event production is divided into several runs, each of which generates events in a short range of $\hat{p}_T$. Table 7.1 summarizes the MC event data sets.

| run ϕ | $\hat{p}_T$[GeV] | | σ_ϕ[pb] | N_ϕ^{gen} | w_ϕ |
	min	max			
rcf1318	3	4	1.30×10^9	686,000	$1.90 \times 10^{+3}$
rcf1317	4	5	3.15×10^8	500,000	$6.30 \times 10^{+2}$
rcf1311	5	7	1.37×10^8	398,000	$3.43 \times 10^{+2}$
rcf1310	7	9	2.30×10^7	420,000	$5.49 \times 10^{+1}$
rcf1309	9	11	5.53×10^6	414,307	$1.33 \times 10^{+1}$
rcf1308	11	15	2.22×10^6	420,000	$5.30 \times 10^{+0}$
rcf1307	15	25	3.90×10^5	397,200	9.81×10^{-1}
rcf1306	25	35	1.02×10^4	400,000	2.56×10^{-2}
rcf1303	35	45	5.01×10^2	110,000	4.56×10^{-3}
rcf1302	45	55	2.86×10^1	118,000	2.43×10^{-4}
rcf1304	55	65	1.46×10^0	120,000	1.20×10^{-5}
	CKIN(3)	CKIN(4)	PARI(1)	MSTI(5)	PARI(2)

Table 7.1: The MC event data sets

Combining the Data Sets

The results from all production runs need to be combined to produce the total results. The total cross sections σ_ϕ and the numbers of the generated events N_ϕ^{gen} are different for different production runs; therefore, events in different runs have different weights of significance w_ϕ,

$$w_\phi = \frac{\sigma_\phi}{N_\phi^{\text{gen}}}. \tag{7.1}$$

Pythia calculates the total cross section σ_ϕ of the production runs ϕ by Monte Carlo integration. The $\hat{p}_T$ ranges of the runs are disjoint so that the weighted results from different runs can be simply added to obtain the total results. For example, the total cross section in the $\hat{p}_T$ bin i is given by the sum of the weights of the events for which the $\hat{p}_T$ falls in the $\hat{p}_T$ bin i:

$$\sigma_i^{\text{MC}} = \sum_{\hat{p}_T \in i} w_\phi. \tag{7.2}$$

Figure 7-1 shows the cross section obtained in this way. The connections between the different MC data sets are smooth, and the combined results show the $\hat{p}_{\mathrm{T}}$ dependence of the total cross section. In this example, the cross section is calculated as a function of the variable in terms of which the phase space of the production is divided. Moreover, all $\hat{p}_{\mathrm{T}}$ boundaries in the production are the boundaries of the $\hat{p}_{\mathrm{T}}$ bins in the cross section. The boundaries of the different data sets can be clearly seen in the figure. The same variable and the same boundaries between the production and the cross section are not necessary conditions for the formula (7.2). In fact, a formula similar to (7.2) works for any variables such as jet p_{T} and η, as long as an adequate number of events are generated in the phase space of interest, and the phase spaces are disjoint between the production runs.

The CDF Tune A Parameter Set

The Pythia version 6.4 adopts the *CDF Tune A parameter set* [37], which is tuned to fit the CDF *underlying event* data. The parameters are shown in Table 7.2.
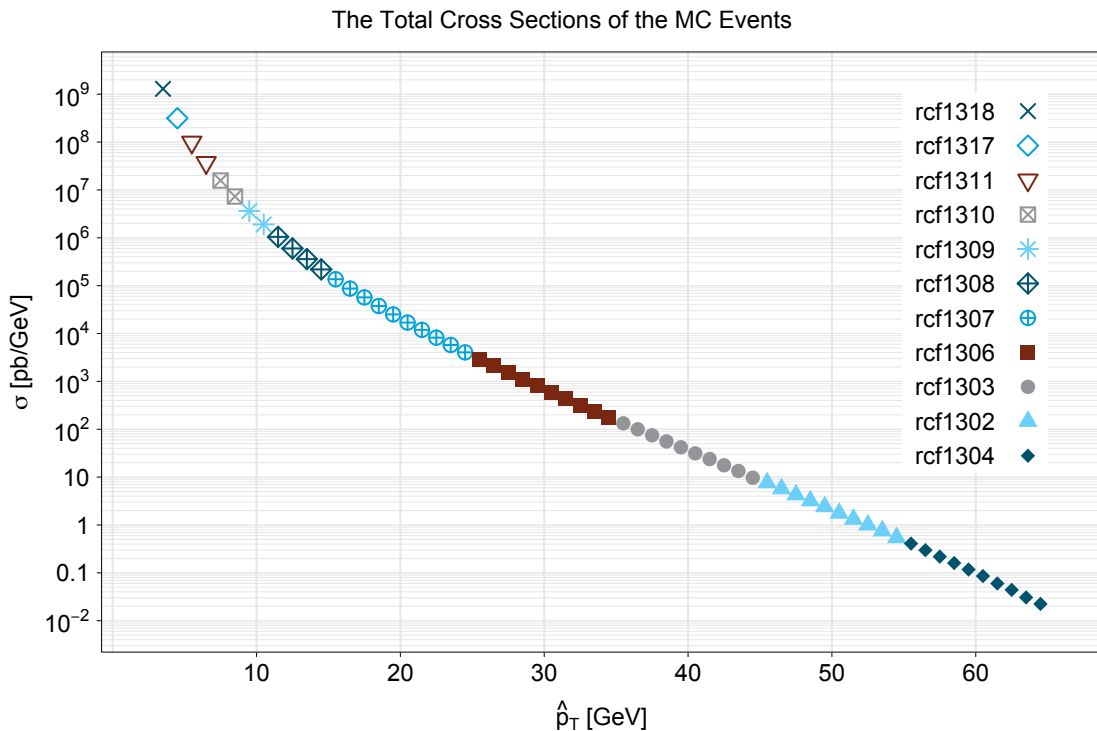
Figure 7-1: The $\hat{p}_{\mathrm{T}}$ dependence of the total cross section of the MC events.

MSTP(51)	=	7	CTEQ5L
MSTP(81)	=	1	Multiple interactions ON
PARP(82)	=	2.0	Regularization scale of $\hat{p}_{\mathrm{T}}$ in multiple interactions
PARP(83)	=	0.5	Parameter of matter overlap in the protons
PARP(85)	=	0.9	Probability relating to multiple interactions
PARP(86)	=	0.95	Probability relating to multiple interactions
PARP(89)	=	1800	Reference energy scale
PARP(90)	=	0.25	Power of a energy-rescaling term
PARP(67)	=	4.0	Scale factor that determines a parton virtuality

Table 7.2: The CDF Tune A Parameter Set

QCD High-p_{T} Processes

The following QCD high-p_{T} processes are simulated.

$$qq \to qq$$

$$q\bar{q} \to q\bar{q}$$

$$q\bar{q} \to gg$$

$$qg \to qg$$

$$gg \to q\bar{q}$$

$$gg \to gg$$

The MC samples do not contain particles from other interactions, such as direct photon production, Drell-Yan process, quarkonium production. Consequently, in the MC events, the parton-level jets contain only quarks and gluons. Leptons and photons in the MC hadron-level jets only come from decay of the hadrons. Furthermore, the MC detector-level jets contain only the detector responses to the final states of the QCD interactions. For example, the MC detector-level jets do not contain a calorimeter response to direct photons. The data, on the other hand, contain all kinds of interactions; however, the cross section of the QCD events are so large compared to other interactions that it is sufficient to generate only the QCD processes for the jet measurements.

Figure [7-2](#) shows the ratios of the processes as a function of $\hat{p}_T$. Quark-quark interactions dominate high-$\hat{p}_T$ events; more gluons are involved in lower-$\hat{p}_T$ events. Parton distributions can explain this trend. High-$\hat{p}_T$ events are dominated by interactions between the partons with high-x, which are predominantly valence quarks; therefore, quark-quark interactions dominate high-$\hat{p}_T$ events. As $\hat{p}_T$ decreases, more partons with lower-x participate in hard interactions. In turn, as x decreases, gluon density increases and valence quark density decreases; therefore, quark-gluon interactions and gluon-gluon interactions dominate low-$\hat{p}_T$ events.
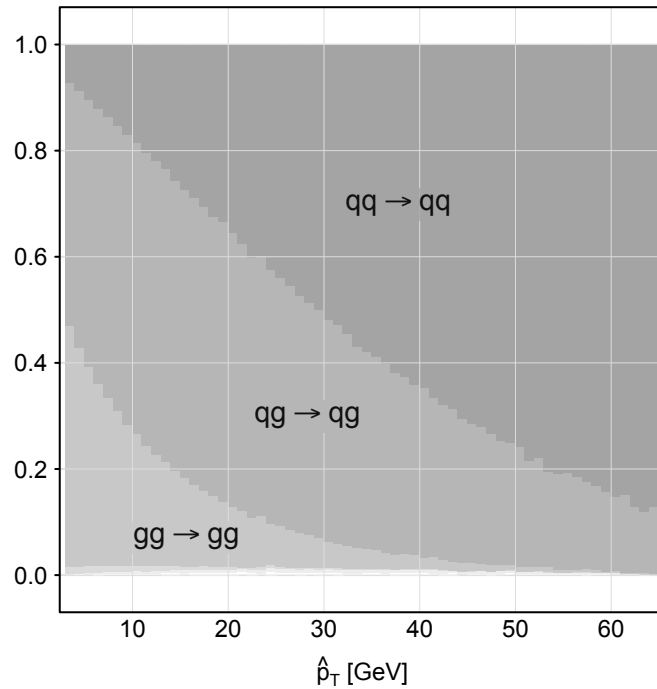
Figure 7-2: The ratios of the simulated processes as a function of $\hat{p}_T$.

Particle Decay in the MC simulation

The way to handle particle decay depends on the lifetime of the particles. Depending on lifetime, particles can be categorized into three groups: *short-lived*, *long-lived*, and *stable*. Short-lived particles are those that decay before they are significantly influenced by their surroundings, e.g. π^0, η. Either the event generator or the detector simulation program can simulate the decay of short-lived particles. Long-lived par-

ticles are those that travel some distance while interacting with material composing the detector. They may decay before they exit from the detector. The charged long-lived particles change their momentum in a magnetic field for tracking systems. For example, a charged kaon K^+ in the TPC changes the direction of its momentum due to the magnetic field while ionizing the gas, and this kaon may decay into a muon μ^+ and a neutrino ν_μ before it exits from the TPC. The detector simulation simulates the motion and the decay of long-lived particles as well as the detector responses to those particles. In the MC simulation, stable particles are defined as the particles with a lifetime so long that they have almost no possibility of decaying before they travel an order of the distance of the detector size. In this definition, stable particles include neutrons and muons in addition to the stable particles in the Standard Model such as protons and electrons. The decay of stable particles is not simulated at all.

In the MC simulation, the decays of the following particles are simulated in the detector simulation:

$$\pi^0, \pi^\pm, \eta, K^+, K^0_S, K^0_L, \Lambda^0, \Sigma^0, \Sigma^\pm, \Xi^\pm, \Xi^0, \Omega^\pm.$$

The following particles and their antiparticles are stable:

$$e^-, \nu_e, \mu^-, \nu_\mu, \nu_\tau, n, p.$$

As described in the next section, the hadron-level jets in the MC events are collections of final state particles in the event generator. Therefore, the composition of the hadron-level jets depends on whether particle decay is simulated in the event generator. For example, since the decay of neutral pions π^0 is simulated not in the event generator but in the detector simulation, a hadron-level jet may contain a π^0 but not 2γ's from the π^0 decay.

7.2 Jets in the MC Simulation

The three levels of jets were introduced in Section 6.1: the parton level, the hadron level and the detector level. While in the data, jets can be reconstructed only at the detector level, in the MC simulation, jets are reconstructed at all three levels.

The definition of the detector-level jets in the MC simulation is the same as that in the data except a correction; the correction for the pile-up effect, described in Section 6.3, is not applied in the MC events, since pile-up events are not simulated. Chapter 8 compares the detector-level jets in the data and those in the MC events.

7.3 Jet Definition (Hadron Level)

The hadron-level jets are composed of products of hadronization and particle decay of the outgoing partons (Figure 6-3). Four-momenta for hadron-level jets are the four-momenta of the final state particles in the MC event. This is in contrast to at the detector level, at which only three variables out of the four components of four-momenta are known. An acceptance cut, $|\eta| < 2.0$, is applied before jets are searched for by the jet finding algorithm described in Section 6.2.

Figure 7-3 shows the average fraction of the hadron-level jet energy carried by the constituent particles. Pions constitute about 60% of the jet energy. The ratio of the jet energy carried by neutral pions and by charged pions is about 1/3, which is roughly the neutral energy ratio of jets. The ratio 1/3 is consistent with the measured neutral ratio of away side jets of dijets (Section 11.3) and high-p_T trigger jets (Section 8.2), for which trigger biases are little.

As discussed in Section 6.7, the following jet η cut is applied to determine the phase space:

$$-0.8 < (\text{jet } \eta) < 0.8.$$

7.4 Jet Definition (Parton Level)

The parton-level jets are outgoing partons of the hard interactions. As in Figure 6-1, in QCD NLO calculations, the parton-level jets are single isolated outgoing partons

Average Fraction of Jet Energy Carried by Each Type of Particles
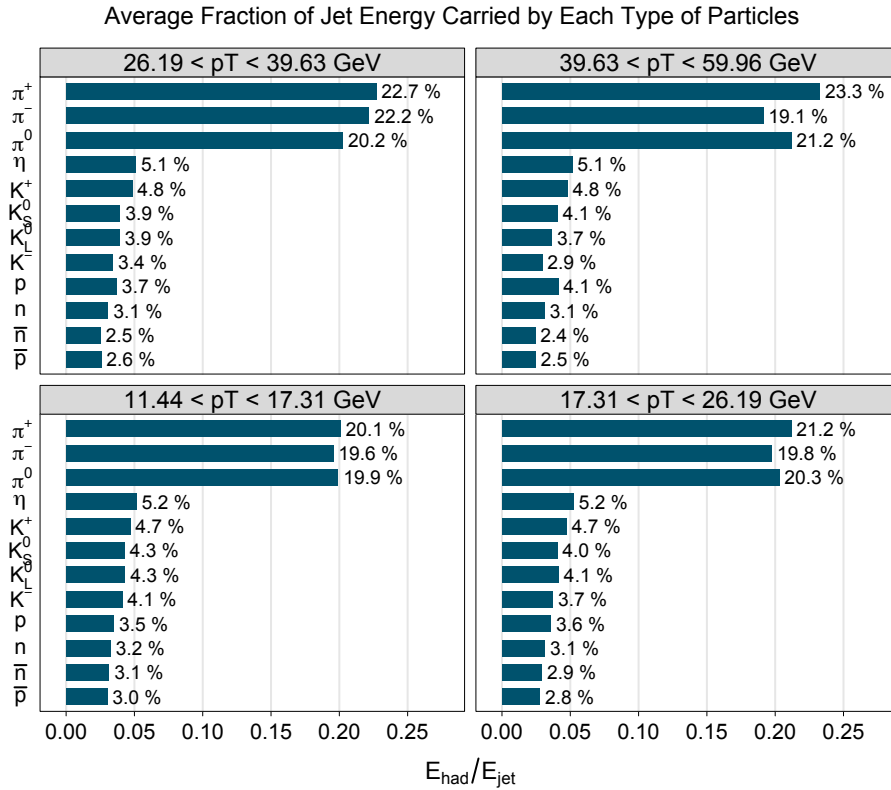
Figure 7-3: The average fraction of hadron-level jet energy carried by the constituent particles in the MC events.

or two collinear outgoing partons. The parton-level jets in the MC simulation are primarily used to estimate the effects of hadronization and underlying events. In particular, they are used to relate QCD NLO predictions of the inclusive jet and dijet cross sections to those at the hadron level so that the data can be compared with the QCD NLO predictions. The parton-level jets int the MC simulation are defined so as to be as close to the jets in QCD NLO calculations as possible.

Partons in Pythia

Pythia calculates the amplitude of the hard interactions only to leading order of α_s. The effects of the higher orders are simulated by initial radiations and final radiations.

Table 7.3 is an example of Pythia event record. This event is a high-p_T gluon-up-quark interaction in a proton-proton collision. The two colliding protons are at line

1 and line 2. Proton 1 moves along the positive z-axis. It emits a gluon (3), which participates in the hard interaction, and splits into the diquark ud_0 (16) and the up-quark (17), which are the remnant moving straight along the positive z-axis. From proton 2, which moves along the negative z-axis, an up-quark (4) participates in the hard interaction. The remnant of the proton 2 is a diquark ud_0 (37), which continues to move towards the negative z-axis. The gluon (3) and the up-quark (4) radiate the partons 18 – 21 before they engage the hard interaction. The incoming partons after the radiation are at line 5 and line 6. The fractions of momentum that these partons carry are the variable x in the parton distribution functions. The hard interaction is 5 + 6 → 7 + 8. Line 7 and 8 are the outgoing partons. The outgoing partons radiate before they fragment into hadrons. The partons 9–10 and the partons 26 – 29 are the outgoing partons after the final radiation and the radiation itself. The partons 11–15, 22–25, and 30–39 are underlying events. A long list of hadrons that follows is not shown in the example.

Parton Selection

Partons in Pythia events can be classified into the seven classes. Table 7.4 gives the classification. As the closest equivalent to the jets in QCD NLO calculations, the parton-level jets are defined as collections of outgoing partons and the radiation from the outgoing partons. In the example of Table 7.3, they are lines 9, 10, 18, 19, 20, 21, 26, 27, 28, 29. As in hadron-level jets, the acceptance cut $|\eta| < 2.0$ is applied to the partons before the jet finding. After the jet finding, the following jet η cut is applied to specify the phase space:

$$-0.8 < (\text{jet } \eta) < 0.8.$$

I	particle/jet	KS	KF	orig	p_x	p_y	p_z	E	m
1	!p+!		21	2212	0	0.000	0.000	99.996	100.000	0.938
2	!p+!		21	2212	0	0.000	0.000	-99.996	100.000	0.938
==
3	!g!		21	21	1	-0.351	-0.363	3.382	3.419	0.000
4	!u!		21	2	2	0.330	1.974	-40.471	40.521	0.000
5	!g!		21	21	3	-0.067	-2.070	1.193	2.391	0.000
6	!u!		21	2	4	0.295	1.768	-36.244	36.288	0.000
7	!g!		21	21	0	-1.533	-8.033	-21.096	22.626	0.000
8	!u!		21	2	0	1.762	7.730	-13.954	16.053	0.330
==
9	(u)	A	12	2	8	1.816	5.592	-9.552	11.222	0.330
10	(g)	I	12	21	8	-0.357	0.780	-2.663	2.798	0.000
11	(g)	I	12	21	0	0.375	0.906	0.733	1.225	0.000
12	(g)	I	12	21	0	0.323	0.249	0.403	0.574	0.000
13	(g)	I	12	21	0	-0.405	0.449	0.394	0.722	0.000
14	(g)	I	12	21	0	-0.219	0.433	2.712	2.755	0.000
15	(g)	I	12	21	0	-0.375	-0.906	16.475	16.504	0.000
16	(ud_0)	V	11	2101	1	-0.585	0.097	53.257	53.264	0.579
17	(u)	A	12	2	1	0.936	0.266	4.187	4.311	0.330
18	(g)	I	12	21	3	1.222	-0.095	0.284	1.258	0.000
19	(g)	I	12	21	3	-0.724	0.373	-0.471	0.941	0.000
20	(g)	I	12	21	3	-0.520	1.648	-2.104	2.723	0.000
21	(g)	I	12	21	3	-0.228	-0.013	0.252	0.340	0.000
22	(g)	I	12	21	0	0.405	-0.449	0.788	0.993	0.000
23	(g)	I	12	21	0	-0.413	-0.356	0.288	0.616	0.000
24	(g)	I	12	21	0	-0.135	-0.166	0.264	0.340	0.000
25	(g)	I	12	21	0	-0.628	-0.525	0.009	0.819	0.000
26	(g)	I	12	21	7	-0.010	-0.896	-0.691	1.131	0.000
27	(g)	I	12	21	7	1.130	-1.514	-3.043	3.581	0.000
28	(g)	I	12	21	7	-1.089	-1.495	-12.969	13.101	0.000
29	(g)	I	12	21	7	-1.261	-2.771	-6.132	6.846	0.000
30	(g)	I	12	21	0	0.171	-0.857	-2.305	2.465	0.000
31	(g)	I	12	21	0	-0.323	-0.249	-2.841	2.870	0.000
32	(g)	I	12	21	0	0.219	-0.433	-1.744	1.810	0.000
33	(g)	I	12	21	0	0.413	0.356	-0.637	0.838	0.000
34	(g)	I	12	21	0	0.135	0.166	-0.517	0.560	0.000
35	(g)	I	12	21	0	0.628	0.525	-2.613	2.738	0.000
36	(g)	I	12	21	0	-0.171	0.857	-7.335	7.387	0.000
37	(ud_0)	V	11	2101	2	-0.330	-1.974	-39.726	39.780	0.579
38	(g)	A	12	21	0	-0.109	-0.411	0.392	0.578	0.000
39	(g)	V	11	21	0	0.109	0.411	14.905	14.911	0.000
==

Table 7.3: A Pythia event record

class	e.g. I in Table 7.3
1. Incoming partons before radiation	3, 4
2. Incoming partons after radiation	5, 6
3. Outgoing partons before radiation	7, 8
4. Radiation from incoming partons	18, 19, 20, 21
5. Outgoing partons after radiation and the radiation	9, 10, 26, 27, 28, 29
6. Remnant	16, 17, 37
7. Underlying events	11, 12, 13, 14, 15, 22, 23, 24, 25, 30, 31, 32, 33, 34, 35, 36, 38, 39

Table 7.4: Classification of the partons in Pythia events.

7.5   Association of Different Level Jets

This section discusses an association between hadron-level jets and detector-level jets. The association is defined in a way in which detector-level jets are the detector responses of the associated hadron-level jets. The association can be used to evaluate detector responses.

The association is established in the following way. First, for a given event, hadron-level jets are sorted by p_T in descending order. Second, starting with the highest-p_T hadron-level jet, for each hadron-level jet, the nearest detector-level jet in the η - φ plane is identified. If the distance between the cone axis of the hadron-level jet and that of the detector-level jet is shorter than 0.5, these two jets are associated. Each jet is associated with at most one other jet. If the nearest detector-level jet is already associated with another hadron-level jet, then the second nearest detector-level jet is considered.

The procedure is independently conducted for the BHT2 trigger and the BJP1 trigger. As a consequence, it is possible that a hadron-level jet is associated with different detector-level jets for different triggers.

The association is not always established. For example, hadron-level jets do not have associated detector-level jets in the following situations: 1) the events did not cause the trigger; 2) the events do not have a vertex; 3) the corresponding detector-level jets are outside of the detector acceptance; 4) the corresponding detector-level jets do not meet the jet selection criteria. On the other hand, detector-level jets do not have associated hadron-level jets in the following situations: 1) the corresponding hadron-level jets do not meet the jet selection criteria; 2) the split-and-merge step split the detector-level jets; 3) the detector-level jets are background.

7.6 Vertex Distribution

7.6.1 Simulation of Vertex Distribution

After events are generated in Pythia, the vertex positions of the events are randomly determined from a Gaussian distribution with the mean = 0 cm and the variance = $(60 \text{ cm})^2$ before the events are processed in the detector simulation. The parameters of the Gaussian distribution are chosen to approximate the vertex distribution of the MINB events in the data. Event vertices greater than $|z| > 120$ cm are not considered. Figure 7-4 shows the vertex distributions of the MC events.
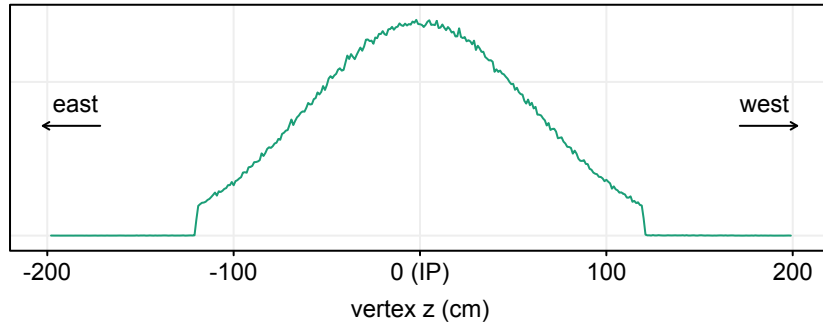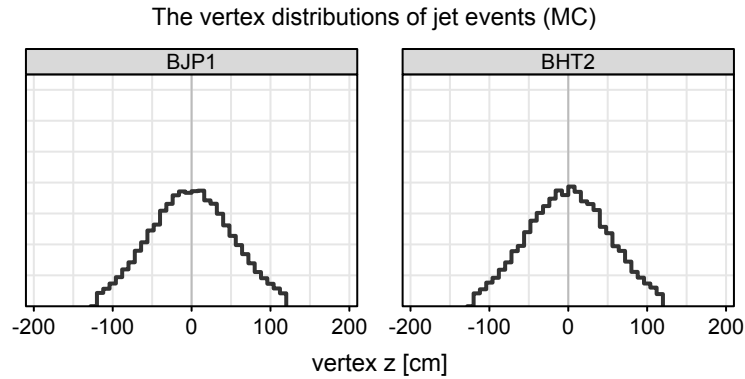

Figure 7-4: The vertex distribution of the MC events.

7.6.2 Timebin Selections and Vertex Corrections

Figure 7-5 shows the vertex distributions of the jet events in the MC simulation. Unless they are produced at the same spacial position, particles with the same momentum hit different parts of the detector, causing different detector responses. Therefore, in order to accurately compare properties of the jets between the data and the MC events, the MC events need to have the same vertex distribution as the data.

The BBC timebin is not simulated in the detector simulation; the timebin selections cannot be applied to the MC events. As an alternative method, for each timebin selection, the MC events are re-weighted by correction factors so that the vertex distributions of the jet events in the MC simulation approximate those of the data. The correction factors $w_{\text{ver}}(z)$, plotted in Figure 7-6, are determined as the ratios of the

The vertex distributions of jet events (MC)

Figure 7-5: The vertex distributions of jet events in the MC events.

vertex distributions between the data and the MC events. Before the ratios are taken, the vertex distributions of the data and the MC events are separately normalized and smoothed by cubic splines [38]. The ratios themselves are smoothed as well.

The correction factors need to be normalized in such a way as to preserve quantities which should be conserved. Since the vertex correction is equivalent to a shift in positions of the events, the vertex correction should not change a property that is intrinsic to the events, but can change properties that involve the position of the detector. In the case of vertex corrections to the jet events, it is the number of generated

Vertex Correction Factors for the MC Jet Events
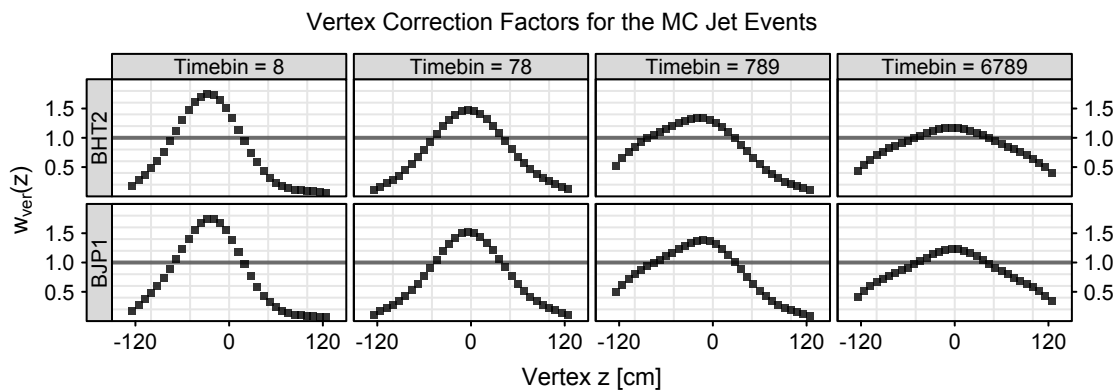
Figure 7-6: The vertex correction factors for the jet events for each timebin set and each trigger.

events, not jet events, that needs to be conserved:

$$N_\phi^{\text{gen}} = \sum_{\substack{\text{all events} \\ \text{in } \phi}} w_{\text{ver}}(z). \tag{7.3}$$

The number of the generated events need to be separately conserved in each MC data set ϕ since the vertex correction does not affect $\hat{p}_{\text{T}}$.

The corrections are larger for the narrower timebin sets. The correction factors determined for the BHT2 jet events and the BJP1 jet events are nearly identical as they should be; the average difference is about three percent.

Re-weighting the MC Events

Each MC event has a weight w_ϕ associated with the production run ϕ, as discussed in Section 7.1. With the vertex correction, each event is now weighted by two factors: w_ϕ and $w_{\text{ver}}(z)$. For example, the jet yield in jet p_{T} bin i is the sum of the products of the two factors;

$$J_i^{\text{MC}} = \sum_{p_{\text{T}}^{\text{jet}} \in i} w_\phi \cdot w_{\text{ver}}(z). \tag{7.4}$$

The sum is taken over the jets with p_{T} in bin i.
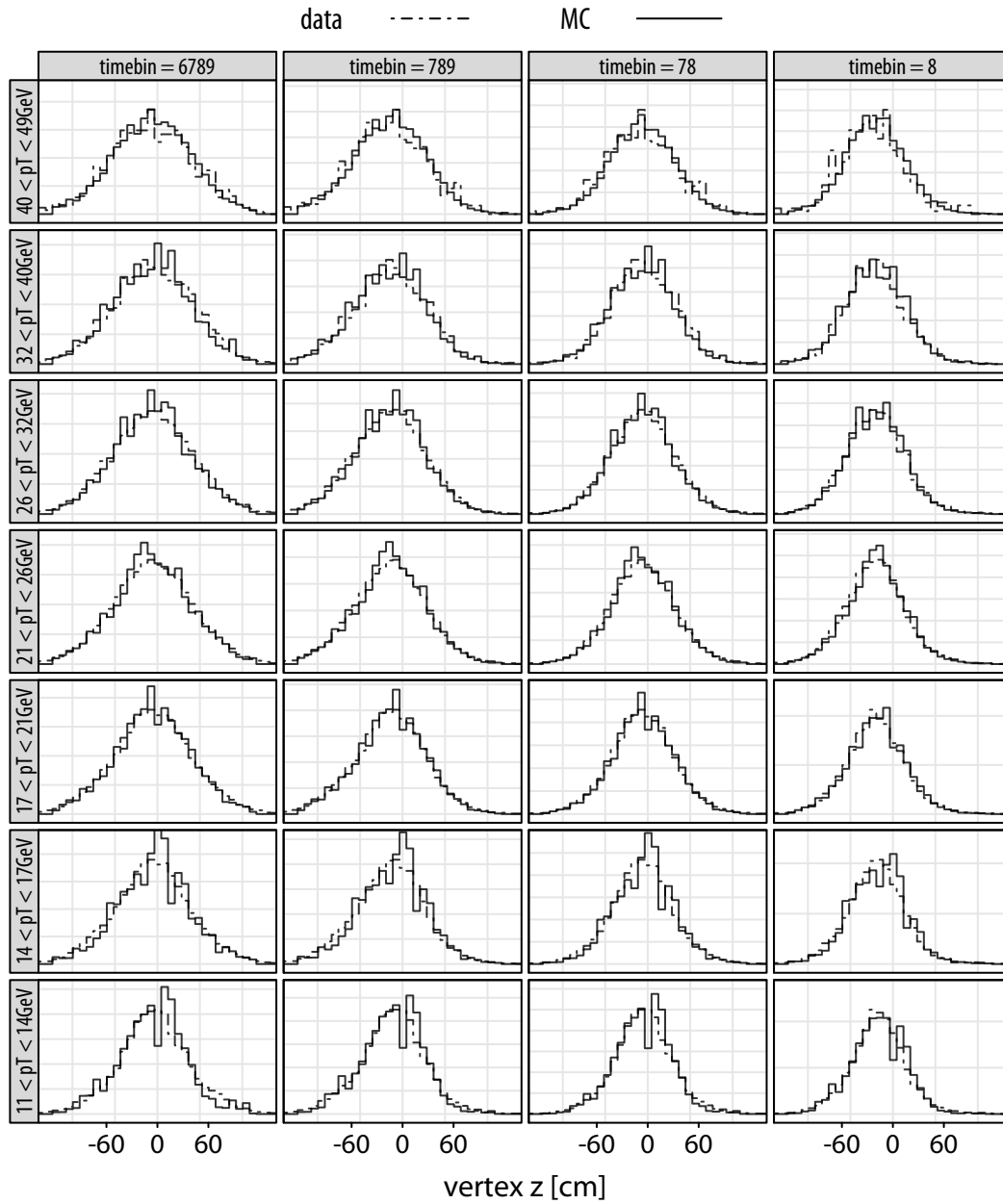
As shown in Figure 7-7 and 7-8, the vertex distributions of the jet events in the vertex corrected MC events well approximate those of the data in all timebin sets and for both triggers for all p_{T} bins. The data-MC comparisons in the next chapter are made with these vertex-corrected MC jet events.

The Vertex Distributions of the BHT2 jet events in Data and MC (w/ correction)

data   ·–·–·–   MC   ———
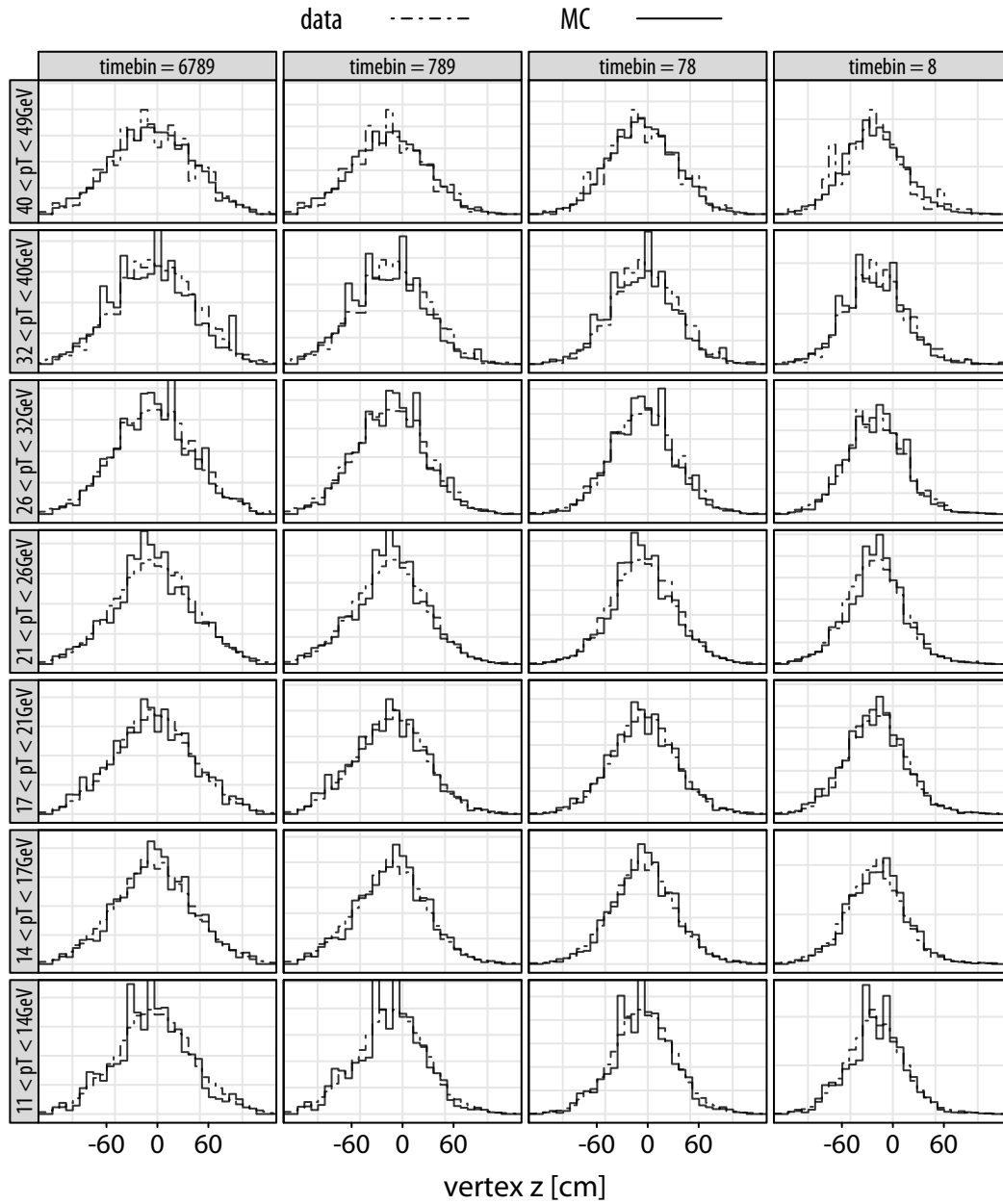
Figure 7-7: The vertex distributions of the BHT2 jet events in the data and the vertex-corrected MC events.

Figure 7-8: The vertex distributions of the BJP1 jet events in the data and the vertex-corrected MC events.

Chapter 8

# Data - MC Comparison of Inclusive Jets

In the cross section measurements, the hadron-level jet yields are estimated from the detector-level jet yields by inverting the response of the detector using the MC simulation. Consequently, the results have a tendency to be biased toward the predictions of the MC simulation. This bias needs to be eliminated or minimized. It is desirable to use MC events that are comparable to the data for an accurate measurement of the cross section. To evaluate to what extent the MC simulation reproduces the data, this chapter compares the jets in the data and the jets in the MC simulation at the detector level.

Chapter 6 defined the jets. As described in Chapter 7, the detector-level jets in the MC events are defined in nearly exactly the same way as the detector-level jets in the data. The only difference is that, in the data, 50 MeV is subtracted from the jet p_T to account for the pile-up effect. In Section 7.6, the vertex distributions of the MC events are corrected to fit those of the data for each timebin set. The kinematic distributions and the particle contents of the jets in the data are compared with those of the vertex-corrected MC events.

8.1   The Kinematic Distributions

In this section, the kinematic distributions of the jet events in the data are compared with the vertex-corrected MC events. The jet four-momenta and *jet profiles* are compared. The jet four-momenta comparisons are made in terms of transverse momen-

tum p_T, pseudo-rapidity η, azimuthal angle φ, and mass m. In jet four-momenta comparisons, jets are treated as single objects; in contrast, in jet profiles comparisons, jets are composite objects.
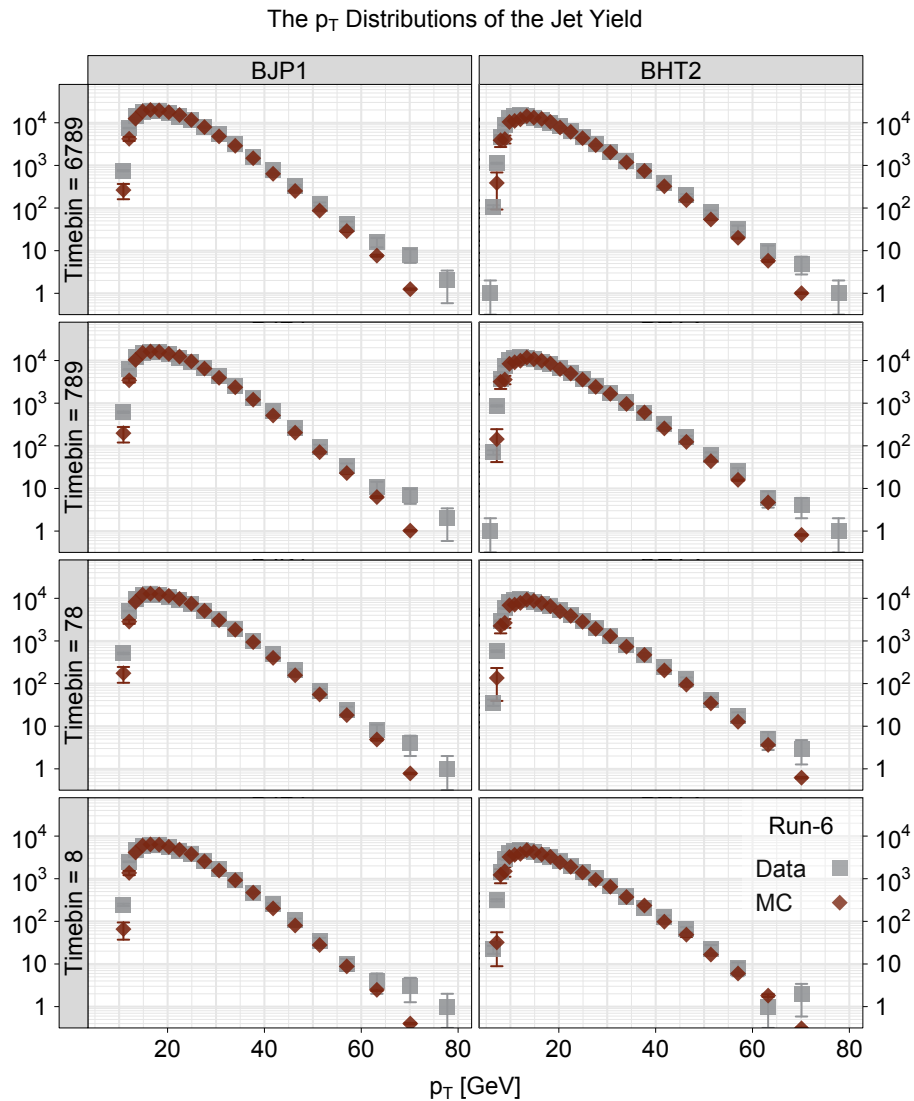
Figure 8-1: The p_T distributions of the jet yield at the detector level for each timebin set and each trigger. In each panel separately, the MC distributions are normalized so that the total jet yields at p_T above 12.69 GeV are the same as the jet yields in the data.

8.1.1 Transverse Momentum p_{T}

The jet transverse momentum p_{T} is the most important kinematic variable in the data-MC comparison since the cross section is measured as a function of p_{T}. Figure 8-1 shows the p_{T} distributions of the jet yields for each timebin set and each trigger. The MC jet distributions are scaled so as to have the same jet yields as the data at p_{T} above 12.69 GeV. The distributions are separately scaled for each timebin and trigger selection. The MC simulation well reproduces the jet p_{T} distributions over four orders of magnitude. Figure 8-2 shows the ratio (data-MC)/MC, which is appropriate for detail comparison. The MC distribution appears to decrease slightly faster than the data distribution at p_{T} above 40 GeV.
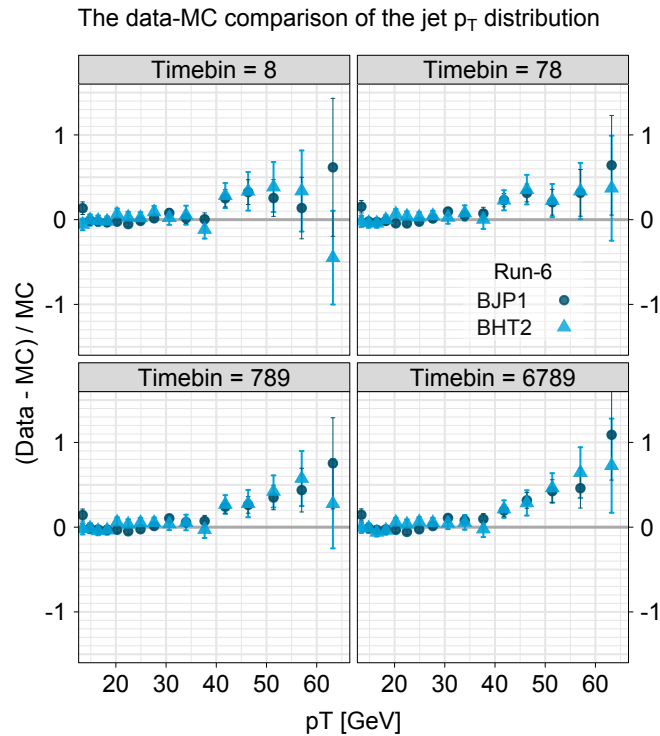
Figure 8-2: The data-MC comparisons of the jet p_{T} distributions for each timebin set and each trigger. The MC events are scaled in the same way as described in Figure 8-1.

8.1.2 Normalization in the η, φ, m comparisons

Since the jet p_T distribution is a steeply decreasing curve, the jet event sample is dominated by low p_T jets. In the η, φ, and m comparisons, to make comparisons between high p_T jets and also low p_T jets, the jet sample is divided into four different p_T ranges. The MC jet yields are scaled so that the data and the MC events have the same jet yields at p_T above 11.44 GeV for each timebin set and each trigger. The same normalization factors are used for the distributions within the same timebin sets and triggers over all p_T ranges.
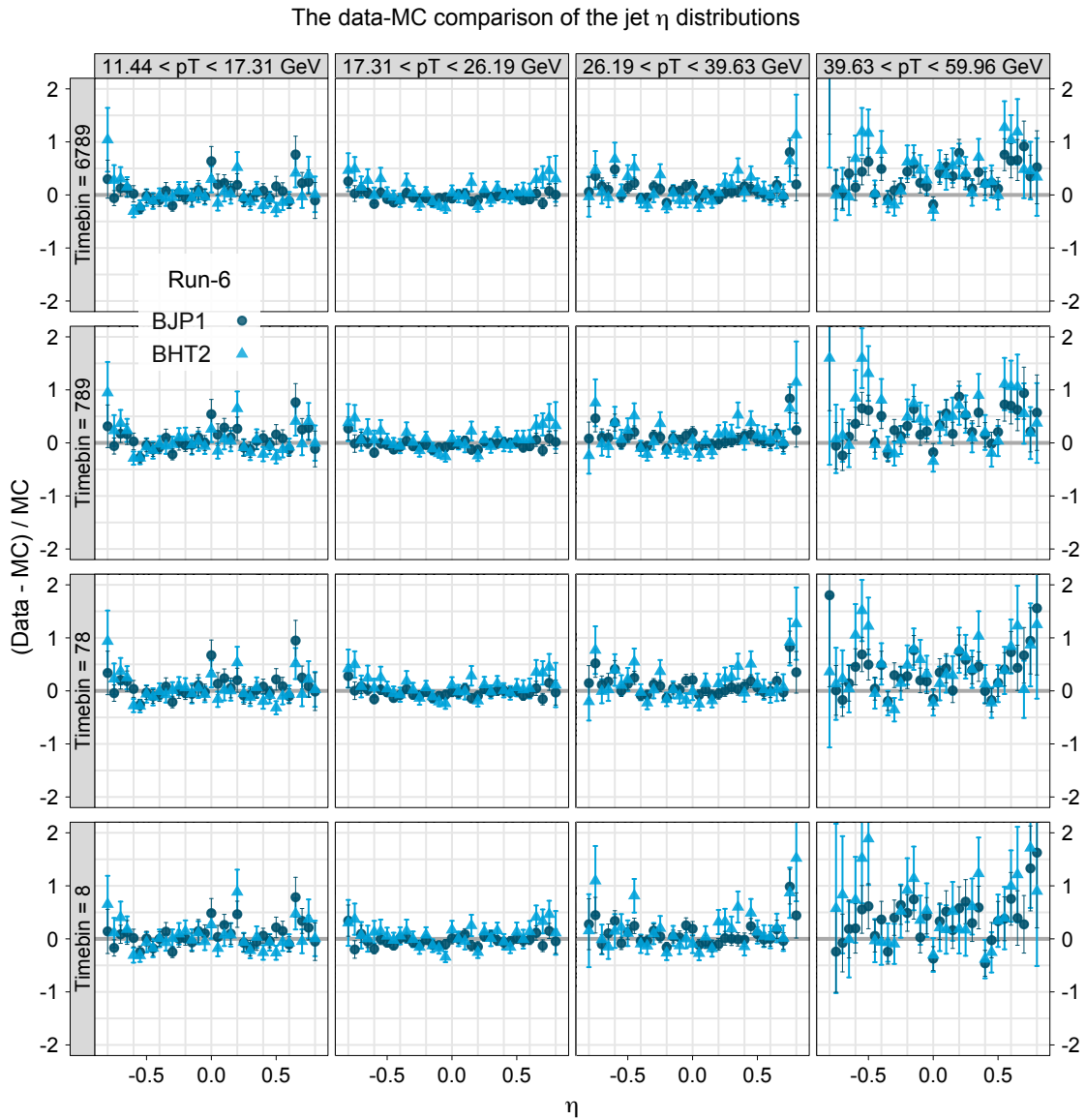
8.1.3 Pseudo-Rapidity η

Agreement between the jet pseudo-rapidity η distributions of the data and of the MC events requires three conditions: that the MC events have the same vertex distributions as the data; that the event generator well simulate the η distribution of real collisions; and that the detector simulation reproduce the η dependence of the detector response. The first condition is met by the vertex correction. Therefore, an agreement between the data and the MC events implies the second and third conditions unless neither of the conditions is met in a way in which the deviations are cancelled each other.

Figure 8-3 shows the jet η distributions in the data for each timebin set and trigger in the four different p_T ranges. Figure 8-4 shows the ratios (Data-MC)/MC. As seen in the comparison of the p_T distributions, the data is greater than the MC simulation in the highest-p_T range. Due the lack of statistics, it is not clear if this excess in the data originates in a particular range of η. The ratios show no significant deviation from the constant. The MC simulation well reproduces the η dependence of the data.

The η dependence of the jet yield
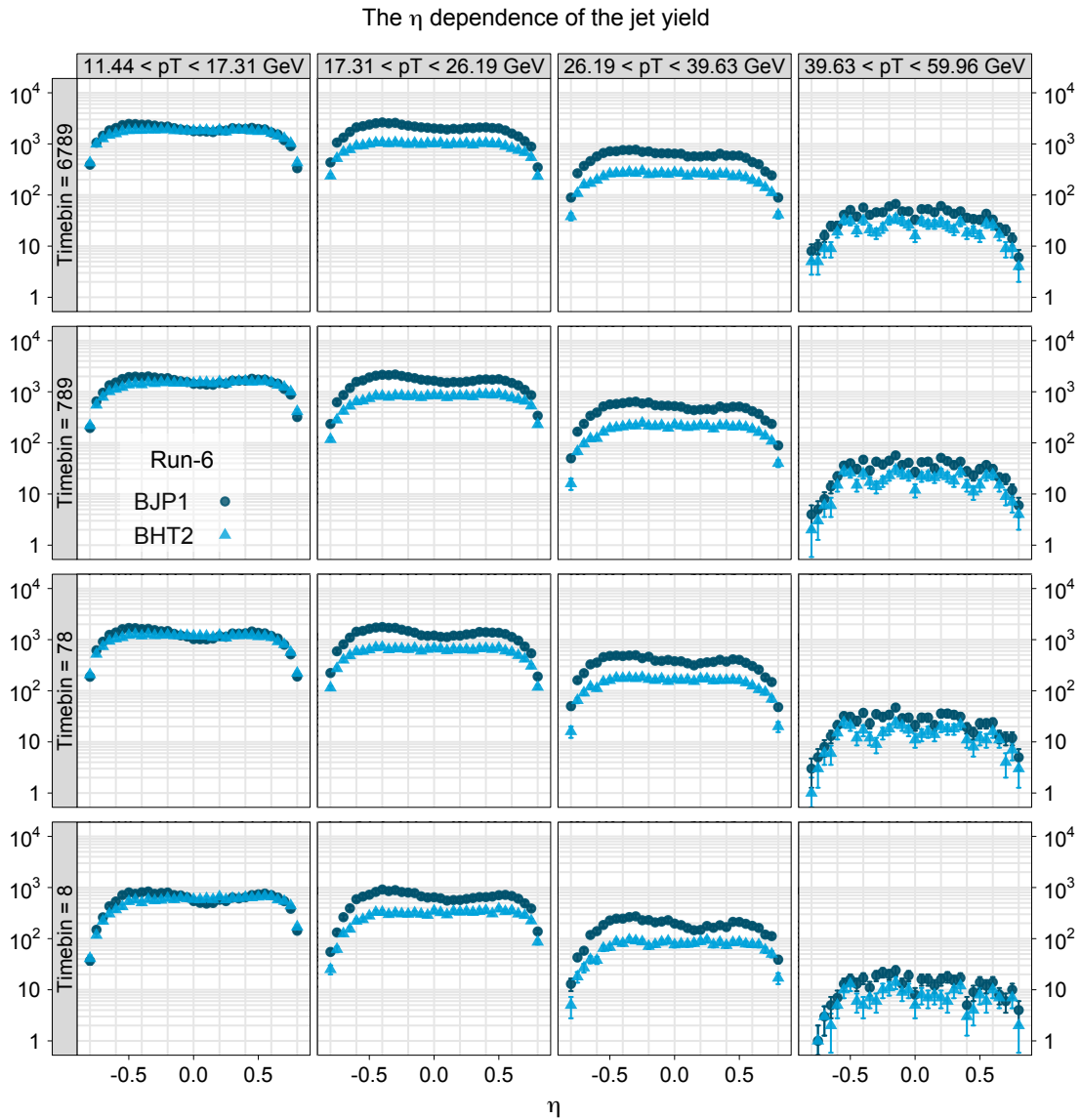
Figure 8-3: The pseudo-rapidity η distributions of the jet yields in the data by p_T bins and timebin sets for each triggers. The comparisons with the MC simulation are shown in Figure 8-4.

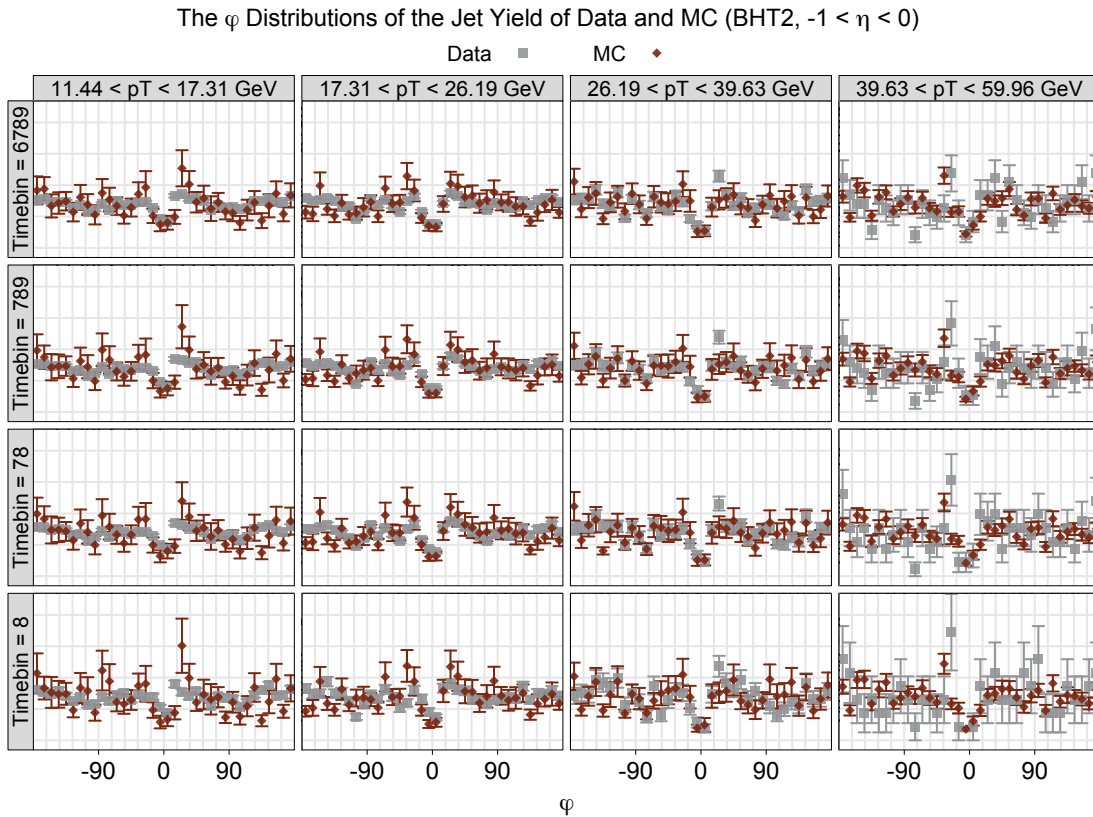The data-MC comparison of the jet η distributions

Figure 8-4: The data-MC comparison of the pseudo-rapidity η dependence.

8.1.4 Azimuth φ

The φ distributions are uniform at the hadron level. The non-uniformity solely comes from the non-uniformity of the trigger and the detector sensitivity. The comparisons are separately made for the east side ($-1 < \eta < 0$) and the west side ($0 < \eta < 1$).

Figure 8-5 and Figure 8-6 show the comparisons for the BHT2 events. The data and the MC simulation are in agreement. A dip is observed around $\varphi = 0$ in the east side. The simulation reproduces the dip as well.

Figure 8-7 and Figure 8-8 show the comparisons for the BJP1 events. The wave-like distributions reflect the locations of the jet patches. The MC simulation well simulates minor tendencies as well as overall distributions.

Figure 8-5: The data-MC comparison of the φ dependence of the jets for the BHT2 events for the east side ($-1 < \eta < 0$).
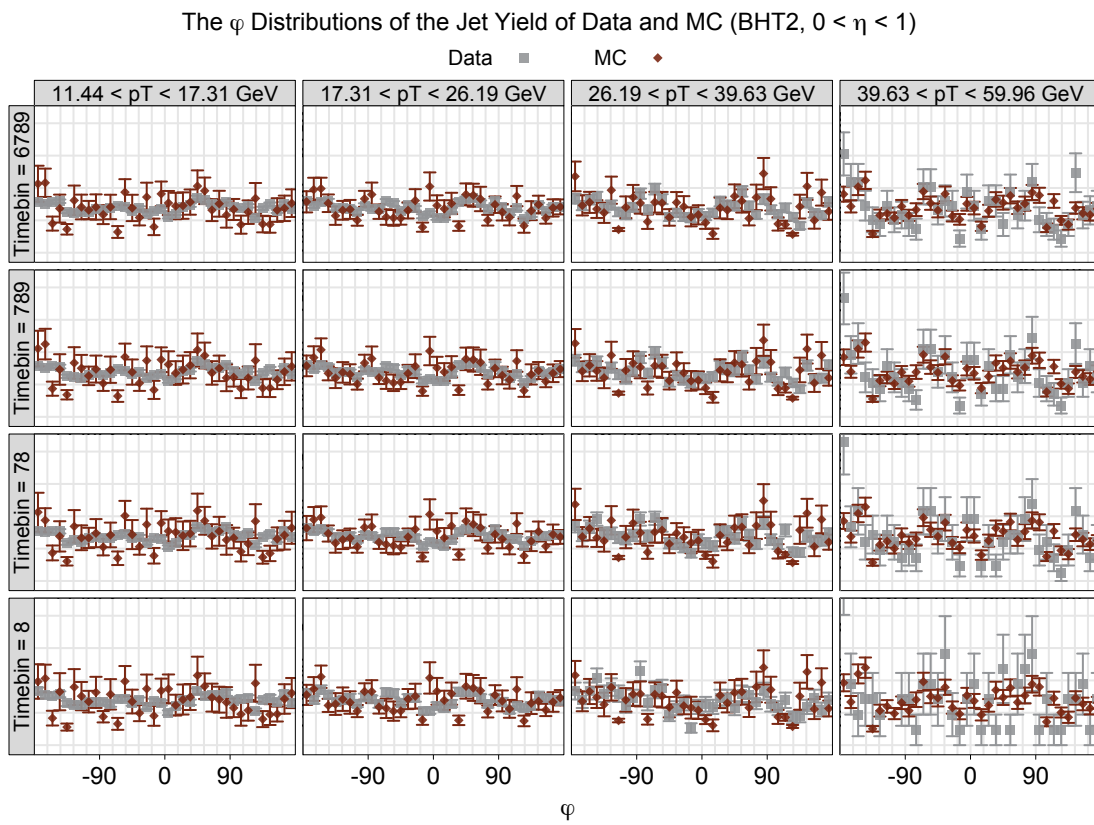
Figure 8-6: The same as the Figure 8-6 but for the west side ($0 < \eta < 1$).
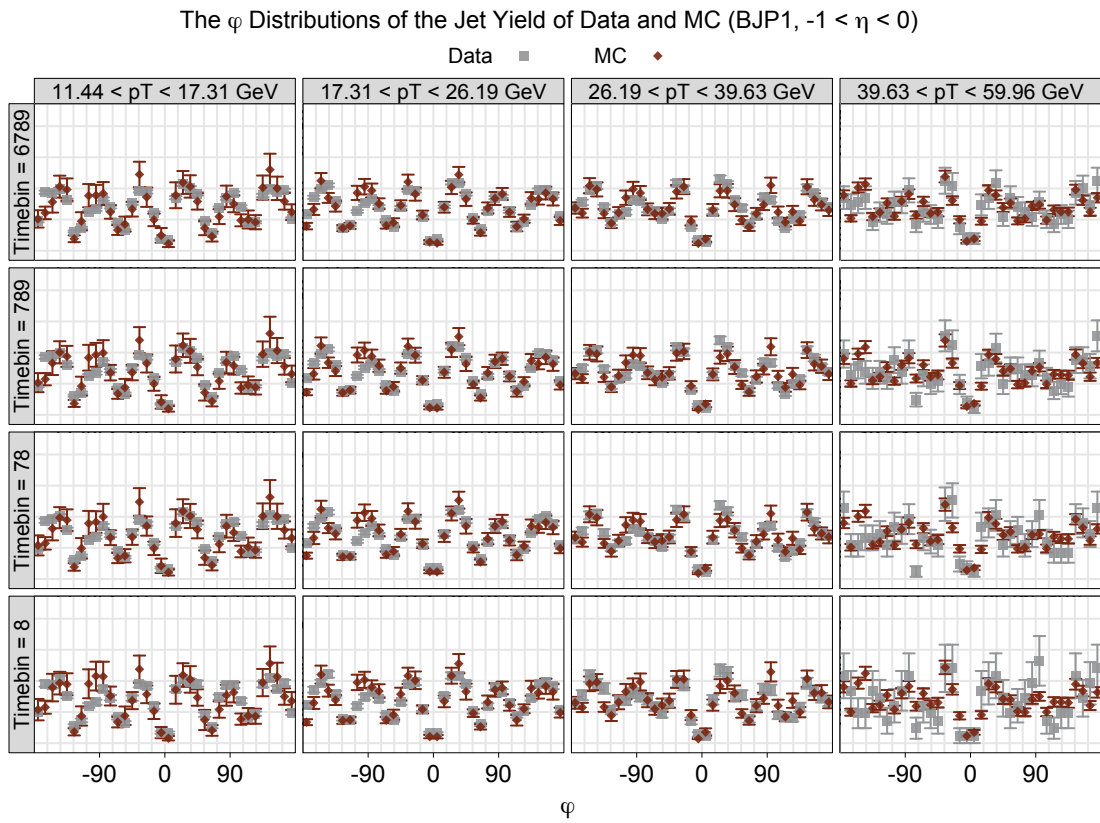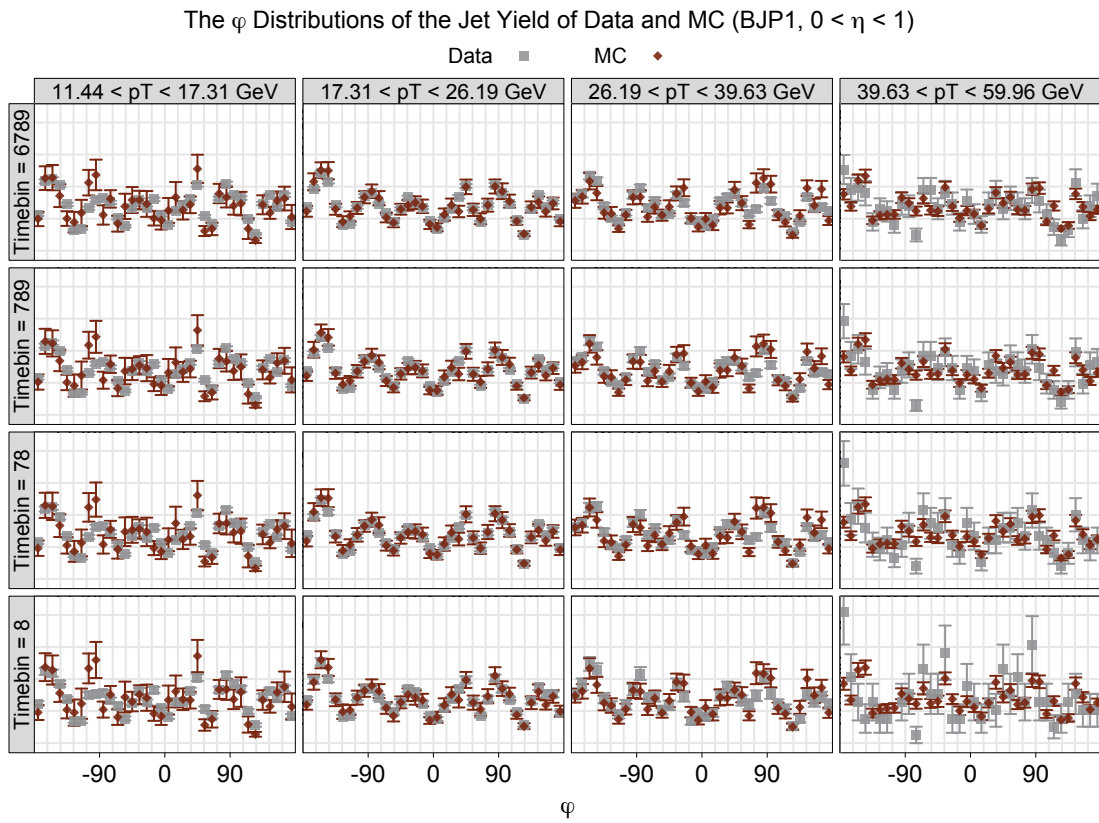
Figure 8-7: The φ dependency comparison of the BJP1 jets for the east side.

Figure 8-8: The same as the Figure 8-7 but for the west side.

8.1.5 Mass *m*

Figure 8-9 shows the jet mass distributions in the data for the four different p_T ranges within each timebin set and trigger. It can be seen that the jets are rarely massless. Figure 8-10 shows the data-MC comparison. The data and the MC simulation are in agreement. This mass comparison concludes the jet four momentum comparison.
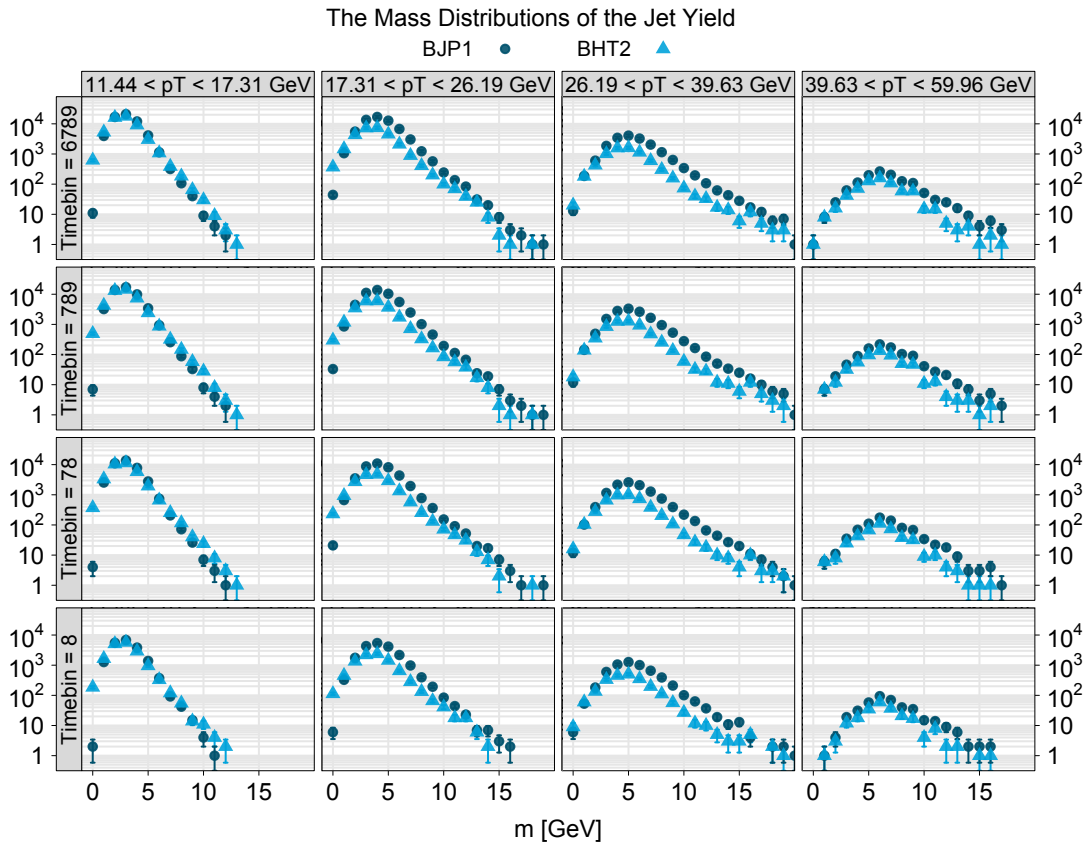
Figure 8-9: The invariant mass distributions of jets in the data by p_T bins and timebin sets for each triggers.
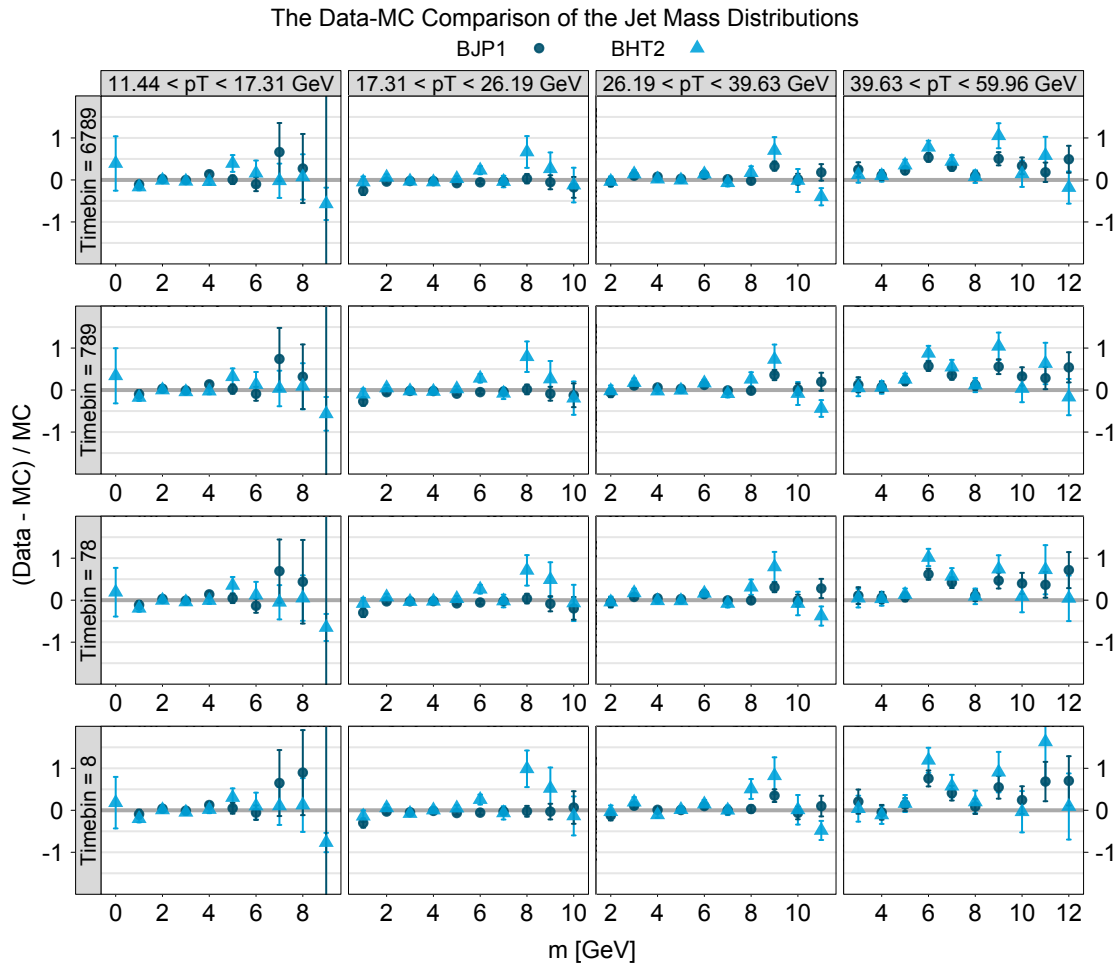
Figure 8-10: The data-MC comparison of the mass *m* dependence.

8.1.6 Jet Profile

In the four-momentum comparisons, jets are regarded as single objects. However, jets are collections of particles; the same jet four-momenta can be realized in a wide variety of arrangement of particles. For example, a 40-GeV jet can be a collection of two 20-GeV particles close to the jet axis or can be a collection of four 10-GeV particles at the edge of the jet cone.

The *jet profile* is defined as the average fraction of the jet energy inside a cone as a function of the cone radius Δr ranging from zero to the jet cone radius of 0.7. In Figure 8-11, the jet profiles in the data and the MC events are plotted. The data and the MC events are in excellent agreement.
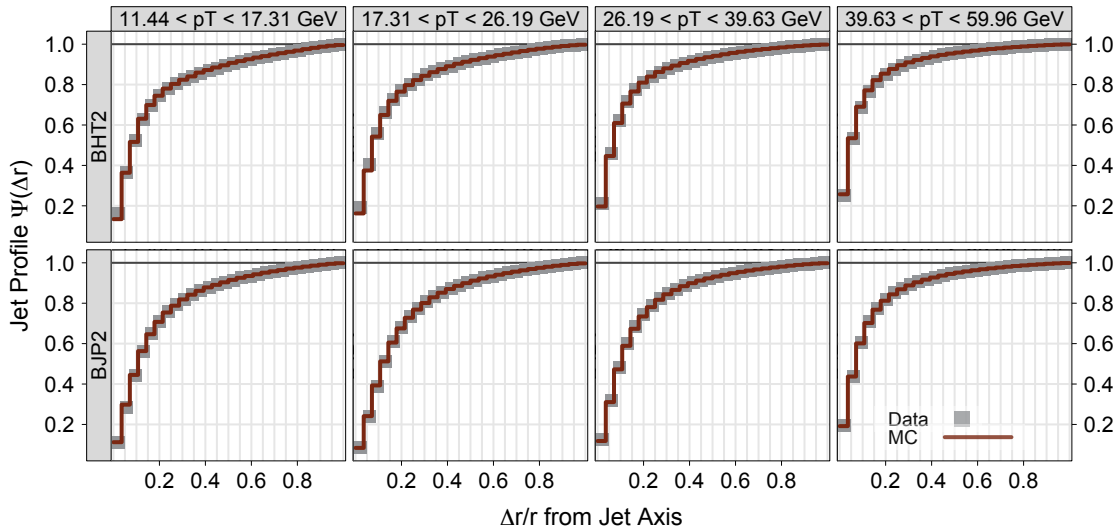
Figure 8-11: The jet profile, the average fraction of the jet energy inside a cone with smaller radius Δr than the jet cone radius of 0.7 for each trigger for four different p_T ranges for timebin set 6789.

8.2   Particle Contents

In addition to the jet kinematic distributions, the data-MC agreement on the particle contents of the jets are also important to the cross section measurement. The detector responses to jets depend on the particle content of jets. In other words, jets with the same four-momentum, the same jet profile, the same vertex and different particle contents may systematically cause different detector responses.

The particle contents of the hadron-level jets in the MC events are shown in Section 7.3. Since particle identification is not employed in the data, it is not possible to compare the particle contents at the hadron level. Instead, properties of the jets that are sensitive to the particle contents are compared: the neutral energy ratio R_T of the jet energy, the multiplicity of the tracks and towers, the track momentum distribution, and the neutral energy distribution. The comparisons in this section are carried out for timebin set 6789.

8.2.1   Neutral Energy Ratio R_T

The neutral energy ratio R_T, as defined in Section 6.5, is the fraction of jet energy reconstructed from the BEMC tower energy; therefore, this variable is sensitive to the ratio of jet energy carried by neutral particles and charged particles. Low-p_T jets have low neutral energy ratio R_T due to the trigger bias as discussed in Section 6.5. As jet p_T increases, the trigger bias becomes weak and R_T decreases. The peak of the R_T distribution of high-p_T jets is approximately 1/3, which is the ratio between the numbers of neutral and charged pions. Pions are the lightest hadrons, so predominantly produced in the hadronization. The three types of pions, π^0, π^+, π^-, are nearly equally likely to be produced, causing the peak of the R_T distribution to be around 1/3. This observation is consistent with the particle contents of the hadron-level jets in the MC simulation, each type of pion carries about 20% of hadron-level jet energy (Figure 7-3).

Figure 8-12 shows the R_T distributions in the data and the MC simulation in five different p_T ranges for each trigger. Overall, the data and the MC simulation are in agreement. However, localized but clear disagreement is observed in the mid-R_T range in the range of $17.31 < p_\text{T} < 26.19$ GeV for BHT2.
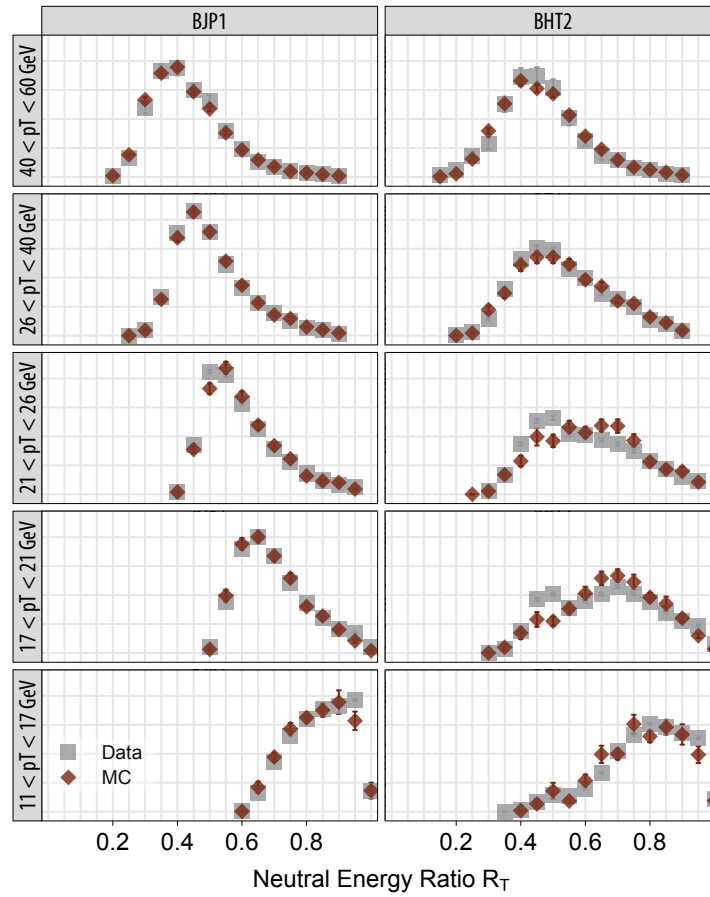
Figure 8-12: The neutral energy ratio of the jets in the data and the MC simulation in five different p_T ranges for each trigger for timebin set 6789. The distributions are separately normalized in each panel.

8.2.2   Track Multiplicity in Jets

Track multiplicity is the number of tracks in jets. Figure 8-13 shows good agreement between the data and the MC events.
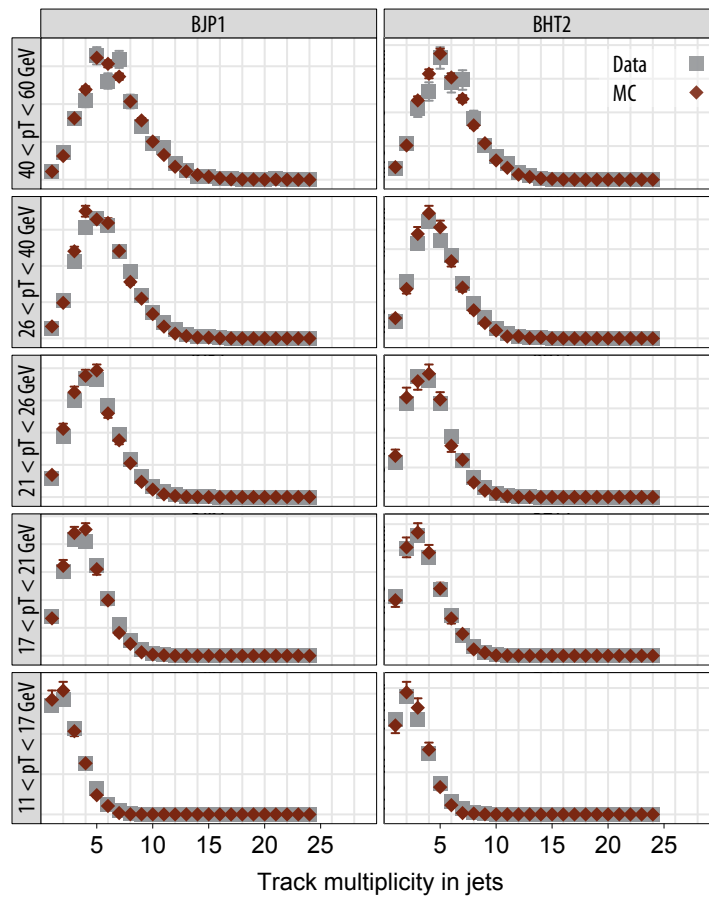
Figure 8-13: The data-MC comparison of the track multiplicities in jets.

8.2.3   Tower Multiplicity in Jets

Tower multiplicity is the number of towers with energy deposits in jets. Figure 8-14 shows the comparisons. The distributions are similar. However, the distributions in the MC events are slightly shifted towards lower multiplicity.
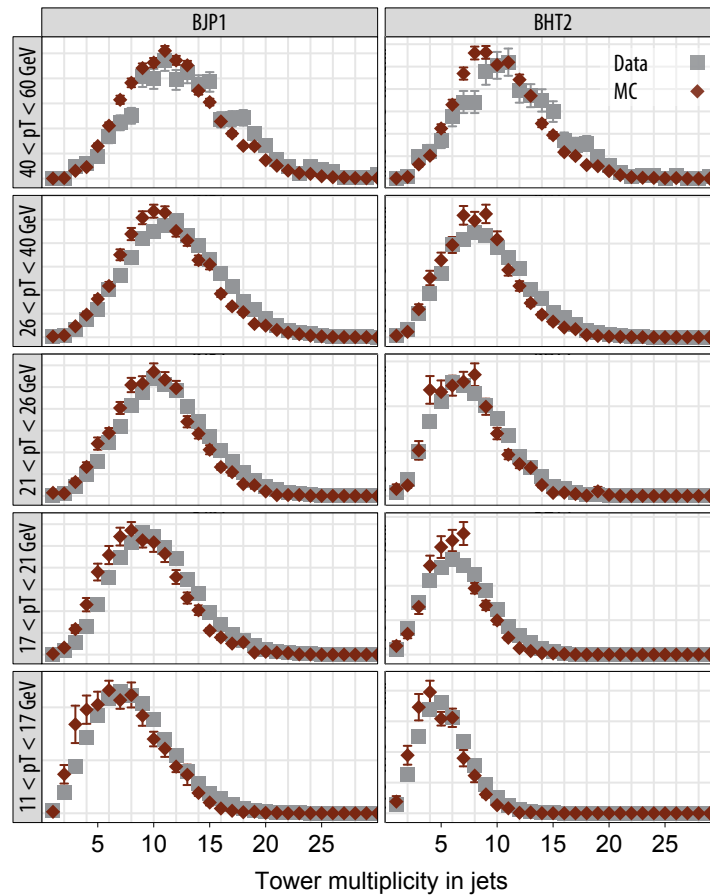
Figure 8-14: The data-MC comparison of the BEMC tower multiplicities with energy deposit in jets.

8.2.4   Track Momentum Distribution in Jets

The track p_T distributions in jets are compared in Figure 8-15. Similar to the neutral energy ratio comparison in Figure 8-12, the overall agreement is good, but a difference is observed in the p_T range $17.31 < p_T < 26.19$ GeV for the BHT2 trigger.
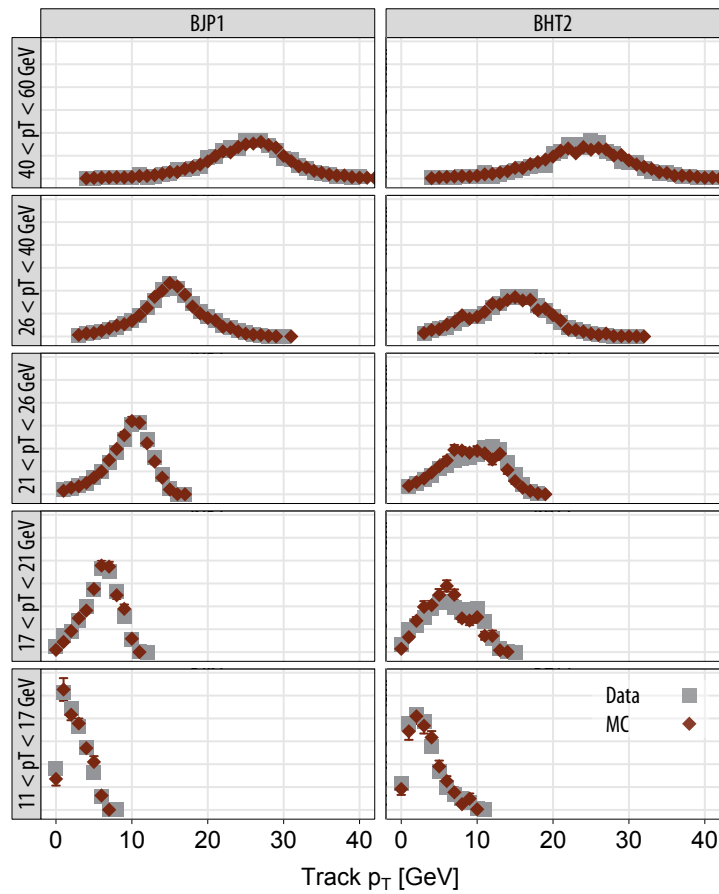
Figure 8-15: The data-MC comparison of the track p_T distributions in jets for different jet p_T ranges.

8.2.5 Neutral Energy Distribution in Jets

The neutral energy R_T distributions in jets are compared in Figure 8-16. Again the overall agreement is good, but a difference is observed in the p_T range $17.31 < p_T < 26.19$ GeV for the BHT2 trigger.

Figure 8-16: The data-MC comparison of the tower E_T distributions in jets for different jet p_T bins.

8.3   Summary

The detector-level jets in the data and those in the MC simulation are compared. The comparisons are carried out in terms of kinematic variables and the components of the jets. Since, in the cross section measurement, the hadron-level jet yields are estimated using MC simulation, the results are subject to a bias from the MC events. The degree of the difference between the data and the MC simulation is related to the degree of the bias that might be introduced by the MC events.

The overall agreement between the data and the MC events is remarkably good. However, some minor discrepancies are found. The p_T dependence of the yield of the jets with p_T greater than 40 GeV in the MC simulation decreases slightly faster than that of the data. It is possible that this excess of high p_T jets is caused by background events since the background level is high in events with high energy deposits in the BEMC towers.

While tower multiplicity is higher in the data than in the MC simulation, such a difference is not observed in the neutral energy distributions. A possible explanation is that the same amount of neutral energy is carried by a larger number of particles in the data than in the MC simulation. Another possibility is that neutral particles in the data are more likely to deposit energy in multiple towers than are neutral particles in the MC simulation. The latter situation is more likely because the jet profiles in the data and those in the MC simulation are in excellent agreement. This difference can be investigated by jet profiles of the neutral energy.

It is found that the BJP1 events are in better agreement than the BHT2 events. In the latter, a localized discrepancy is observed in the range of $17.31 < p_T < 26.19$ GeV. This discrepancy is apparent in the neutral energy ratio distributions, the tower multiplicity distributions, the track momentum distributions, and the neutral energy distributions. However, no apparent discrepancy is observed in the track multiplicity distributions. In the comparison of the p_T distributions in Figure 8-2, the data is systematically higher than the MC simulation in this p_T range for the BHT2 trigger.

Investigating the cause of these discrepancies perhaps leads to further understanding of the quality of the collected data, the performance of the detector, the efficiency of the triggers, and the reliability of the MC simulation. In this comparison, Pythia with the CDF tune A parameter set with the CTEQ5L parton distributions are used. It is preferable to use multiple event generators with several parameter sets and parton distributions to reduce a bias toward a particular configuration of MC simulation. Nevertheless, the level of the agreement is satisfactory for the purpose and the precision of the current measurement.

Chapter 9

Inclusive Jet Cross Section

The inclusive jet cross section in proton-proton collisions at $\sqrt{s} = 200$ GeV is measured with a data sample of 5.4 pb^{-1} using a mid-point cone algorithm with the cone radius equal to 0.7. The cross section is measured as a function of jet transverse momentum p_T in the range of $13 < p_\mathrm{T} < 66$ GeV in the mid-rapidity region $|\eta| \leq 0.8$. The results are in agreement with next-to-leading-order perturbative QCD predictions with CTEQ6M parton distributions. The results are consistent with previous results with smaller acceptance and cone size.

9.1 Introduction

The inclusive jet cross section is an essential quantity to test the prediction power of QCD. Several improvements have been made from the previous measurement from STAR [18]; the data size increased from 0.3 pb^{-1} to 5.4 pb^{-1}; while the previous measurement used the TPC and only the west side of the BEMC ($0 < \eta < 1$), this measurement uses the TPC and both sides of the BEMC ($-1 < \eta < 1$); accordingly, the jet cone radius changed from 0.4 to 0.7, which is more suitable for the comparison with QCD predictions; the range of the jet p_T was raised from $5 < p_\mathrm{T} < 50$ GeV to $13 < p_\mathrm{T} < 66$ GeV.

The results are in agreement with next-to-leading-order (NLO) perturbative QCD predictions [33] with CTEQ6M parton distributions [39]. This agreement is an evidence that the measured inclusive jet A_LL can be interpreted in the framework of the QCD factorization with NLO perturbative QCD calculations. Furthermore, having a

Proton-Proton	$\sqrt{s} = 200$ GeV
Luminosity	$\int \mathcal{L} \mathrm{d}t = 5.4 \, \mathrm{pb}^{-1}$
Cone Radius	$R = 0.7$
As a function of p_T	$13 < p_\mathrm{T} < 66$ GeV
At the mid-rapidity	$-0.8 < \eta < 0.8$

Table 9.1: The parameters of the inclusive jet cross section measurement

theoretical model that well describes the inclusive jet cross section is a crucial step toward dijet measurement.

The data were collected with the STAR detector during RHIC Run-6 (Section 5.1). The events are selected by the BHT2 trigger and the BJP1 trigger (Section 5.6), and timebins are used to select events occurring close to the IP (Section 5.7). The jets are defined by a mid-point cone algorithm [32] as collections of energy deposits in the BEMC towers and charged tracks left in the TPC (Chapter 6).

This chapter describes the measurement of the inclusive jet cross section. The cross section is measured in bins of p_T. The binning is shown in Section 9.2. The evaluation of the cross section is described from Section 9.3 to Section 9.5. Section 9.6 discusses the systematic uncertainty. Section 9.7 discusses theoretical predictions. Section 9.8 describes how to interpret data points in wide bins. Section 9.9 shows the results and the comparison with NLO pQCD predictions. Section 9.10 shows the cone radius dependence of the inclusive jet cross section. Section 9.11 shows the consistency with the previous results.

9.2 Binning and Phase Space Volume

The cross section is evaluated in bins of p_T. In general, narrower bins are preferred since they offer better accuracy. However, at the same time, they require more statistics. In this measurement, the bins are determined in such a way to balance accuracy and statistics. The rate at which the p_T distribution decreases is so rapid that a suitable bin width becomes exponentially wider to accommodate low-rate high-p_T jet events. The lower bin boundary $p_{\mathrm{T}i}^{\mathrm{low}}$ and the upper bin boundary $p_{\mathrm{T}i}^{\mathrm{up}}$ for bin i follow

the formula:

$$p_{\mathrm{T}i}^{\mathrm{low}} = 5 \times 1.23^{(i-1)/2},$$
$$p_{\mathrm{T}i}^{\mathrm{up}} = p_{\mathrm{T}i+1}^{\mathrm{low}}.$$

The cross section is obtained for bin $i = 10$ to bin $i = 25$, which corresponds to $12.69 < p_{\mathrm{T}} < 66.49$ GeV. The bins are perhaps too wide for the cross section to be interpreted as a function of p_{T}. Section 9.8 describes a way to interpret values in wide bins.

The values of the cross section are normalized to those per unit phase space volume. Phase space volumes can be represented as $2\pi \Delta p_{\mathrm{T}} \Delta \eta$. 2π is for the azimuth. The η bin width is $\Delta \eta = 0.8 - (-0.8) = 1.6$. The p_{T} bin widths Δp_{T} are given in Table 9.2 along with the phase space volumes and the bin boundaries.

bin	boundaries [GeV]		width	volume
i	$p_{\mathrm{T}i}^{\mathrm{low}}$	$p_{\mathrm{T}i}^{\mathrm{up}}$	Δp_{T}	$2\pi\Delta p_{\mathrm{T}}\Delta\eta$
1	5.00	5.55	0.55	5.53
2	5.55	6.15	0.60	6.03
3	6.15	6.82	0.67	6.74
4	6.82	7.56	0.74	7.44
5	7.56	8.39	0.83	8.34
6	8.39	9.30	0.91	9.15
7	9.30	10.32	1.02	10.25
8	10.32	11.44	1.12	11.26
9	11.44	12.69	1.25	12.57
10	12.69	14.08	1.39	13.97
11	14.08	15.61	1.53	15.38
12	15.61	17.31	1.70	17.09
13	17.31	19.20	1.89	19.00
14	19.20	21.30	2.10	21.11
15	21.30	23.62	2.32	23.32
16	23.62	26.19	2.57	25.84
17	26.19	29.05	2.86	28.75
18	29.05	32.22	3.17	31.87
19	32.22	35.73	3.51	35.29
20	35.73	39.63	3.90	39.21
21	39.63	43.95	4.32	43.43
22	43.95	48.74	4.79	48.15
23	48.74	54.06	5.32	53.48
24	54.06	59.96	5.90	59.31
25	59.96	66.49	6.53	65.65
26	66.49	73.75	7.26	72.99
27	73.75	81.79	8.04	80.83
28	81.79	90.71	8.92	86.25

Table 9.2: The bin boundaries, the bin widths, and the phase space volumes of p_{T} bins used in the inclusive jet cross section measurement.

9.3 Evaluation of the Cross Section

The inclusive jet cross section is evaluated for each p_T bin with the formula:

$$\frac{\mathrm{d}^2\sigma}{2\pi\mathrm{d}p_\mathrm{T}\mathrm{d}\eta} = \frac{1}{\int\mathcal{L}\mathrm{d}t} \cdot \frac{1}{2\pi\Delta p_\mathrm{T}\Delta\eta} \cdot \frac{1}{\mathcal{C}} \cdot J. \tag{9.1}$$

$$
\begin{aligned}
J &: \quad \text{Detector-level jet yields} \\
\mathcal{C} &: \quad \text{Correction factors} \\
2\pi\Delta p_\mathrm{T}\Delta\eta &: \quad \text{Phase space volume} \\
\int\mathcal{L}\mathrm{d}t &: \quad \text{Luminosity}
\end{aligned}
$$

The detector-level jet yields J are given in Table 6.5. The correction factors $\mathcal{C}$ are determined in Section 9.4 and applied in Section 9.5 to estimate the hadron-level jet yields:

$$K \equiv \frac{J}{C} : \quad \text{Hadron-level jet yields.} \tag{9.2}$$

The phase space volumes are given in Table 9.2 of the previous section. The luminosity is obtained in Section 5.3. The cross section in each p_T bin is presented in Section 9.9.

9.4 The Correction Factors

In Section 7.3, the hadron-level jets in the MC simulation are defined, event by event, as collections of final state particles selected by the mid-point cone algorithm, the same jet-finding algorithm that defines the detector-level jets. In the data, on the other hand, the hadron-level jets have conceptually the same definition as in the MC simulation; however, they cannot be searched for by a jet-finding algorithm since the final state particles are not reconstructed. Instead, the hadron-level jet yields are estimated from the detector-level jet yields by using the MC simulation.

As the relation (9.2) implies, the correction factors $\mathcal{C}$ encapsulate the inverse of the detector responses. The corrections are estimated in two stages: corrections for the effects related to the jet p_T measurement $\mathcal{C}_\mathrm{det}$ and corrections for the timebin

selections $\mathcal{C}_{\mathrm{tb}}$:

$$\mathcal{C} = \mathcal{C}_{\mathrm{tb}} \cdot \mathcal{C}_{\mathrm{det}}. \tag{9.3}$$

$\mathcal{C}_{\mathrm{tb}}$ was evaluated using the number of MINB events in Section 5.7. $\mathcal{C}_{\mathrm{det}}$ is estimated in this section.

The Definition of $\mathcal{C}_{\mathbf{det}}$

The correction factors $\mathcal{C}_{\mathrm{det}}$ correct for the effects accompanied by the measurement of jet p_{T}, including energy smearing, energy shift, trigger bias, and trigger efficiencies. In other words, the correction factors $\mathcal{C}_{\mathrm{det}}$ relate the detector-level jet yields in a given timebin set to the hadron-level jet yields in the same timebin set:

$$K_{\mathrm{tb}\,i}^{\mathrm{DATA}} = \frac{J_{\mathrm{trg\,tb}\,i}^{\mathrm{DATA}}}{\mathcal{C}_{\mathrm{det}\,i}^{\mathrm{trg,\,tb}}}. \tag{9.4}$$

The labels "tb" and "trg" are added to emphasize that the timebin selections and the trigger selections are applied. Although $K_{\mathrm{tb}\,i}^{\mathrm{DATA}}$ does not depend on triggers, there are different estimates of $K_{\mathrm{tb}\,i}^{\mathrm{DATA}}$ for different triggers. This relation is similar to (9.2); the difference is that the timebin selections are applied in RHS of (9.4) but not in RHS of (9.2).

The Estimate of $\mathcal{C}_{\mathbf{det}}$

Chapter 8 showed an excellent agreement between the data and the MC events. This agreement drastically simplifies the estimation of the correction factors $\mathcal{C}_{\mathrm{det}\,i}^{\mathrm{trg,\,tb}}$. The correction factors $\mathcal{C}_{\mathrm{det}\,i}^{\mathrm{trg,\,tb}}$ are estimated from the MC events as bin-by-bin ratios of the jet yields at the detector level and at the hadron level:

$$\mathcal{C}_{\mathrm{det}\,i}^{\mathrm{trg\,tb}} = \frac{J_{\mathrm{trg\,tb}\,i}^{\mathrm{MC}}}{K_{\mathrm{tb}\,i}^{\mathrm{MC}}}. \tag{9.5}$$

Figure 9-1 shows the correction factors. The numerical values are given in Table 9.3 to 9.6.
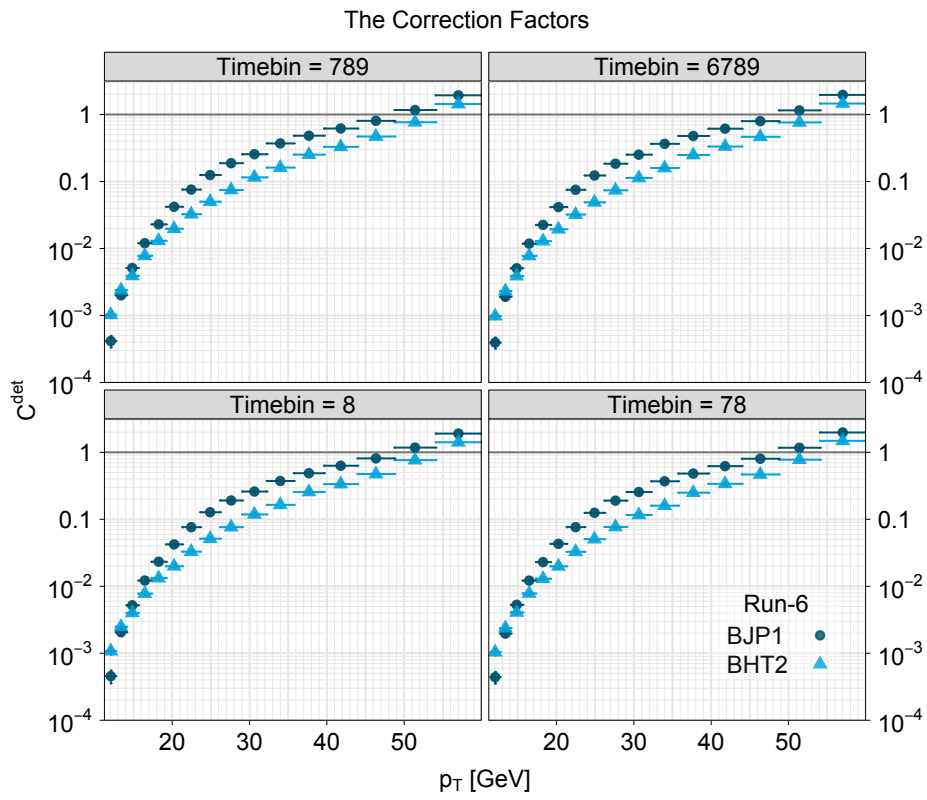
Figure 9-1: The correction factors $\mathcal{C}_{\text{det}}$

	BHT2	BJP1
p_T [GeV]	$C_{det} \pm \delta C_{det}$(stat.)	$C_{det} \pm \delta C_{det}$(stat.)
11.44-12.69	$(1.08 \pm 0.12) \times 10^{-3}$	$(4.55 \pm 0.99) \times 10^{-4}$
12.69-14.08	$(2.49 \pm 0.23) \times 10^{-3}$	$(2.06 \pm 0.20) \times 10^{-3}$
14.08-15.61	$(4.01 \pm 0.27) \times 10^{-3}$	$(5.20 \pm 0.29) \times 10^{-3}$
15.61-17.31	$(7.78 \pm 0.46) \times 10^{-3}$	$(1.22 \pm 0.05) \times 10^{-2}$
17.31-19.20	$(1.32 \pm 0.08) \times 10^{-2}$	$(2.33 \pm 0.10) \times 10^{-2}$
19.20-21.30	$(1.99 \pm 0.12) \times 10^{-2}$	$(4.22 \pm 0.16) \times 10^{-2}$
21.30-23.62	$(3.29 \pm 0.19) \times 10^{-2}$	$(7.63 \pm 0.27) \times 10^{-2}$
23.62-26.19	$(5.14 \pm 0.30) \times 10^{-2}$	$(1.27 \pm 0.05) \times 10^{-1}$
26.19-29.05	$(7.64 \pm 0.44) \times 10^{-2}$	$(1.91 \pm 0.07) \times 10^{-1}$
29.05-32.22	$(1.18 \pm 0.09) \times 10^{-1}$	$(2.60 \pm 0.11) \times 10^{-1}$
32.22-35.73	$(1.65 \pm 0.16) \times 10^{-1}$	$(3.73 \pm 0.19) \times 10^{-1}$
35.73-39.63	$(2.56 \pm 0.19) \times 10^{-1}$	$(4.88 \pm 0.22) \times 10^{-1}$
39.63-43.95	$(3.35 \pm 0.25) \times 10^{-1}$	$(6.31 \pm 0.34) \times 10^{-1}$
43.95-48.74	$(4.73 \pm 0.17) \times 10^{-1}$	$(8.12 \pm 0.21) \times 10^{-1}$
48.74-54.06	$(7.65 \pm 0.34) \times 10^{-1}$	$(1.18 \pm 0.04) \times 10^{0}$
54.06-59.96	$(1.41 \pm 0.08) \times 10^{0}$	$(1.90 \pm 0.10) \times 10^{0}$
59.96-66.49	$(3.85 \pm 0.26) \times 10^{0}$	$(4.81 \pm 0.29) \times 10^{0}$

Table 9.3: The correction factors $\mathcal{C}_{det}$ for the events in the timebin 8.

	BHT2	BJP1
p_T [GeV]	$C_{det} \pm \delta C_{det}$(stat.)	$C_{det} \pm \delta C_{det}$(stat.)
11.44-12.69	$(1.04 \pm 0.11) \times 10^{-3}$	$(4.40 \pm 0.87) \times 10^{-4}$
12.69-14.08	$(2.38 \pm 0.21) \times 10^{-3}$	$(1.97 \pm 0.17) \times 10^{-3}$
14.08-15.61	$(4.07 \pm 0.25) \times 10^{-3}$	$(5.29 \pm 0.28) \times 10^{-3}$
15.61-17.31	$(7.82 \pm 0.43) \times 10^{-3}$	$(1.22 \pm 0.05) \times 10^{-2}$
17.31-19.20	$(1.30 \pm 0.07) \times 10^{-2}$	$(2.30 \pm 0.09) \times 10^{-2}$
19.20-21.30	$(1.99 \pm 0.11) \times 10^{-2}$	$(4.30 \pm 0.16) \times 10^{-2}$
21.30-23.62	$(3.27 \pm 0.18) \times 10^{-2}$	$(7.63 \pm 0.26) \times 10^{-2}$
23.62-26.19	$(5.06 \pm 0.28) \times 10^{-2}$	$(1.25 \pm 0.04) \times 10^{-1}$
26.19-29.05	$(7.69 \pm 0.41) \times 10^{-2}$	$(1.90 \pm 0.07) \times 10^{-1}$
29.05-32.22	$(1.16 \pm 0.08) \times 10^{-1}$	$(2.55 \pm 0.10) \times 10^{-1}$
32.22-35.73	$(1.60 \pm 0.12) \times 10^{-1}$	$(3.69 \pm 0.17) \times 10^{-1}$
35.73-39.63	$(2.50 \pm 0.17) \times 10^{-1}$	$(4.82 \pm 0.21) \times 10^{-1}$
39.63-43.95	$(3.39 \pm 0.26) \times 10^{-1}$	$(6.21 \pm 0.31) \times 10^{-1}$
43.95-48.74	$(4.67 \pm 0.15) \times 10^{-1}$	$(8.02 \pm 0.20) \times 10^{-1}$
48.74-54.06	$(7.76 \pm 0.33) \times 10^{-1}$	$(1.17 \pm 0.04) \times 10^{0}$
54.06-59.96	$(1.48 \pm 0.09) \times 10^{0}$	$(1.98 \pm 0.10) \times 10^{0}$
59.96-66.49	$(3.80 \pm 0.25) \times 10^{0}$	$(4.73 \pm 0.27) \times 10^{0}$

Table 9.4: The correction factors $\mathcal{C}_{det}$ for the events in the timebin set 78.

p_{T} [GeV]	BHT2 $C_{\mathrm{det}} \pm \delta C_{\mathrm{det}}(\text{stat.})$	BJP1 $C_{\mathrm{det}} \pm \delta C_{\mathrm{det}}(\text{stat.})$
11.44-12.69	$(1.02 \pm 0.11) \times 10^{-3}$	$(4.15 \pm 0.83) \times 10^{-4}$
12.69-14.08	$(2.39 \pm 0.21) \times 10^{-3}$	$(2.00 \pm 0.19) \times 10^{-3}$
14.08-15.61	$(3.90 \pm 0.24) \times 10^{-3}$	$(5.11 \pm 0.27) \times 10^{-3}$
15.61-17.31	$(7.77 \pm 0.43) \times 10^{-3}$	$(1.20 \pm 0.05) \times 10^{-2}$
17.31-19.20	$(1.30 \pm 0.07) \times 10^{-2}$	$(2.29 \pm 0.09) \times 10^{-2}$
19.20-21.30	$(1.97 \pm 0.11) \times 10^{-2}$	$(4.19 \pm 0.15) \times 10^{-2}$
21.30-23.62	$(3.25 \pm 0.18) \times 10^{-2}$	$(7.58 \pm 0.25) \times 10^{-2}$
23.62-26.19	$(4.99 \pm 0.27) \times 10^{-2}$	$(1.25 \pm 0.04) \times 10^{-1}$
26.19-29.05	$(7.47 \pm 0.40) \times 10^{-2}$	$(1.88 \pm 0.07) \times 10^{-1}$
29.05-32.22	$(1.15 \pm 0.08) \times 10^{-1}$	$(2.55 \pm 0.10) \times 10^{-1}$
32.22-35.73	$(1.61 \pm 0.13) \times 10^{-1}$	$(3.70 \pm 0.18) \times 10^{-1}$
35.73-39.63	$(2.52 \pm 0.17) \times 10^{-1}$	$(4.82 \pm 0.20) \times 10^{-1}$
39.63-43.95	$(3.29 \pm 0.23) \times 10^{-1}$	$(6.18 \pm 0.31) \times 10^{-1}$
43.95-48.74	$(4.69 \pm 0.15) \times 10^{-1}$	$(8.05 \pm 0.20) \times 10^{-1}$
48.74-54.06	$(7.67 \pm 0.32) \times 10^{-1}$	$(1.17 \pm 0.04) \times 10^{0}$
54.06-59.96	$(1.43 \pm 0.08) \times 10^{0}$	$(1.94 \pm 0.09) \times 10^{0}$
59.96-66.49	$(3.79 \pm 0.24) \times 10^{0}$	$(4.73 \pm 0.26) \times 10^{0}$

Table 9.5: The correction factors $\mathcal{C}_{\mathrm{det}}$ for the events in the timebin set 789.

p_{T} [GeV]	BHT2 $C_{\mathrm{det}} \pm \delta C_{\mathrm{det}}(\text{stat.})$	BJP1 $C_{\mathrm{det}} \pm \delta C_{\mathrm{det}}(\text{stat.})$
11.44-12.69	$(9.78 \pm 0.96) \times 10^{-4}$	$(3.94 \pm 0.74) \times 10^{-4}$
12.69-14.08	$(2.31 \pm 0.20) \times 10^{-3}$	$(1.90 \pm 0.17) \times 10^{-3}$
14.08-15.61	$(3.87 \pm 0.23) \times 10^{-3}$	$(5.06 \pm 0.26) \times 10^{-3}$
15.61-17.31	$(7.75 \pm 0.41) \times 10^{-3}$	$(1.18 \pm 0.05) \times 10^{-2}$
17.31-19.20	$(1.29 \pm 0.07) \times 10^{-2}$	$(2.25 \pm 0.08) \times 10^{-2}$
19.20-21.30	$(1.94 \pm 0.10) \times 10^{-2}$	$(4.15 \pm 0.15) \times 10^{-2}$
21.30-23.62	$(3.21 \pm 0.17) \times 10^{-2}$	$(7.52 \pm 0.25) \times 10^{-2}$
23.62-26.19	$(4.88 \pm 0.25) \times 10^{-2}$	$(1.23 \pm 0.04) \times 10^{-1}$
26.19-29.05	$(7.39 \pm 0.38) \times 10^{-2}$	$(1.84 \pm 0.06) \times 10^{-1}$
29.05-32.22	$(1.13 \pm 0.07) \times 10^{-1}$	$(2.52 \pm 0.09) \times 10^{-1}$
32.22-35.73	$(1.59 \pm 0.12) \times 10^{-1}$	$(3.65 \pm 0.17) \times 10^{-1}$
35.73-39.63	$(2.49 \pm 0.16) \times 10^{-1}$	$(4.78 \pm 0.19) \times 10^{-1}$
39.63-43.95	$(3.33 \pm 0.24) \times 10^{-1}$	$(6.14 \pm 0.30) \times 10^{-1}$
43.95-48.74	$(4.65 \pm 0.14) \times 10^{-1}$	$(7.97 \pm 0.19) \times 10^{-1}$
48.74-54.06	$(7.62 \pm 0.31) \times 10^{-1}$	$(1.15 \pm 0.04) \times 10^{0}$
54.06-59.96	$(1.46 \pm 0.08) \times 10^{0}$	$(1.96 \pm 0.10) \times 10^{0}$
59.96-66.49	$(3.76 \pm 0.23) \times 10^{0}$	$(4.66 \pm 0.25) \times 10^{0}$

Table 9.6: The correction factors $\mathcal{C}_{\mathrm{det}}$ for the events in the timebin set 6789.

9.5   Estimates of the Hadron-Level Jet Yield

The correction factors $\mathcal{C}_{tb}$ and $\mathcal{C}_{det}$ are determined in Section 5.7 and Section 9.4, respectively. With the relations (9.2) and (9.3), the hadron-level jet yields $K = J/(\mathcal{C}_{tb} \cdot \mathcal{C}_{det})$ are estimated, which are given in Table 9.7 to 9.10.

The definition of the hadron-level jets does not involve a measurement since the hadron-level jet yields are intrinsic to the collisions. Therefore, after the correction, all dependence on the experimental conditions should vanish. For instance, from Section 5.7, the analyses have been carried out for four timebin sets and two triggers in parallel. The hadron-level jet yields K derived from different timebins and different triggers are estimates of the same quantities.

	BHT2	BJP1
p_T [GeV]	$K \pm \delta K(\text{stat.})$	$K \pm \delta K(\text{stat.})$
11.44-12.69	$(1.70 \pm 0.20) \times 10^7$	$(2.10 \pm 0.46) \times 10^7$
12.69-14.08	$(6.76 \pm 0.64) \times 10^6$	$(8.68 \pm 0.85) \times 10^6$
14.08-15.61	$(4.00 \pm 0.28) \times 10^6$	$(4.35 \pm 0.25) \times 10^6$
15.61-17.31	$(1.81 \pm 0.11) \times 10^6$	$(1.95 \pm 0.09) \times 10^6$
17.31-19.20	$(9.28 \pm 0.57) \times 10^5$	$(1.00 \pm 0.04) \times 10^6$
19.20-21.30	$(4.94 \pm 0.32) \times 10^5$	$(4.94 \pm 0.20) \times 10^5$
21.30-23.62	$(2.27 \pm 0.14) \times 10^5$	$(2.29 \pm 0.09) \times 10^5$
23.62-26.19	$(1.06 \pm 0.07) \times 10^5$	$(1.12 \pm 0.05) \times 10^5$
26.19-29.05	$(5.10 \pm 0.33) \times 10^4$	$(5.19 \pm 0.22) \times 10^4$
29.05-32.22	$(2.14 \pm 0.18) \times 10^4$	$(2.47 \pm 0.12) \times 10^4$
32.22-35.73	$(9.10 \pm 0.97) \times 10^3$	$(9.58 \pm 0.58) \times 10^3$
35.73-39.63	$(3.10 \pm 0.31) \times 10^3$	$(3.72 \pm 0.24) \times 10^3$
39.63-43.95	$(1.43 \pm 0.17) \times 10^3$	$(1.53 \pm 0.13) \times 10^3$
43.95-48.74	$(5.24 \pm 0.68) \times 10^2$	$(4.99 \pm 0.50) \times 10^2$
48.74-54.06	$(1.15 \pm 0.24) \times 10^2$	$(1.14 \pm 0.20) \times 10^2$
54.06-59.96	$(2.16 \pm 0.77) \times 10^1$	$(2.00 \pm 0.64) \times 10^1$
59.96-66.49	$(9.91 \pm 9.93) \times 10^{-1}$	$(3.17 \pm 1.60) \times 10^0$

Table 9.7: The estimates of the hadron-level jet yields K_i from the events in the time-bin 8.

p_T [GeV]	BHT2 $K \pm \delta K$(stat.)	BJP1 $K \pm \delta K$(stat.)
11.44-12.69	$(1.76 \pm 0.19) \times 10^7$	$(2.17 \pm 0.43) \times 10^7$
12.69-14.08	$(7.28 \pm 0.64) \times 10^6$	$(9.22 \pm 0.82) \times 10^6$
14.08-15.61	$(3.91 \pm 0.25) \times 10^6$	$(4.26 \pm 0.23) \times 10^6$
15.61-17.31	$(1.79 \pm 0.10) \times 10^6$	$(1.96 \pm 0.08) \times 10^6$
17.31-19.20	$(9.60 \pm 0.54) \times 10^5$	$(1.02 \pm 0.04) \times 10^6$
19.20-21.30	$(5.00 \pm 0.29) \times 10^5$	$(4.83 \pm 0.19) \times 10^5$
21.30-23.62	$(2.34 \pm 0.13) \times 10^5$	$(2.31 \pm 0.08) \times 10^5$
23.62-26.19	$(1.09 \pm 0.06) \times 10^5$	$(1.11 \pm 0.04) \times 10^5$
26.19-29.05	$(4.96 \pm 0.29) \times 10^4$	$(5.17 \pm 0.20) \times 10^4$
29.05-32.22	$(2.18 \pm 0.16) \times 10^4$	$(2.50 \pm 0.11) \times 10^4$
32.22-35.73	$(9.45 \pm 0.80) \times 10^3$	$(9.88 \pm 0.52) \times 10^3$
35.73-39.63	$(3.60 \pm 0.29) \times 10^3$	$(3.98 \pm 0.21) \times 10^3$
39.63-43.95	$(1.40 \pm 0.14) \times 10^3$	$(1.51 \pm 0.10) \times 10^3$
43.95-48.74	$(5.21 \pm 0.49) \times 10^2$	$(4.88 \pm 0.36) \times 10^2$
48.74-54.06	$(1.03 \pm 0.16) \times 10^2$	$(1.09 \pm 0.14) \times 10^2$
54.06-59.96	$(2.18 \pm 0.54) \times 10^1$	$(2.31 \pm 0.49) \times 10^1$
59.96-66.49	$(2.50 \pm 1.13) \times 10^0$	$(3.22 \pm 1.15) \times 10^0$

Table 9.8: The estimates of the hadron-level jet yields K_i from the events in the time-bin set 78.

	BHT2	BJP1
p_{T} [GeV]	$K \pm \delta K(\text{stat.})$	$K \pm \delta K(\text{stat.})$
11.44-12.69	$(1.74 \pm 0.18) \times 10^7$	$(2.19 \pm 0.44) \times 10^7$
12.69-14.08	$(7.12 \pm 0.64) \times 10^6$	$(8.74 \pm 0.82) \times 10^6$
14.08-15.61	$(4.01 \pm 0.25) \times 10^6$	$(4.30 \pm 0.23) \times 10^6$
15.61-17.31	$(1.79 \pm 0.10) \times 10^6$	$(1.95 \pm 0.08) \times 10^6$
17.31-19.20	$(9.26 \pm 0.52) \times 10^5$	$(9.95 \pm 0.39) \times 10^5$
19.20-21.30	$(4.99 \pm 0.28) \times 10^5$	$(4.88 \pm 0.18) \times 10^5$
21.30-23.62	$(2.33 \pm 0.13) \times 10^5$	$(2.29 \pm 0.08) \times 10^5$
23.62-26.19	$(1.11 \pm 0.06) \times 10^5$	$(1.10 \pm 0.04) \times 10^5$
26.19-29.05	$(5.00 \pm 0.28) \times 10^4$	$(5.15 \pm 0.19) \times 10^4$
29.05-32.22	$(2.20 \pm 0.15) \times 10^4$	$(2.50 \pm 0.10) \times 10^4$
32.22-35.73	$(9.24 \pm 0.81) \times 10^3$	$(9.92 \pm 0.51) \times 10^3$
35.73-39.63	$(3.44 \pm 0.27) \times 10^3$	$(3.94 \pm 0.20) \times 10^3$
39.63-43.95	$(1.45 \pm 0.13) \times 10^3$	$(1.52 \pm 0.10) \times 10^3$
43.95-48.74	$(4.95 \pm 0.43) \times 10^2$	$(4.70 \pm 0.31) \times 10^2$
48.74-54.06	$(1.19 \pm 0.16) \times 10^2$	$(1.21 \pm 0.13) \times 10^2$
54.06-59.96	$(2.57 \pm 0.53) \times 10^1$	$(2.51 \pm 0.45) \times 10^1$
59.96-66.49	$(2.33 \pm 0.96) \times 10^0$	$(3.42 \pm 1.05) \times 10^0$

Table 9.9: The estimates of the hadron-level jet yields K_i from the events in the time-bin set 789.

p_T [GeV]	BHT2 $K \pm \delta K$(stat.)	BJP1 $K \pm \delta K$(stat.)
11.44-12.69	$(1.80 \pm 0.18) \times 10^7$	$(2.27 \pm 0.43) \times 10^7$
12.69-14.08	$(7.34 \pm 0.62) \times 10^6$	$(8.98 \pm 0.80) \times 10^6$
14.08-15.61	$(4.03 \pm 0.24) \times 10^6$	$(4.29 \pm 0.22) \times 10^6$
15.61-17.31	$(1.78 \pm 0.10) \times 10^6$	$(1.95 \pm 0.08) \times 10^6$
17.31-19.20	$(9.33 \pm 0.50) \times 10^5$	$(1.00 \pm 0.04) \times 10^6$
19.20-21.30	$(5.04 \pm 0.27) \times 10^5$	$(4.91 \pm 0.18) \times 10^5$
21.30-23.62	$(2.35 \pm 0.13) \times 10^5$	$(2.28 \pm 0.08) \times 10^5$
23.62-26.19	$(1.13 \pm 0.06) \times 10^5$	$(1.10 \pm 0.04) \times 10^5$
26.19-29.05	$(5.06 \pm 0.28) \times 10^4$	$(5.18 \pm 0.19) \times 10^4$
29.05-32.22	$(2.23 \pm 0.15) \times 10^4$	$(2.52 \pm 0.10) \times 10^4$
32.22-35.73	$(9.33 \pm 0.77) \times 10^3$	$(1.01 \pm 0.05) \times 10^4$
35.73-39.63	$(3.48 \pm 0.26) \times 10^3$	$(4.03 \pm 0.19) \times 10^3$
39.63-43.95	$(1.41 \pm 0.12) \times 10^3$	$(1.47 \pm 0.09) \times 10^3$
43.95-48.74	$(5.04 \pm 0.39) \times 10^2$	$(4.94 \pm 0.30) \times 10^2$
48.74-54.06	$(1.23 \pm 0.15) \times 10^2$	$(1.28 \pm 0.12) \times 10^2$
54.06-59.96	$(2.69 \pm 0.49) \times 10^1$	$(2.55 \pm 0.41) \times 10^1$
59.96-66.49	$(3.17 \pm 1.02) \times 10^0$	$(4.08 \pm 1.04) \times 10^0$

Table 9.10: The estimates of the hadron-level jet yields K_i from the events in the timebin set 6789.

9.6   Systematic Uncertainty

The systematic uncertainties are shown in Figure 9-2 and given in Table 9.11. The major systematic uncertainty is due the uncertainty on the jet energy scale (JES). Because the p_T dependence is steeply decreasing, the uncertainty of the cross section is very sensitive to systematic uncertainty of the JES. For example, 5% of the JES uncertainty results in 30% of the cross section uncertainty at 20 GeV and 60% at 40 GeV.
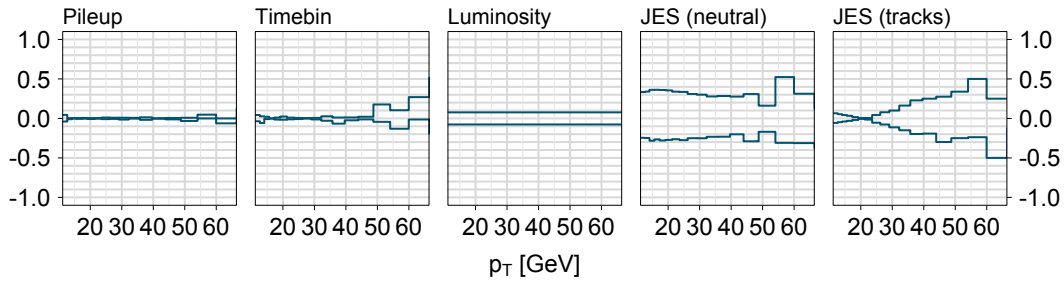
Figure 9-2: The systematic uncertainty on the inclusive jet cross section.

Jet Energy Scale (Tracks)

The track portion of the jet energy has 5.6 % of systematic uncertainty [40, 41]. To evaluate the effect of this uncertainty on the inclusive jet cross section, the cross section is reevaluated with the 5.6 % variation of the track portion of the jet energy.

The effect of this variation is only a shift of the track portion of the jet energy and does not include a change of the trigger rates. Therefore, this variation does not change the total jet cross section as much as the neutral energy variation does. As the track portion of the jet energy is raised (lowered), the jet cross section decreases (increases) in the low-p_T range and increases (decreases) in the high-p_T range. The cross section is insensitive to the variation at around p_T 20GeV. The uncertainty is large in the high-p_T range because the neutral energy ratio is small and the p_T dependence is steep at the detector level.

p_T [GeV]	JES (neutral)	JES (tracks)	Pile-up	Timebin	Total
11.44-12.69	+0.33	+0.07	+0.0444	+0.043	+0.35
	-0.25	-0.06	-0.0393	-0.036	-0.26
12.69-14.08	+0.34	+0.05	+0.0039	+0.027	+0.34
	-0.25	-0.05	-0.0103	-0.059	-0.26
14.08-15.61	+0.36	+0.04	+0.0045	+0.021	+0.37
	-0.28	-0.04	-0.0026	-0.008	-0.29
15.61-17.31	+0.36	+0.03	+0.0038	+0.001	+0.36
	-0.27	-0.03	-0.0052	-0.002	-0.27
17.31-19.20	+0.36	+0.02	+0.0064	+0.011	+0.36
	-0.28	-0.02	-0.0033	-0.015	-0.28
19.20-21.30	+0.35	+0.01	+0.0042	+0.024	+0.36
	-0.27	-0.01	-0.0073	-0.016	-0.27
21.30-23.62	+0.34	+0.01	+0.0040	+0.010	+0.34
	-0.26	-0.01	-0.0033	-0.012	-0.26
23.62-26.19	+0.34	+0.04	+0.0112	+0.006	+0.34
	-0.28	-0.05	-0.0089	-0.008	-0.28
26.19-29.05	+0.31	+0.08	+0.0088	+0.004	+0.32
	-0.25	-0.08	-0.0064	-0.002	-0.26
29.05-32.22	+0.30	+0.10	+0.0086	+0.007	+0.32
	-0.25	-0.11	-0.0143	-0.013	-0.28
32.22-35.73	+0.28	+0.16	+0.0074	+0.027	+0.32
	-0.23	-0.15	-0.0026	-0.030	-0.28
35.73-39.63	+0.28	+0.23	+0.0136	+0.011	+0.36
	-0.23	-0.20	-0.0179	-0.066	-0.31
39.63-43.95	+0.28	+0.25	+0.0026	+0.012	+0.37
	-0.20	-0.19	-0.0039	-0.024	-0.28
43.95-48.74	+0.31	+0.27	+0.0060	+0.021	+0.41
	-0.29	-0.30	-0.0121	-0.012	-0.42
48.74-54.06	+0.16	+0.34	+0.0081	+0.176	+0.41
	-0.17	-0.25	-0.0323	-0.043	-0.31
54.06-59.96	+0.52	+0.50	+0.0476	+0.104	+0.73
	-0.31	-0.24	+0.0000	-0.131	-0.41
59.96-66.49	+0.31	+0.25	+0.0000	+0.270	+0.48
	-0.31	-0.50	-0.0625	-0.014	-0.59

Table 9.11: The systematic uncertainty on the inclusive jet cross section. 7.6% of the systematic uncertainty on the integrated luminosity is not included in the total.

Jet Energy Scale (Neutral)

Energy deposits in the BEMC towers have 4.8 % of systematic uncertainty [40, 41]. The effect of this uncertainty is evaluated by varying the BEMC tower energies. After the energies are varied, the offline trigger thresholds (Section 5.6) are reapplied and the jet finding algorithm (Section 6.2) is reran. The effect of the neutral energy variation is more complicated than that of the track portion of the jet energy variation because it changes trigger rates as well as shifts the jet energy. This variation changes the total jet cross section because it changes trigger rates.

Pile-up

The correction for the pile-up was made in Section 6.3, where 50 MeV was subtracted from jet p_{T}. The systematic effect of this correction is estimated by reevaluating the jet cross section with no subtraction and 100 MeV subtraction.

Timebin

The systematic effect of the timebin selections are estimated by comparing the hadron-level jet yields evaluated from the events in the different timebin sets in the previous section.

Luminosity

The luminosity was calculated from the number of the MINB events and the MINB cross section in Section 5.3. The inclusive jet cross section has 7.6% ($\approx 0.41/5.39$) of systematic uncertainty due to the uncertainty of the integrated luminosity.

9.7 Theoretical Predictions

In perturbative QCD calculations, the correction of the next-to-leading order (NLO) in α_s to the leading order (LO) is sizable and is necessary to be taken into account in order to make quantitative comparison with data. Furthermore, jets in perturbative QCD are at the parton level while the cross section is measured at the hadron level. In order to make comparison with the data at the hadron level, the effects of the hadronization and the underlying events are evaluated by MC simulation.

9.7.1 NLO pQCD Predictions

Figure 9-3 shows a NLO pQCD prediction of the inclusive jet cross section and the contributions from parton-level cross sections. The cross sections are calculated with a program used in ref. [33] with the CTEQ6M parton distributions [39]. As discussed in Section 6.1, in NLO pQCD, there are at most three partons in the final state (Figure 6-1). Jets are defined by small cone approximation (SCA) with cone radius 0.7. SCA is a good approximation of jets with cone radius up to 0.7 [33]. 0.7 is used in the mid-point cone algorithm in the definition of jets in the data. In the calculation, both the renormalization scale and the factorization scale are $\mu = p_T$. The scale uncertainty is calculated by varying the scale from $0.5p_T$ to $2p_T$. The scale uncertainty is shown in Figure 9-6.
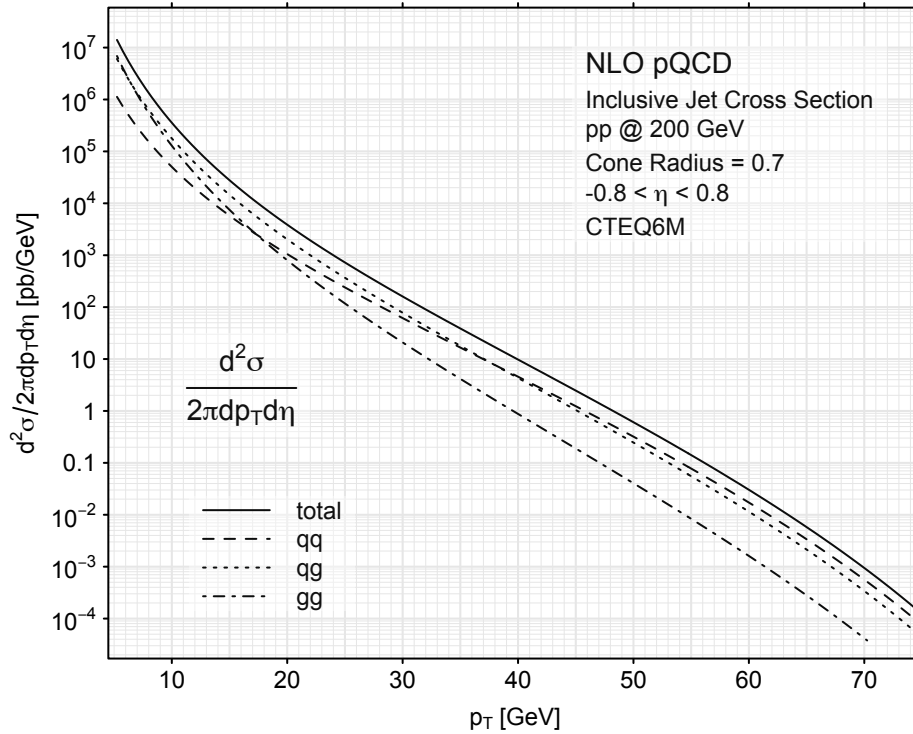
Figure 9-3: QCD NLO predictions of the inclusive jet cross section with the
CTEQ6M parton distributions.

9.7.2   Hadronization and Underlying Event Corrections

The effects of the hadronization and the underlying events are evaluated by using the
MC events described in Chapter 7. The hadron-level jets and the parton-level jets in
the MC events are defined in Section 7.2. The correction factors C_{HAD} are obtained
for each p_{T} bin as the ratios of the cross section at the hadron level and at the parton
level.

$$C_{\text{HAD}} = \frac{\sigma^{\text{hadron}}}{\sigma^{\text{parton}}}$$

The systematic uncertainty is calculated by varying the cone radius from 0.6 to 0.8.
The correction factors C_{HAD} are given in Table 9.12 and plotted in Figure 9-4.

p_T [GeV]	$C_\mathrm{HAD} \pm \delta C_\mathrm{HAD}(\text{stat.}) \pm \delta C_\mathrm{HAD}(\text{sys.})$
9.30-10.32	$2.272 \pm 0.026 \; {}^{+0.727}_{-0.595}$
10.32-11.44	$2.084 \pm 0.028 \; {}^{+0.734}_{-0.534}$
11.44-12.69	$1.917 \pm 0.030 \; {}^{+0.634}_{-0.491}$
12.69-14.08	$1.572 \pm 0.027 \; {}^{+0.507}_{-0.332}$
14.08-15.61	$1.352 \pm 0.022 \; {}^{+0.306}_{-0.255}$
15.61-17.31	$1.156 \pm 0.014 \; {}^{+0.323}_{-0.126}$
17.31-19.20	$1.099 \pm 0.016 \; {}^{+0.157}_{-0.124}$
19.20-21.30	$1.056 \pm 0.014 \; {}^{+0.110}_{-0.112}$
21.30-23.62	$0.991 \pm 0.012 \; {}^{+0.106}_{-0.078}$
23.62-26.19	$0.974 \pm 0.010 \; {}^{+0.073}_{-0.078}$
26.19-29.05	$0.949 \pm 0.010 \; {}^{+0.068}_{-0.053}$
29.05-32.22	$0.941 \pm 0.010 \; {}^{+0.057}_{-0.047}$
32.22-35.73	$0.931 \pm 0.011 \; {}^{+0.049}_{-0.051}$
35.73-39.63	$0.922 \pm 0.015 \; {}^{+0.048}_{-0.033}$
39.63-43.95	$0.924 \pm 0.020 \; {}^{+0.019}_{-0.060}$
43.95-48.74	$0.920 \pm 0.007 \; {}^{+0.040}_{-0.038}$
48.74-54.06	$0.895 \pm 0.010 \; {}^{+0.055}_{-0.046}$
54.06-59.96	$0.888 \pm 0.008 \; {}^{+0.045}_{-0.027}$
59.96-66.49	$0.844 \pm 0.007 \; {}^{+0.050}_{-0.060}$

Table 9.12: The hadronization and underlying event corrections estimated with the MC events.
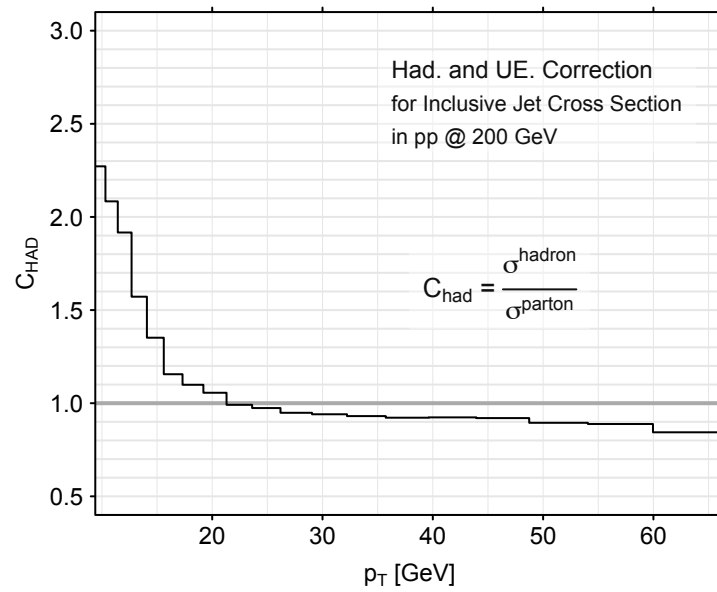
Figure 9-4: The hadronization and underlying event corrections estimated with the MC events.

9.8 Data Points within Wide Bins

The formula (9.1),

$$\frac{d^2\sigma}{2\pi dp_T d\eta} = \frac{1}{\int \mathcal{L}dt} \cdot \frac{1}{2\pi\Delta p_T \Delta\eta} \cdot \frac{1}{C} \cdot J,$$

is used to calculate the differential cross section. As RHS indicates, the values for the cross section are obtained in bins of p_T and η with bin widths Δp_T and $\Delta\eta$, respectively. It is of interest to measure the cross section as a function of p_T in a specific η range. The size of the η range is expressed as $\Delta\eta$. It is not straightforward to interpret the formula as a function of p_T, especially when Δp_T is large. Only in the limit of $\Delta p_T \to 0$ is the formula exact as a function of p_T. In order for the cross section to be interpreted as a function of p_T, each measured value for the cross section needs to be associated with a value of p_T, not a bin of p_T. An appropriate way to select a value of abscissa within a wide bin is suggested in ref [42].

If LHS of (9.1) is a function of p_T, its integral over the p_T bin divided by the bin width Δp_T is equal to RHS:

$$\frac{1}{\Delta p_T} \int\limits_{p_T^{\text{low}}}^{p_T^{\text{low}}+\Delta p_T} \frac{d^2\sigma(p_T)}{2\pi dp_T d\eta} dp_T = \frac{1}{\int \mathcal{L}dt} \cdot \frac{1}{2\pi\Delta p_T \Delta\eta} \cdot \frac{1}{C} \cdot J.$$

In other words, a value in a p_T bin is the mean value of the cross section in the p_T bin, which is not the same as the cross section at the mean value of p_T in the p_T bin. If the cross section is monotonically decreasing as a function of p_T, there is a value $p_T^{\text{l.w.}}$ in a p_T bin that satisfies the relation:

$$\frac{d^2\sigma}{2\pi dp_T d\eta}(p_T^{\text{l.w.}}) = \frac{1}{\Delta p_T} \int\limits_{p_T^{\text{low}}}^{p_T^{\text{low}}+\Delta p_T} \frac{d^2\sigma(p_T)}{2\pi dp_T d\eta} dp_T. \tag{9.6}$$

The measured values for the cross section in p_T bins represent the cross section at $p_T = p_T^{\text{l.w.}}$.

This method requires a functional form for the cross section in order to find such $p_T^{l.w.}$. The NLO pQCD calculation in the previous section is used. Figure 9-5 shows the NLO pQCD calculation as a continuous function of p_T and in the bins of p_T. The figure also shows the points that satisfy the relation (9.6). The values of $p_T^{l.w.}$ are given in Table 9.13.
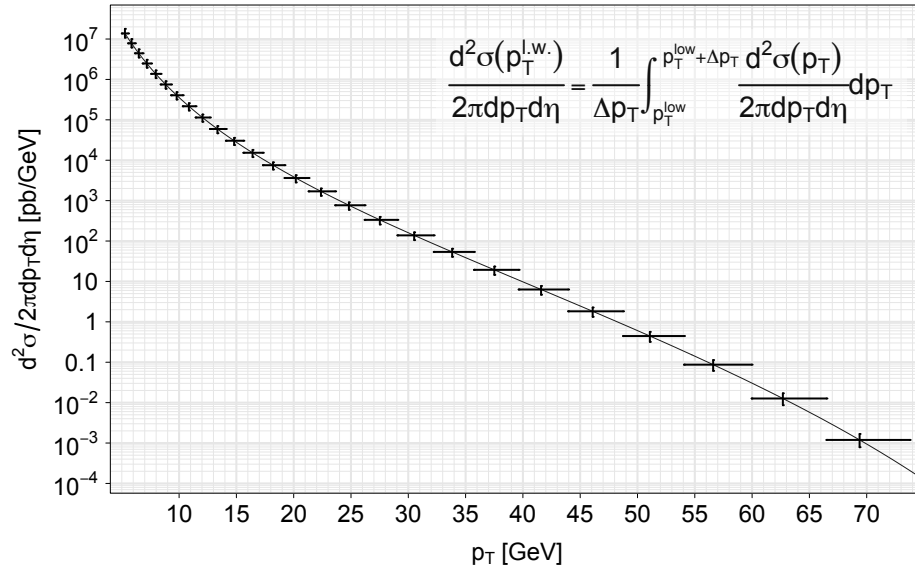
Figure 9-5: NLO pQCD calculations of the inclusive jet cross section as a smooth function of p_T and in bins of p_T. The vertical lines show where the smooth curve intercepts the binned values.

| p_T bin | boundaries | | | | [GeV] |
	low	up	width	center	$p_T^{l.w.}$
1	5.00	5.55	0.55	5.28	5.27
2	5.55	6.15	0.60	5.85	5.85
3	6.15	6.82	0.67	6.49	6.48
4	6.82	7.56	0.74	7.19	7.18
5	7.56	8.39	0.83	7.97	7.96
6	8.39	9.30	0.91	8.85	8.83
7	9.30	10.32	1.02	9.81	9.79
8	10.32	11.44	1.12	10.88	10.85
9	11.44	12.69	1.25	12.06	12.04
10	12.69	14.08	1.39	13.38	13.35
11	14.08	15.61	1.53	14.85	14.80
12	15.61	17.31	1.70	16.46	16.41
13	17.31	19.20	1.89	18.25	18.20
14	19.20	21.30	2.10	20.25	20.18
15	21.30	23.62	2.32	22.46	22.38
16	23.62	26.19	2.57	24.91	24.82
17	26.19	29.05	2.86	27.62	27.52
18	29.05	32.22	3.17	30.64	30.51
19	32.22	35.73	3.51	33.98	33.83
20	35.73	39.63	3.90	37.68	37.51
21	39.63	43.95	4.32	41.79	41.59
22	43.95	48.74	4.79	46.34	46.09
23	48.74	54.06	5.32	51.40	51.08
24	54.06	59.96	5.90	57.01	56.60
25	59.96	66.49	6.53	63.23	62.69
26	66.49	73.75	7.26	70.12	69.38

Table 9.13: $p_T^{l.w.}$

9.9   Results

The inclusive jet cross section in proton-proton collisions at $\sqrt{s} = 200$ GeV is measured as a function of jet p_{T} in the region of $13 < p_{\mathrm{T}} < 66$ GeV and $|\eta| \leq 0.8$. The detector effects are evaluated using MC simulation. The results are compared to a NLO pQCD prediction with corrections for the effects of the hadronization and the underlying events. Table 9.14 gives the results. Figure 9-6 shows the results compared with the theoretical prediction. Figure 9-7 shows the ratios (data - theory)/theory for each p_{T} bin. 7.6% of uncertainly due to the uncertainly of the integrated luminosity is not included in the table or shown in the figures. The measured cross section, while decreasing more than 7 orders of magnitude with p_{T}, is in agreement with the theory.

This is the first inclusive jet cross section result using both sides of the BEMC of the STAR detector. The agreement with a theoretical prediction is important to interpret the inclusive jet $\mathcal{A}_{\mathrm{LL}}$ within a framework of QCD factorization. The agreement is also important for dijet cross section and dijet $\mathcal{A}_{\mathrm{LL}}$ measurements.

p_T	$\sigma \pm \delta\sigma(\text{stat.}) \pm \delta\sigma(\text{sys.})$		
[GeV]	[pb/GeV]		
12.69-14.08	$(1.19 \pm 0.11$	$^{+0.41}_{-0.30}$	$) \times 10^5$
14.08-15.61	$(5.18 \pm 0.26$	$^{+1.89}_{-1.48}$	$) \times 10^4$
15.61-17.31	$(2.12 \pm 0.08$	$^{+0.77}_{-0.57}$	$) \times 10^4$
17.31-19.20	$(9.82 \pm 0.38$	$^{+3.54}_{-2.75}$	$) \times 10^3$
19.20-21.30	$(4.31 \pm 0.16$	$^{+1.53}_{-1.17}$	$) \times 10^3$
21.30-23.62	$(1.81 \pm 0.06$	$^{+0.62}_{-0.48}$	$) \times 10^3$
23.62-26.19	$(7.92 \pm 0.27$	$^{+2.68}_{-2.22}$	$) \times 10^2$
26.19-29.05	$(3.34 \pm 0.12$	$^{+1.07}_{-0.88}$	$) \times 10^2$
29.05-32.22	$(1.47 \pm 0.06$	$^{+0.46}_{-0.40}$	$) \times 10^2$
32.22-35.73	$(5.33 \pm 0.26$	$^{+1.72}_{-1.48}$	$) \times 10^1$
35.73-39.63	$(1.91 \pm 0.09$	$^{+0.69}_{-0.58}$	$) \times 10^1$
39.63-43.95	$(6.29 \pm 0.38$	$^{+2.34}_{-1.75}$	$) \times 10^0$
43.95-48.74	$(1.91 \pm 0.11$	$^{+0.79}_{-0.79}$	$) \times 10^0$
48.74-54.06	$(4.44 \pm 0.42$	$^{+1.67}_{-1.35}$	$) \times 10^{-1}$
54.06-59.96	$(7.97 \pm 1.29$	$^{+5.78}_{-3.11}$	$) \times 10^{-2}$
59.96-66.49	$(1.15 \pm 0.30$	$^{+0.46}_{-0.68}$	$) \times 10^{-2}$

Table 9.14: Inclusive jet cross section $\dfrac{\text{d}^2\sigma}{2\pi\text{d}p_T\text{d}\eta}$ [pb/GeV]. The statistical uncertainty includes the statistical uncertainty on the correction factors from the MC samples as well as the statistical uncertainty on the jet yield in the data. 7.6% of the systematic uncertainty on the integrated luminosity is not included.

Figure 9-6: The inclusive jet cross section in proton-proton collisions at $\sqrt{s} = 200$ GeV from RHIC Run-6 data compared to theoretical predictions. The measured cross sections are shown by the circles. The vertical lines on the data points indicate the statistical errors. The systematic uncertainly is shown by the rectangles, in which 7.68% of uncertainly due to the uncertainly on the integrated luminosity is not included. The gray bands show the theoretical predictions. The light gray band is NLO perturbative QCD prediction with the CTEQ6M parton distribution. The dark gray band includes the corrections for the effects of hadronization and underlying events. The height of the bands indicate the size of the theoretical uncertainly.

Figure 9-7: The comparison of the measured inclusive jet cross section and the NLO pQCD prediction: (data - NLO)/NLO. The NLO pQCD prediction is corrected for the effects of hadronization and underlying events. The ratios are taken bin by bin. The horizontal lines on the data points show the bin widths. The vertical lines on the data points indicate the statistical errors. The gray rectangles show the systematic uncertainly on the measured cross section. Theoretical uncertainly is indicated by the solid lines.

9.10   Cone Radius Dependence

This section shows how the inclusive jet cross section in the data and the theory changes as the cone radius changes from 0.4 to 0.8 by 0.1.

Data

At low p_T, the cone radius dependence depends on p_T. The smaller the p_T, the larger the dependence. At p_T above about 30 GeV, the changes become uniform and the cross section increases by approximately 13% as the cone radius increases by 0.1 (Figure 9-8).
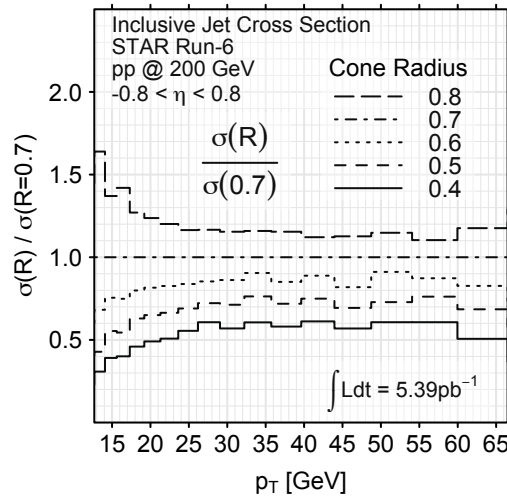
Figure 9-8: The cone radius dependence of the inclusive jet cross section.

Theory

The cone radius dependence of the next-to-leading order calculation is small and has little p_T dependence (Figure 9-9). The cross section increases by 3 to 4 % as the cone radius increases by 0.1.

When the cone radius is 0.4, the hadroninzation and the underlying event corrections are around 0.8 and uniform over the whole p_T range (Figure 9-10). As the cone radius increases, the correction increases rapidly in the low-p_T range and slowly in the high-p_T range. The p_T dependence of the correction becomes less uniform for jets
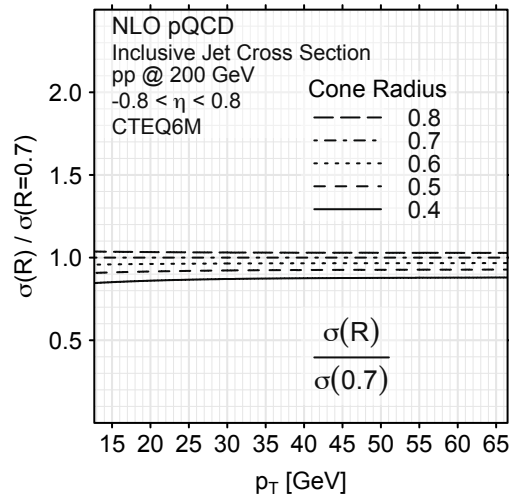
Figure 9-9: The cone radius dependence of the inclusive jet cross section in next-to-leading order pQCD calculations.

with larger cone size. The corrections are less than one in the high-p_T range while they are greater than one in the low-p_T range when the cone radius is bigger than 0.5.

In the low-p_T range, the corrections are mostly due to the underlying events, which are dominated by low-p_T particles. Jets with larger cone radius are likely to cotain more underlying events. In the high-p_T ranges, the corrections address what fraction of the energy moves outside of the cone at the hadroninzation.

When the hadroninzation and the underlying event correction is applied, the NLO calculations have similar trend with the data (Figure 9-11). The cone radius dependence depends on p_T at low p_T and becomes uniform over p_T at high p_T. However, in general, the cone radius dependence is weaker in theory than in the data.
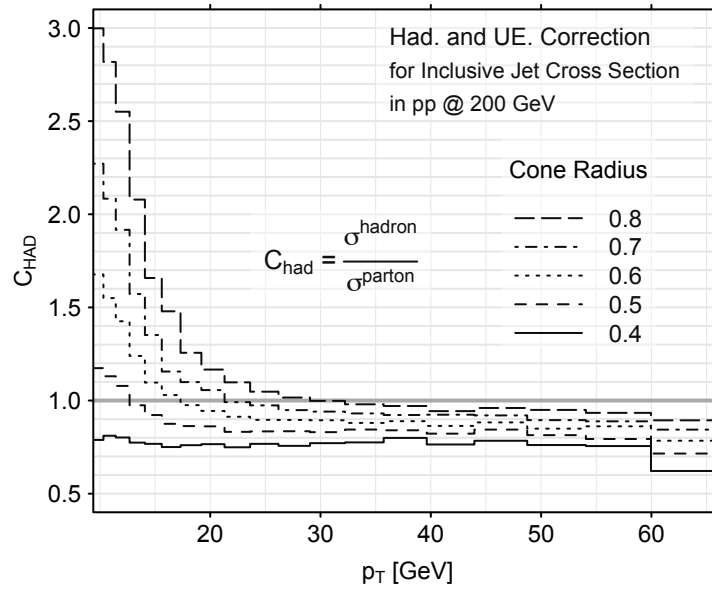
Figure 9-10: The cone radius dependence of the hadroninzation and the underlying event correction.
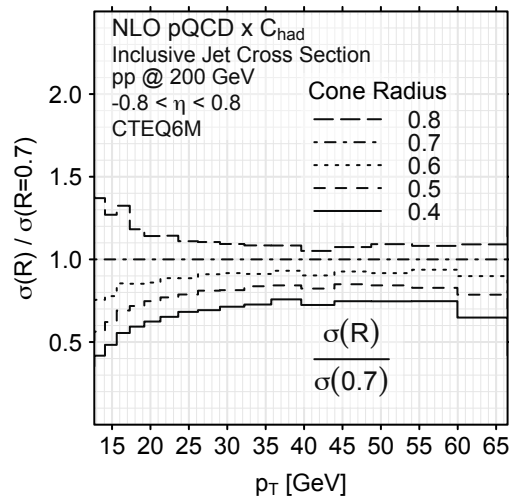
Figure 9-11: The cone radius dependence of the inclusive jet cross section in the NLO pQCD calculations with the hadronization and the underlying event correction.

Data-theory Comparison

At the cone radius 0.4, the data is about 30% smaller than the NLO calculation over the entire p_T range (Figure 9-12 (left)). As the cone radius increases, the data increases faster than the theory calculation, especially at low p_T. The data-theory agreement improves when the hadronization and the underlying event corrections are applied (Figure 9-12 (right)). The data-theory agreement is at the best when the cone radius is around 0.6.
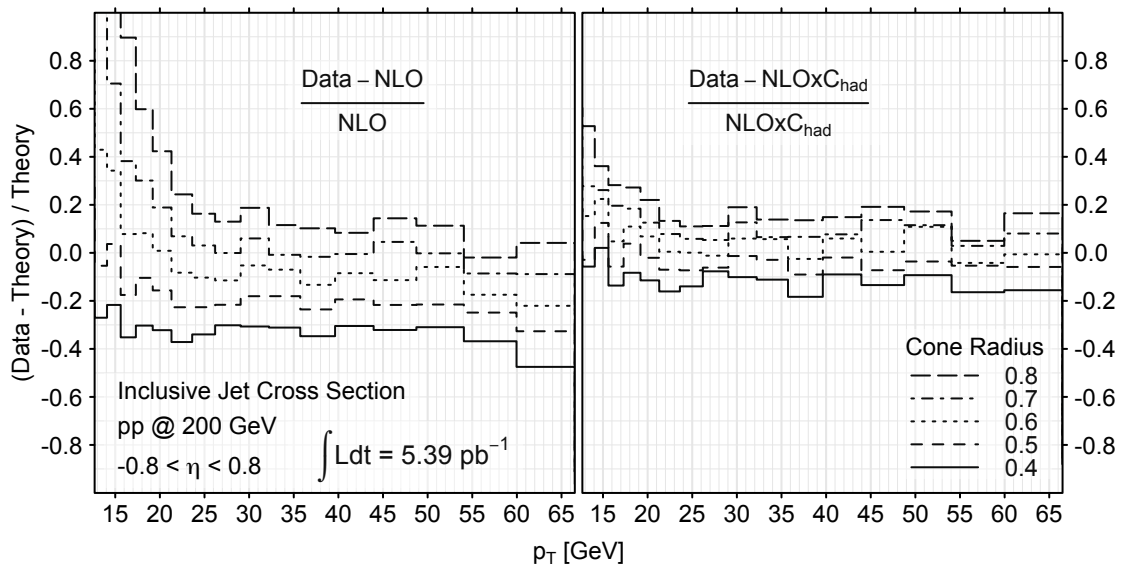
Figure 9-12: The data-theory comparison of the inclusive jet cross section at five different cone radii. (left) The comparison with the NLO pQCD calculations. (right) The comparison with the NLO pQCD calculations plus the hadronization and underlying event corrections.

9.11   Comparison with the Previous Results

The previous measurement from STAR was made with the data collected during RHIC Run-3 and Run-4 [18]. The pseudo-rapidity range of the measurement was $0.2 < \eta < 0.8$. Accordingly, the cone radius was 0.4. To compare with the previous measurement, the inclusive jet cross section in this pseudo-rapidity range with this cone radius is evaluated using the Run-6 data. Figure 9-13 shows the cross sections measured with the Run-6 data along with the previous results and the ratio between them. The size of the difference is comparable to the size of the statistical uncertainty. At the p_T above 17 GeV, the Run-6 results are systematically about 10 % smaller than the previous results.
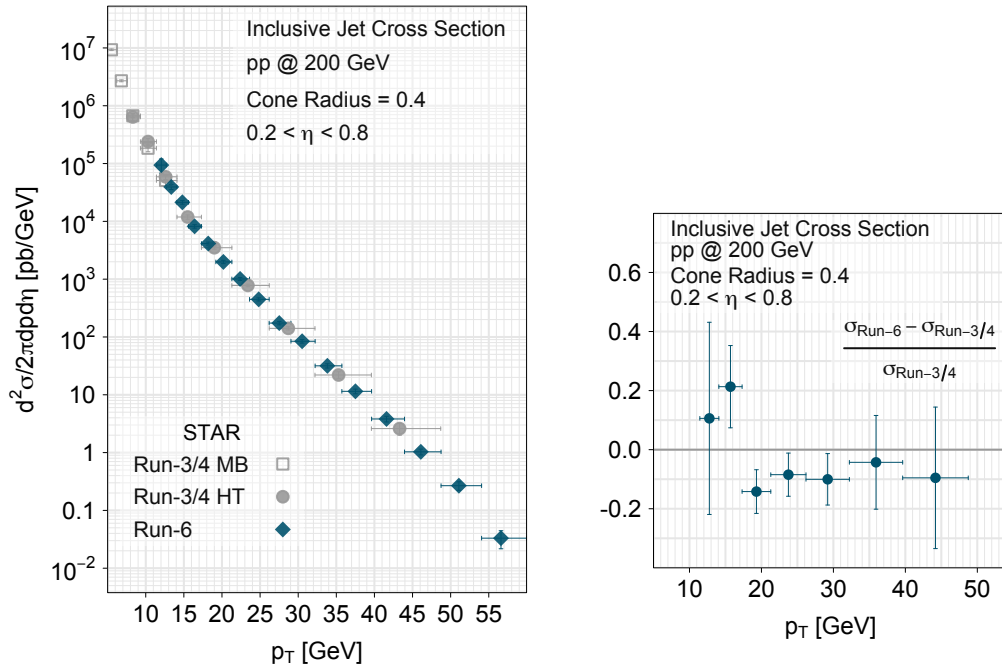
Figure 9-13: (left) The inclusive jet cross section in the pseudo-rapidity range $0.2 < \eta < 0.8$ with the cone radius 0.4 using the Run-6 data along with the previous results from the Run-3/4 data [18]. The statistical errors are shown by the vertical lines. The systematic errors are not shown. (right) The ratio between the Run-6 and Run-3/4 HT. The vertical lines indicate the statistical errors.

Part III

Dijets

Chapter 10

Dijet Definition

Section 6.1 showed that jets are defined at three different levels: the parton level, the hadron level, and the detector level. Jets can be reconstructed only at the detector level in the data, whereas, in the MC simulation, jets are reconstructed at all three levels. Chapter 6 described the parts of the jet definition common to all three levels and those specific to the detector-level jets. In Section 7.2, the jet definition specific to the hadron-level jets and the parton-level jets in the MC simulation was described.

This chapter defines dijets. Like jets, dijets are defined at the three levels; dijets are reconstructed only at the detector level in the data and at all three levels in the MC simulation.

10.1   Dijet Reconstruction

At most a single pair of jets per event is defined as a dijet. Dijets are defined as the two leading-p_T jets of events. However, this definition does not uniquely define dijets in events which contain three or more jets. As in Chapter 6 and Section 7.2, jet reconstruction involves several selections after jets are defined by a jet-finding algorithm. Which pair of jets is defined as a dijet depend on the order of the operations of the jet selections and the dijet definition. For example, suppose an event contains three jets: jet A, jet B, and jet C in descending order of p_T before any selection is applied, and jet A and jet C meet the condition of a selection but jet B does not. If the selection is applied before a dijet is defined, jet A and jet C become a dijet. However, if a dijet is

defined first, the pair of jet A and jet B is the candidate for a dijet, but the selection rejects jet B, as a result, no dijet is defined in the event. Therefore, it is necessary to specify the order of the operations in order to define dijets unambiguously.

10.1.1   Detector Level

In the definition of the detector-level jets in Chapter 6, the selections which are described from Section 6.4 to Section 6.7 are applied in the order of the sections. After the neutral energy ratio cut in Section 6.5 is applied, two leading p_T jets are selected as dijets. If neither one of the two jets is a trigger jet, which is defined in Section 6.6, no dijet is defined in the event. In other words, dijets are required to contain at least one trigger jet.

10.1.2   Hadron Level and Parton Level

At the hadron level and the parton level, as described in Section 7.3 and Section 7.4, only the jet η cut is applied after jets are reconstructed. Two leading p_T jets are selected before this cut is applied.

10.1.3   Definitions of Jet 3 and Jet 4

Jets in a dijet system are numbered for convenience of reference. As the numbers 1 and 2 are reserved for two incoming protons, the numbers 3 and 4 are used to refer outgoing jets. Of the two jets of a dijet system, the jet with larger η is defined as *jet 3*, and the jet with smaller η is defined as *jet 4*:

$$\eta_4 \leq \eta_3.$$

In other words, jet 3 is in the west side, and jet 4 is in the east side.

Jet 3   The jet in a dijet system with larger η.

Jet 4   The jet in a dijet system with smaller η.

10.1.4   Definitions of Same Side Jets and Away Side Jets

A detector-level dijet contains at least one trigger jet. If only one jet is a trigger jet, the jet is called the *same side jet*. If both jets are trigger jets, the jet that triggered with higher E_T is the same side jet. The other jet is called the *away side jet*. These names are relevant for only at the detector level.

The definition of dijets and the definitions of same side jets and away side jets have several consequences. If an event triggered both a BHT2 event and a BJP1 event and is a dijet event for the both triggers, the same pair of jets are always the dijet for both triggers. It is not possible that different two jets are selected as a dijet for different triggers. However, it is possible that the same side jet and the away side jet are flipped for the two triggers. It is possible that an event caused the both triggers, and the event is a dijet event for one trigger but not for the other.

Same side jet   The jet in a dijet system which is a trigger jet. If both jets are
trigger jets, the jet that caused trigger with higher E_T.

Away side jet   The jet in a dijet system which is not the same side jet.

10.1.5   Definition of Dijet Four-momenta

Four-momenta of dijets are defined as the four-vector sum of the two jets:

$$p^{\text{dijet}} = p_3 + p_4.$$

This definition is common to all three jet levels. In this definition, the dijet invariant mass is:

$$M = \sqrt{m_3^2 + m_4^2 + 2\sqrt{m_3^2 + p_{T3}^2}\sqrt{m_4^2 + p_{T4}^2}\cosh(\eta_3 - \eta_4) - 2p_{T3}p_{T4}\cos(\varphi_3 - \varphi_4)}.$$

If jet mass is ignored:

$$M = \sqrt{2p_{T3}^2 p_{T4}^2 (\cosh(\eta_3 - \eta_4) - \cos(\varphi_3 - \varphi_4))}.$$

10.2 Phase Space

Section 6.7 specified the phase space of the inclusive jet measurement. This section specifies a phase space of the dijet measurement. A relevant phase space is the one in which dijet production can be both experimentally measured and theoretically predicted. Table 10.1 gives the phase space of the dijet measurement.

The p_T cuts are asymmetric because a NLO pQCD calculation has little prediction power of dijets cross section and $\mathcal{A}_\mathrm{LL}$ with symmetric p_T cuts. The η cuts are applied for the detector acceptance. The $|\eta_3 - \eta_4|$ cut is necessary for both jets to be in the acceptance at the same time. The $\Delta\varphi$ cut is applied to select back-to-back dijet events.

10.3 p_T Balance (Detector Level)

Dijets with balanced p_T are selected,

$$0.73 \le \frac{p_\mathrm{T}^\mathrm{away}}{p_\mathrm{T}^\mathrm{same}} \le 1.1.$$

p_T-balanced dijets are more likely to carry momentum closer to that of parton level than do unbalanced jets. Figure 10-1 and Figure 10-2 show level plots of the dijet p_T balance and the selection.

In QCD hard collisions, the sum of p_T of outgoing partons are zero if transverse momenta of initial states are ignored. In QCD NLO calculation, if all outgoing partons from the hard collisions, the number of which is at most three, are included in a dijet system, this dijet has balanced p_T. The hadron level jets moderately lose

$\max(p_\mathrm{T}) > 10.0\,\mathrm{GeV}$
$\min(p_\mathrm{T}) > 7.0\,\mathrm{GeV}$
$-0.8 < \eta < 0.8$
$|\eta_3 - \eta_4| < 1.0$
$|\Delta\varphi| > 2.0$

Table 10.1: Phase space of the dijet measurement

the balance due to soft effects such as underlying events and momentum outside the cone radius. If p_T of a reconstructed dijet system is not balanced, this dijet is likely to have lost much parton-level kinematic information or not the dijet system which corresponds to the parton-level dijets.
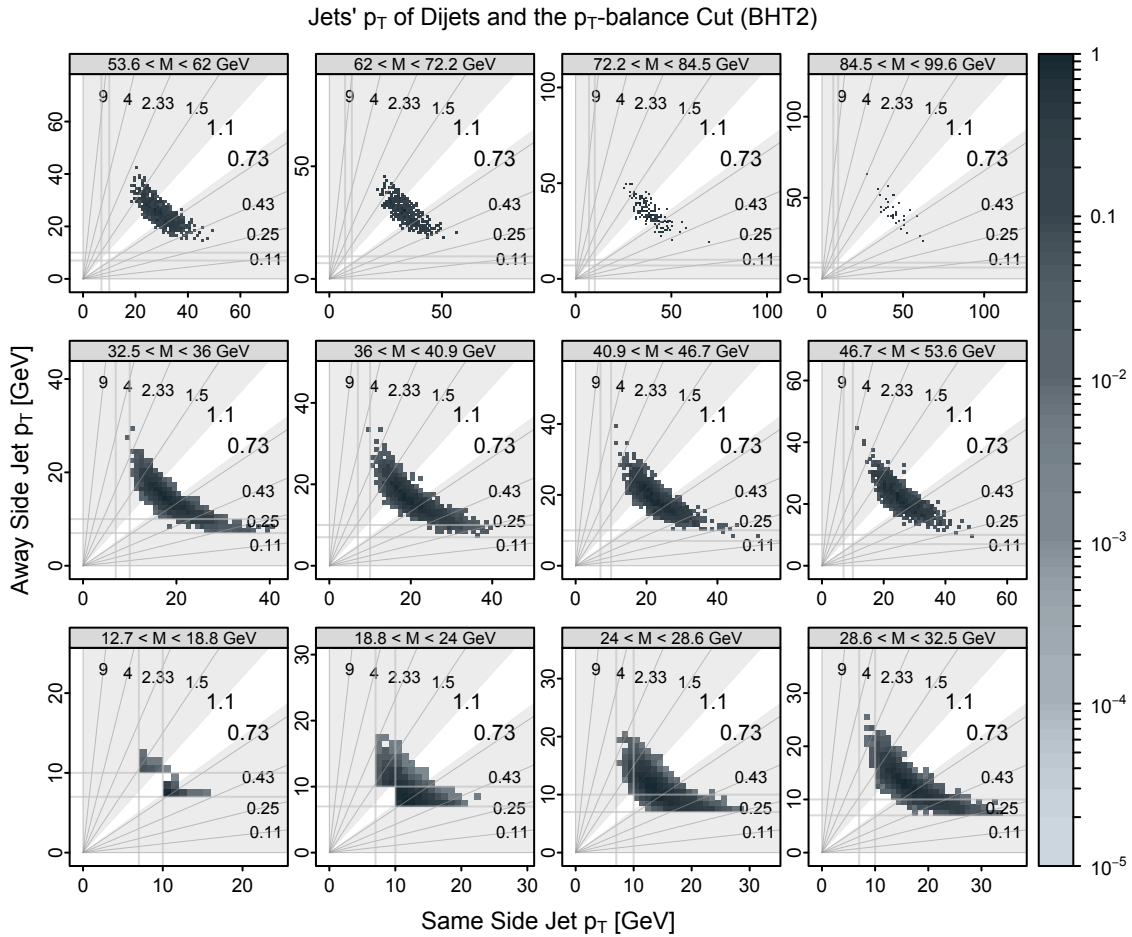
Figure 10-1: Level plots of same side jet p_T distributions and away side jet p_T distributions in sixteen different dijet mass ranges for the BHT2 events. The shaded area indicates the p_T-balance cut.
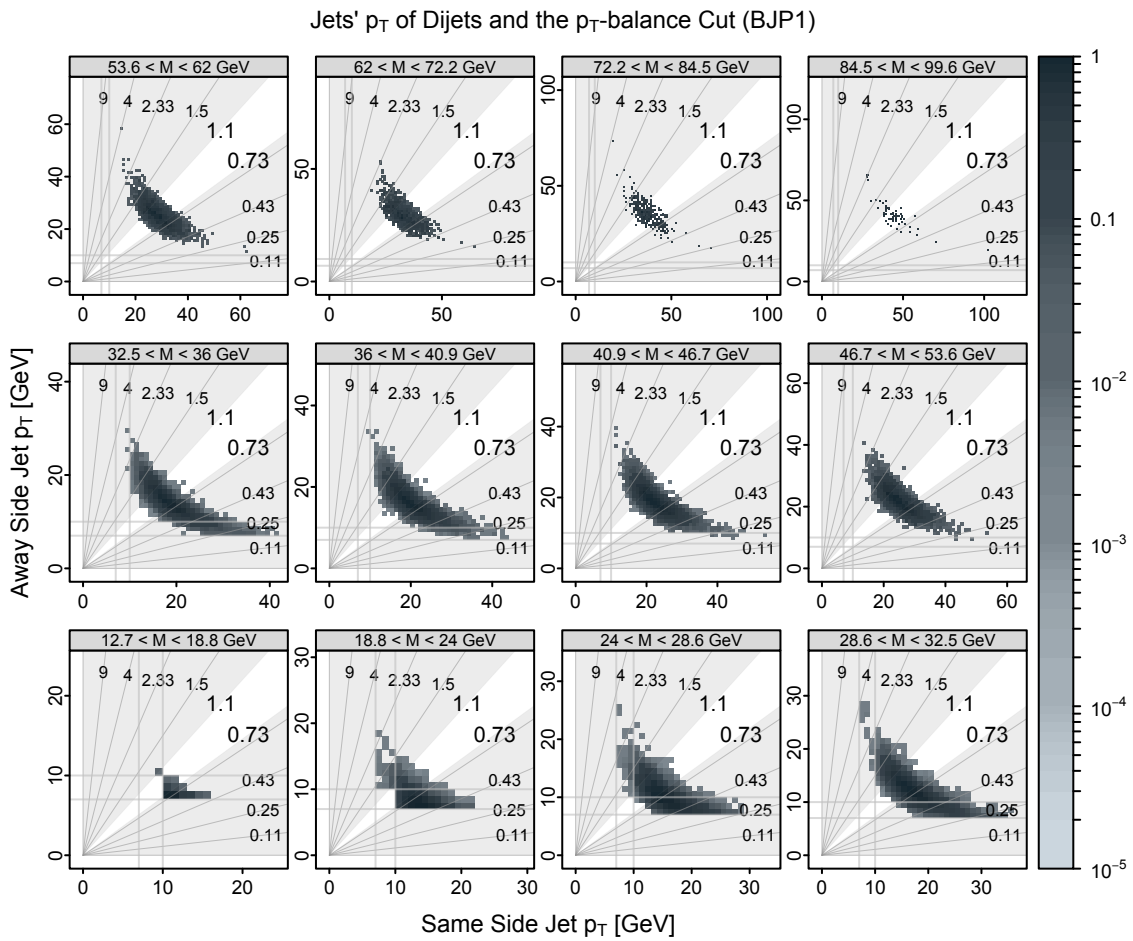
Figure 10-2: Level plots of same side jet p_T distributions and away side jet p_T distributions in sixteen different dijet mass ranges for the BJP1 events. The shaded area indicates the p_T-balance cut.

10.4 Dijet Yields

Table 10.2 gives the reconstructed dijet yields in each timebin set for each trigger.

M_{jj} [GeV]	BJP1				BHT2			
	Timebin 8	78	789	6789	8	78	789	6789
12.70-18.80	0	1	1	2	39	87	109	137
18.80-24.00	248	493	606	723	1149	2347	2907	3514
24.00-28.60	1109	2230	2712	3252	1209	2442	3045	3714
28.60-32.50	1280	2620	3259	3976	831	1644	2059	2544
32.50-36.00	1123	2276	2875	3492	603	1216	1516	1830
36.00-40.90	1358	2754	3444	4164	589	1193	1506	1831
40.90-46.70	1179	2376	3028	3707	430	933	1178	1441
46.70-53.60	901	1733	2230	2721	344	653	829	1029
53.60-62.00	579	1109	1422	1717	232	432	557	687
62.00-72.20	250	526	684	841	113	228	284	347
72.20-84.50	94	212	270	330	44	101	134	167
84.50-99.60	34	51	63	79	21	29	40	50

Table 10.2: The reconstructed dijet yield in each M_{jj} bins and timebin set for each trigger.
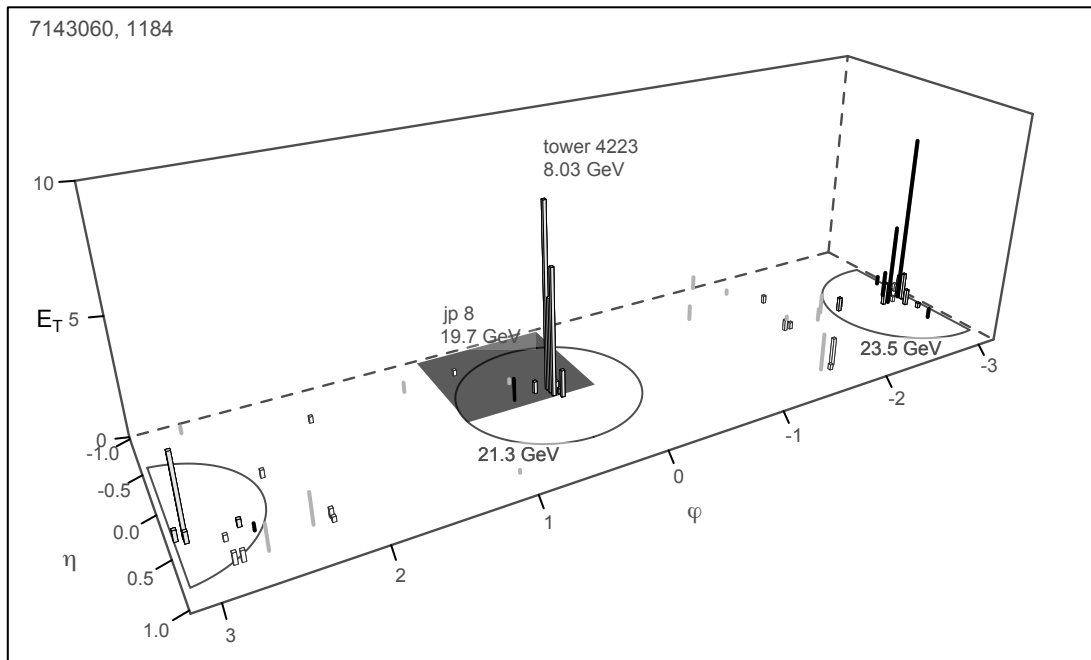
Figure 10-3: An example of dijet events. This event triggered both a BJP1 event and a BHT2 event. The shaded area indicates the location of the triggered jet patch. The tower 4223 is triggered with $E_\mathrm{T} = 8.03$ GeV. The two circles are the radius of the reconstructed jets. In this dijet event, the same side jet is the same jet for both triggers; the away side jet is track dominated. The away side jet is jet 3, and the same side jet is jet 4. The away side jet has higher p_T than the same side jet.
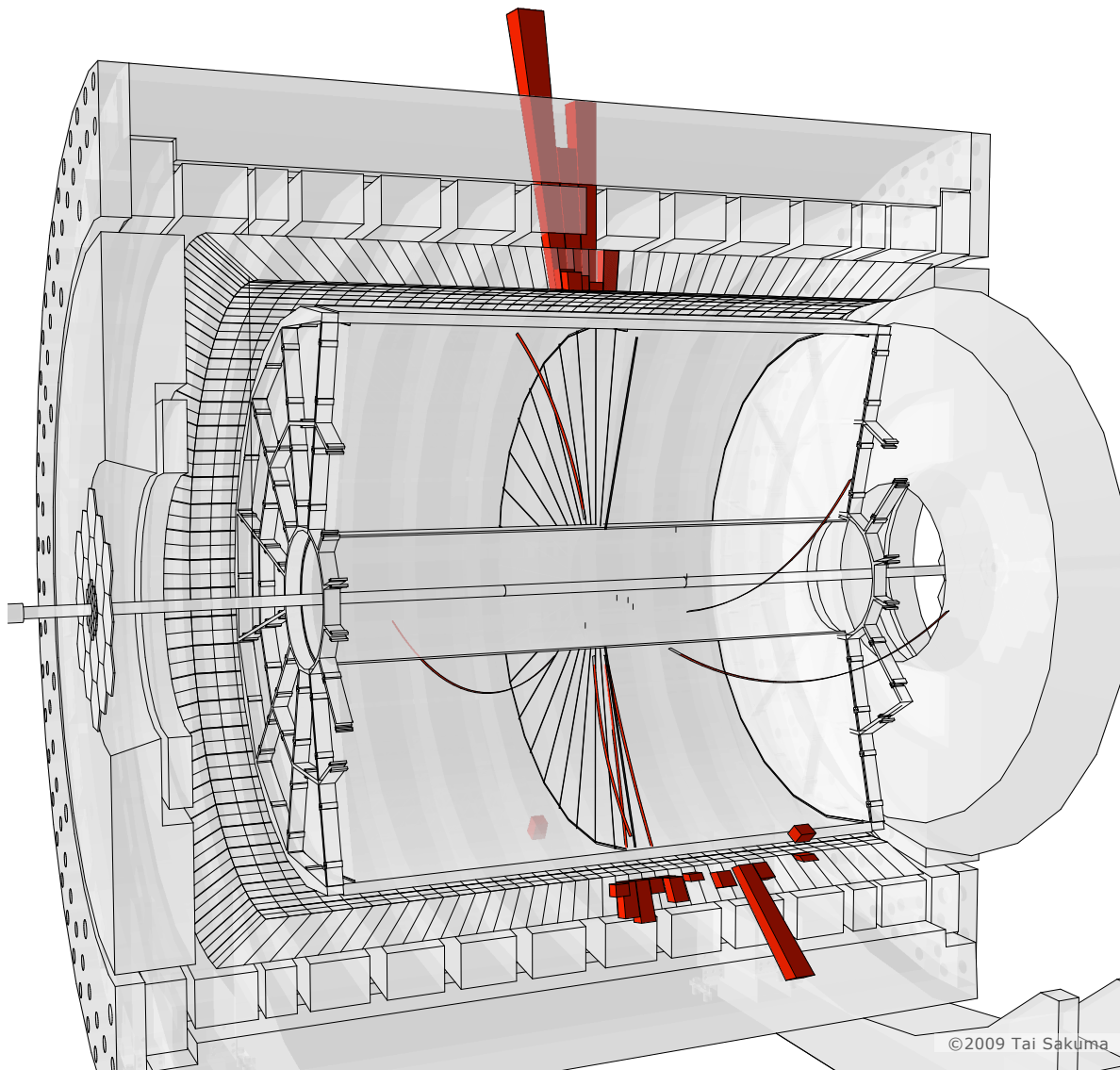
Figure 10-4: An example of dijet events.

Chapter 11

Data - MC Comparison of Dijets

Chapter 8 compared the inclusive jets in the data and the MC simulation. It was found that overall the MC simulation well reproduced the inclusive jets in the data except some minor discrepancies. The agreement was better for the BJP1 than for the BHT2.

This chapter compares dijets in the data and the MC simulation. As the data-MC agreement of the inclusive jets is a premise of the inclusive jet cross section measurement, the data-MC agreement of the dijets is a premise of the dijet cross section measurement.

Before comparing the properties of dijets, jet multiplicities are compared as a connection between inclusive jets and dijets. The vertex correction factors of the MC events are re-calculated with the dijet events. After properties of the away side jets and the same side jets are compared, kinematic variables of dijets are compared.

11.1   Jet Multiplicity

A jet multiplicity is the number of jets in an event. The jet multiplicity distribution is measured as a function of the trigger jet p_T, which implies an event needs to contain at least one trigger jet. Other jets do not have to be trigger jets but need to satisfy the criteria of the selections based on the detector η and the neutral energy ratio described in section 6.4 and section 6.5, respectively. The jet multiplicity is a variable that relates the inclusive jets and the dijet events.

Figure 11-1 and Figure 11-2 show the jet multiplicities as a function of trigger jet p_T in the data and the MC simulation, respectively. The data and the MC events have similar tendency. Most events are either mono-jet events or two-jet events; the fraction of two-jet events increase with trigger jet p_T. There are small fraction of three-jet events.
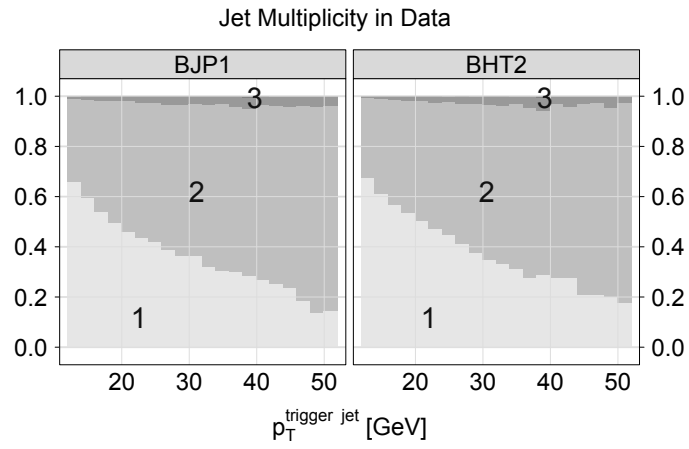
Figure 11-1: Jet multiplicity as a function of trigger jet p_T in the data.
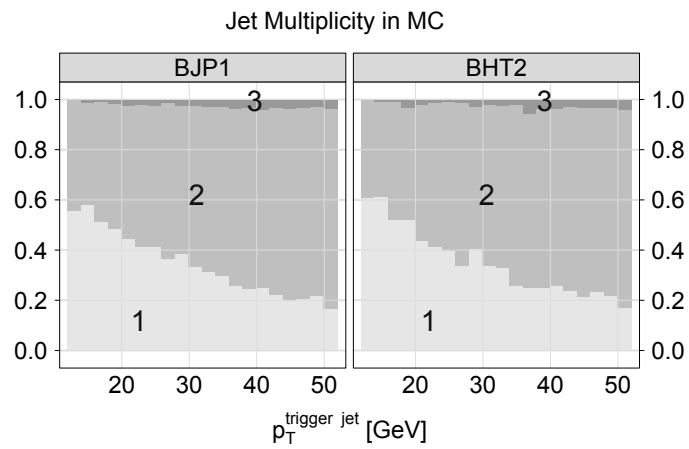
Figure 11-2: Jet multiplicity as a function of trigger jet p_T in the MC simulation.

11.2   Vertex Corrections of the MC events

In Section 7.6, the MC events are re-weighted so that the jet events in the data and the jet events in the MC simulation have the same vertex distributions for each timebin selection. Vertex correction factors are re-calculated so that the dijet events in the data and the dijet events in the MC simulation have the same vertex distributions. The vertex correction factors for the dijet events (Figure 11-3) are nearly identical to those for the inclusive jet events (Figure 7-6). Figure 11-4 and Figure 11-5 demonstrate that with the vertex corrections the data and the MC events have approximately the same vertex distributions.
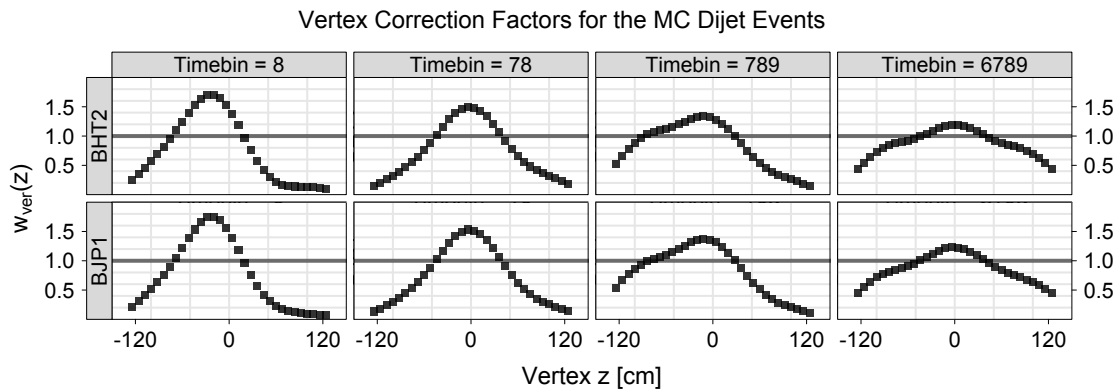
Figure 11-3: The vertex correction factors for the dijet events for each timebin set and trigger.

The Vertex Distributions of the BHT2 dijet events in Data and MC (w/ correction)
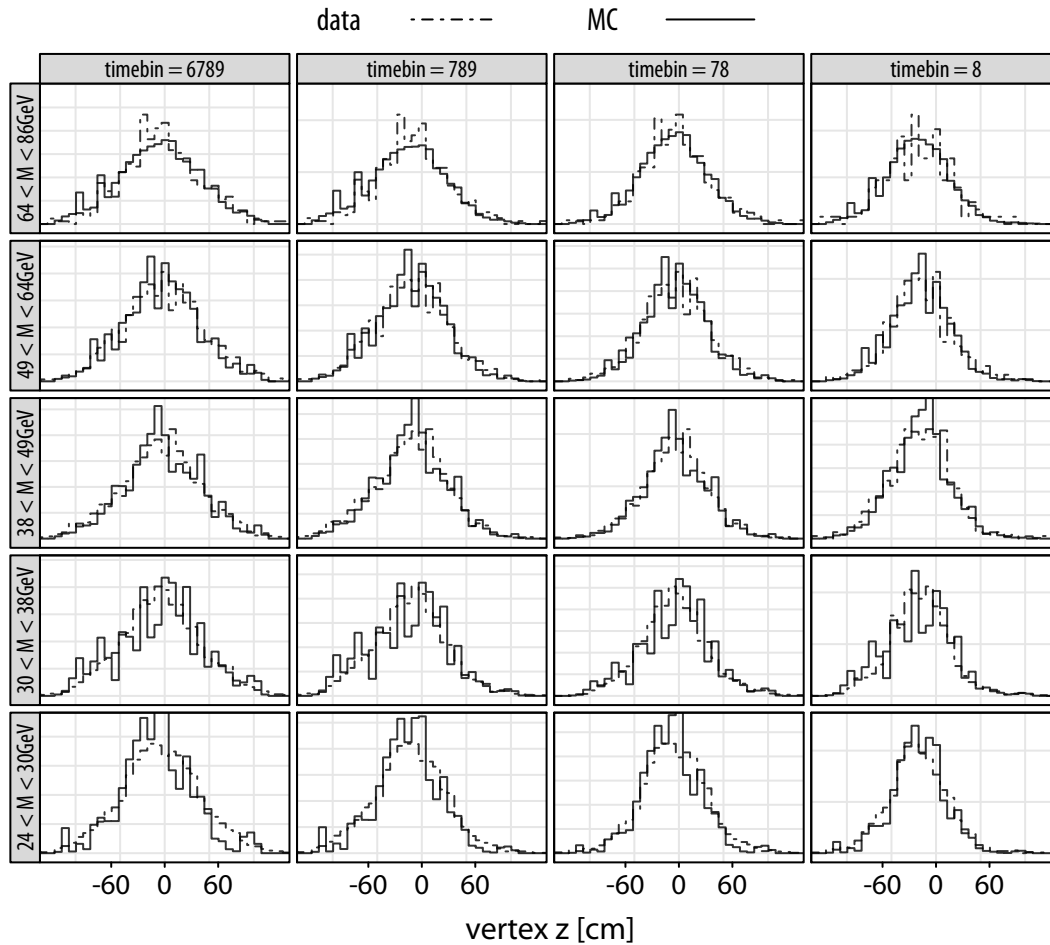
Figure 11-4: The vertex distributions of the BHT2 dijet events in the data and the vertex-corrected MC events.

The Vertex Distributions of the BJP1 dijet events in Data and MC (w/ correction)
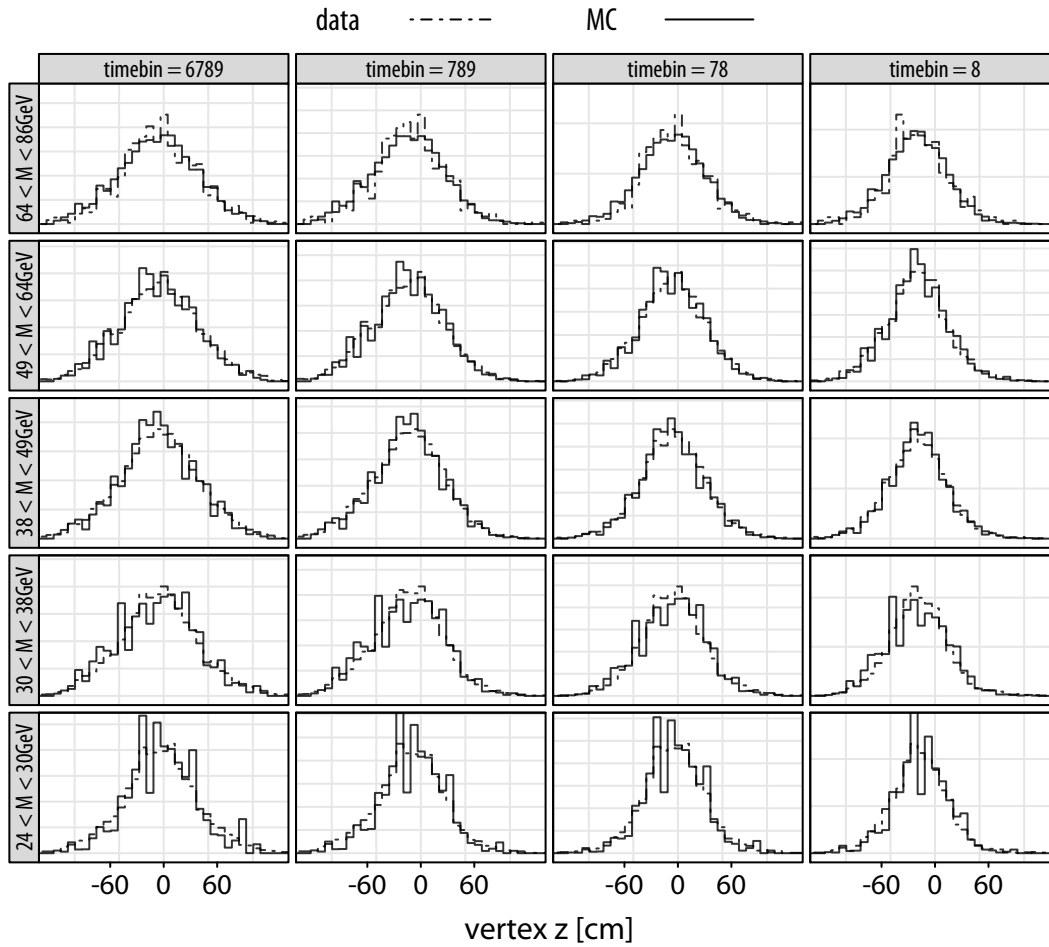
Figure 11-5: The vertex distributions of the BJP1 dijet events in the data and the vertex-corrected MC events.

11.3 Away Side Jets

As defined in Section 10.1, the away side jets do not have to be trigger jets. Therefore, the away side jets are not a subset of the jets which are compared in Chapter 8, nor a subset of the jets used in the inclusive jet cross section measurement in Chapter 9. The transverse momenta p_T and the neutral energy ratios R_T of the away side jets are compared.

11.3.1 Transverse Momentum p_T

Figure 11-6 shows the p_T distributions of the away side jets. The BHT2 events and the BJP1 events have quite different p_T dependence. This differs from the p_T distribution of the inclusive jets in Figure 8-1, in which both trigger events have similar p_T dependence. In the p_T distribution of the inclusive jets in Figure 8-1, after the peak, the rate at which the distribution decreases becomes smoothly faster. In contrast, in the p_T distribution of the away side jets in Figure 11-6, the way in which the distribution decreases appear to be more involved.

The p_T distribution can be seen as the sum of two distributions. The two distributions are for the away side jets with p_T larger than the p_T of the same side jets and those with smaller p_T. The asymmetric p_T cut, discussed in Section 10.2, causes these two samples to have different p_T distributions. The peak of the higher distribution is around 19 GeV. This peak is evident for the BJP1 events and subtle for the BHT2 events. The lower peak is around 13 GeV for the BJP1 events and around 10 GeV or below for the BHT2 trigger.

Figure 11-7 shows the ratios (data-MC)/MC. The agreement is better for the BJP1 events (10% - 20%) than for the BHT2 events (30% - 40%). One point around 19 GeV, which is the location of the second peak, sticks out toward the MC simulation for all timebin sets, in particular, for the BHT2 trigger. This indicates that the two distributions are better distinguished in the MC simulation than in the data.
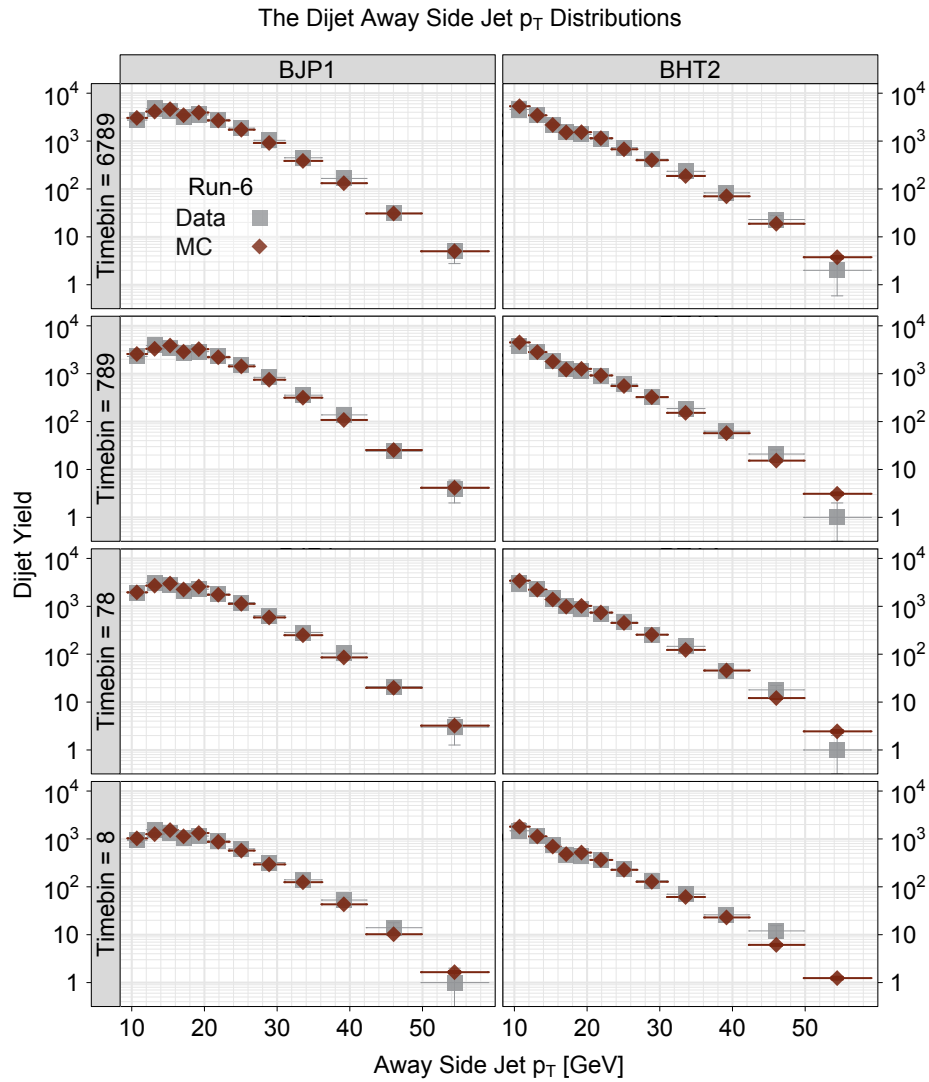
Figure 11-6: The p_T distributions of the away side jet yield of the dijets for each timebin set and each trigger. In each panel separately, the MC distributions are normalized so that the total yields at p_T above 12 GeV are the same as the jet yields in the data.

The Data-MC Comparison of the Dijet Away Side Jet p_T Distributions
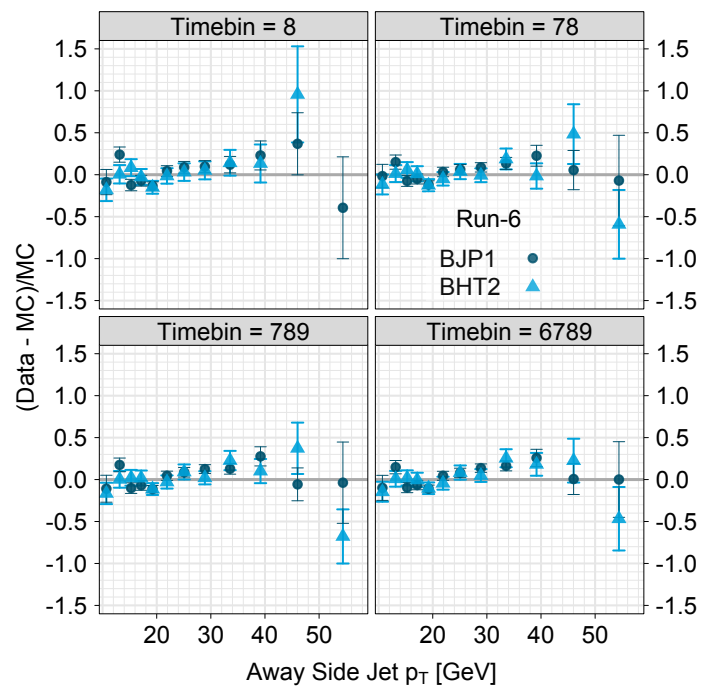
Figure 11-7: The data-MC comparisons of the away side jet p_T distributions for each timebin set and each trigger. The MC events are scaled in the same way as described in Figure 11-6.

11.3.2   Neutral Energy Ratio R_T

The neutral energy ratio R_T is defined in Section 6.5. Figure 11-8 shows the R_T distributions of the away side jets in the data and the MC events. As discussed in Section 7.3, since the away side jets are little trigger biased, the peak is around one third independent of energy. The BJP1 events are in better agreement than in the BHT2 events.
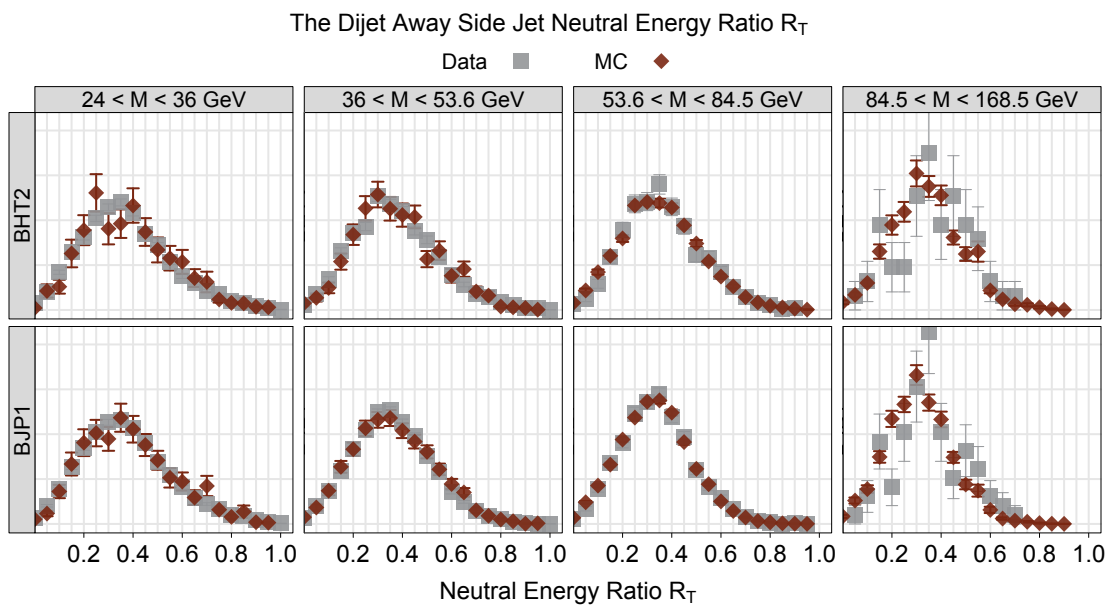
Figure 11-8: The data-MC comparison of the neutral energy ratio of the away side jets of the dijets in three different M_{jj} bins and for each trigger for the timebin set 6789. The distributions are separately normalized in each panel.

11.4 Same Side Jets

Same side jets are defined in Section 10.1. The same side jets are a subset of the jets used in the inclusive jet cross section measurement and a subset of the jets which are compared in Chapter 8.

11.4.1 Transverse Momentum p_T

Figure 11-9 shows the p_T distributions of the same side jets in the data and the MC events. Like the p_T distributions of the away side jets, the p_T distributions are the sum of the two distributions. The contribution from the higher-p_T distributions are larger for the same side jets than for the away side jets because the same side jets are more likely to have larger-p_T than the away side jets. Figure 11-10 shows the ratios. The agreement are better than for the away side jets.
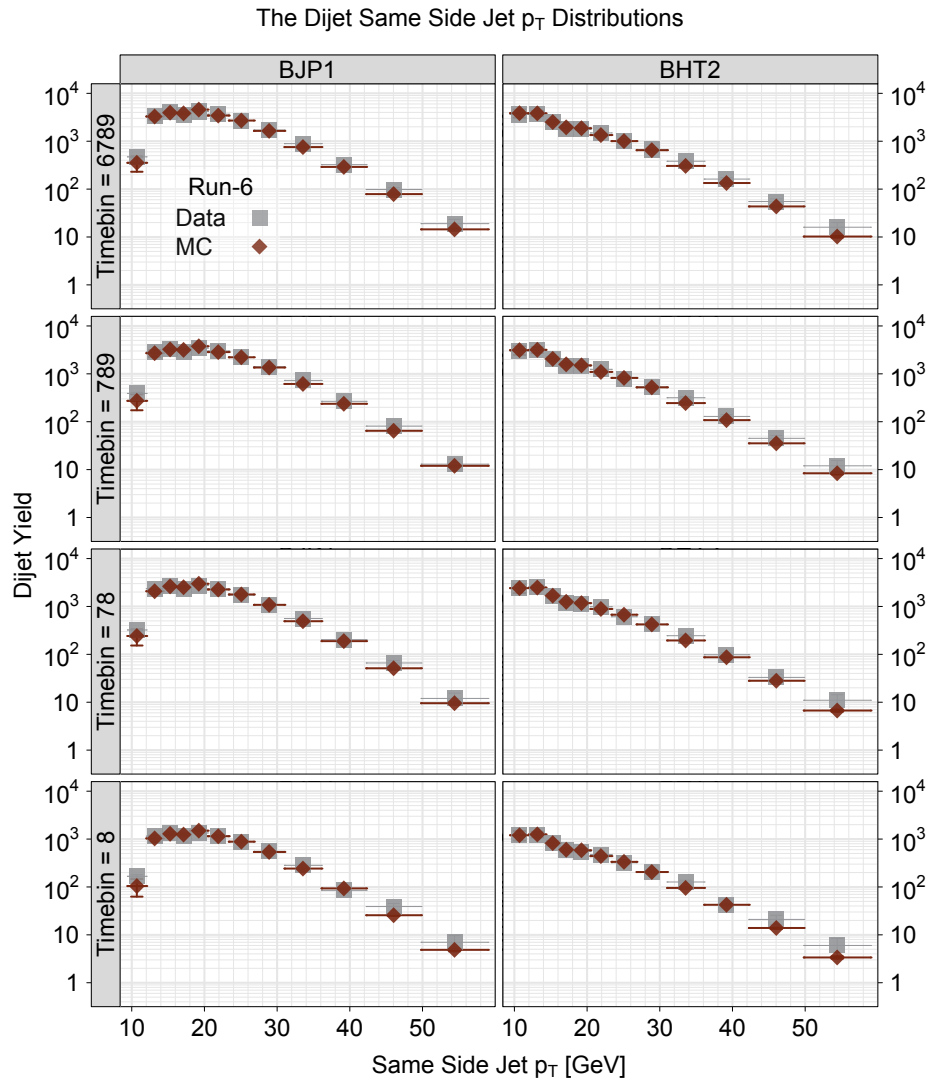
Figure 11-9: The p_T distributions of the same side jet yield of the dijets for each timebin set and each trigger. In each panel separately, the MC distributions are normalized so that the total yields at p_T above 12 GeV are the same as the jet yields in the data.
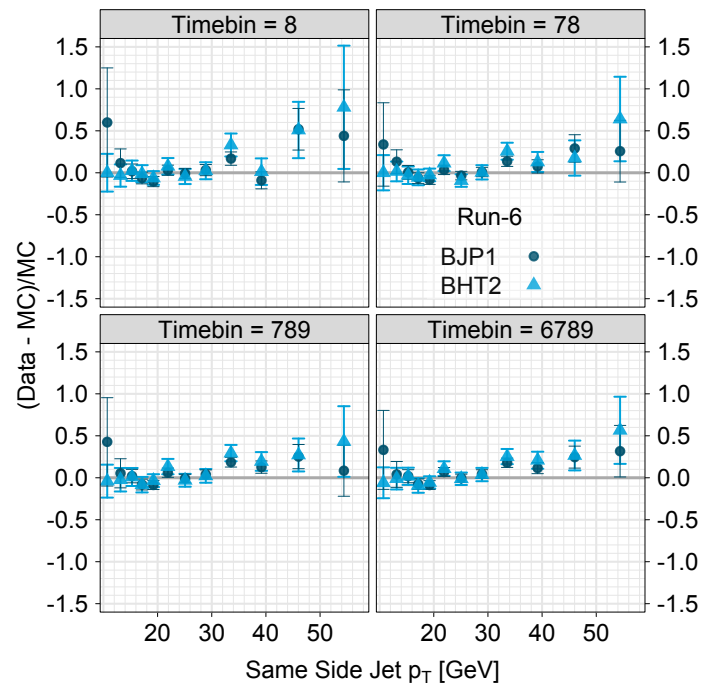
Figure 11-10: The data-MC comparisons of the same side jet p_T distributions for each timebin set and each trigger. The MC events are scaled in the same way as described in Figure 11-9

11.4.2   Neutral Energy Ratio R_T

Figure 11-11 shows the data-MC comparison of the neutral energy ratio R_T of the same side jets. The data and the MC events are in agreement. The agreement is better for the BJP1 events than for the BHT2 events. The same side jets have a trigger bias. The bias is larger for the BHT2 events than for the BJP1 events.
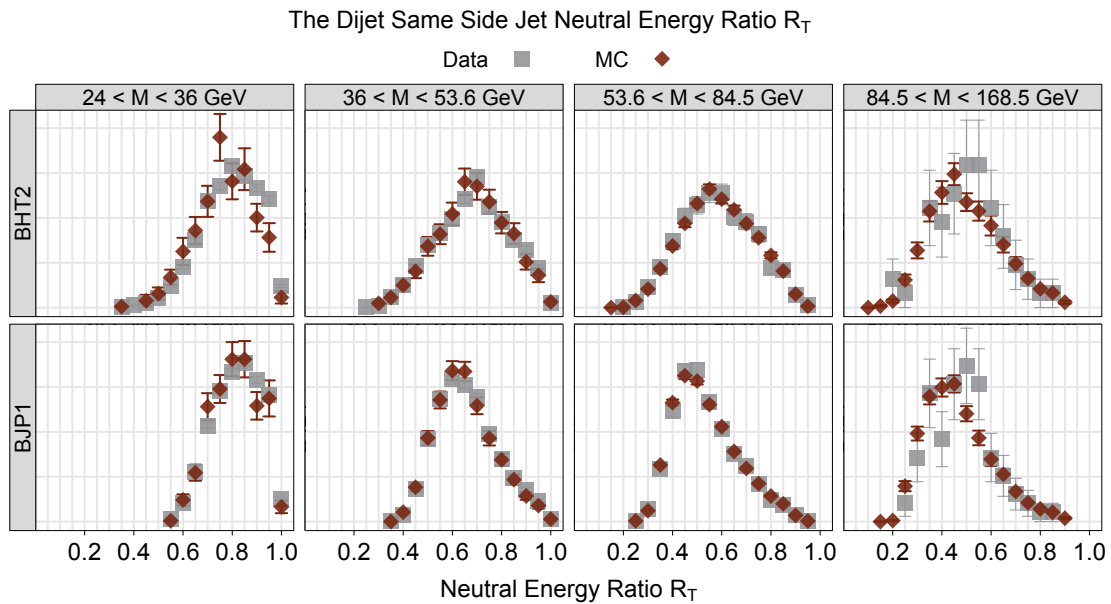
Figure 11-11: The data-MC comparison of the neutral energy ratio of the same side jets of the dijets in three different M_{jj} bins and for each trigger for the timebin set 6789. The distributions are separately normalized in each panel.

11.5 The Dijet Kinematics

This section compares dijet kinematic distributions. The distributions of the invariant mass M_{jj}, the average pseudo-rapidity $\eta = (\eta_3 + \eta_4)/2$, the pseudo-rapidity difference $\Delta\eta = \eta_3 - \eta_4$, and the angle between two jet axes $\Delta\varphi$ in the φ plane are compared.

The η, $\Delta\eta$, and $\Delta\varphi$ comparisons are carried out in three different invariant mass ranges. In these comparisons, the distributions for each trigger and each timebin set are separately normalized so that the data and the MC events have the same dijet yields. The same normalizations are used for all invariant mass ranges.

11.5.1 Invariant Mass M_{jj}

Figure 11-12 shows the distributions. The invariant mass M_{jj} is important for the data-MC comparison. The cross section is measured as a function of this variable. Like the p_T distributions of the away side jets and the same side jets, the M_{jj} distributions are the sum of two different distributions. Figure 11-13 shows the ratios. The data and the MC events are in agreement.
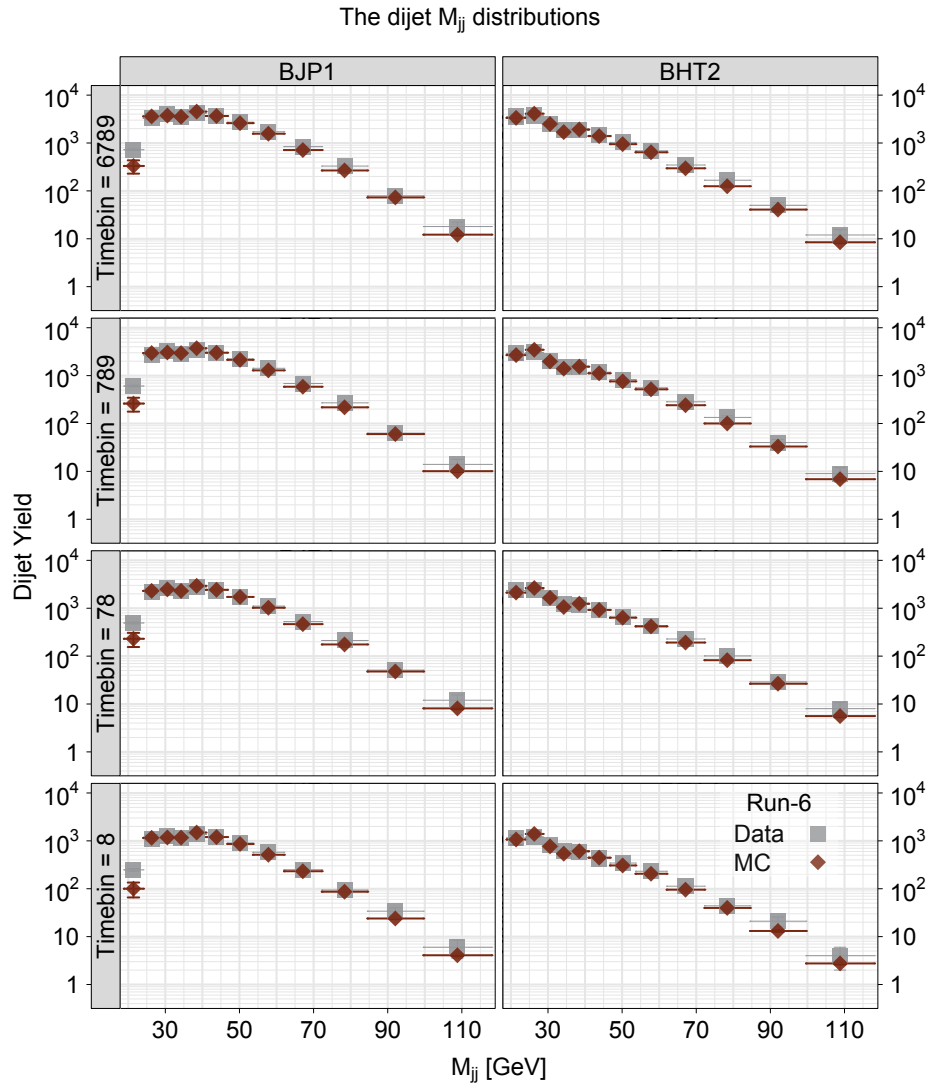
Figure 11-12: The invariant mass M_{jj} dependency of the dijet yield. The MC yields are scaled so that the yield becomes the same as the data for M_{jj} above 24 GeV.
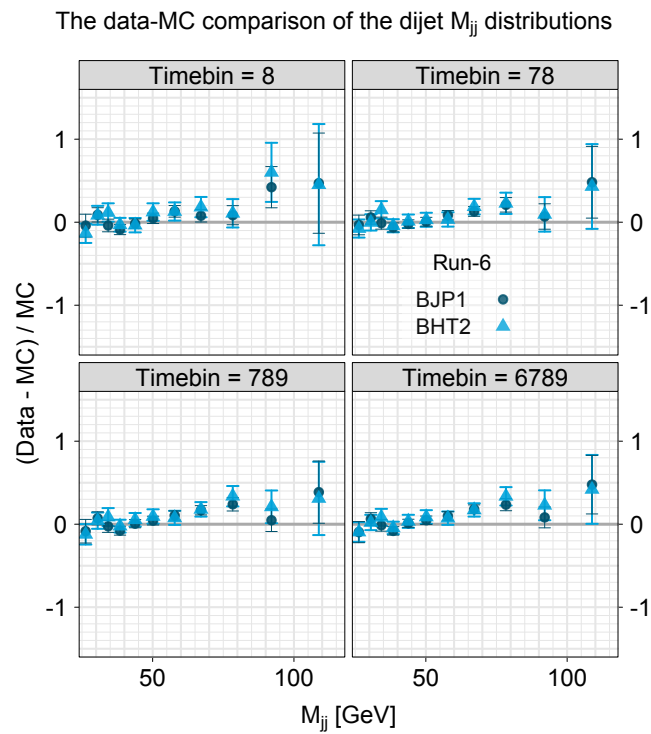
Figure 11-13: The data-MC comparison of the dijet invariant mass distributions. The MC are normalized in the way described in Figure 11-12.

11.5.2 Average Pseudo-Rapidity η

The average pseudo-rapidity η

$$\eta = \frac{1}{2}(\eta_3 + \eta_4)$$

is compared. This variable η is equal to the rapidity which boosts from the laboratory frame to the center of mass frame of the parton-level interaction and proportional to the logarithm of the ratio of x_1 and x_2:

$$\eta = \frac{1}{2}\log\frac{x_2}{x_1}.$$

Figure 11-14 shows the dijet average η distributions in the data and the MC simulation for each trigger in the three different M_{jj} ranges for the timebin set 6789. Figure 11-15 shows the ratios (Data-MC)/MC. The MC simulation well reproduces the average η dependence of the data.
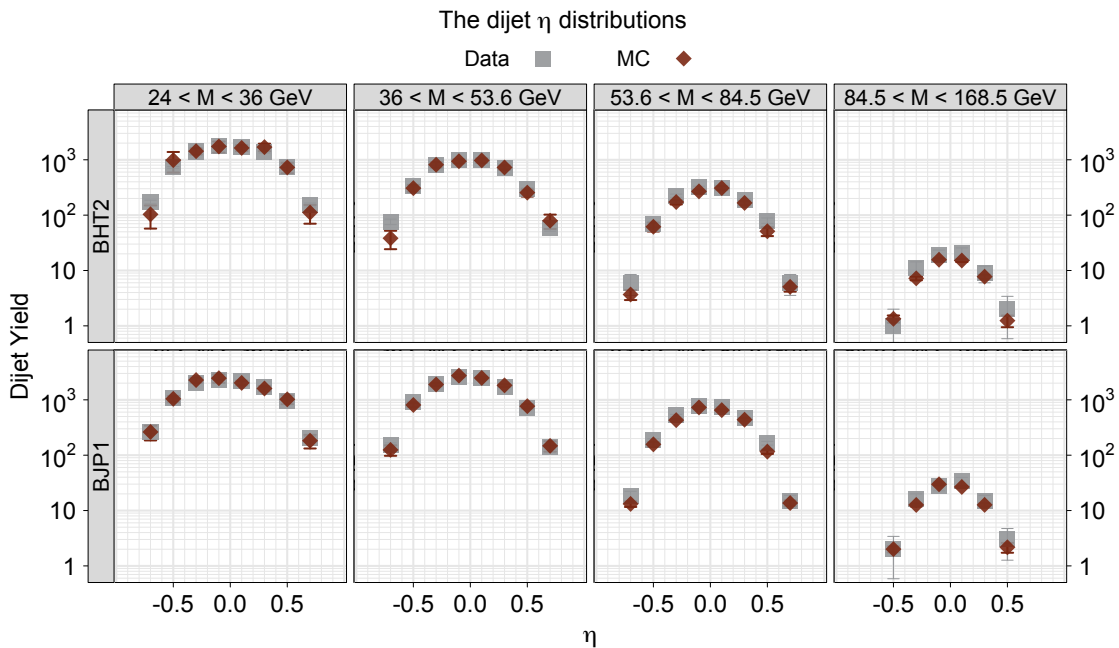
Figure 11-14: The average pseudo-rapidity η of the dijet events in the data and the MC simulation for each trigger in three different M_{jj} ranges for the timebin set 6789.
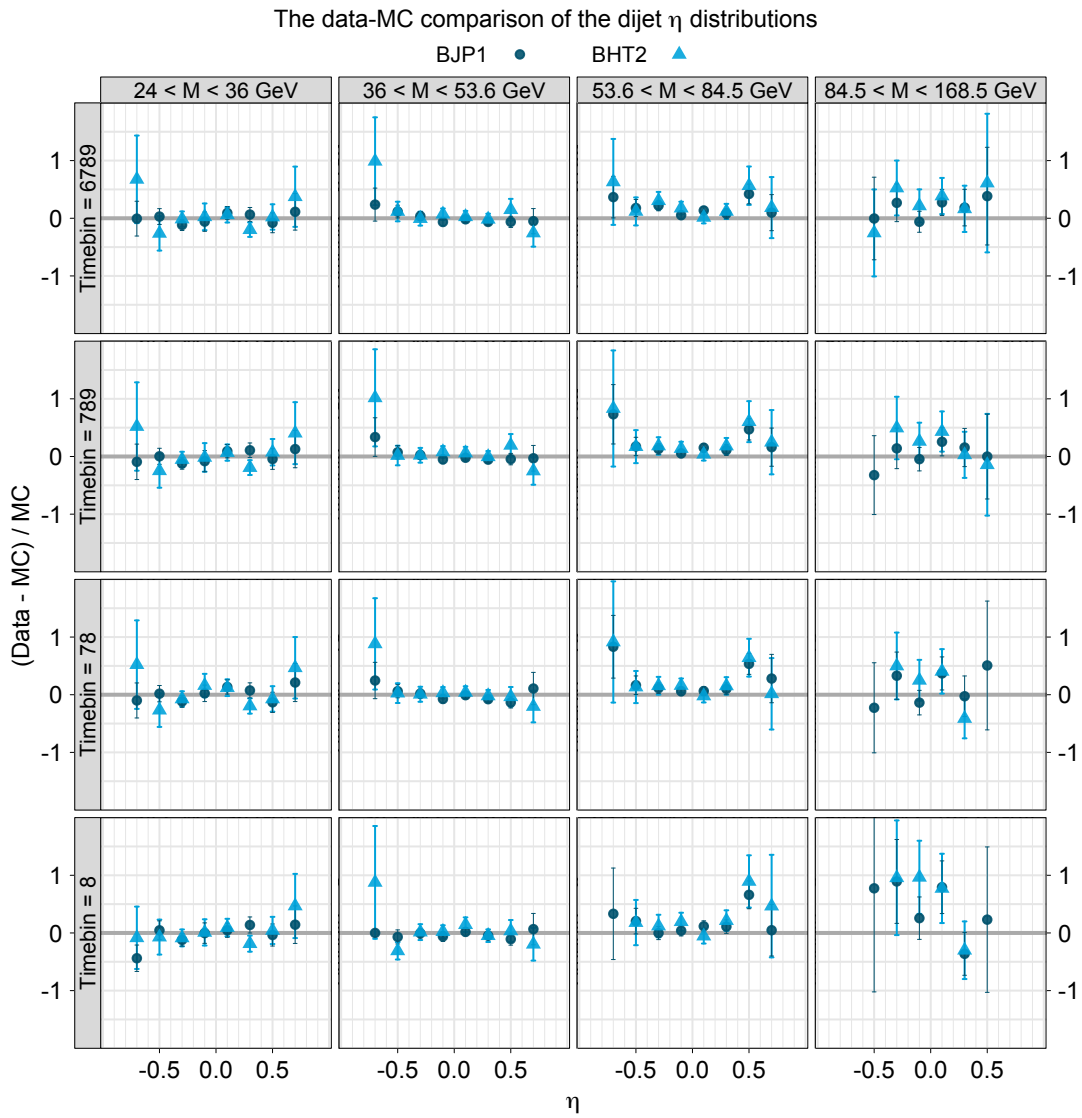
Figure 11-15: The data-MC comparison of the average pseudo-rapidity η dependence.

11.5.3   Pseudo-Rapidity Difference $\Delta\eta$

The pseudo-rapidity difference

$$\Delta\eta = \eta_3 - \eta_4$$

is compared. The pseudo-rapidity difference at the parton level is twice of the rapidity of the parton 3 in the center of mass frame of the parton-level interaction:

$$\eta_* = \frac{1}{2}(\hat{\eta}_3 - \hat{\eta}_4).$$

Figure 11-16 shows the dijet pseudo-rapidity difference $\Delta\eta$ distributions in the data and the MC simulation for each trigger in the three different M_{jj} ranges for the time-bin set 6789. Figure 11-17 shows the ratios (Data-MC)/MC. The $\Delta\eta$ cut is not applied in the figures. The data and the MC events are in agreement.
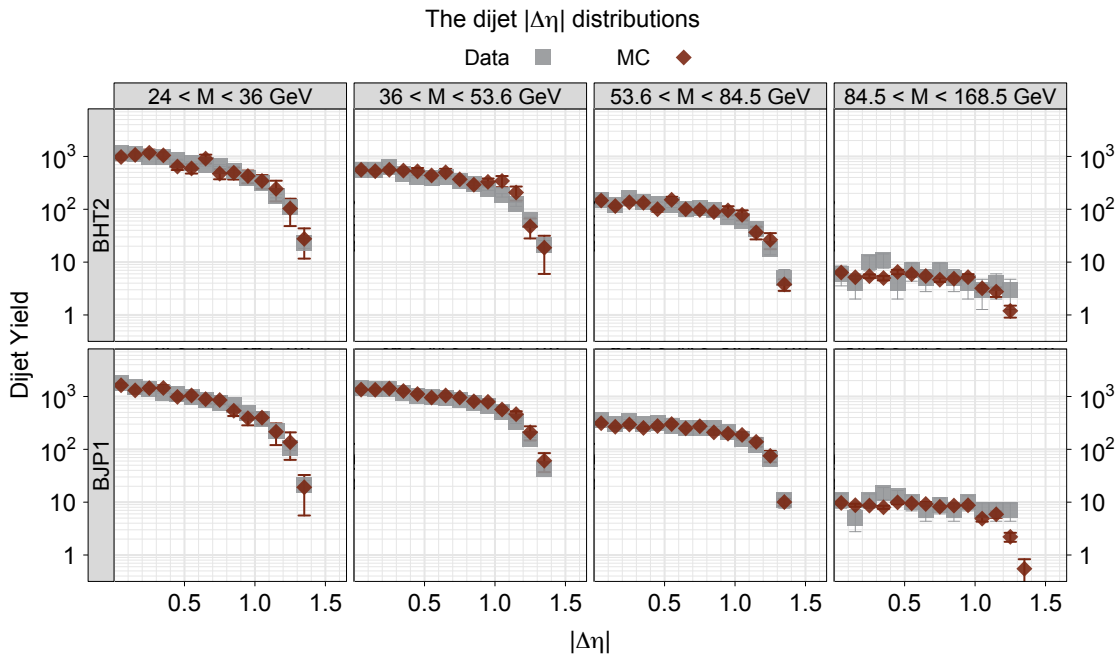
Figure 11-16: The pseudo-rapidity difference $\Delta\eta$ of the dijet events in the data and the MC simulation for each trigger in three different M_{jj} ranges for the timebin set 6789. The $\Delta\eta$ cut is not applied.
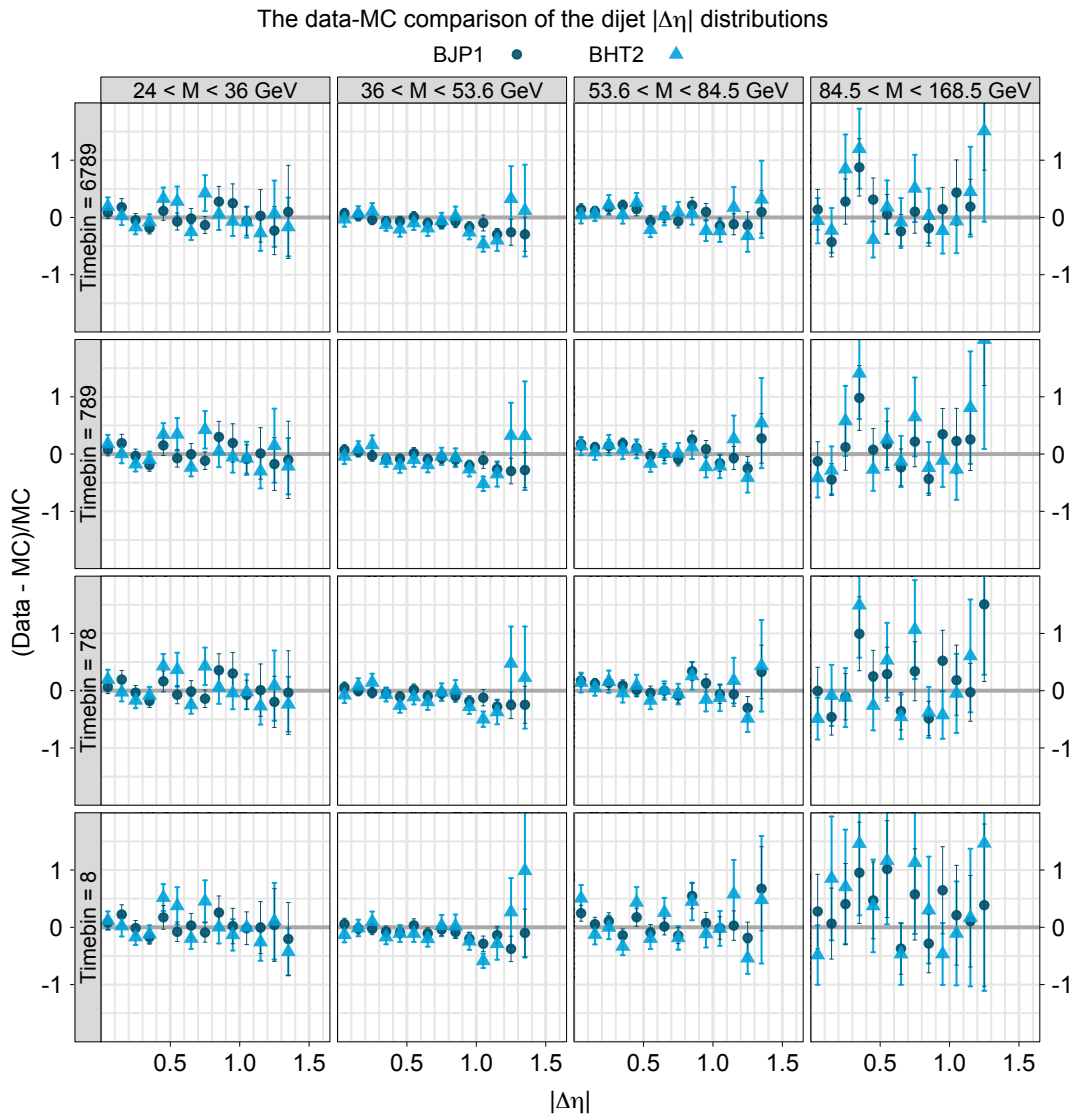
Figure 11-17: The data-MC comparison of the pseudo-rapidity difference $\Delta\eta$ dependence. The $\Delta\eta$ cut is not applied.

11.5.4   Azimuth $\Delta\varphi$

The distributions of the angles between the two jets on the φ plane is compared. Figure 11-18 shows the φ distributions in the data and the MC simulation for each trigger in the three different M_{jj} ranges for the timebin set 6789. Figure 11-19 shows the ratios (Data-MC)/MC. The agreement is not as good as the other comparisons. The dijets in the MC simulation are more back-to-back than the dijets in the data.
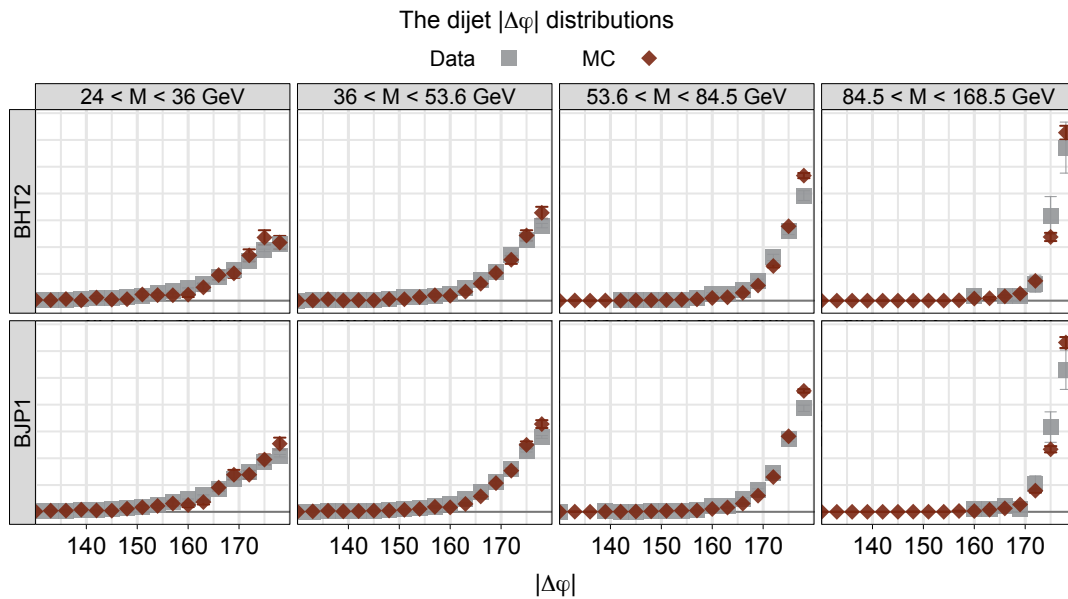
Figure 11-18: The $\Delta\varphi$ of the dijet events in the data and the MC simulation for each trigger in three different M_{jj} ranges for the timebin set 6789.
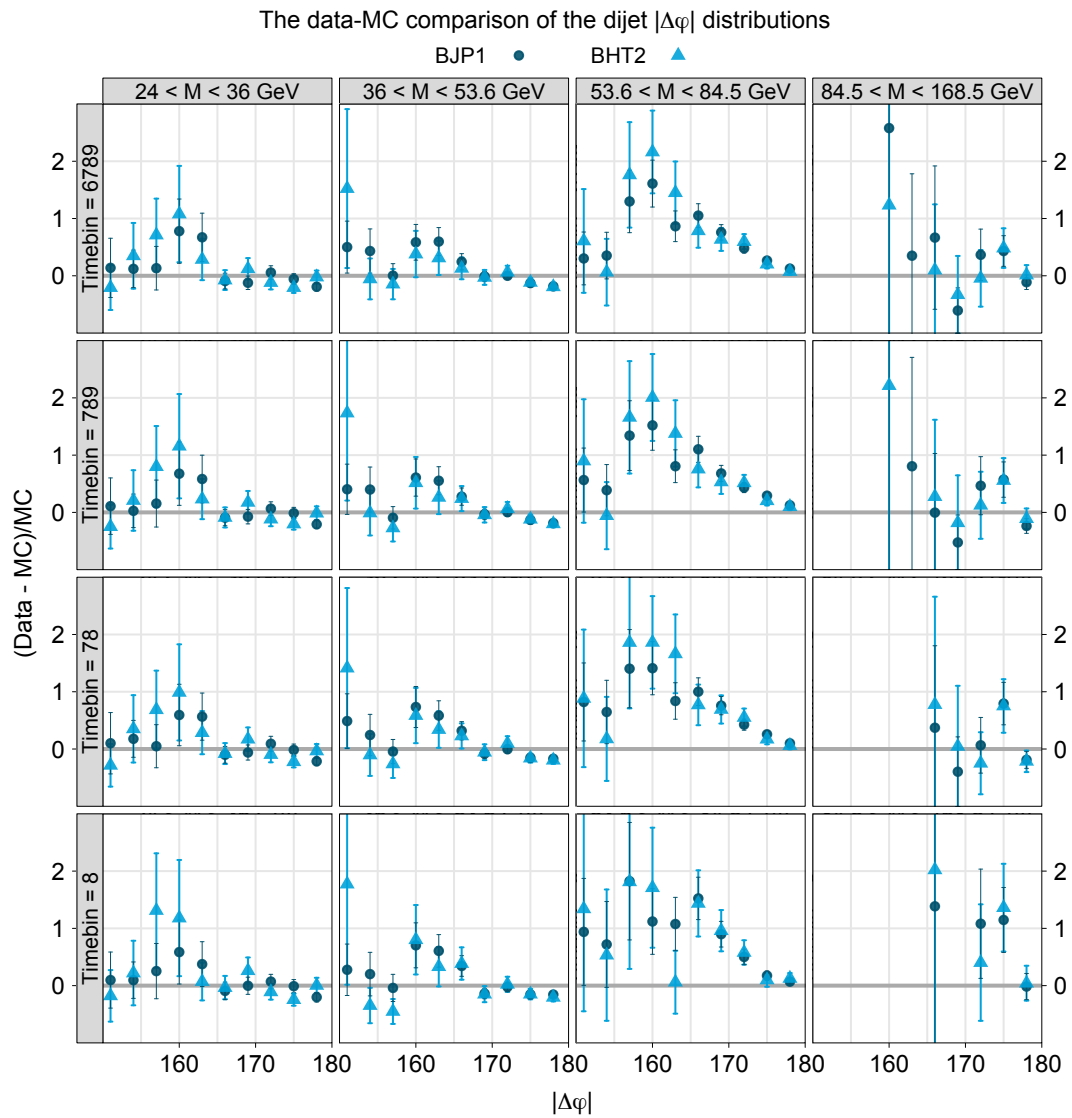
Figure 11-19: The data-MC comparison of the φ dependence.

Chapter 12

Dijet Cross Section

The dijet cross section is measured using a data sample of $5.4\,\text{pb}^{-1}$ in proton-proton collisions at $\sqrt{s} = 200$ GeV. The cross section is measured at the mid-rapidity $|\eta| \leq 0.8$ as a function of dijet mass M_{jj} in the range of $24 < M_{\text{jj}} < 118$ GeV. The results are in agreement with NLO pQCD predictions with CTEQ6M parton distributions.

12.1 Introduction

The dijet cross section provides an essential test of the QCD factorization and perturbative QCD calculations. This measurement is indispensable for extracting the polarized gluon distribution of the proton from the longitudinal double spin asymmetry $\mathcal{A}_{\text{LL}}$ of dijet production, which is the subject of Chapter 13. The dijet cross section in proton-proton collisions is measured for the first time at RHIC. In Chapter 9, it is shown that the measured inclusive jet cross section is in agreement with NLO pQCD predictions. This chapter shows that the measured dijet cross section is also in agreement with NLO pQCD predictions.

The dijet cross section is obtained from the dijet yields at the detector level in nearly the same way in which the inclusive jet cross section is obtained from the detector-level jet yields in Chapter 9. The structure of this chapter is nearly identical to that of Chapter 9.

Proton-Proton	$\sqrt{s} = 200$ GeV
Luminosity	$\int \mathcal{L} \mathrm{d}t = 5.4$ pb^{-1}
Cone Radius	$R = 0.7$

As a function of mass	24 GeV $< M_{jj} < 118$ GeV

Phase Space	$\max(p_T) > 10.0$ GeV
	$\min(p_T) > 7.0$ GeV
	$-0.8 < \eta < 0.8$
	$|\Delta\eta| < 1.0$
	$|\Delta\varphi| > 2.0$

Table 12.1: The parameters of the dijet cross section measurement

12.2 Binning and Phase Space Volume

The dijet cross section is evaluated in bins of dijet mass M_{jj}. The M_{jj} bins are determined so as to balance accuracy and statistics. Due to the scarcity of low M_{jj} dijet events in the MC simulation, the bins are wide at the low M_{jj} range as well as the high M_{jj} range. The bins are narrow in the mid M_{jj} range; the narrowest bin is bin 5. The lower bin boundary M_{jj}^{low} and the upper bin boundary M_{jj}^{up} for bin i follow the formula:

$$
M_{jji}^{\mathrm{low}} = \begin{cases} 36 \cdot \{2 - (1 + 0.01\,(21 + (9/16)(6 - i)))\}^{(8/17)(6-i)} & \text{for } 1 \le i \le 6 \\ 36 \cdot \{1 + 0.01\,(20 + (10/16)(i - 6))\}^{(8/17)(i-6)} & \text{for } 7 \le i \end{cases}
$$

$$
M_{jji}^{\mathrm{up}} = M_{jji+1}^{\mathrm{low}}.
$$

Table 12.2 gives the bin boundaries for $i = 1$ to 15. The cross section is measured for bin 3 to bin 13, which corresponds to $24.0 < M_{jj} < 118.0$ GeV. The phase space volume can be written as $\Delta M_{jj}\Delta\eta_3\Delta\eta_4$. ΔM_{jj} is a M_{jj} bin width. $\Delta\eta_3\Delta\eta_4$ is the area on the $\eta_3 - \eta_4$ plane covered by the η cuts: $-0.8 < \eta < 0.8$ and $|\Delta\eta| < 1.0$, which is equal to 2.2.

bin	boundaries [GeV]		width	volume
i	M_{jji}^{low}	M_{jji}^{up}	ΔM_{jj}	$\Delta M_{jj}\Delta\eta_3\Delta\eta_4$
1	12.7	18.8	6.1	13.42
2	18.8	24.0	5.2	11.44
3	24.0	28.6	4.6	10.12
4	28.6	32.5	3.9	8.58
5	32.5	36.0	3.5	7.70
6	36.0	40.9	4.9	10.78
7	40.9	46.7	5.8	12.76
8	46.7	53.6	6.9	15.18
9	53.6	62.0	8.4	18.48
10	62.0	72.2	10.2	22.44
11	72.2	84.5	12.3	27.06
12	84.5	99.6	15.1	33.22
13	99.6	118.0	18.4	40.48
14	118.0	140.6	22.6	49.72
15	140.6	168.5	27.9	61.38

Table 12.2: The bin boundaries, the bin widths, and the phase space volumes of M_{jj} bins used in the dijet cross section measurement.

12.3 Evaluation of the Cross Section

The evaluation method is similar to the one used in the inclusive jet cross section measurement in Chapter 9. The invariant mass M_{jj} of dijets and the transverse momentum p_T of inclusive jets are similar in that both are a measure of the "hardness" of the hard interactions and the cross section rapidly decreases with these variables.

The dijet cross section is calculated for each M_{jj} bin with the formula:

$$\frac{d^3\sigma}{dM_{jj}d\eta_3 d\eta_4} = \frac{1}{\int \mathcal{L}dt} \cdot \frac{1}{\Delta M_{jj}\Delta\eta_3\Delta\eta_4} \cdot \frac{1}{\mathcal{C}} \cdot J. \tag{12.1}$$

$$\begin{aligned}
J&: \quad \text{Detector-level dijet yields} \\
\mathcal{C}&: \quad \text{Correction factors} \\
\Delta M_{jj}\Delta\eta_3\Delta\eta_4&: \quad \text{Phase space volume} \\
\int \mathcal{L}dt&: \quad \text{Luminosity}
\end{aligned}$$

The detector-level dijet yields are given in Table 10.2. The correction factors are obtained in the following section. The phase space volume is shown in the previous

section. The luminosity, which is common to all cross section measurements, is given in Section 5.3.

12.4 The Correction Factors

As discussed in Section 9.4, the correction factors $\mathcal{C}$ are the products of the two correction factors:

$$\mathcal{C} = \mathcal{C}_{tb} \cdot \mathcal{C}_{det}. \tag{12.2}$$

$\mathcal{C}_{tb}$, which corrects for the effect of the timebin selections, is common to all final state and is determined in Section 5.7.

$\mathcal{C}_{det}$ is estimated as the ratios of the detector-level dijet yields and the hadron-level dijet yields in the MC events:

$$\mathcal{C}_{det\ i}^{trg\ tb} = \frac{J_{trg\ tb\ i}^{MC}}{K_{tb\ i}^{MC}}. \tag{12.3}$$

Figure 12-1 shows $\mathcal{C}_{det}$. Table 12.3 to Table 12.6 give the numerical values.

	BHT2	**BJP1**
p_T [GeV]	$\mathcal{C}_{det} \pm \delta\mathcal{C}_{det}$(stat.)	$\mathcal{C}_{det} \pm \delta\mathcal{C}_{det}$(stat.)
24.00-28.60	$(1.25 \pm 0.15) \times 10^{-3}$	$(9.23 \pm 1.11) \times 10^{-4}$
28.60-32.50	$(2.42 \pm 0.25) \times 10^{-3}$	$(3.37 \pm 0.27) \times 10^{-3}$
32.50-36.00	$(4.11 \pm 0.47) \times 10^{-3}$	$(8.27 \pm 0.88) \times 10^{-3}$
36.00-40.90	$(8.60 \pm 0.67) \times 10^{-3}$	$(1.85 \pm 0.10) \times 10^{-2}$
40.90-46.70	$(1.35 \pm 0.10) \times 10^{-2}$	$(3.32 \pm 0.17) \times 10^{-2}$
46.70-53.60	$(2.23 \pm 0.18) \times 10^{-2}$	$(5.68 \pm 0.31) \times 10^{-2}$
53.60-62.00	$(3.73 \pm 0.27) \times 10^{-2}$	$(8.43 \pm 0.40) \times 10^{-2}$
62.00-72.20	$(4.99 \pm 0.22) \times 10^{-2}$	$(1.10 \pm 0.04) \times 10^{-1}$
72.20-84.50	$(7.32 \pm 0.26) \times 10^{-2}$	$(1.45 \pm 0.04) \times 10^{-1}$
84.50-99.60	$(1.12 \pm 0.05) \times 10^{-1}$	$(1.85 \pm 0.06) \times 10^{-1}$

Table 12.3: The correction factors $\mathcal{C}_{det}$ for the events in the timebin 8.

	BHT2	BJP1
p_T [GeV]	$C_{det} \pm \delta C_{det}(\text{stat.})$	$C_{det} \pm \delta C_{det}(\text{stat.})$
24.00-28.60	$(1.20 \pm 0.14) \times 10^{-3}$	$(9.51 \pm 1.11) \times 10^{-4}$
28.60-32.50	$(2.50 \pm 0.25) \times 10^{-3}$	$(3.45 \pm 0.28) \times 10^{-3}$
32.50-36.00	$(4.05 \pm 0.45) \times 10^{-3}$	$(8.18 \pm 0.83) \times 10^{-3}$
36.00-40.90	$(8.73 \pm 0.69) \times 10^{-3}$	$(1.84 \pm 0.10) \times 10^{-2}$
40.90-46.70	$(1.34 \pm 0.10) \times 10^{-2}$	$(3.27 \pm 0.16) \times 10^{-2}$
46.70-53.60	$(2.25 \pm 0.17) \times 10^{-2}$	$(5.61 \pm 0.29) \times 10^{-2}$
53.60-62.00	$(3.70 \pm 0.26) \times 10^{-2}$	$(8.29 \pm 0.37) \times 10^{-2}$
62.00-72.20	$(4.91 \pm 0.22) \times 10^{-2}$	$(1.09 \pm 0.03) \times 10^{-1}$
72.20-84.50	$(7.39 \pm 0.26) \times 10^{-2}$	$(1.44 \pm 0.04) \times 10^{-1}$
84.50-99.60	$(1.11 \pm 0.05) \times 10^{-1}$	$(1.83 \pm 0.06) \times 10^{-1}$

Table 12.4: The correction factors $\mathcal{C}_{det}$ for the events in the timebin set 78.

	BHT2	BJP1
p_T [GeV]	$C_{det} \pm \delta C_{det}(\text{stat.})$	$C_{det} \pm \delta C_{det}(\text{stat.})$
24.00-28.60	$(1.19 \pm 0.14) \times 10^{-3}$	$(8.98 \pm 1.02) \times 10^{-4}$
28.60-32.50	$(2.41 \pm 0.23) \times 10^{-3}$	$(3.37 \pm 0.26) \times 10^{-3}$
32.50-36.00	$(4.03 \pm 0.44) \times 10^{-3}$	$(7.94 \pm 0.79) \times 10^{-3}$
36.00-40.90	$(8.50 \pm 0.66) \times 10^{-3}$	$(1.82 \pm 0.10) \times 10^{-2}$
40.90-46.70	$(1.30 \pm 0.09) \times 10^{-2}$	$(3.20 \pm 0.15) \times 10^{-2}$
46.70-53.60	$(2.15 \pm 0.16) \times 10^{-2}$	$(5.51 \pm 0.28) \times 10^{-2}$
53.60-62.00	$(3.64 \pm 0.25) \times 10^{-2}$	$(8.21 \pm 0.36) \times 10^{-2}$
62.00-72.20	$(4.89 \pm 0.22) \times 10^{-2}$	$(1.08 \pm 0.03) \times 10^{-1}$
72.20-84.50	$(7.18 \pm 0.20) \times 10^{-2}$	$(1.41 \pm 0.03) \times 10^{-1}$
84.50-99.60	$(1.10 \pm 0.04) \times 10^{-1}$	$(1.81 \pm 0.06) \times 10^{-1}$

Table 12.5: The correction factors $\mathcal{C}_{det}$ for the events in the timebin set 789.

	BHT2	BJP1
p_T [GeV]	$C_{det} \pm \delta C_{det}(\text{stat.})$	$C_{det} \pm \delta C_{det}(\text{stat.})$
24.00-28.60	$(1.14 \pm 0.12) \times 10^{-3}$	$(8.97 \pm 0.98) \times 10^{-4}$
28.60-32.50	$(2.40 \pm 0.22) \times 10^{-3}$	$(3.31 \pm 0.25) \times 10^{-3}$
32.50-36.00	$(3.95 \pm 0.41) \times 10^{-3}$	$(7.78 \pm 0.73) \times 10^{-3}$
36.00-40.90	$(8.43 \pm 0.65) \times 10^{-3}$	$(1.79 \pm 0.09) \times 10^{-2}$
40.90-46.70	$(1.26 \pm 0.09) \times 10^{-2}$	$(3.09 \pm 0.15) \times 10^{-2}$
46.70-53.60	$(2.14 \pm 0.15) \times 10^{-2}$	$(5.39 \pm 0.26) \times 10^{-2}$
53.60-62.00	$(3.58 \pm 0.24) \times 10^{-2}$	$(8.02 \pm 0.34) \times 10^{-2}$
62.00-72.20	$(4.78 \pm 0.21) \times 10^{-2}$	$(1.06 \pm 0.03) \times 10^{-1}$
72.20-84.50	$(7.14 \pm 0.21) \times 10^{-2}$	$(1.40 \pm 0.03) \times 10^{-1}$
84.50-99.60	$(1.07 \pm 0.04) \times 10^{-1}$	$(1.77 \pm 0.05) \times 10^{-1}$

Table 12.6: The correction factors $\mathcal{C}_{det}$ for the events in the timebin set 6789.
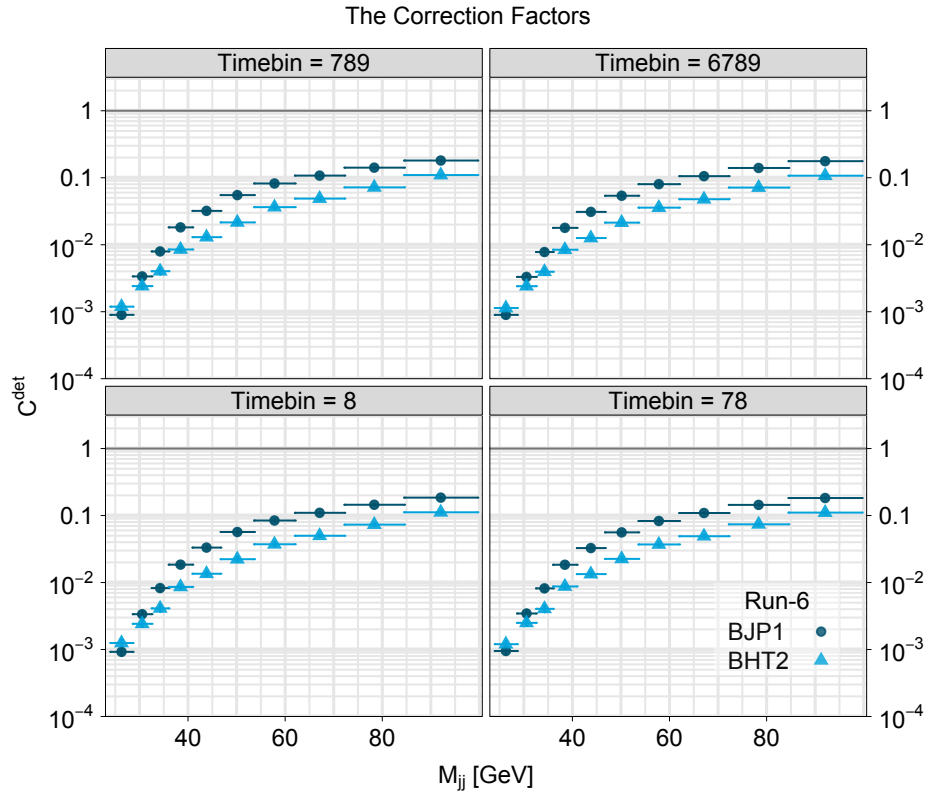
Figure 12-1: The correction factors $\mathcal{C}_{\mathrm{det}}$

12.5 Estimates of the Hadron-Level Dijet Yield

The hadron-level dijet yields $K = J/(\mathcal{C}_{\mathrm{tb}} \cdot \mathcal{C}_{\mathrm{det}})$ are estimated. J, $\mathcal{C}_{\mathrm{tb}}$ are given in Table 10.2 and Table 5.5, respectively. $\mathcal{C}_{\mathrm{det}}$ was obtained in the previous section. Table 12.7 to 12.10 give the numerical values for the estimated hadron-level dijet yields.

p_T [GeV]	BHT2 $K \pm \delta K$(stat.)	BJP1 $K \pm \delta K$(stat.)
18.80-24.00	$(7.63 \pm 1.35) \times 10^6$	$(1.58 \pm 0.55) \times 10^7$
24.00-28.60	$(3.69 \pm 0.45) \times 10^6$	$(4.59 \pm 0.57) \times 10^6$
28.60-32.50	$(1.31 \pm 0.14) \times 10^6$	$(1.45 \pm 0.12) \times 10^6$
32.50-36.00	$(5.59 \pm 0.68) \times 10^5$	$(5.19 \pm 0.57) \times 10^5$
36.00-40.90	$(2.61 \pm 0.23) \times 10^5$	$(2.80 \pm 0.17) \times 10^5$
40.90-46.70	$(1.21 \pm 0.11) \times 10^5$	$(1.35 \pm 0.08) \times 10^5$
46.70-53.60	$(5.89 \pm 0.57) \times 10^4$	$(6.06 \pm 0.39) \times 10^4$
53.60-62.00	$(2.38 \pm 0.23) \times 10^4$	$(2.62 \pm 0.16) \times 10^4$
62.00-72.20	$(8.64 \pm 0.90) \times 10^3$	$(8.68 \pm 0.62) \times 10^3$
72.20-84.50	$(2.29 \pm 0.35) \times 10^3$	$(2.48 \pm 0.27) \times 10^3$
84.50-99.60	$(7.17 \pm 1.59) \times 10^2$	$(7.01 \pm 1.23) \times 10^2$
99.60-118.00	$(9.03 \pm 4.54) \times 10^1$	$(1.01 \pm 0.41) \times 10^2$

Table 12.7: The estimates of the hadron-level jet yields K_i from the events in the timebin 8.

p_T [GeV]	BHT2 $K \pm \delta K$(stat.)	BJP1 $K \pm \delta K$(stat.)
18.80-24.00	$(7.44 \pm 1.18) \times 10^6$	$(1.38 \pm 0.46) \times 10^7$
24.00-28.60	$(3.87 \pm 0.45) \times 10^6$	$(4.46 \pm 0.53) \times 10^6$
28.60-32.50	$(1.25 \pm 0.13) \times 10^6$	$(1.44 \pm 0.12) \times 10^6$
32.50-36.00	$(5.70 \pm 0.66) \times 10^5$	$(5.29 \pm 0.55) \times 10^5$
36.00-40.90	$(2.60 \pm 0.22) \times 10^5$	$(2.84 \pm 0.16) \times 10^5$
40.90-46.70	$(1.33 \pm 0.11) \times 10^5$	$(1.38 \pm 0.07) \times 10^5$
46.70-53.60	$(5.50 \pm 0.47) \times 10^4$	$(5.87 \pm 0.33) \times 10^4$
53.60-62.00	$(2.22 \pm 0.19) \times 10^4$	$(2.54 \pm 0.14) \times 10^4$
62.00-72.20	$(8.82 \pm 0.70) \times 10^3$	$(9.16 \pm 0.49) \times 10^3$
72.20-84.50	$(2.60 \pm 0.27) \times 10^3$	$(2.79 \pm 0.21) \times 10^3$
84.50-99.60	$(4.98 \pm 0.95) \times 10^2$	$(5.31 \pm 0.76) \times 10^2$
99.60-118.00	$(9.02 \pm 3.22) \times 10^1$	$(1.02 \pm 0.30) \times 10^2$

Table 12.8: The estimates of the hadron-level jet yields K_i from the events in the timebin set 78.

p_T [GeV]	BHT2 $K \pm \delta K$(stat.)	BJP1 $K \pm \delta K$(stat.)
18.80-24.00	$(7.26 \pm 1.15) \times 10^6$	$(1.47 \pm 0.48) \times 10^7$
24.00-28.60	$(3.76 \pm 0.43) \times 10^6$	$(4.44 \pm 0.51) \times 10^6$
28.60-32.50	$(1.26 \pm 0.12) \times 10^6$	$(1.42 \pm 0.11) \times 10^6$
32.50-36.00	$(5.54 \pm 0.63) \times 10^5$	$(5.33 \pm 0.54) \times 10^5$
36.00-40.90	$(2.61 \pm 0.21) \times 10^5$	$(2.79 \pm 0.16) \times 10^5$
40.90-46.70	$(1.34 \pm 0.10) \times 10^5$	$(1.39 \pm 0.07) \times 10^5$
46.70-53.60	$(5.66 \pm 0.46) \times 10^4$	$(5.96 \pm 0.32) \times 10^4$
53.60-62.00	$(2.25 \pm 0.18) \times 10^4$	$(2.55 \pm 0.13) \times 10^4$
62.00-72.20	$(8.55 \pm 0.64) \times 10^3$	$(9.35 \pm 0.46) \times 10^3$
72.20-84.50	$(2.74 \pm 0.25) \times 10^3$	$(2.81 \pm 0.18) \times 10^3$
84.50-99.60	$(5.37 \pm 0.88) \times 10^2$	$(5.13 \pm 0.67) \times 10^2$
99.60-118.00	$(8.06 \pm 2.72) \times 10^1$	$(9.40 \pm 2.55) \times 10^1$

Table 12.9: The estimates of the hadron-level jet yields K_i from the events in the timebin set 789.

p_T [GeV]	BHT2 $K \pm \delta K$(stat.)	BJP1 $K \pm \delta K$(stat.)
18.80-24.00	$(6.93 \pm 1.02) \times 10^6$	$(1.38 \pm 0.43) \times 10^7$
24.00-28.60	$(3.89 \pm 0.43) \times 10^6$	$(4.31 \pm 0.48) \times 10^6$
28.60-32.50	$(1.26 \pm 0.12) \times 10^6$	$(1.43 \pm 0.11) \times 10^6$
32.50-36.00	$(5.51 \pm 0.59) \times 10^5$	$(5.34 \pm 0.51) \times 10^5$
36.00-40.90	$(2.58 \pm 0.21) \times 10^5$	$(2.77 \pm 0.15) \times 10^5$
40.90-46.70	$(1.36 \pm 0.10) \times 10^5$	$(1.43 \pm 0.07) \times 10^5$
46.70-53.60	$(5.72 \pm 0.44) \times 10^4$	$(6.01 \pm 0.31) \times 10^4$
53.60-62.00	$(2.28 \pm 0.17) \times 10^4$	$(2.55 \pm 0.12) \times 10^4$
62.00-72.20	$(8.64 \pm 0.60) \times 10^3$	$(9.48 \pm 0.43) \times 10^3$
72.20-84.50	$(2.78 \pm 0.23) \times 10^3$	$(2.81 \pm 0.17) \times 10^3$
84.50-99.60	$(5.54 \pm 0.81) \times 10^2$	$(5.32 \pm 0.62) \times 10^2$
99.60-118.00	$(8.84 \pm 2.59) \times 10^1$	$(1.00 \pm 0.24) \times 10^2$

Table 12.10: The estimates of the hadron-level jet yields K_i from the events in the timebin set 6789.

12.6 Systematic Uncertainty

The systematic uncertainties on the dijet cross section are estimated in a similar way in which those on the inclusive jet cross section are estimated in Section 9.6. Figure 12-2 shows the uncertainties, and Table 12.11 gives the numerical values.
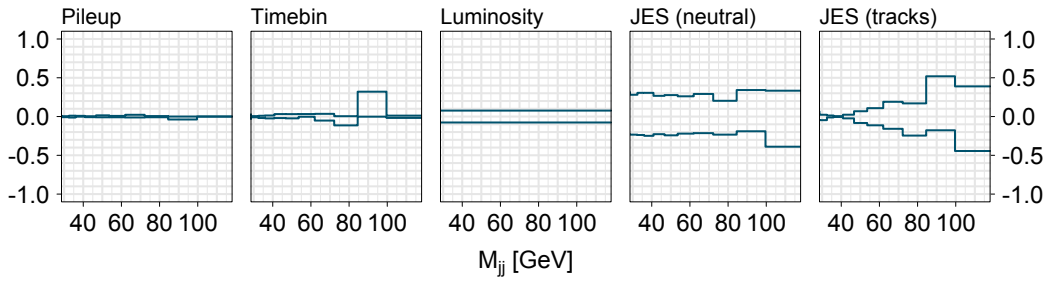
Figure 12-2: The systematic uncertainty on the dijet cross section.

M_{jj} [GeV]	JES (neutral)	JES (tracks)	Pile-up	Timebin	Total
24.00-28.60	+0.32	+0.07	+0.0132	+0.030	+0.32
	-0.23	-0.04	-0.0028	-0.033	-0.23
28.60-32.50	+0.28	+0.02	+0.0045	+0.006	+0.28
	-0.23	-0.05	-0.0080	-0.010	-0.24
32.50-36.00	+0.31	+0.01	+0.0109	+0.010	+0.31
	-0.24	-0.01	-0.0129	-0.019	-0.24
36.00-40.90	+0.31	+0.01	+0.0089	+0.014	+0.31
	-0.25	-0.01	-0.0014	-0.024	-0.25
40.90-46.70	+0.27	+0.02	+0.0040	+0.032	+0.27
	-0.23	-0.02	-0.0081	-0.020	-0.23
46.70-53.60	+0.28	+0.07	+0.0154	+0.031	+0.29
	-0.24	-0.08	-0.0096	-0.023	-0.26
53.60-62.00	+0.26	+0.11	+0.0082	+0.032	+0.28
	-0.22	-0.11	-0.0093	-0.003	-0.25
62.00-72.20	+0.29	+0.19	+0.0226	+0.035	+0.35
	-0.21	-0.16	-0.0119	-0.052	-0.27
72.20-84.50	+0.20	+0.17	+0.0061	+0.004	+0.26
	-0.23	-0.25	-0.0091	-0.114	-0.36
84.50-99.60	+0.34	+0.52	+0.0000	+0.321	+0.70
	-0.19	-0.18	-0.0380	-0.002	-0.26

Table 12.11: The systematic uncertainty on the dijet cross section. 7.6% of the systematic uncertainty on the integrated luminosity is not included in the total.

12.7   Theoretical Predictions

As for the inclusive jet cross section in section 9.7, the dijet cross section is calculated by next-to-leading order perturbative QCD and corrected for the effects of hadronization and underlying events evaluated by the MC simulation.

12.7.1   NLO pQCD Predictions

Figure 12-3 shows a NLO pQCD prediction of the dijet cross section and the contributions from parton-level cross sections.
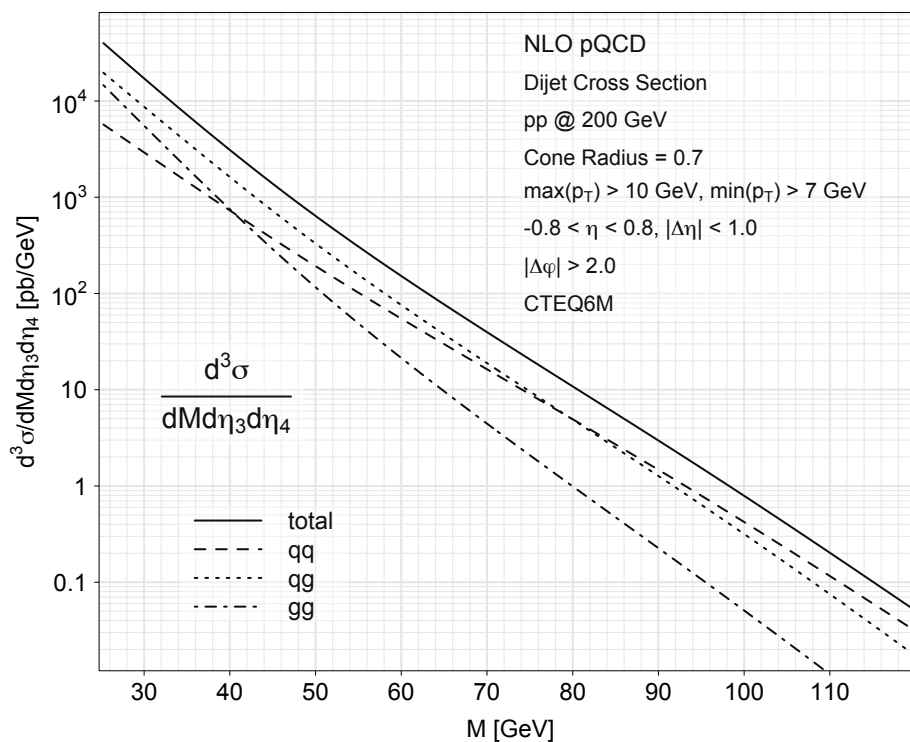
Figure 12-3: NLO pQCD predictions of the dijet cross section with the CTEQ6M parton distributions [43] .

12.7.2 Hadronization and Underlying Event Corrections

The effects of the hadronization and the underlying events are evaluated by using the MC events. Table 12.12 gives the correction factors, which are plotted on Figure 12-4.

M_{jj} [GeV]	$C_{HAD} \pm \delta C_{HAD}$(stat.)
24.00-28.60	2.199 ± 0.047
28.60-32.50	1.998 ± 0.059
32.50-36.00	1.778 ± 0.113
36.00-40.90	1.491 ± 0.031
40.90-46.70	1.401 ± 0.040
46.70-53.60	1.308 ± 0.025
53.60-62.00	1.246 ± 0.019
62.00-72.20	1.150 ± 0.014
72.20-84.50	1.091 ± 0.019
84.50-99.60	1.069 ± 0.024
99.60-118.00	1.062 ± 0.017

Table 12.12: The hadronization and underlying event corrections estimated with the MC events.
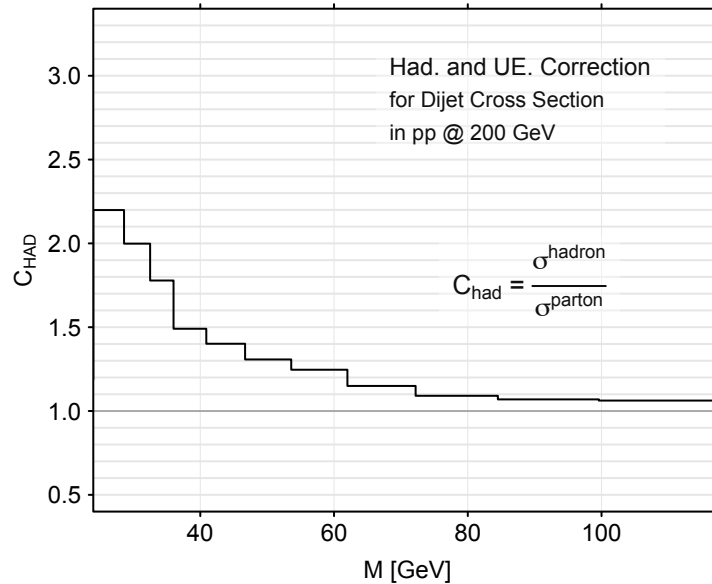
Figure 12-4: The hadronization and underlying event corrections estimated with the MC events.

12.8   Data Points within Wide Bins

The values $M_{\text{jj}}^{\text{l.w.}}$ that satisfy the relation:

$$\frac{\mathrm{d}^3\sigma}{\mathrm{d}M_{\text{jj}}\mathrm{d}\eta_3\mathrm{d}\eta_4}(M_{\text{jj}}^{\text{l.w.}}) = \frac{1}{\Delta M_{\text{jj}}}\int\limits_{M_{\text{jj}}^{\text{low}}}^{M_{\text{jj}}^{\text{low}}+\Delta M_{\text{jj}}}\frac{\mathrm{d}^3\sigma(M_{\text{jj}})}{\mathrm{d}M_{\text{jj}}\mathrm{d}\eta_3\mathrm{d}\eta_4} \tag{12.4}$$

are obtained. These values represent the invariant mass M_{jj} for the measured cross section in each bin as discussed in the inclusive jet cross section measurement in Section 9.8. NLO pQCD predictions of the dijet cross section as a function of M_{jj} and in bins of M_{jj} are plotted in Figure 12-5. The values for $M_{\text{jj}}^{\text{l.w.}}$ are given in Table 12.13.
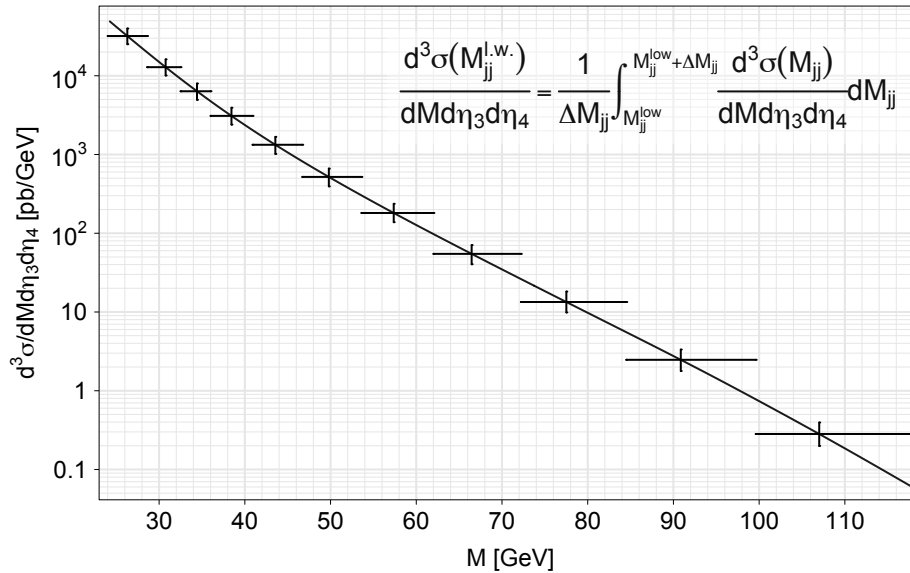
Figure 12-5: NLO pQCD calculations of the dijet cross section as a smooth function of M_{jj} and in bins of M_{jj}. The vertical lines show where the smooth curve intercepts the binned values.

| M_{jj} bin | boundaries | | | | [GeV] |
	low	up	width	center	$M_{jj}^{l.w.}$
3	24.00	28.60	4.60	26.30	26.29
4	28.60	32.50	3.90	30.55	30.76
5	32.50	36.00	3.50	34.25	34.42
6	36.00	40.90	4.90	38.45	38.44
7	40.90	46.70	5.80	43.80	43.56
8	46.70	53.60	6.90	50.15	49.80
9	53.60	62.00	8.40	57.80	57.37
10	62.00	72.20	10.20	67.10	66.46
11	72.20	84.50	12.30	78.35	77.51
12	84.50	99.60	15.10	92.05	90.86
13	99.60	118.00	18.40	108.80	107.01

Table 12.13: $M_{jj}^{l.w.}$

12.9   Results

The dijet cross section in proton-proton collisions at $\sqrt{s}$ = 200 GeV is measured as a function of dijet invariant mass M_{jj} at the mid-rapidity $|\eta| \leq 0.8$. The measured cross section is corrected for the effects of the detector by using MC simulation. The results are compared to a NLO pQCD prediction with corrections for the effects of the hadroninzation and the underlying events. Table 12.14 gives the numerical values. Figure 12-6 shows the results compared with the theory prediction. Figure 12-7 shows the ratios (data - theory)/theory for each M_{jj} bin. 7.6% of uncertainly due to the uncertainly on the integrated luminosity is not shown in the figures.

The measured dijet cross section is well described by in the framework of the QCD factorization with next-to-leading perturbative QCD calculations. This implies that measured $\mathcal{A}_{LL}$ as well can be interpreted in the same theoretical framework and suggests ways to constrain the polarized gluon distributions from dijet $\mathcal{A}_{LL}$.

p_{T} [GeV]	$\sigma \pm \delta\sigma(\text{stat.})\pm\delta\sigma(\text{sys.})$ [pb/GeV]
24.00-28.60	$(7.91 \pm 0.88\ ^{+2.56}_{-1.86}) \times 10^4$
28.60-32.50	$(3.09 \pm 0.24\ ^{+0.87}_{-0.74}) \times 10^4$
32.50-36.00	$(1.29 \pm 0.12\ ^{+0.39}_{-0.31}) \times 10^4$
36.00-40.90	$(4.77 \pm 0.26\ ^{+1.46}_{-1.19}) \times 10^3$
40.90-46.70	$(2.07 \pm 0.11\ ^{+0.56}_{-0.48}) \times 10^3$
46.70-53.60	$(7.35 \pm 0.38\ ^{+2.11}_{-1.89}) \times 10^2$
53.60-62.00	$(2.56 \pm 0.12\ ^{+0.73}_{-0.63}) \times 10^2$
62.00-72.20	$(7.84 \pm 0.36\ ^{+2.75}_{-2.13}) \times 10^1$
72.20-84.50	$(1.92 \pm 0.12\ ^{+0.51}_{-0.69}) \times 10^1$
84.50-99.60	$(2.97 \pm 0.35\ ^{+2.08}_{-0.78}) \times 10^0$
99.60-118.00	$(4.59 \pm 1.10\ ^{+2.35}_{-2.71}) \times 10^{-1}$

Table 12.14: Dijet cross section $\dfrac{\mathrm{d}^3\sigma}{\mathrm{d}M_{\mathrm{jj}}\mathrm{d}\eta_3\mathrm{d}\eta_4}$. The statistical uncertainty includes the statistical uncertainty on the correction factors from the MC samples as well as the statistical uncertainty on the dijet yield in the data. 7.6% of the systematic uncertainty on the integrated luminosity is not included.

Figure 12-6: The dijet cross section in proton-proton collisions at $\sqrt{s} = 200$ GeV from RHIC Run-6 data compared to theoretical predictions. The measured cross sections are shown by the circles. The vertical lines on the data points indicate the statistical errors. The systematic uncertainly is shown by the rectangles, in which 7.68% of uncertainly due to the uncertainly on the integrated luminosity is not included. The gray bands show the theoretical predictions. The light gray band is NLO perturbative QCD prediction with the CTEQ6M parton distribution. The dark gray band includes the corrections for the effects of hadronization and underlying events. The height of the bands indicate the size of the theoretical uncertainly.

Figure 12-7: The comparison of the measured dijet cross section and the NLO pQCD prediction: (data - NLO)/NLO. The NLO pQCD prediction is corrected for the effects of hadronization and underlying events. The ratios are taken bin by bin. The horizontal lines on the data points show the bin widths. The vertical lines on the data points indicate the statistical errors. The gray rectangles show the systematic uncertainly on the measured cross section. Theoretical uncertainly is indicated by the solid lines.

12.10 Cone Radius Dependence

This section discusses the cone radius dependence of the dijet cross section.

Data

Figure 12-8 shows the cone radius dependence of the dijet cross section in the data. The trend that the cone radius dependence is stronger at low M_{jj} than at high M_{jj} is similar to the case of the inclusive jet cross section, which was shown in Section 9.10. However, this trend is not as clear for the dijet cross section.
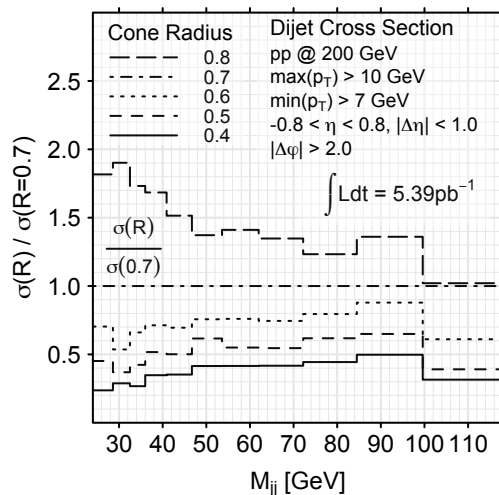
Figure 12-8: The cone radius dependence of the dijet cross section in the data.

Theory

Figure 12-9 shows the cone radius dependence of the dijet cross section in the NLO pQCD calculations. It shows little p_T dependence. The cross section increases by 5 to 6 % as the cone radius increases by 0.1, which is very similar to the case of the inclusive jet cross section, but the amount of the increase is slightly larger.

Figure 12-10 shows the cone radius dependence of the hadronization and underlying event corrections. When the cone radius is 0.4, the hadroninzation and the underlying event corrections are uniform over the whole M_{jj} range at the value around
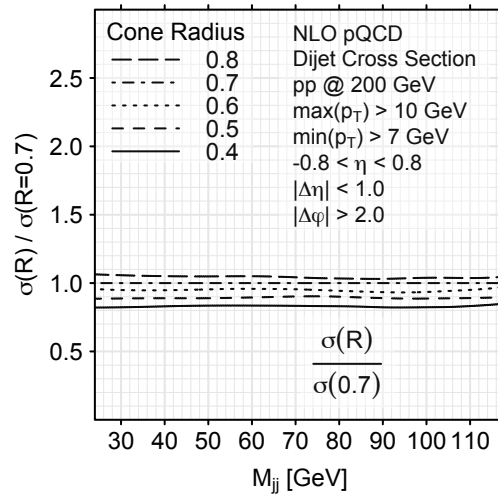
Figure 12-9: The cone radius dependence of the dijet cross section in next-to-leading order pQCD calculations.

0.9, which is about 10% larger than the case of the inclusive jet cross section. The correction increases rapidly in the low-M_{jj} range and slowly in the high-M_{jj} range with the cone radius. This trend is similar to the case of the inclusive jet cross section. However, the corrections become greater than one in the whole M_{jj} range, which is different from the case of the inclusive jet cross section, in which the corrections remain below one in the high-p_T range.

Figure 12-11 shows the cone radius dependence of the dijet cross section in the NLO pQCD calculations plus the hadroninzation and underlying event corrections.
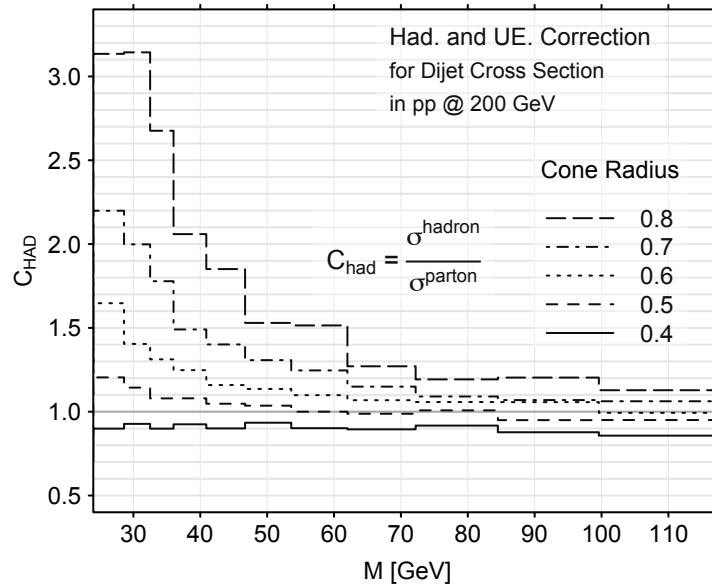
Figure 12-10: The cone radius dependence of the hadroninzation and the underlying event corrections.
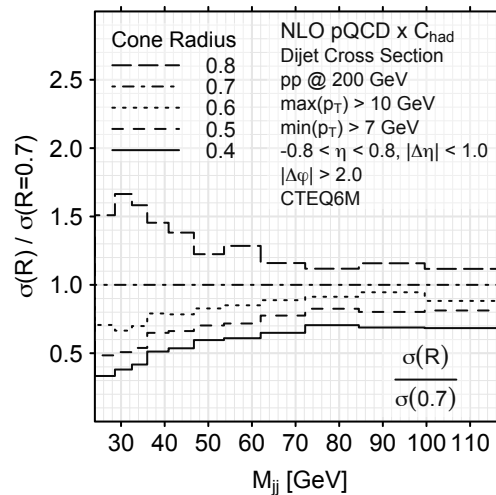
Figure 12-11: The cone radius dependence of the dijet cross section in the NLO pQCD calculations with the hadronization and the underlying event correction.

Data-theory Comparison

Figure 12-12 shows the dijet cross sections at five different cone radii with the theoretical predictions. It can be seen that the hadronization and underlying event corrections are necessary for the theory to describe the data.
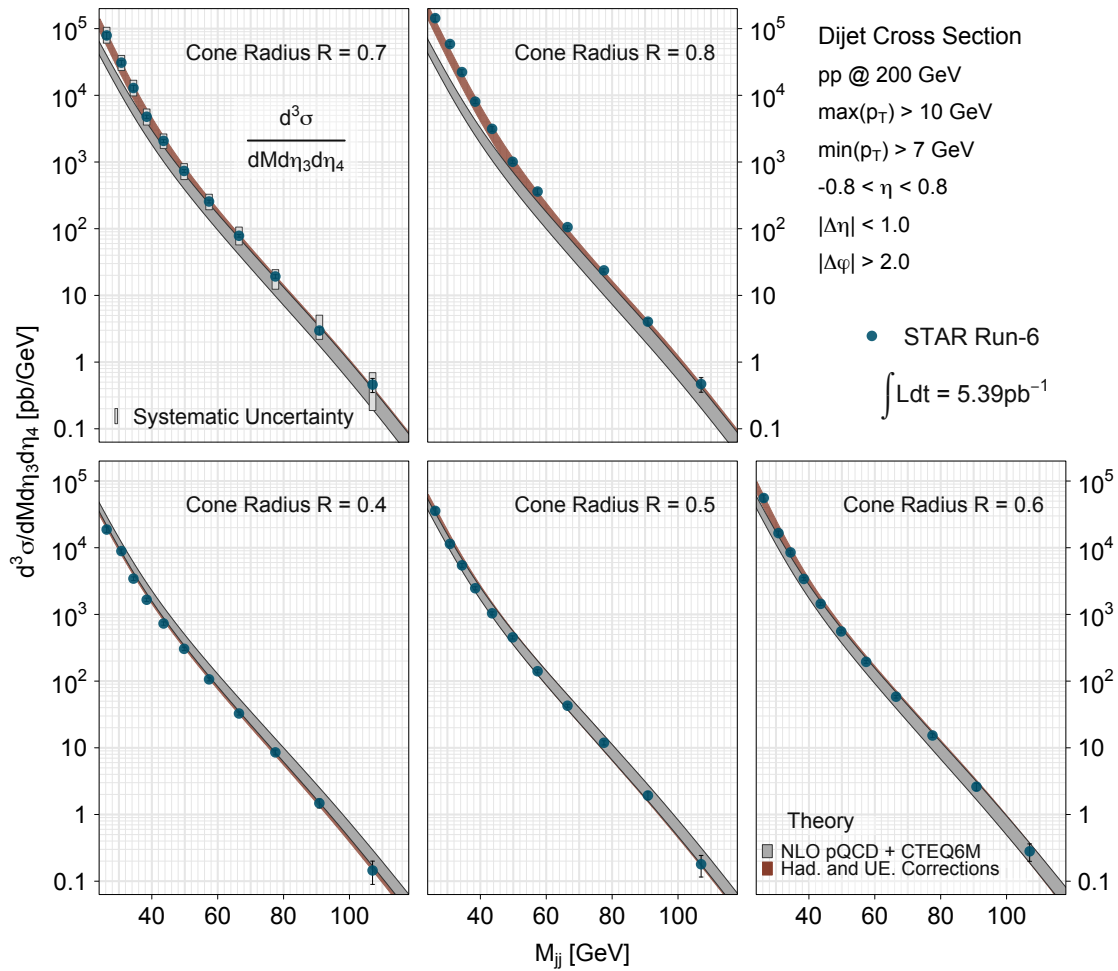
Figure 12-12: The dijet cross sections at five different cone radii with the theoretical predictions.

Figure 12-13 shows the cone radius dependence of the data-theory comparisons. When the hadronization and the underlying event corrections are applied, the agreement is at the best if the cone radius is around 0.6, which is the same as in the case of the inclusive jet cross section (Figure 9-12).
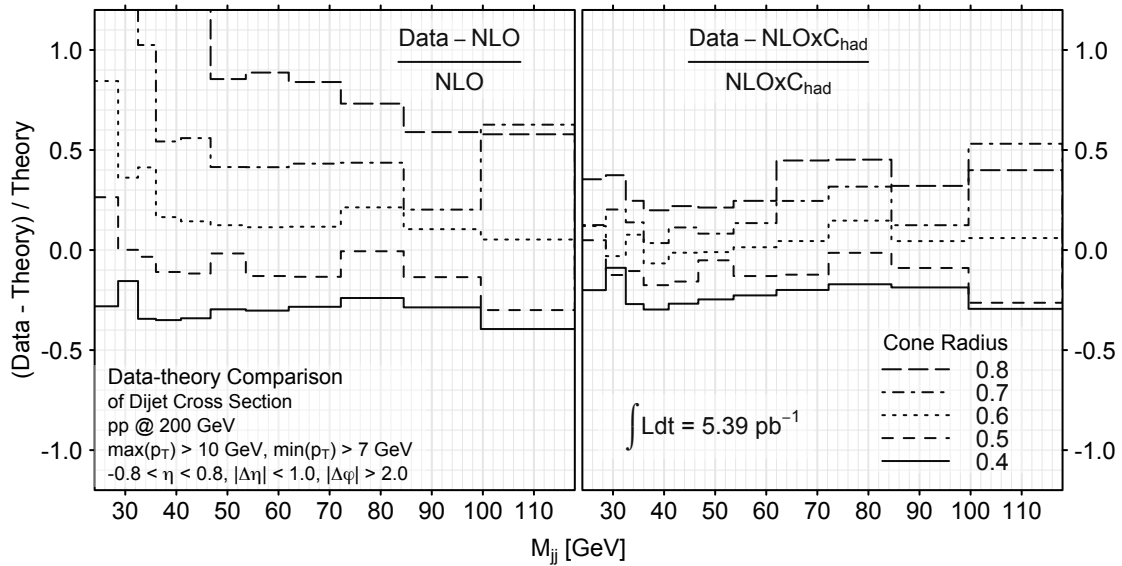
Figure 12-13: The data-theory comparison of the dijet cross section at five different cone radii. (left) The comparison with the NLO pQCD calculations. (right) The comparison with the NLO pQCD calculations plus the hadronization and underlying event corrections.

Chapter 13

Dijet Longitudinal Double Spin Asymmetry $\mathcal{A}_{LL}$

The longitudinal double spin asymmetry $\mathcal{A}_{LL}$ of the dijet production in polarized proton-proton collisions at $\sqrt{s}$ = 200 GeV at the mid-rapidity $|\eta| \leq 0.8$ is measured. The $\mathcal{A}_{LL}$ is measured as a function of the dijet invariant mass M_{jj}. The results are compared with NLO pQCD predictions based on various parametrizations of polarized gluon distributions of the proton. The results are inconsistent with large gluon polarization and expected to lead to a constrain on the polarized gluon distribution.

13.1   Introduction

The longitudinal double spin asymmetry $\mathcal{A}_{LL}$ of the dijet production in polarized proton-proton collisions is sensitive to the polarized gluon distribution of the proton. The dijet $\mathcal{A}_{LL}$ is measured for the first time. The dijet $\mathcal{A}_{LL}$ is measured as a function of the dijet invariant mass M_{jj} in the range of 25 GeV $< M_{jj} <$ 100 GeV at the mid-rapidity $|\eta| \leq 0.8$.

Chapter 12 described the dijet cross section measurement and showed that the results are well described by a NLO pQCD calculation. This implies that the NLO pQCD has a prediction power of the production of the dijets with jets defined by the mid-point cone algorithm with cone radius R = 0.7 in proton collisions at the center of mass energy $\sqrt{s}$ = 200 GeV. The dijet $\mathcal{A}_{LL}$ is measured from the same data sample and compared with predictions of NLO pQCD calculated from variety of models of the polarized gluon distribution.

Longitudinally Polarized Proton-Proton	
Center of Mass Energy	$\sqrt{s} = 200$ GeV
Luminosity	$\int \mathcal{L} \mathrm{d}t = 5.4$ pb^{-1}
Average Polarization	$P = 58\%$
Cone Radius	R = 0.7
Dijet Mass Range	25 GeV $< M_{jj} < 100$ GeV
Phase Space	$\max(p_T) > 10.0$ GeV
	$\min(p_T) > 7.0$ GeV
	$-0.8 < \eta < 0.8$
	$|\Delta\eta| < 1.0$
	$|\Delta\varphi| > 2.0$

Table 13.1: The parameters of the dijet longitudinal double spin asymmetry $\mathcal{A}_{LL}$ measurement.

13.2 Calculation of $\mathcal{A}_{LL}$

Spin Bits

The following spin bits are used to indicate the spin states of the initial protons.

Spin Bit	Yellow	Blue
5	+	+
6	−	+
9	+	−
10	−	−

+: Spin up
−: Spin down

The Definition of $\mathcal{A}_{LL}$ in the Measurement

In this measurement, the $\mathcal{A}_{LL}$ is defined by the formula:

$$\mathcal{A}_{LL} = \frac{\sum P_Y P_B \{(N_5 + N_{10}) - R_3(N_9 + N_6)\}}{\sum P_Y^2 P_B^2 \{(N_5 + N_{10}) + R_3(N_9 + N_6)\}}.$$

$$P_Y, P_B: \quad \text{Polarization}$$

$$R_3: \quad \text{Relative luminosity}$$

$$N_5, N_6, N_9, N_{10}: \quad \text{Spin sorted yields}$$

If the luminosity were the same for all spin states and the polarization were 100%, $\mathcal{A}_{\mathrm{LL}}$ would be merely an asymmetry of the spin sorted yields $\{(N_5 + N_6) - (N_9 + N_{10})\}/\{(N_5 + N_6) + (N_9 + N_{10})\}$. The relative luminosity $R_3 = (\mathcal{L}_5 + \mathcal{L}_{10})/(\mathcal{L}_9 + \mathcal{L}_6)$, which is shown in Section 5.4, corrects for the asymmetry due to the luminosity difference. P_{Y} and P_{B} are the polarizations for the Yellow beam and the Blue beam respectively. The polarizations are given in Section 5.5. The asymmetry of the spin sorted yields is smaller than the $\mathcal{A}_{\mathrm{LL}}$ if protons are not perfectly polarized, which is corrected for by the polarizations $P_{\mathrm{Y}} P_{\mathrm{B}}$. The spin sorted yields are given in Table 13.2 and Table 13.3.

BHT2	Spin Sorted Yields			
M_{jj} [GeV]	N_5	N_6	N_9	N_{10}
20.00-30.01	12758	12516	12658	12776
30.01-48.83	9415	9184	9127	9239
48.83-85.92	1858	1875	1809	1911

Table 13.2: The spin sorted yields of dijet events for the BHT2 trigger

BJP1	Spin Sorted Yields			
M_{jj} [GeV]	N_5	N_6	N_9	N_{10}
20.00-30.01	62990	62424	62140	62951
30.01-48.83	44827	44287	44064	44386
48.83-85.92	5078	4967	4921	5027

Table 13.3: The spin sorted yields of dijet events for the BJP1 trigger

13.3 False Asymmetries

Four false asymmetries which should vanish are calculated for a systematic check of the data.

13.3.1 Single Spin Asymmetries

The single spin asymmetries are spin asymmetries when only one of the proton beams is polarized. The single spin asymmetries for each beam are obtained by summing up the spin sorted yields for the other beam. The single spin asymmetry for the Yellow

beam can be written as

$$\mathcal{A}_{L}^{YB} = \frac{\sum P_Y\{(N_5 + N_9) - R_1(N_6 + N_{10})\}}{\sum P_Y^2\{(N_5 + N_9) + R_1(N_6 + N_{10})\}},$$

and for the Blue beam

$$\mathcal{A}_{L}^{BB} = \frac{\sum P_B\{(N_5 + N_6) - R_2(N_9 + N_{10})\}}{\sum P_B^2\{(N_5 + N_6) + R_2(N_9 + N_{10})\}}.$$

Figure 13-1 and Figure 13-2 show the single spin asymmetries for each fill. Figure 13-3 and Figure 13-4 the single spin asymmetries as a function of the invariant mass M_{jj}.
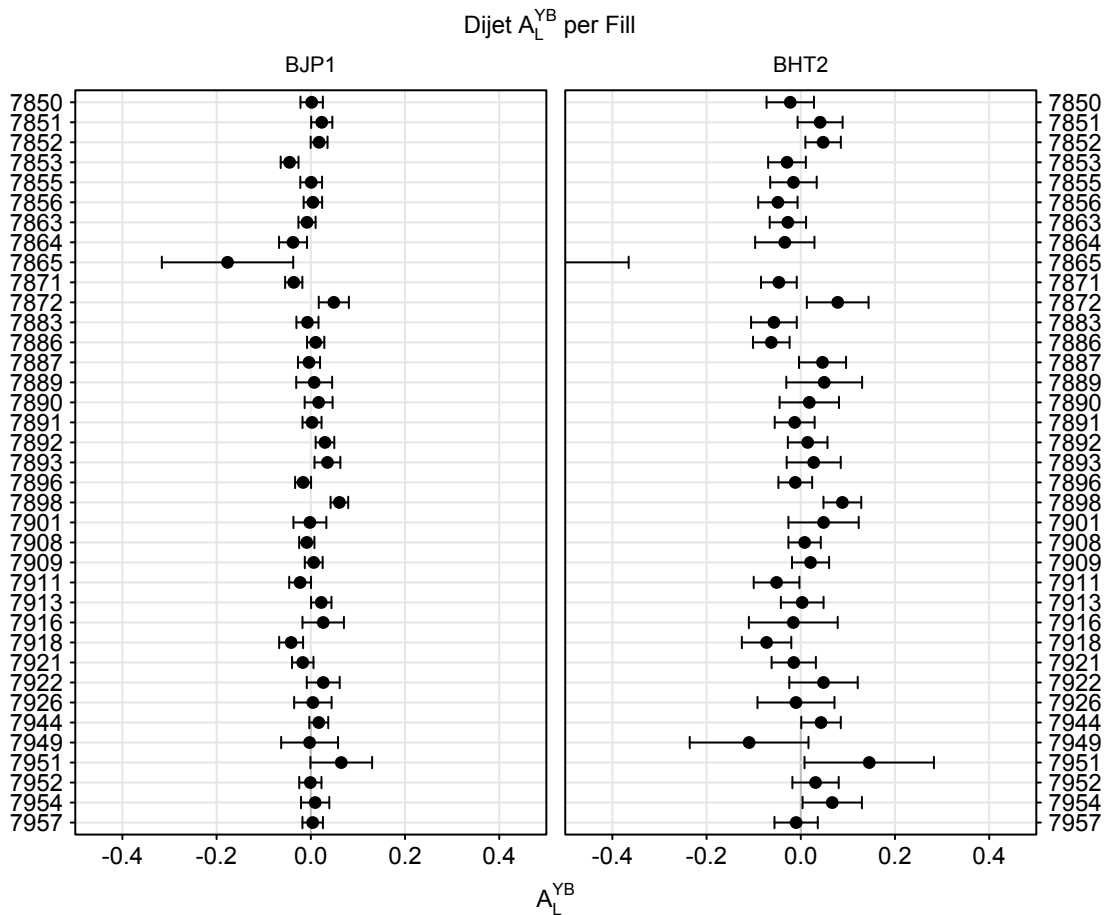
Figure 13-1: The single spin asymmetry for the Yellow beam $\mathcal{A}_{L}^{YB}$ for each fill for each trigger.
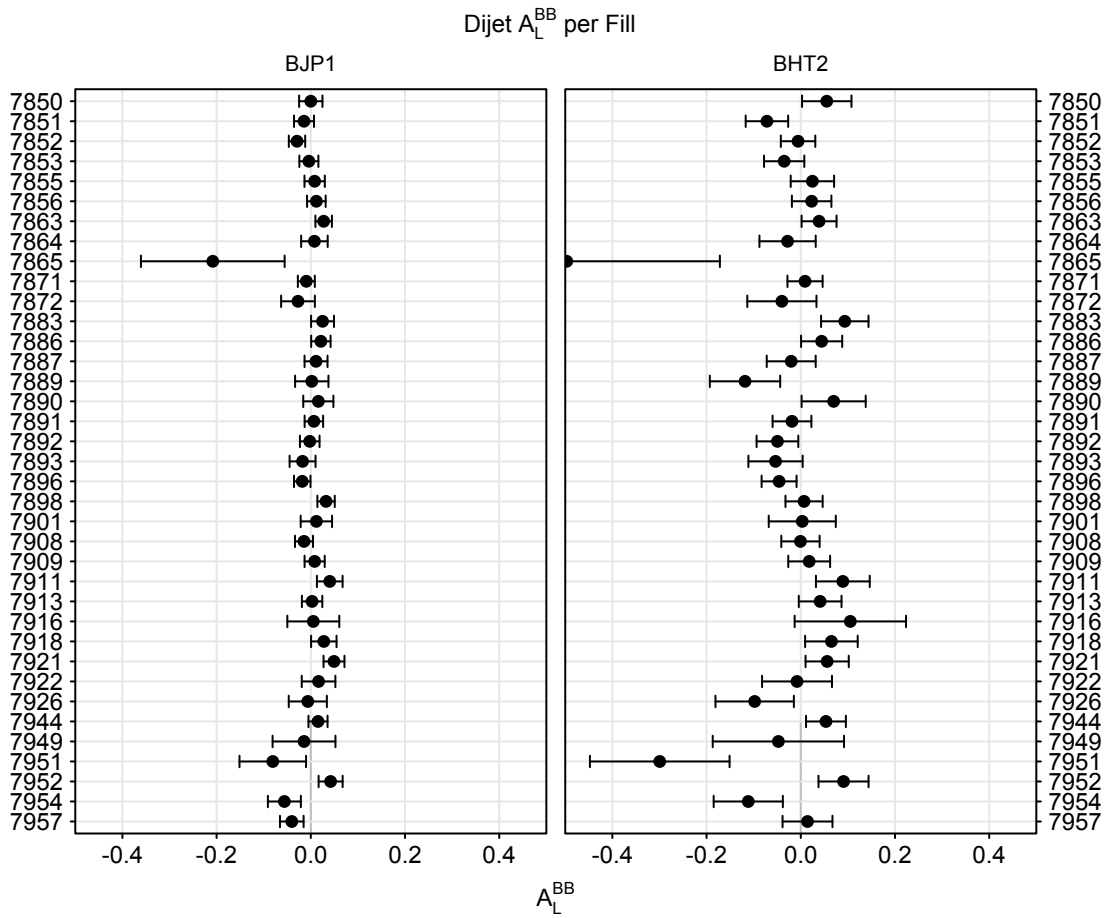
Figure 13-2: The single spin asymmetry for the Blue beam $\mathcal{A}_L^{BB}$ for each fill for each trigger.

Dijets A_L^{YB}
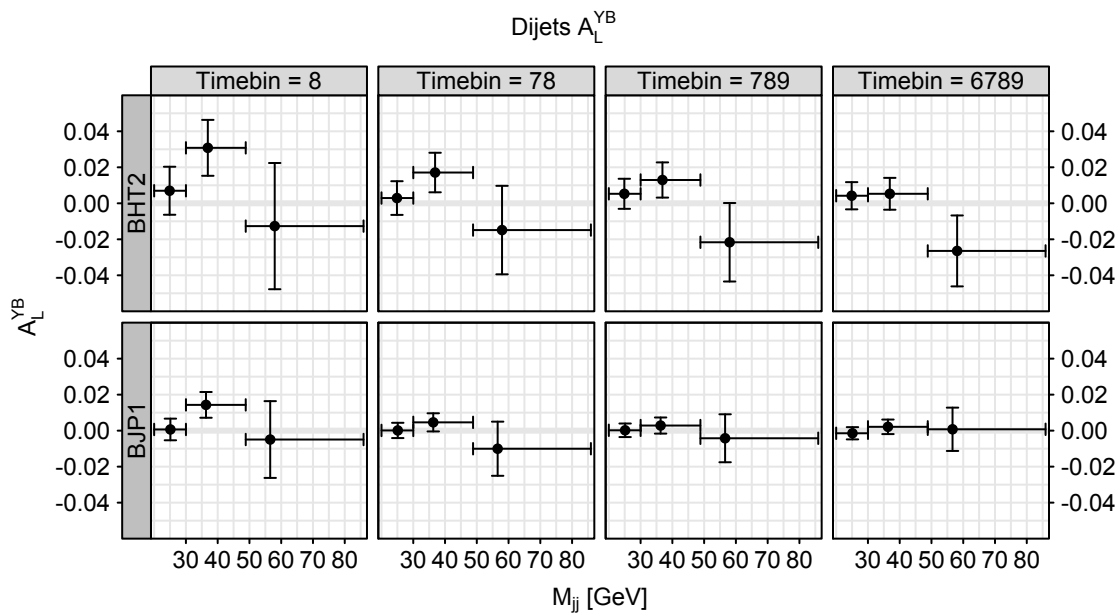
Figure 13-3: The single spin asymmetry for the Yellow beam $\mathcal{A}_L^{YB}$ as a function of the dijet invariant mass M_{jj} for each timebin set for each trigger.

Dijets A_L^{BB}
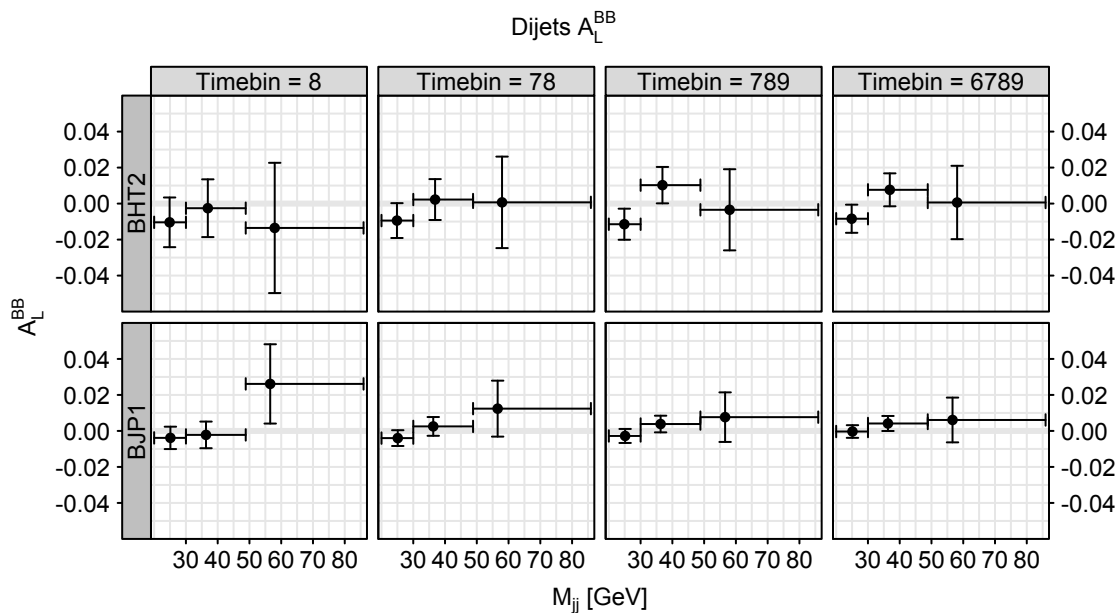
Figure 13-4: The single spin asymmetry for the Blue beam $\mathcal{A}_L^{BB}$ as a function of the dijet invariant mass M_{jj} for each timebin set for each trigger.

13.3.2 Wrong-Sign Spin Asymmetries

Two wrong-sign spin asymmetries are defined as follows. The like-sign asymmetry is

$$\mathcal{A}_{\text{LL}}^{\text{l.s}} = \frac{\sum P_{\text{Y}} P_{\text{B}}(N_5 - R_4 N_{10})}{\sum P_{\text{Y}}^2 P_{\text{B}}^2 (N_5 + R_4 N_{10})}.$$

The unlike-sign spin asymmetry is

$$\mathcal{A}_{\text{LL}}^{\text{u.s}} = \frac{\sum P_{\text{Y}} P_{\text{B}}(R_6 N_9 - R_5 N_6)}{\sum P_{\text{Y}}^2 P_{\text{B}}^2 (R_6 N_9 + R_5 N_6)}.$$

Figure 13-5 and Figure 13-6 show the wrong-sign spin asymmetries for each fill. Figure 13-7 and Figure 13-8 show the wrong-sign spin asymmetries as a function of the dijet invariant mass M_{jj}.
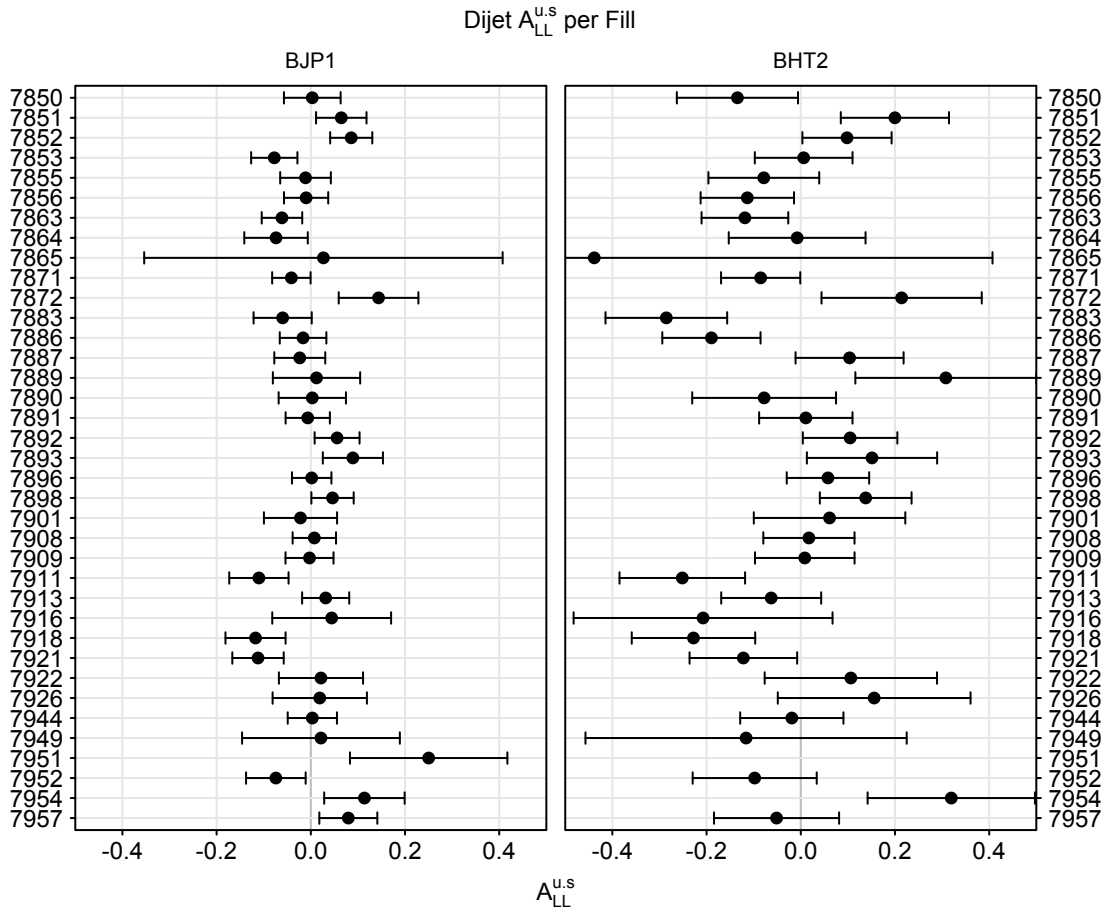
Figure 13-5: The like-sign spin asymmetry $\mathcal{A}_{LL}^{l.s}$ for each fill for each trigger.
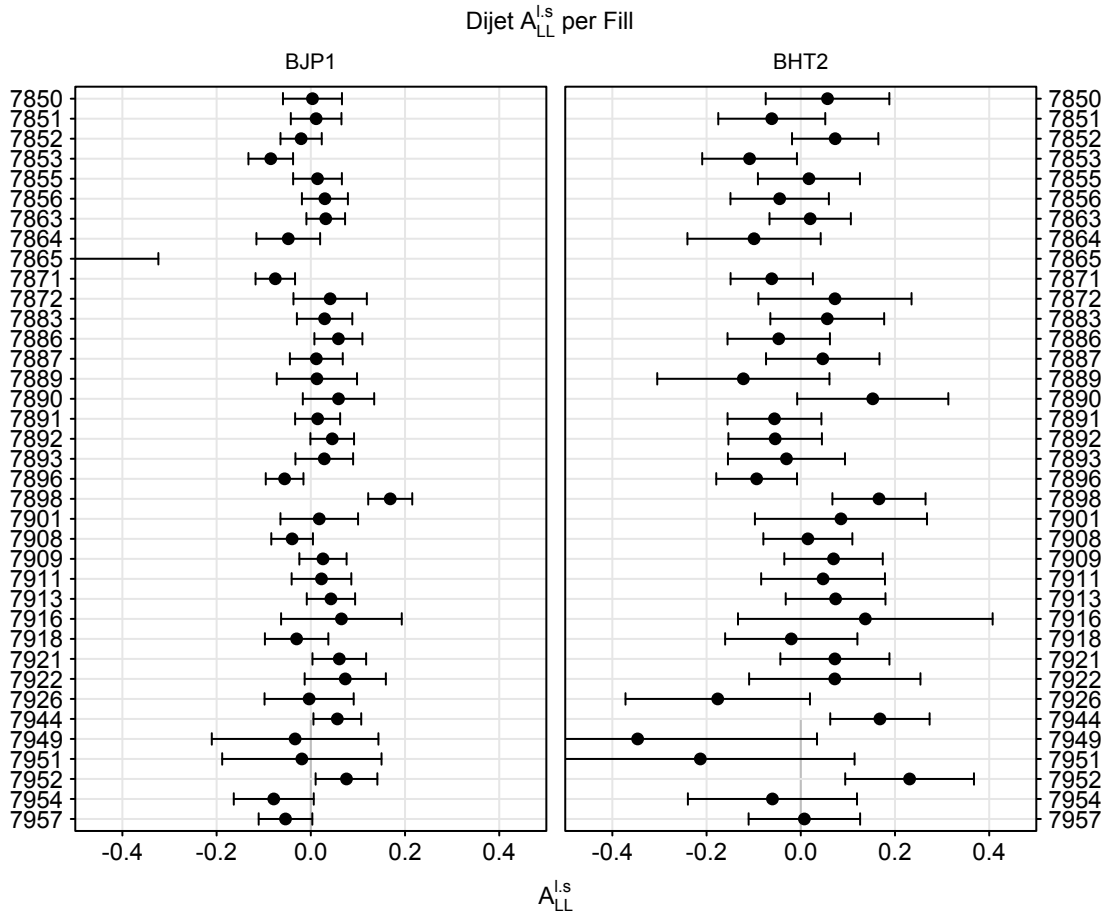
Figure 13-6: The unlike-sign spin asymmetry $\mathcal{A}_{LL}^{u,s}$ for each fill for each trigger.
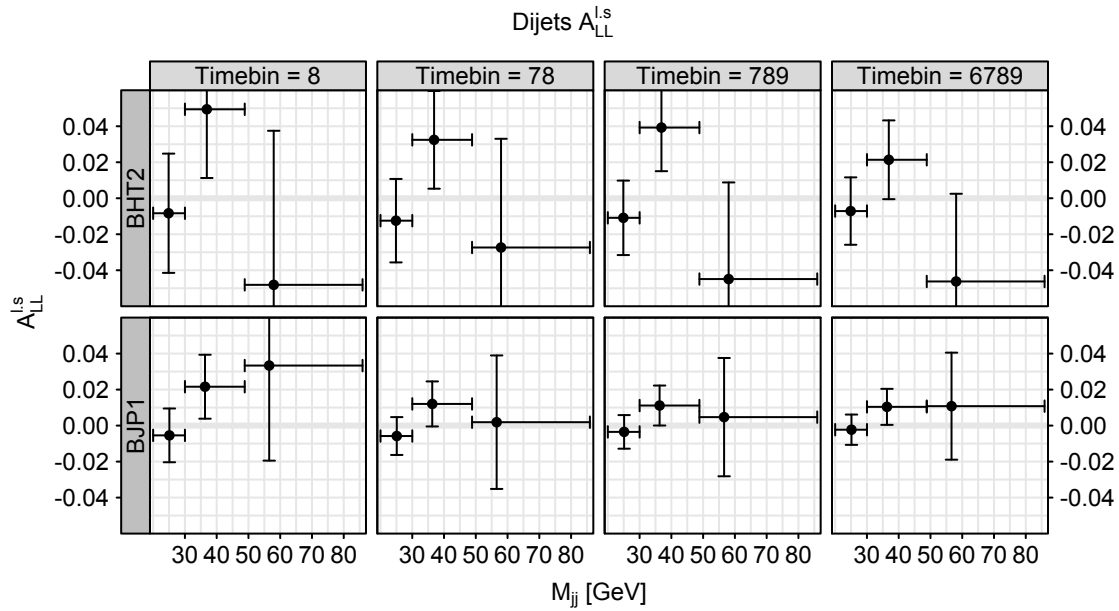
Figure 13-7: The like-sign spin asymmetry $\mathcal{A}_{LL}^{l.s}$ as a function of the dijet invariant mass M_{jj} for each timebin set for each trigger.
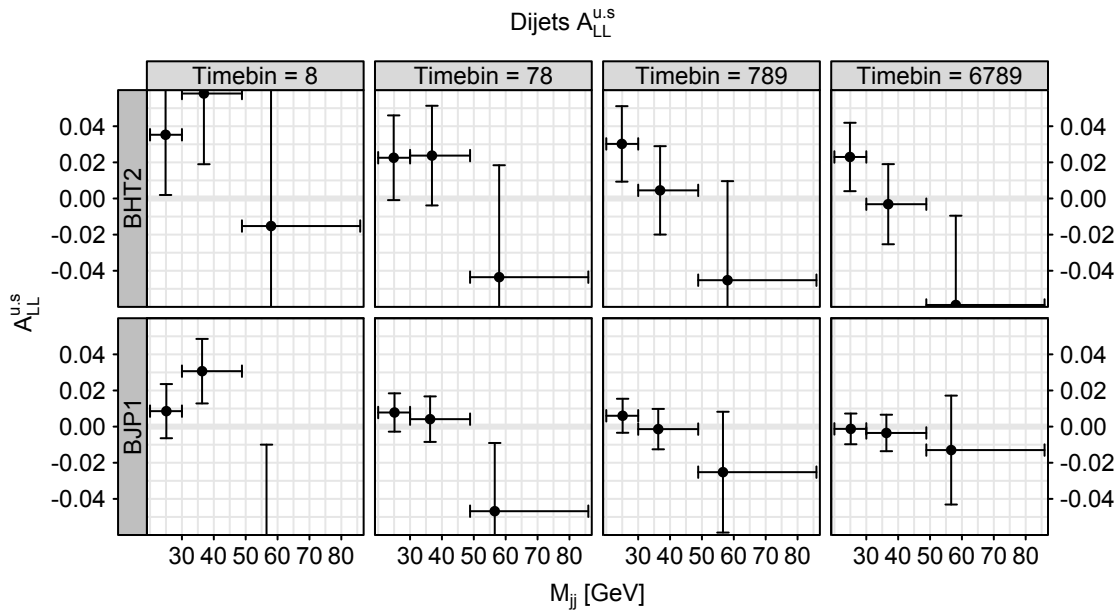
Figure 13-8: The unlike-sign spin asymmetry $\mathcal{A}_{LL}^{u.s}$ as a function of the dijet invariant mass M_{jj} for each timebin set for each trigger.

Figure 13-9 show the total asymmetries for the four false asymmetries for each timebin set and each trigger.
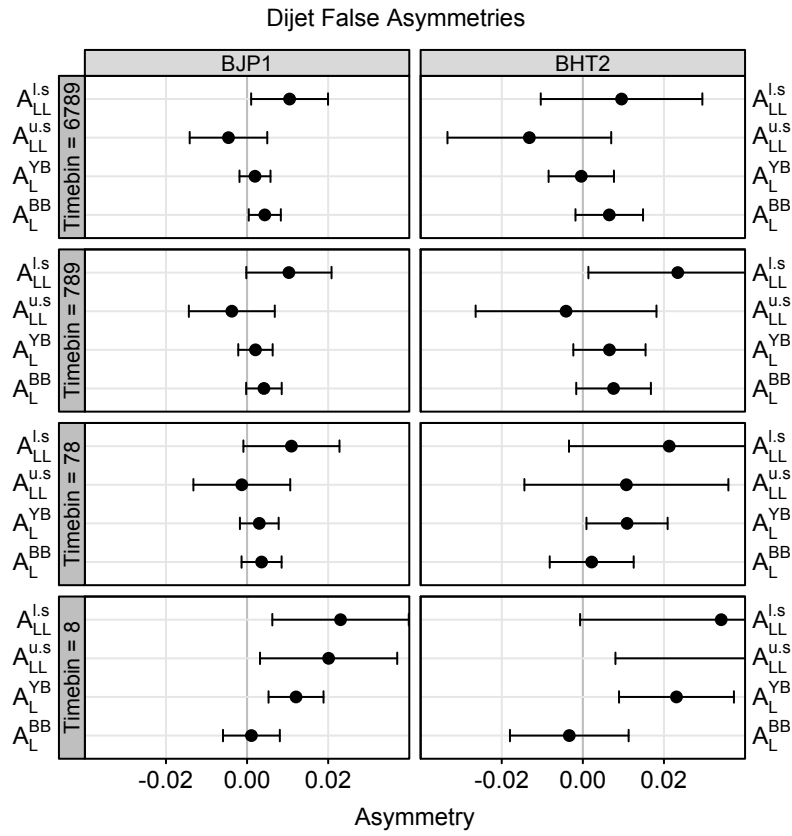
Figure 13-9: Dijet false asymmetries.

13.4   The Invariant Mass M_{jj} shift

The invariant mass shift from hadron level to detector level is evaluated with MC sample. The hadron-level jets and the detector-level jets are associated in the way described in Section 7.5. Table 13.4 gives the shifts and Figure 13-10 shows the distributions of the shifts. The Invariant Mass M_{jj} shifts are small.

$M_{jj}^{\mathbf{det}}$	$\Delta M_{jj} = M_{jj}^{\mathbf{det}} - M_{jj}^{\mathbf{had}}$	
	ΔM_{jj}	$\delta(\Delta M_{jj})$
Timebin = 8		
20.00-30.01	-0.824	0.905
30.01-48.83	0.823	1.111
48.83-85.92	3.934	0.299
Timebin = 78		
20.00-30.01	-1.255	0.830
30.01-48.83	0.037	1.067
48.83-85.92	3.961	0.282
Timebin = 789		
20.00-30.01	-1.045	0.828
30.01-48.83	0.620	1.038
48.83-85.92	3.952	0.277
Timebin = 6789		
20.00-30.01	-1.243	0.780
30.01-48.83	0.127	1.006
48.83-85.92	3.991	0.269

Table 13.4: The invariant mass M_{jj} shift.
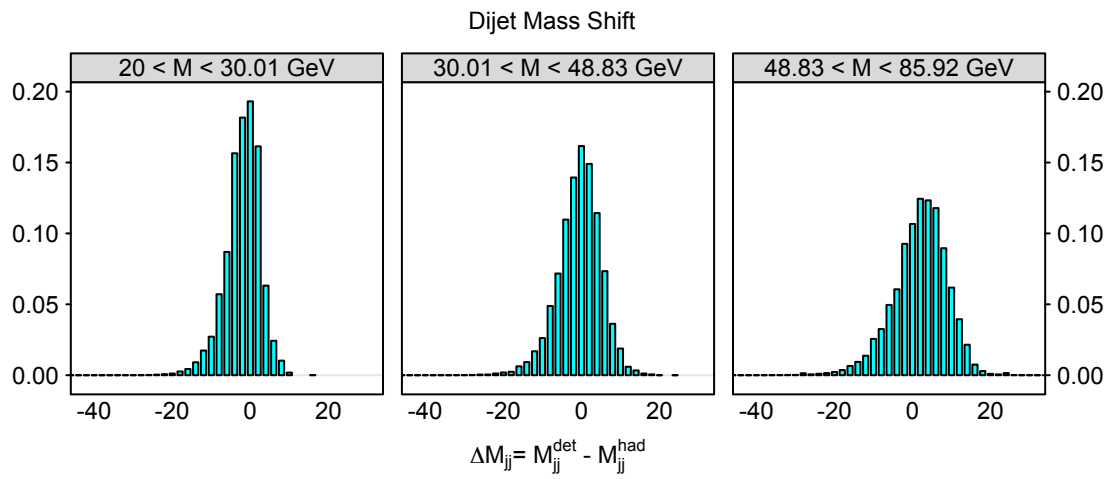
Figure 13-10: The invariant mass M_{jj} shift.

13.5 Results

Figure 13-11 shows the double longitudinal spin asymmetry $\mathcal{A}_{LL}$ for dijet production in polarized proton-proton collisions at $\sqrt{s} = 200$ GeV as a function of dijet mass M_{jj} in the mid-rapidity region $\eta < 0.8$.

The results are consistent with the next-to-leading perturbative QCD prediction with the DSSV polarized parton distributions. The results are consistent the inclusive jet $\mathcal{A}_{LL}$.
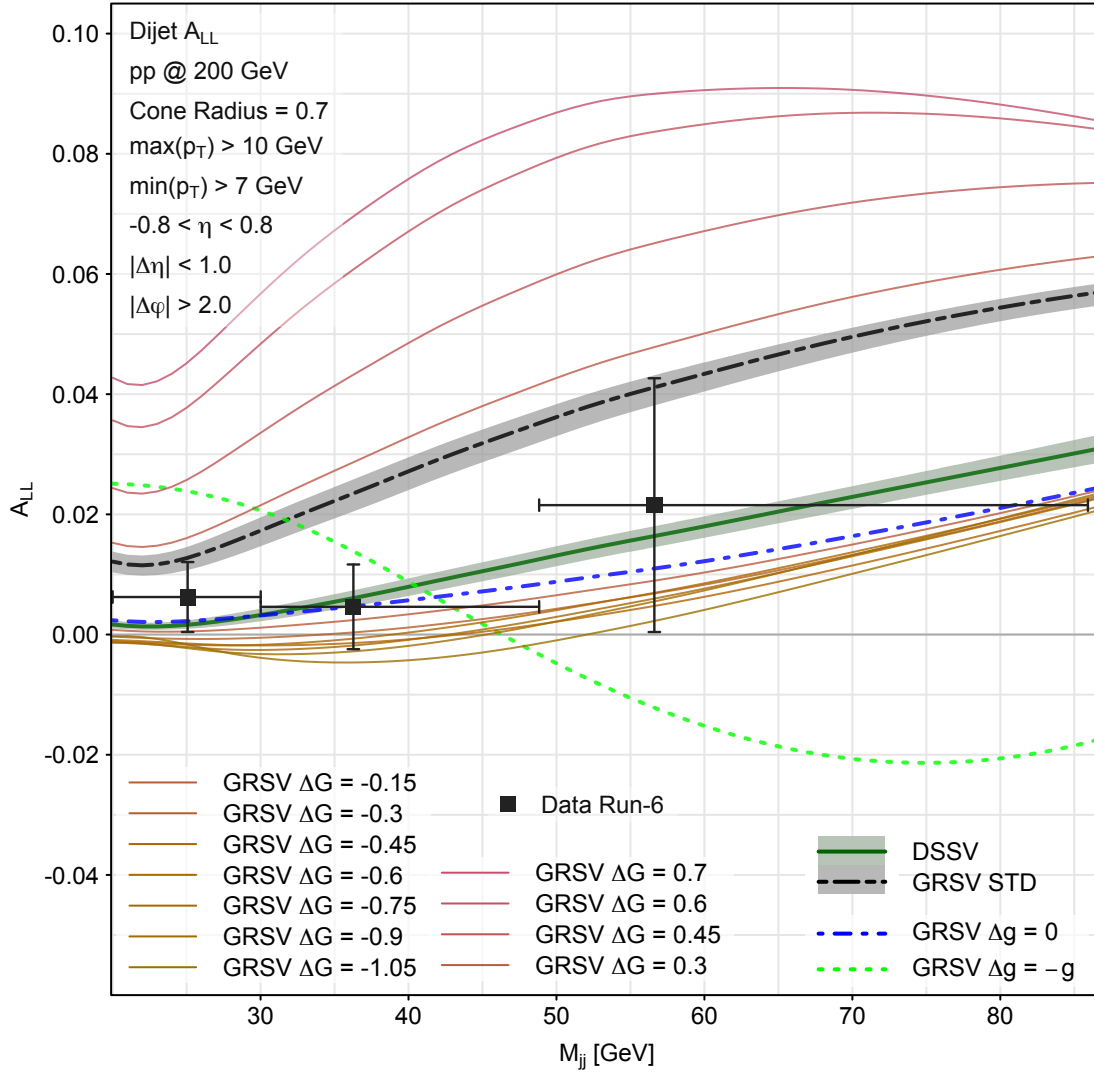
Figure 13-11: The double longitudinal spin asymmetry $\mathcal{A}_{LL}$ for the dijet production as a function of dijet mass M_{jj} in polarized proton-proton collisions at $\sqrt{s} = 200$ GeV from RHIC Run-6 data. The vertical bars on the data points indicate the size of the statistical errors. The horizontal bars on the data points indicate the bin widths. The data points are plotted at the mean values of M_{jj} of the events in the bins. Predictions of next-to-leading perturbative QCD with various models of the polarized gluon distributions are shown.

Chapter 14

Conclusion

It has not been successful to describe the proton spin in terms the spin and orbital motions of quarks and gluons. Polarized deep inelastic scattering has shown that the quark spin carry only a fraction of the proton spin. It was suggested by theorists that the gluon spin and the orbital motions of quarks and gluons carry the rest of the proton spin.

The double longitudinal spin asymmetry $\mathcal{A}_{\mathrm{LL}}$ in polarized proton-proton collisions has been measured for various final states at RHIC in order to investigate the gluon polarization inside the proton. The results of inclusive measurements, including the inclusive jet $\mathcal{A}_{\mathrm{LL}}$, suggested a possibility of the small gluon spin contribution ΔG.

In this thesis, dijet $\mathcal{A}_{\mathrm{LL}}$ is shown along with the dijet cross section and the inclusive jet cross section. The cross sections are in agreement with the NLO pQCD predictions, which provides the interpretation of $\mathcal{A}_{\mathrm{LL}}$. The dijet $\mathcal{A}_{\mathrm{LL}}$ is compared with the NLO pQCD predictions based on a variety of models of the polarized gluon distribution. The result also supports the possibility of the small gluon contribution ΔG.

So far, the data from RHIC have probed only a limited range of x. It is possible that gluons with small-x or even large-x carry a large fraction of the proton spin. It is possible to extend the range of x with jet measurement at STAR. So far the jet $\mathcal{A}_{\mathrm{LL}}$ has been measured only at the mid-rapidity $|\eta| < 1$ with the BEMC. Extending the

analysis to include the endcap EMC, which covers $1 < \eta < 2$, corresponds to probe smaller-x. The STAR detector has a calorimeter at further forward area: FMS, which covers $2.5 < \eta < 4.0$. Jet measurement with FMS might be challenging, however neutral pion measurement with FMS can extend the range of x even smaller. The present $\mathcal{A}_{\mathrm{LL}}$ measurements have been carried out with 200 GeV collisions. Data have been collected with higher energy 500 GeV also. Results of analyses of the data are expected to probe smaller-x.

An advantage of the dijet is its sensitivity to parton-level kinematics. In this thesis, the dijet $\mathcal{A}_{\mathrm{LL}}$ was measured as a function of the dijet invariant mass. This is a relevant choice of variable for the first measurement of dijets. However the dijet invariant mass is not an optimal variable to probe the proton structure. It is desirable to measure dijet $\mathcal{A}_{\mathrm{LL}}$ in terms of variables which have more direct relations with the parton-level interactions: such as average η, which is an estimate of the boost to the CM frame of the parton-level interaction: $\Delta\eta$, which has a simple relation with the scattering angle of the parton-level interaction: and estimates of x_1 and x_2.

In order to determine the parton-level kinematics in proton-proton collisions, it is necessary to estimate momenta of both outgoing partons. Dijets are a natural choice of final states to measure in order to observe the parton-level interactions whose final states are quarks and gluons. Measuring the parton-level interactions whose final states are particles which are not subject to confinement might make estimating the parton-level kinematics easier. For example, in Drell-Yan processes, the final states are leptons. Measuring the momentum of leptons is simpler than measuring the jet momentum. However, since gluons do not participate in Drell-Yan processes, this channel is not useful to probe gluons in the proton. In the photon-jet production, photons can be measured as photons, so it might be easier to determine the parton-level kinematics with this channel. Direct photons are produced only from gluon-gluon collisions or quark-gluon collisions, therefore the photon-jet production is an ideal channel for probing gluons, especially for large-x. In contrast, dijet production in large-x region is dominated by quark-quark interactions.

The gluon contribution has been little constrained from polarized deep inelastic scattering since all pDIS experiments have been target experiments. pDIS in a collider provides better data for probing the polarized gluon distribution. With collider pDIS, it will be possible to measure the structure function $g_1(x, Q^2)$ in the wide range of Q^2, which might make it possible to extract polarized gluon distribution from the Q^2 evolution of $g_1(x, Q^2)$. In collider pDIS, it is easier to observe hard interactions in which gluons are directly involved. Dijet production in a collider pDIS provides an access to the polarized gluon distribution with parton-level kinematics.

Appendix A

Kinematics of $2 \rightarrow 2$ Interactions

Initial State in the Lab Frame

The four-momenta of the incoming partons are determined by two variables: x_1 and x_2, the fractions of the proton momenta carried by the initial partons.

$$\hat{p}_1 = \frac{\sqrt{s}}{2} \begin{pmatrix} x_1 \\ 0 \\ 0 \\ x_1 \end{pmatrix}, \qquad \hat{p}_2 = \frac{\sqrt{s}}{2} \begin{pmatrix} x_2 \\ 0 \\ 0 \\ -x_2 \end{pmatrix}, \tag{A.1}$$

where $\sqrt{s}$ is the center of mass energy of the proton-proton collision. The two body system of the incoming partons has the momentum $q = p_1 + p_2$.

$$q = \frac{\sqrt{s}}{2} \begin{pmatrix} x_1 + x_2 \\ 0 \\ 0 \\ x_1 - x_2 \end{pmatrix} \tag{A.2}$$

In the s-channel, the propagator of the hard interaction has this momentum. Since $(q^0)^2 - (q^3)^2 = sx_1x_2$, the *rapidity y* of q has the following relations with x_1 and x_2:

$$\cosh y = \frac{q^0}{\sqrt{(q^0)^2 - (q^3)^2}} = \frac{1}{2} \cdot \frac{x_1 + x_2}{\sqrt{x_1 x_2}} = \frac{1}{2} \left(\sqrt{\frac{x_1}{x_2}} + \sqrt{\frac{x_2}{x_1}} \right)$$

$$\sinh y = \frac{q^3}{\sqrt{(q^0)^2 - (q^3)^2}} = \frac{1}{2} \cdot \frac{x_1 - x_2}{\sqrt{x_1 x_2}} = \frac{1}{2} \left(\sqrt{\frac{x_1}{x_2}} - \sqrt{\frac{x_2}{x_1}} \right).$$

Since $e^y = \cosh y + \sinh y = \sqrt{x_2/x_1}$,

$$y = \frac{1}{2} \log \frac{x_2}{x_1}. \tag{A.3}$$

Initial State in the CM Frame

The CM frame is the frame in which q is at rest; therefore, the boost from the lab frame to the CM frame is the boost along the direction of q with the rapidity $-y$. Such a boost always exists since q is a time-like momentum.
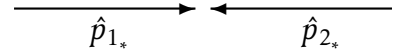
$$K(-y) = \begin{pmatrix} \cosh y & 0 & 0 & -\sinh y \\ 0 & 1 & 0 & 0 \\ 0 & 0 & 1 & 0 \\ -\sinh y & 0 & 0 & \cosh y \end{pmatrix} = \frac{1}{2\sqrt{x_1 x_2}} \begin{pmatrix} x_1 + x_2 & 0 & 0 & -x_1 + x_2 \\ 0 & 1 & 0 & 0 \\ 0 & 0 & 1 & 0 \\ -x_1 + x_2 & 0 & 0 & x_1 + x_2 \end{pmatrix}. \tag{A.4}$$

This boost brings q at rest by definition.

$$q_* = K(-y) \cdot q = \begin{pmatrix} \sqrt{sx_1 x_2} \\ 0 \\ 0 \\ 0 \end{pmatrix} \tag{A.5}$$

Either by sharing the momentum q_* equally between two light-like momenta along the z-axis or equivalently by boosting the momentum (A.1) by $K(-y)$, the momenta

of the initial partons are:

$$\hat{p}_{1*} = \frac{\sqrt{s x_1 x_2}}{2} \begin{pmatrix} 1 \\ 0 \\ 0 \\ 1 \end{pmatrix}, \quad \hat{p}_{2*} = \frac{\sqrt{s x_1 x_2}}{2} \begin{pmatrix} 1 \\ 0 \\ 0 \\ -1 \end{pmatrix}. \tag{A.6}$$

Final State in the CM Frame

The kinematical properties of the hard interactions are determined by the two kinematical variables: the *rapidity* y_* and the *azimuthal angle* φ. φ are invariant and y_* is additive under the boost along the z-axis. While φ is significant in transversely polarized collisions, it is not significant in longitudinally polarized collisions, which is the case in this thesis.
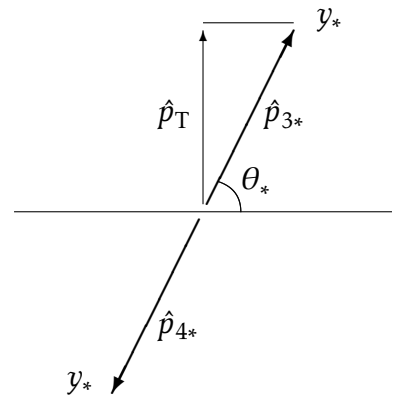
If an outgoing parton i is massless and has the transverse momentum $\hat{p}_\mathrm{T}$, $(\hat{p}_{i*}^1)^2 + (\hat{p}_{i*}^2)^2 = \hat{p}_\mathrm{T}^2$, $(\hat{p}_{i*}^0)^2 - (\hat{p}_{i*}^3)^2 = \hat{p}_\mathrm{T}^2$. While the angle φ determines $\hat{p}_{i*}^1$ and $\hat{p}_{i*}^2$, the rapidity y_* determines $\hat{p}_{i*}^0$ and $\hat{p}_{i*}^3$.

$$\hat{p}_{3*} = \hat{p}_\mathrm{T} \begin{pmatrix} \cosh y_* \\ \cos \varphi \\ \sin \varphi \\ \sinh y_* \end{pmatrix}, \quad \hat{p}_{4*} = \hat{p}_\mathrm{T} \begin{pmatrix} \cosh y_* \\ -\cos \varphi \\ -\sin \varphi \\ -\sinh y_* \end{pmatrix}. \tag{A.7}$$

Since $q_* = \hat{p}_{3*} + \hat{p}_{4*}$, from (A.5) and (A.7), the transverse momentum $\hat{p}_\mathrm{T}$ is determined by the rapidity y_* and the initial parton momentum fractions x_1 and x_2.

$$\sqrt{s x_1 x_2} = 2 \hat{p}_\mathrm{T} \cosh y_* \tag{A.8}$$

$$\hat{p}_{3*} = \frac{\sqrt{sx_1x_2}}{2\cosh y_*}\begin{pmatrix} \cosh y_* \\ \cos\varphi \\ \sin\varphi \\ \sinh y_* \end{pmatrix}, \qquad \hat{p}_{4*} = \frac{\sqrt{sx_1x_2}}{2\cosh y_*}\begin{pmatrix} \cosh y_* \\ -\cos\varphi \\ -\sin\varphi \\ -\sinh y_* \end{pmatrix}. \tag{A.9}$$

The energies of the outgoing partons $\hat{p}_{3*}^0$ and $\hat{p}_{4*}^0$ are independent of the rapidity y_*.

The scattering angle θ_* is the angle between the direction of the momentum of an outgoing parton and the z-axis; $\cos\theta_* = \hat{p}_{3*}^3/|\hat{\boldsymbol{p}}_{3*}|$. Since, $\hat{p}_{3*}^3/|\hat{\boldsymbol{p}}_{3*}| = \sinh y_*/\sqrt{1 + \sinh^2 y_*} = \tanh y_*$, θ_* and y_* have simple relations.

$$\cos\theta_* = \tanh y_* \tag{A.10}$$

$$\csc\theta_* = \cosh y_* \tag{A.11}$$

$$\cot\theta_* = \sinh y_* \tag{A.12}$$

In terms of θ_*, p_{3*} and p_{4*} are

$$\hat{p}_{3*} = \hat{p}_{\mathrm{T}}\begin{pmatrix} \csc\theta_* \\ \cos\varphi \\ \sin\varphi \\ \cot\theta_* \end{pmatrix}, \qquad \hat{p}_{4*} = \hat{p}_{\mathrm{T}}\begin{pmatrix} \csc\theta_* \\ -\cos\varphi \\ -\sin\varphi \\ -\cot\theta_* \end{pmatrix}. \tag{A.13}$$

Final State in the Lab Frame

Finally, to describe the final state kinematics in the lab frame in terms of kinematical variables of the initial state and the hard interaction in the CM frame, the momenta $\hat{p}_{3*}$ and $\hat{p}_{4*}$ are boosted back from the lab frame to the CM frame. The boost from the lab frame to the CM frame is the inverse of the transformation (A.4); $K^{-1}(-y) = K(y)$.
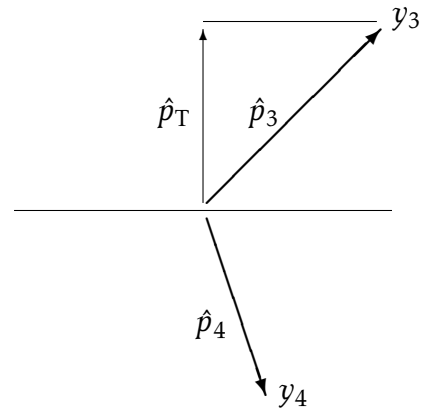
$$
K(y) = \begin{pmatrix} \cosh y & 0 & 0 & \sinh y \\ 0 & 1 & 0 & 0 \\ 0 & 0 & 1 & 0 \\ \sinh y & 0 & 0 & \cosh y \end{pmatrix} = \frac{1}{2\sqrt{x_1 x_2}} \begin{pmatrix} x_1 + x_2 & 0 & 0 & x_1 - x_2 \\ 0 & 1 & 0 & 0 \\ 0 & 0 & 1 & 0 \\ x_1 - x_2 & 0 & 0 & x_1 + x_2 \end{pmatrix}.
$$

With this Boost, the momenta (A.7) are:

$$
\hat{p}_3 = K(y)\hat{p}_{3*} = \hat{p}_{\mathrm{T}} \begin{pmatrix} \cosh(y + y_*) \\ \cos\varphi \\ \sin\varphi \\ \sinh(y + y_*) \end{pmatrix}, \qquad \hat{p}_4 = K(y)\hat{p}_{4*} = \hat{p}_{\mathrm{T}} \begin{pmatrix} \cosh(y + y_*) \\ -\cos\varphi \\ -\sin\varphi \\ -\sinh(y + y_*) \end{pmatrix}. \tag{A.14}
$$

The invariance of $\hat{p}_{\mathrm{T}}$ and φ and the additive property of the rapidity under a boost along z-axis are manifested in the relation between (A.7) and (A.14).

$$
y_3 = y + y_*
$$

$$
y_4 = y - y_*
$$

Therefore,

$$
\hat{p}_3 = \hat{p}_{\mathrm{T}} \begin{pmatrix} \cosh y_3 \\ \cos\varphi \\ \sin\varphi \\ \sinh y_3 \end{pmatrix}, \qquad \hat{p}_4 = \hat{p}_{\mathrm{T}} \begin{pmatrix} \cosh y_4 \\ -\cos\varphi \\ -\sin\varphi \\ -\sinh y_4 \end{pmatrix}. \tag{A.15}
$$

In the above formulae, the final state momenta in the lab frame $\hat{p}_3$ and $\hat{p}_4$ are determined by the four variables: $\hat{p}_{\mathrm{T}}$, y_3, y_4, φ

With (A.3) and (A.8), the momenta $\hat{p}_3$ and $\hat{p}_4$ can be written in terms of the kinematical variables that characterize the initial state (x_1 and x_2) and the hard interaction (y_*

and φ).

$$\hat{p}_3 = \frac{\sqrt{s}}{4\cosh y_*} \begin{pmatrix} (x_1 + x_2)\cosh y_* + (x_1 - x_2)\sinh y_* \\ 2\sqrt{x_1 x_2}\cos\varphi \\ 2\sqrt{x_1 x_2}\sin\varphi \\ (x_1 + x_2)\sinh y_* + (x_1 - x_2)\cosh y_* \end{pmatrix} \tag{A.16}$$

$$\hat{p}_4 = \frac{\sqrt{s}}{4\cosh y_*} \begin{pmatrix} (x_1 + x_2)\cosh y_* - (x_1 - x_2)\sinh y_* \\ -2\sqrt{x_1 x_2}\cos\varphi \\ -2\sqrt{x_1 x_2}\sin\varphi \\ -(x_1 + x_2)\sinh y_* + (x_1 - x_2)\cosh y_* \end{pmatrix}. \tag{A.17}$$

Initial State in the CM Frame in Terms of Final State in the Lab Frame

From (A.6) and (A.8), in terms of $\hat{p}_T$ and y_*, the momenta of the incoming partons in the CM frame are

$$\hat{p}_{1*} = \hat{p}_T\cosh y_* \begin{pmatrix} 1 \\ 0 \\ 0 \\ 1 \end{pmatrix}, \qquad \hat{p}_{2*} = \hat{p}_T\cosh y_* \begin{pmatrix} 1 \\ 0 \\ 0 \\ -1 \end{pmatrix}.$$

The boost from the CM frame to the lab frame brings them in the lab frame:

$$\hat{p}_1 = K(y)\hat{p}_{1*} = \hat{p}_T\cosh y_* e^y \begin{pmatrix} 1 \\ 0 \\ 0 \\ 1 \end{pmatrix}, \qquad \hat{p}_2 = K(y)\hat{p}_{2*} = \hat{p}_T\cosh y_* e^{-y} \begin{pmatrix} 1 \\ 0 \\ 0 \\ -1 \end{pmatrix}.$$

By comparing them with (A.1), $\hat{p}_T\cosh y_* e^y = (\sqrt{s}/2)x_1$, $\hat{p}_T\cosh y_* e^{-y} = (\sqrt{s}/2)x_2$. Therefore,

$$x_1 = \frac{2}{\sqrt{s}}\hat{p}_T\cosh y_* e^y \tag{A.18}$$

$$x_2 = \frac{2}{\sqrt{s}}\hat{p}_T\cosh y_* e^{-y}. \tag{A.19}$$

Since $2\cosh y_* e^y = (e^{y_*}+e^{-y_*})e^y = e^{y+y_*}+e^{y-y_*} = e^{y_3}+e^{y_4}$ and $2\cosh y_* e^{-y} = (e^{y_*}+e^{-y_*})e^{-y} = e^{-y-y_*} + e^{-y+y_*} = e^{-y_3} + e^{-y_4}$,

$$x_1 = \frac{\hat{p}_T}{\sqrt{s}}(e^{+y_3} + e^{+y_4}) \tag{A.20}$$

$$x_2 = \frac{\hat{p}_T}{\sqrt{s}}(e^{-y_3} + e^{-y_4}), \tag{A.21}$$

in which x_1 and x_2 are written in terms of kinematical variables of the final states.

Mandelstam Variables

The Mandelstam variables are

$$\hat{s} = (\hat{p}_{1*} + \hat{p}_{2*})^2 \tag{A.22}$$

$$\hat{t} = (\hat{p}_{1*} - \hat{p}_{3*})^2 \tag{A.23}$$

$$\hat{u} = (\hat{p}_{1*} - \hat{p}_{4*})^2. \tag{A.24}$$

In terms of kinematic variables of the final states,

$$\hat{s} = \frac{4\hat{p}_T^2}{\sin_*^\theta} = 4\hat{p}_T^2 \cosh^2 y_* \tag{A.25}$$

$$\hat{t} = -\frac{1}{2}\hat{s}(1 - \cos\theta_*) = -2\hat{p}_T^2 \cosh y_* e^{-y_*} \tag{A.26}$$

$$\hat{u} = -\frac{1}{2}\hat{s}(1 + \cos\theta_*) = -2\hat{p}_T^2 \cosh y_* e^{y_*}. \tag{A.27}$$

Massive Outgoing Particles

When the mass of the outgoing partons cannot be ignored, (A.7) becomes

$$
\hat{p}_{3*} =
\begin{pmatrix}
\sqrt{\hat{p}_{\mathrm{T}}^2 + m_3^2}\,\cosh y_{3*} \\
\hat{p}_{\mathrm{T}}\cos\varphi \\
\hat{p}_{\mathrm{T}}\sin\varphi \\
\sqrt{\hat{p}_{\mathrm{T}}^2 + m_3^2}\,\sinh y_{3*}
\end{pmatrix},
\qquad
\hat{p}_{4*} =
\begin{pmatrix}
\sqrt{\hat{p}_{\mathrm{T}}^2 + m_4^2}\,\cosh y_{4*} \\
-\hat{p}_{\mathrm{T}}\cos\varphi \\
-\hat{p}_{\mathrm{T}}\sin\varphi \\
-\sqrt{\hat{p}_{\mathrm{T}}^2 + m_4^2}\,\sinh y_{4*}
\end{pmatrix}.
\tag{A.28}
$$

Unlike the case of massless outgoing partons, $y_{3*} \neq -y_{4*}$. From energy and momentum conservation:

$$
\sqrt{\hat{p}_{\mathrm{T}}^2 + m_3^2}\,\cosh y_{3*} + \sqrt{\hat{p}_{\mathrm{T}}^2 + m_4^2}\,\cosh y_{4*} = \sqrt{\hat{s}}
$$

$$
\sqrt{\hat{p}_{\mathrm{T}}^2 + m_3^2}\,\sinh y_{3*} - \sqrt{\hat{p}_{\mathrm{T}}^2 + m_4^2}\,\sinh y_{4*} = 0,
$$

y_{3*} and y_{4*} are

$$
y_3^* = \frac{1}{2}\ln\left(\frac{(\hat{s} + m_3^2 - m_4^2) + \sqrt{\hat{s}^2 - 2\hat{s}(m_3^2 + m_4^2 + 2\hat{p}_{\mathrm{T}}^2) + (m_3^2 - m_4^2)^2}}{(\hat{s} + m_3^2 - m_4^2) - \sqrt{\hat{s}^2 - 2\hat{s}(m_3^2 + m_4^2 + 2\hat{p}_{\mathrm{T}}^2) + (m_3^2 - m_4^2)^2}} \right)
$$

$$
y_4^* = \frac{1}{2}\ln\left(\frac{(\hat{s} - m_3^2 + m_4^2) - \sqrt{\hat{s}^2 - 2\hat{s}(m_3^2 + m_4^2 + 2\hat{p}_{\mathrm{T}}^2) + (m_3^2 - m_4^2)^2}}{(\hat{s} - m_3^2 + m_4^2) + \sqrt{\hat{s}^2 - 2\hat{s}(m_3^2 + m_4^2 + 2\hat{p}_{\mathrm{T}}^2) + (m_3^2 - m_4^2)^2}} \right).
$$

Therefore, $\hat{p}_{3*}$ and $\hat{p}_{3*}$ are

$$
\hat{p}_{3*} =
\begin{pmatrix}
(\hat{s} + m_3^2 - m_4^2)/2\sqrt{\hat{s}} \\
\hat{p}_{\mathrm{T}}\cos\varphi \\
\hat{p}_{\mathrm{T}}\sin\varphi \\
\sqrt{\hat{s}^2 - 2\hat{s}(m_3^2 + m_4^2 + 2\hat{p}_{\mathrm{T}}^2) + (m_3^2 - m_4^2)^2}/2\sqrt{\hat{s}}
\end{pmatrix}
\tag{A.29}
$$

$$\hat{p}_{4*} = \begin{pmatrix} (\hat{s} - m_3^2 + m_4^2)/2\sqrt{\hat{s}} \\ -\hat{p}_{\mathrm{T}}\cos\varphi \\ -\hat{p}_{\mathrm{T}}\sin\varphi \\ -\sqrt{\hat{s}^2 - 2\hat{s}(m_3^2 + m_4^2 + 2\hat{p}_{\mathrm{T}}^2) + (m_3^2 - m_4^2)^2}/2\sqrt{\hat{s}} \end{pmatrix}. \tag{A.30}$$

(A.13) becomes

$$\hat{p}_{3*} = \begin{pmatrix} \sqrt{m_3^2 + \hat{p}_{\mathrm{T}}^2\csc^2\theta_*} \\ \hat{p}_{\mathrm{T}}\cos\varphi \\ \hat{p}_{\mathrm{T}}\sin\varphi \\ \hat{p}_{\mathrm{T}}\cot\theta_* \end{pmatrix}, \quad \hat{p}_{4*} = \begin{pmatrix} \sqrt{m_4^2 + \hat{p}_{\mathrm{T}}^2\csc^2\theta_*} \\ -\hat{p}_{\mathrm{T}}\cos\varphi \\ -\hat{p}_{\mathrm{T}}\sin\varphi \\ -\hat{p}_{\mathrm{T}}\cot\theta_* \end{pmatrix}. \tag{A.31}$$

Appendix B

Covariance between Counts and Weighted Counts

If X_i is a random sample from Bernoulli distribution with the parameter p, the sum $X = \sum_{i=1}^{N} X_i$ will have Binomial distribution with parameter p and N. In the limit of $N \to \infty$ while keeping $pN = n$, the distribution of X becomes close to Poisson distribution with the mean n. In other words,

$$E(X) = E\left(\sum_{i=1}^{N} X_i\right) = \sum_{i=1}^{N} (E(X_i)) = \sum_{i=1}^{N} p = Np \to n(N \to \infty)$$

$$\mathrm{Var}(X) = \sum_{i=1}^{N} \mathrm{Var}(X_i) = \sum_{i=1}^{N} p(1-p) = Np(1-p) \to n(N \to \infty).$$

If Y is a weighted sum of X_i, $Y = \sum_{i=1}^{N} w_i X_i$; then,

$$E(Y) = E\left(\sum_{i=1}^{N} w_i X_i\right) = \sum_{i=1}^{N} (w_i E(X_i)) = \sum_{i=1}^{N} w_i p = p \sum_{i=1}^{N} w_i \to \sum_{i=1}^{n} w_i (N \to \infty)$$

$$\mathrm{Var}(Y) = \sum_{i=1}^{N} \mathrm{Var}(w_i X_i) = \sum_{i=1}^{N} w_i^2 \mathrm{Var}(X_i) = \sum_{i=1}^{N} w_i^2 p(1-p) = p(1-p) \sum_{i=1}^{N} w_i^2 \to \sum_{i=1}^{n} w_i^2 (N \to \infty).$$

The means of X^2 and Y^2 are

$$E(X^2) = \mathrm{Var}(X) + E(X)^2 = n + n^2$$

$$E(Y^2) = \text{Var}(Y) + E(Y)^2 = \sum_{i=1}^{n} w_i^2 + \left(\sum_{i=1}^{n} w_i \right)^2.$$

In a similar way, the mean of XY is

$$E(XY) = \sum_{i=1}^{n} w_i + n \sum_{i=1}^{n} w_i.$$

Incidentally, had X been weighted with the weight of v_i,

$$E(XY) = \sum_{i=1}^{n} (v_i w_i) + \left(\sum_{i=1}^{n} v_i \right) \left(\sum_{i=1}^{n} w_i \right).$$

The covariacne is

$$\text{Cov}(X, Y) = E(XY) - E(X)E(Y)$$
$$= \sum_{i=1}^{n} w_i + n \sum_{i=1}^{n} w_i - n \sum_{i=1}^{n} w_i$$
$$= \sum_{i=1}^{n} w_i.$$

The covariacne is the sum of the weights.

Bibliography

[1] M. Breidenbach *et al.*, "Observed Behavior of Highly Inelastic electron-Proton Scattering," *Phys. Rev. Lett.* **23** (1969) 935–939.

[2] **European Muon** Collaboration, J. Ashman *et al.*, "A measurement of the spin asymmetry and determination of the structure function g(1) in deep inelastic muon proton scattering," *Phys. Lett.* **B206** (1988) 364.

[3] **COMPASS** Collaboration, V. Y. Alexakhin *et al.*, "The Deuteron Spin-dependent Structure Function g1d and its First Moment," *Phys. Lett.* **B647** (2007) 8–17, `arXiv:hep-ex/0609038`.

[4] G. Altarelli and G. G. Ross, "The Anomalous Gluon Contribution to Polarized Leptoproduction," *Phys. Lett.* **B212** (1988) 391.

[5] T. Gehrmann and W. J. Stirling, "Polarized Parton Distributions in the Nucleon," *Phys. Rev.* **D53** (1996) 6100–6109, `arXiv:hep-ph/9512406`.

[6] M. Gluck, E. Reya, M. Stratmann, and W. Vogelsang, "Models for the polarized parton distributions of the nucleon," *Phys. Rev.* **D63** (2001) 094005, `arXiv:hep-ph/0011215`.

[7] E. Leader, A. V. Sidorov, and D. B. Stamenov, "Longitudinal polarized parton densities updated," *Phys. Rev.* **D73** (2006) 034023, `arXiv:hep-ph/0512114`.

[8] **Asymmetry Analysis** Collaboration, M. Hirai, S. Kumano, and N. Saito, "Determination of polarized parton distribution functions and their uncertainties," *Phys. Rev.* **D69** (2004) 054021, `arXiv:hep-ph/0312112`.

[9] D. de Florian, G. A. Navarro, and R. Sassot, "Sea quark and gluon polarization in the nucleon at NLO accuracy," *Phys. Rev.* **D71** (2005) 094018, arXiv:hep-ph/0504155.

[10] **HERMES** Collaboration, A. Airapetian *et al.*, "Measurement of the spin asymmetry in the photoproduction of pairs of high p(T) hadrons at HERMES," *Phys. Rev. Lett.* **84** (2000) 2584–2588, arXiv:hep-ex/9907020.

[11] **Spin Muon (SMC)** Collaboration, B. Adeva *et al.*, "Spin asymmetries for events with high p(T) hadrons in DIS and an evaluation of the gluon polarization," *Phys. Rev.* **D70** (2004) 012002, arXiv:hep-ex/0402010.

[12] **COMPASS** Collaboration, E. S. Ageev *et al.*, "Gluon polarization in the nucleon from quasi-real photoproduction of high-p(T) hadron pairs," *Phys. Lett.* **B633** (2006) 25–32, arXiv:hep-ex/0511028.

[13] **COMPASS** Collaboration, M. Alekseev *et al.*, "Gluon polarisation in the nucleon and longitudinal double spin asymmetries from open charm muoproduction," *Phys. Lett.* **B676** (2009) 31–38, arXiv:0904.3209 [hep-ex].

[14] **E581** Collaboration, D. L. Adams *et al.*, "First results for the two spin parameter A(LL) in pi0 production by 200-GeV polarized protons and anti-protons," *Phys. Lett.* **B261** (1991) 197–200.

[15] **PHENIX** Collaboration, S. S. Adler *et al.*, "Double helicity asymmetry in inclusive mid-rapidity pi0 production for polarized p + p collisions at s**(1/2) = 200-GeV," *Phys. Rev. Lett.* **93** (2004) 202002, arXiv:hep-ex/0404027.

[16] **PHENIX** Collaboration, S. S. Adler *et al.*, "Improved measurement of double helicity asymmetry in inclusive midrapidity pi0 production for polarized p + p collisions at s**(1/2) = 1200-GeV," *Phys. Rev.* **D73** (2006) 091102, arXiv:hep-ex/0602004.

[17] **PHENIX** Collaboration, A. Adare *et al.*, "Inclusive cross section and double helicity asymmetry for pi0 production in p+p collisions at sqrt(s)=200 GeV:

Implications for the polarized gluon distribution in the proton," *Phys. Rev.* **D76** (2007) 051106, arXiv:0704.3599 [hep-ex].

[18] **STAR** Collaboration, B. I. Abelev *et al.*, "Longitudinal double-spin asymmetry and cross section for inclusive jet production in polarized proton collisions at s**(1/2) = 200-GeV," *Phys. Rev. Lett.* **97** (2006) 252001, arXiv:hep-ex/0608030.

[19] **STAR** Collaboration, B. I. Abelev *et al.*, "Longitudinal double-spin asymmetry for inclusive jet production in p+p collisions at sqrt(s)=200 GeV," *Phys. Rev. Lett.* **100** (2008) 232003, arXiv:0710.2048 [hep-ex].

[20] D. de Florian, R. Sassot, M. Stratmann, and W. Vogelsang, "Global Analysis of Helicity Parton Densities and Their Uncertainties," *Phys. Rev. Lett.* **101** (2008) 072001, arXiv:0804.0422 [hep-ph].

[21] I. Alekseev *et al.*, "Polarized proton collider at RHIC," *Nucl. Instrum. Meth.* **A499** (2003) 392–414.

[22] A. Zelensky *et al.*, "On optically-pumped polarized H- ion source for RHIC spin physics," *Rev. Sci. Instrum.* **73** (2002) 888–891.

[23] Y. S. Derbenev *et al.*, "RADIATIVE POLARIZATION: OBTAINING, CONTROL, USING," *Part. Accel.* **8** (1978) 115–126.

[24] T. Roser, "PROPERTIES OF PARTIALLY EXCITED SIBERIAN SNAKES," *AIP Conf. Proc.* **187** (1989) 1442–1446.

[25] A. Zelenski *et al.*, "Absolute polarized H-jet polarimeter development, for RHIC," *Nucl. Instrum. Meth.* **A536** (2005) 248–254.

[26] M. Anderson *et al.*, "The STAR time projection chamber: A unique tool for studying high multiplicity events at RHIC," *Nucl. Instrum. Meth.* **A499** (2003) 659–678, arXiv:nucl-ex/0301015.

[27] **STAR** Collaboration, M. Beddo *et al.*, "The STAR barrel electromagnetic calorimeter," *Nucl. Instrum. Meth.* **A499** (2003) 725–739.

[28] **STAR** Collaboration, F. Bergsma *et al.*, "The STAR detector magnet subsystem," *Nucl. Instrum. Meth.* **A499** (2003) 633–639.

[29] **STAR** Collaboration, J. Adams *et al.*, "Transverse momentum and collision energy dependence of high p(T) hadron suppression in Au + Au collisions at ultrarelativistic energies," *Phys. Rev. Lett.* **91** (2003) 172302, arXiv:nucl-ex/0305015.

[30] A. Drees and Z. Xu, "Results from Luminosity Scans during the RHIC 2000 Run,". Presented at IEEE Particle Accelerator Conference (PAC2001), Chicago, Illinois, 18-22 Jun 2001.

[31] V. Ptitsyn *et al.*, "RHIC performance as polarized proton collider in Run-6,". Prepared for European Particle Accelerator Conference (EPAC 06), Edinburgh, Scotland, 26-30 Jun 2006.

[32] G. C. Blazey *et al.*, "Run II jet physics," arXiv:hep-ex/0005012.

[33] B. Jager, M. Stratmann, and W. Vogelsang, "Single inclusive jet production in polarized pp collisions at $O(alpha_s^3)$," *Phys. Rev.* **D70** (2004) 034010, arXiv:hep-ph/0404057.

[34] T. Sjostrand, S. Mrenna, and P. Skands, "PYTHIA 6.4 Physics and Manual," *JHEP* **05** (2006) 026, arXiv:hep-ph/0603175.

[35] **CTEQ** Collaboration, H. L. Lai *et al.*, "Global QCD analysis of parton structure of the nucleon: CTEQ5 parton distributions," *Eur. Phys. J.* **C12** (2000) 375–392, arXiv:hep-ph/9903282.

[36] R. Brun *et al. Technical Report CERN-DD/EE/84-1* (1987) .

[37] **CDF** Collaboration, R. Field and R. C. Group, "PYTHIA tune A, HERWIG, and JIMMY in Run 2 at CDF," arXiv:hep-ph/0510198.

[38] J. M. Chambers, *Statistical Models in S.* CRC Press, Inc., Boca Raton, FL, USA, 1991.

[39] J. Pumplin *et al.*, "New generation of parton distributions with uncertainties from global QCD analysis," *JHEP* **07** (2002) 012, `arXiv:hep-ph/0201195`.

[40] J. Millane, "Longitudinal Double Spin Asymmetry for Inclusive Jet Production in Polarized Proton-Proton Collisions at 200 GeV," *MIT Thesis* (2008) .

[41] M. Sarsour, "Inclusive Jets Double Helicity Asymmetry for Polarized p+p Collisions at 200 GeV Analysis Note," *STAR Analysis Note* (2008) .

[42] G. D. Lafferty and T. R. Wyatt, "Where to stick your data points: The treatment of measurements within wide bins," *Nucl. Instrum. Meth.* **A355** (1995) 541–547.

[43] A. D. Martin, R. G. Roberts, W. J. Stirling, and R. S. Thorne, "Physical gluons and high E(T) jets," *Phys. Lett.* **B604** (2004) 61–68, `arXiv:hep-ph/0410230`.

Index